AFRPL-TR-71-103

LONG-LIFE MONOPROPELLANT HYDRAZINE ENGINE DEVELOPMENT PROGRAM

Bruce W. Schmitz
Walter W. Wilson

FINAL REPORT AFRPL-TR-71-103

September 1971

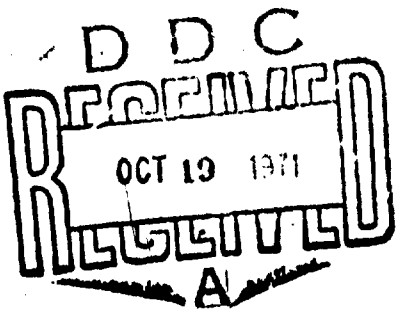

Air Force Rocket Propulsion Laboratory
Edwards Air Force Base
Edwards, California 93523

DOCUMENT CONTROL DATA - R & D

(Security classification of title, body of abstract and indexing annotation must be entered when the overall report is classified)

1. ORIGINATING ACTIVITY (Corporate author) Rocket Research Corporation York Center Redmond, Washington 98052	2a. REPORT SECURITY CLASSIFICATION Unclassified 2b. GROUP —

3. REPORT TITLE

LONG-LIFE MONOPROPELLANT HYDRAZINE ENGINE DEVELOPMENT PROGRAM – FINAL REPORT

4. DESCRIPTIVE NOTES (Type of report and inclusive dates)

Final Report April 6, 1970, to June 25, 1971

5. AUTHOR(S) (First name, middle initial, last name)

Bruce W. Schmitz
Walter W. Wilson

6. REPORT DATE	7a. TOTAL NO. OF PAGES	7b. NO. OF REFS
	179	5

8a. CONTRACT OR GRANT NO.	9a. ORIGINATOR'S REPORT NUMBER(S)
F04611-70-C-0036 b. PROJECT NO.	RRC-71-R-257
c.	9b. OTHER REPORT NO(S) (Any other numbers that may be assigned this report) AFRPL-TR-71-103
d.	

10. DISTRIBUTION STATEMENT

Approved for public release; distribution unlimited.

11. SUPPLEMENTARY NOTES	12. SPONSORING MILITARY ACTIVITY
	Air Force Rocket Propulsion Laboratory Edwards Air Force Base Edwards, California 93523

13. ABSTRACT

Rocket Research Corporation has conducted a research and development program under Contract F04611-70-C-0036 from AFRPL. The objective of the program was to demonstrate the capability of 1 x 10⁶ pulses without performance loss on a flightweight monopropellant hydrazine 5-lbf thruster. This report describes the design, analysis, and tests which evolved into the final flightweight rocket engine assembly (REA) design during Phase I of the program.

Phase IA testing of this REA accumulated 400,000 cycles of operation while delivering in excess of 80,000 lbf-sec with 20 ambient (40°F) cold starts prior to performance degradation. Results of the testing are presented, together with recommendations for extending life capability on the basis of REA teardown and failure analysis. Concurrent testing of workhorse REA's to evaluate the relationship of propellant and catalyst temperatures upon catalyst life characteristics is also reported.

DD FORM 1 NOV 68 1473 REPLACES DD FORM 1473, 1 JAN 64, WHICH IS OBSOLETE FOR ARMY USE.

Unclassified

Security Classification

NOTICES

When U. S. Government drawings, specifications, or other data are used for any purpose other than a definitely related Government procurement operation, the Government thereby incurs no responsibility nor any obligation whatsoever, and the fact that the Government may have formulated, furnished, or in any way supplied the said drawings, specifications, or other data, is not to be regarded by implication or otherwise, or in any manner licensing the holder or any other person or corporation, or conveying any rights or permission to manufacture, use, or sell any patented invention that may in any way be related thereto.

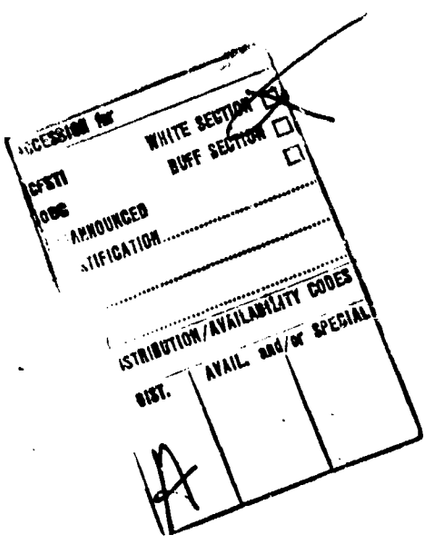

14. KEY WORDS	LINK A		LINK B		LINK C	
	ROLE	WT	ROLE	WT	ROLE	WT
Monopropellant hydrazine						
5-lbf thrust						
Rocket engine assembly						
Life demonstration tests						

LONG-LIFE MONOPROPELLANT HYDRAZINE ENGINE DEVELOPMENT PROGRAM

Bruce W. Schmitz
Walter W. Wilson

FINAL REPORT AFRPL-TR-71-103
September 1971

Air Force Rocket Propulsion Laboratory
Edwards Air Force Base
Edwards, California 93523

FOREWORD

This report covers work performed at Rocket Research Corporation (RRC), Redmond, Washington, for the Air Force Rocket Propulsion Laboratory under Contract FO4611-70-C-0036. The work under this contract was carried out during the period April 6, 1970, through June 25, 1971. The program manager was Mr. B. W. Schmitz; the project engineer was Mr. W. W. Wilson; and the test engineer was Mr. W. A. Arrera.

The program was completed under the technical management of Lt. Frank N. Fredrickson, USAF/LKDA. The contracting officer was Mr. D. G. Jorgensen of Edwards Air Force Base, Edwards, California.

This report has been assigned a supplementary report number 71-R-257.

This technical report has been reviewed and is approved.

Walter A. Detjen, Chief
Engine Development Branch

ABSTRACT

Rocket Research Corporation has conducted a research and development program under contract F04611-70-C-0036 from AFRPL. The objective of the program was to demonstrate the capability of 1 x 10^6 pulses without performance loss on a flightweight monopropellant hydrazine 5-lbf thruster. This report describes the design, analysis, and tests which evolved into the final flightweight rocket engine assembly (REA) design during Phase I of the program. Phase IA testing of this REA accumulated 400,000 cycles of operation while delivering in excess of 80,000 lbf-sec with 20 ambient (40°F) cold starts prior to performance degradation. Results of the testing are presented, together with recommendations for extending life capability on the basis of REA teardown and failure analysis. Concurrent testing of workhorse REA's to evaluate the relationship of propellant and catalyst temperatures upon catalyst life characteristics is also reported.

(Reverse side blank)

TABLE OF CONTENTS

LIST OF FIGURES

LIST OF FIGURES (Concluded)

LIST OF TABLES

LIST OF TABLES (Concluded)

(Reverse side blank)

BLANK PAGE

SECTION I

INTRODUCTION

With the development of Shell 405 catalyst, the inherent advantages of monopropellant hydrazine propulsion systems for attitude control and orbit adjust of spacecraft have resulted in their selection as replacements for bipropellants on existing vehicles (e.g., Transtage) and their selection for newer vehicles (e.g., P-95, Intelsat, NASA ERTS, NASA ATS F&G). These advantages of cost, simplicity, and reliability command the use of monopropellant hydrazine for generations of vehicles yet to come.

Monopropellant hydrazine qualification test programs completed to date have established significant milestones in demonstrating the capability of the Shell 405 catalyst to withstand extensive firing durations. At the attitude control thrust range (5 lbf), these programs have demonstrated up to 200,000-cycle capability while delivering as much as 20,000 lbf-sec impulse. Future vehicle requirements, however, have projected requirements of up to 1,000,000 cycles with 200,000 lbf-sec impulse delivered. To develop technology and engine design approaches which would meet these long life requirements, RRC was awarded Contract F04611-70-C-0036 by the Air Force Rocket Propulsion Laboratory. Work under the contract was initiated on April 6, 1970.

The objective of this research and development program was to demonstrate the capability of 1 x 10^6 pulses without performance loss on a flightweight monopropellant hydrazine 5-lbf thruster. The program performance goals were:

Thrust	5 lb (vacuum) ±6%
Impulse bit repeatability	±7% *
Centroid location	±5% *
Chamber pressure roughness	±7%
Steady-state I_{sp}	220 sec

*For 20 ms pulses only

Impulse bit repeatability	±10%
Centroid location	±5 ms

Specific areas of work studied during the program were:

a. *Phase I*

Design Iteration and Test – Those design improvements which were determined to improve engine life were incorporated and tested to verify their capability.

Thermal Analysis – A transient and steady-state thermal analysis was performed on the injector design improvements with thermal margin tests conducted to verify the analysis.

Catalyst Test – Nonflow cycle tests were conducted to verify the catalyst preload design criteria.

Cold Start Test Series – Steady-state starts were conducted on the selected design with both engine and propellant at 40°F and at maximum inlet pressure to evaluate cold-start capability.

Abbreviated Life Test – A cycling/cold-start test series was conducted to demonstrate the cycling capability of the selected design.

b. *Phase IA*

Life Cycle Test – The Phase I final design, as approved by AFRPL, was subjected to a life cycle test simulating typical mission duty cycles with a goal of 1,000,000 cycles.

Cold Start Catalyst Evaluation Test Series – A series of special tests were conducted on an engine simulating the flight design, in order to evaluate the independent effects of propellant temperature, catalyst temperature, and bed loading on catalyst life.

SECTION II

TECHNICAL PROGRAM

2.1 PHASE I DESIGN

The requirements of the contract were reviewed with respect to the capabilities of 5-lbf engine hardware currently developed and qualified at RRC. The 5-lbf thrust engine experience at RRC dates back to 1965, during which time experimental hardware was fabricated and parametrically evaluated under NASA Contract NAS7-372 to develop generalized design and scaling criteria for monopropellant hydrazine reactors. On the basis of these studies, a flightweight 5-lbf engine was developed and subjected to evaluation testing in pulse and steady-state modes of operation. Approximately 3 years ago, RRC was awarded a contract from Lockheed Missiles and Space Company for the design, development, qualification, and delivery of flight 5-lbf rocket engine assemblies mounted in a modular arrangement and termed REM-Mono (Reaction Engine Model – Monopropellant). This engine has completed its formal flight qualification test program and is currently in production for several space programs. This engine was considered as a baseline for the program described herein, and product improvements were incorporated to meet the longer life requirements. The following paragraphs describe the REM-Mono engine baseline and product improvement changes which were investigated.

2.1.1 REM-Mono 5-lbf Engine Characteristics

Mission requirements for the REM-Mono REA include operation in pulse mode at duty cycles ranging from 0.01-cps to steady-state conditions, pulse-mode life of 175,000 pulses, capability of steady-state burn times up to 20 minutes, delivery of 1[illegible],000 lbf-sec total impulse, and delivery of impulse bits not exceeding 0.15 lbf-sec (22-millisecond width).

Design -- The engine operates in blowdown mode over a nominal thrust range of 5.69 to 3.34 lbf. Table I summarizes the design characteristics of the engine, and a cutaway drawing is included in Figure 1. Figure 2 is a photograph of an assembled engine. Monopropellant hydrazine flows from a trim orifice through the thrust chamber valve and on through an all-welded single feed tube to a rigimesh dispersion element. Hydrazine is distributed from the rigimesh spud through the upper 0.25-inch, 25- to 30-mesh Shell 405 catalyst bed. An intermediate bed plate with screens welded on each side separates the upper bed from the lower bed, which is 0.65 inch of 14- to 18-mesh Shell 405 catalyst. A lower bed plate with screen retains the catalyst. Decomposed hydrazine exits through a 40:1 RAO nozzle. A 1/16-inch OD x 0.010-inch wall tube is provided to measure thrust chamber pressure, and a flight thermocouple is welded to the external convergent section of the nozzle to measure chamber temperature. The propellant valve is solenoid-operated and is manufactured by Parker Aircraft Company.

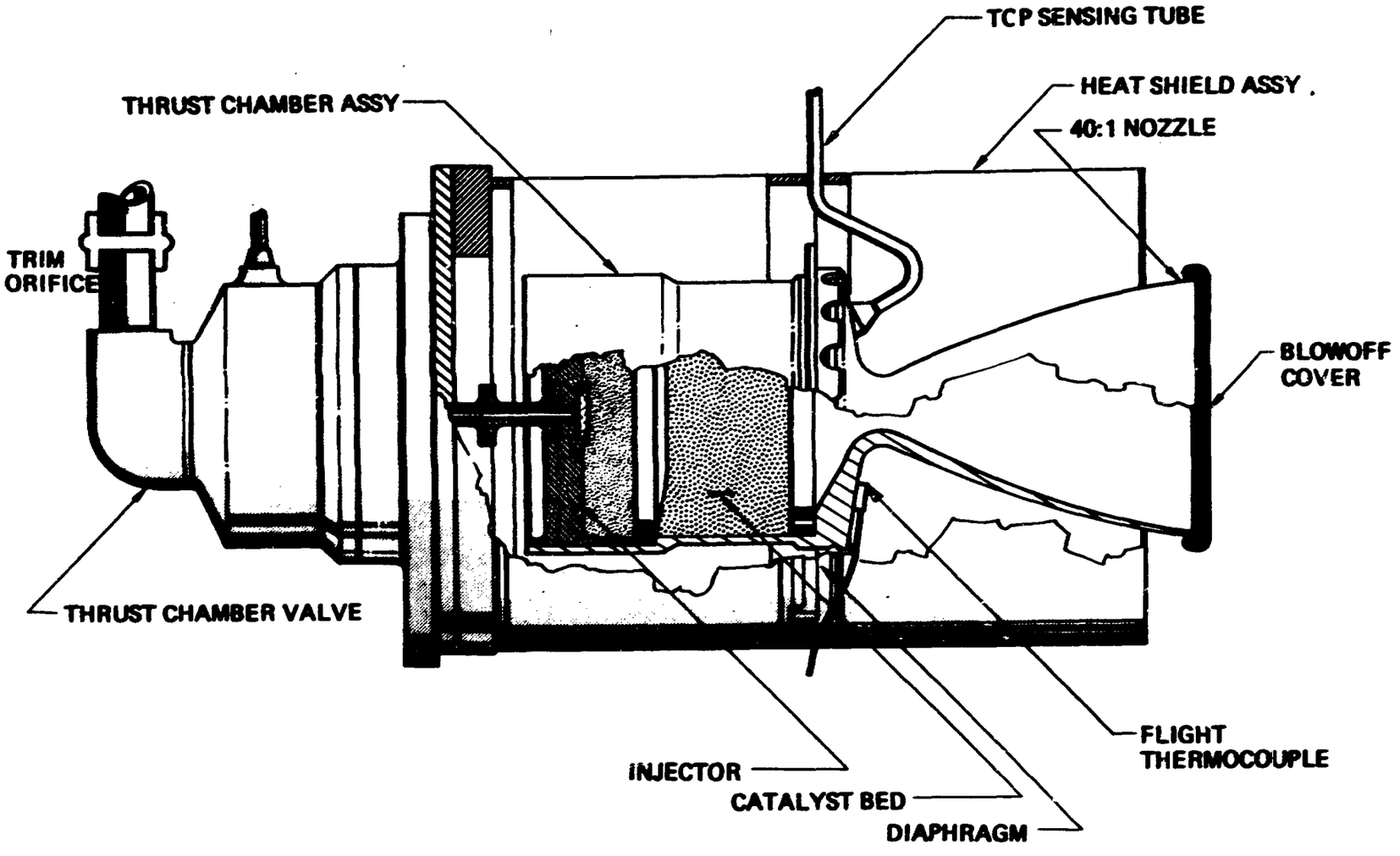

Figure 1. Reaction Engine Assembly

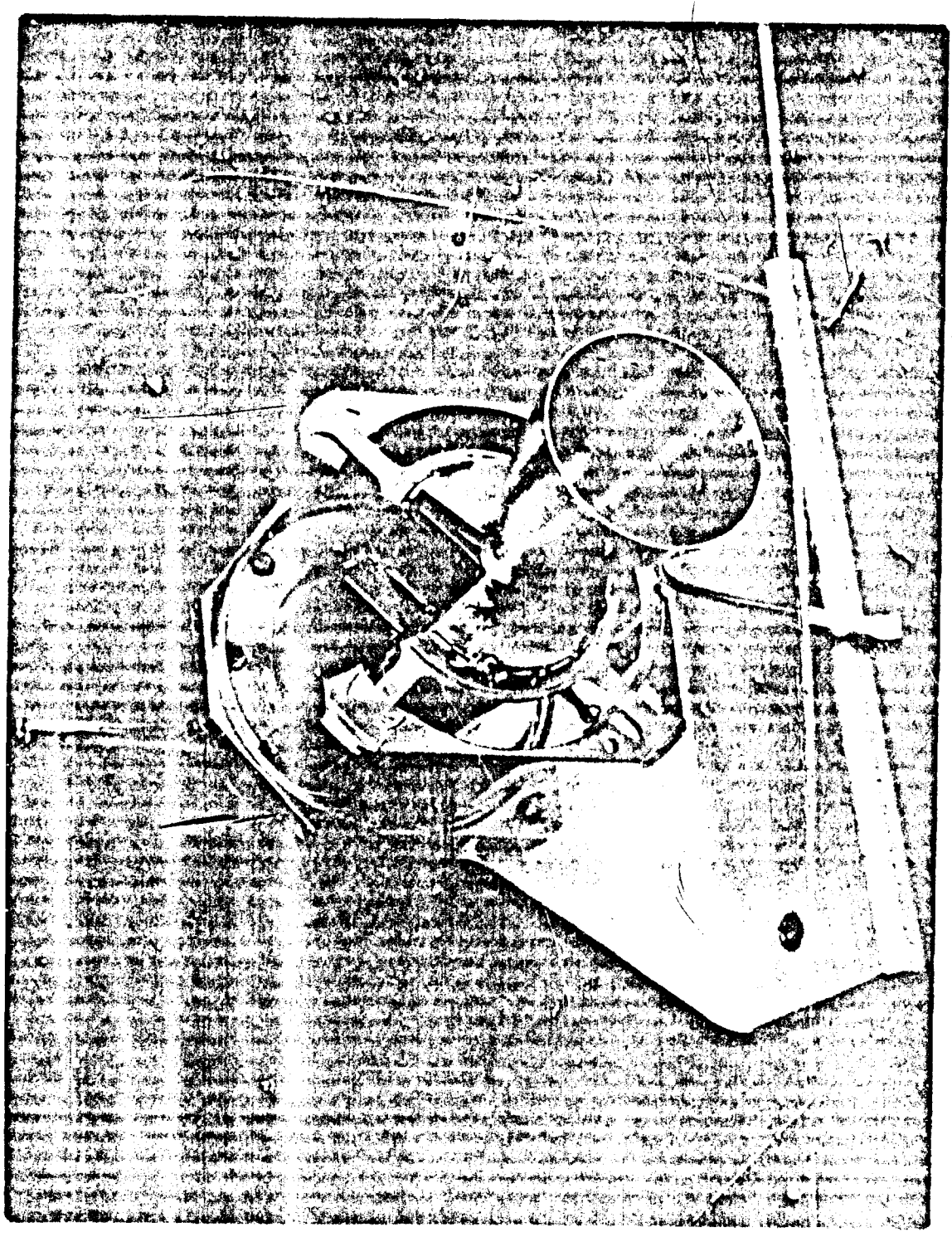

Figure 2. Long-Life Monopropellant Hydrazine Rocket Engine Assembly

Table I. REM-Mono REA Design Summary

Bed diameter, inches		1.179
Bed length, inches		0.90
Upper bed, inches		0.25
Lower bed, inches		0.65
Catalyst		
Upper bed	6.2 grams	25 to 30 mesh granules
Lower bed	16.2 grams	14 to 18 mesh granules
Nozzle		RAO contour
Expansion ratio		40
Throat diameter, inches		0.197 A_t = 0.03048 $in.^2$
Exit diameter, inches		1.246
Material selection		
Thrust chamber and nozzle		Haynes 25
Injector		Inconel 600
Rigimesh insert		Haynes 25
Bed plates and screens		Haynes 25
Weight, lbm		1.20

The engine is enclosed in a thermal shield for thermal control. At the aft end of the chamber, a diaphragm is welded between the chamber and heat shield. This provides for lateral structural support, differential thermal expansion, and also presents a high thermal resistance to limit heat transfer from the chamber to the heat shield. Axial loads are taken out by the propellant feed tube, which is welded to the propellant valve outlet to minimize propellant holdup volume.

The REA is mounted from the upper heat shield flange. Total REA weight is 1.20 lbm.

To satisfy the broad range of operating requirements of the REM-Mono Program, a conservative engine design was used. The catalyst bed is designed with a bed loading at 5 lbf of 0.020 lbm/in^2-sec to ensure long engine life. Program requirements include the capability of successfully operating at feed pressures as high as 315 psia. Consequently, all parts of the TCA are stressed to 375 psia at operating temperature.

The catalyst consists of Shell 405 ABSG 25- to 30-mesh granules for the upper bed and 14- to 18-mesh ABSG granules for the lower bed. No special treatment of the catalyst is conducted at Shell Development Corporation beyond calcining the basic carrier. Water-attrited catalyst has been used throughout the program based on superior strength characteristics determined from evaluation testing at RRC. After receipt at RRC, the catalyst undergoes special thermal processing. The catalyst bed packing procedures use an overpack to account for differential thermal expansion between the catalyst and the chamber walls.

Development History – The duty cycles under which the REM-Mono REA operates impose severe thermal design requirements on the engine. Worst-case thermal operation occurs at minimum thrust conditions with the propellant supply temperature at 140°F and the engine operating at approximately 1.2% duty cycle. Under these conditions, heat soakback raises the propellant valve temperature to approximately 220°F. The high valve temperature results in appreciable heating of the propellant before entering the injector. This situation is further aggravated by the combined requirements of minimum final thrust of 2.5 lbf and a maximum impulse bit of 0.15 lbf-sec. This combination results in a short pulse width and yields long residence time of the propellant in the valve during worst-case thermal conditions. The propellant, therefore, undergoes significant heating in the valve before entering the injector. The resulting thermal balance requirements are the most difficult that RRC has been required to meet in hydrazine engine programs.

After award of the REM-Mono contract to RRC, two injector design approaches were pursued. One was a scaleup of a 2.5-lbf engine design using a single feed tube feeding a single rigimesh spud of approximately the same diameter as that of the 2.5-lbf engine. The second used an annular rigimesh element fed by three passages branching from a single supply tube. The annular injector design represented a scaled-down version of the Transtage REA injector design. The annular injector design was pursued to provide better dispersion of the propellant across the catalyst bed than was available with the single spud.

Each design was fabricated under the REM-Mono Program and subjected to a severe altitude thermal and life design verification test. These tests were conducted over the complete range of operating pressures with inlet propellant temperatures from ambient to 160°F. Propellant boiling was evidenced with the annular injector design and was believed to be precipitated at the junction of the main feed passage with the three feed passages. The single-element injectors evidenced no boiling whatsoever; however, their steady-state roughness as a function of life was greater than that of the annular injector as shown in Figure 3. The engine did, however, satisfy the program requirements and was selected for REM-Mono. It is significant that the annular injector design exhibited significantly greater life capability than the single-spud design and for many space applications has sufficient thermal margins. The improved life characteristics of the annular injector design, shown in Table II, are believed due to better propellant dispersion into the catalyst bed and less sensitivity to small catalyst loss in the upper bed.

Based on results of the REM-Mono injector evaluation, the major product improvement was aimed at providing an injector with improved propellant dispersion capabilities while still maintaining unlimited thermal duty cycle capability. Injector designs which potentially could improve engine life are presented and discussed in the following paragraphs.

2.1.2 Baseline REA Design

The baseline REA used for the Long-Life Monopropellant Hydrazine Development Program is based on a product improvement to the REM-Mono 5-lbf rocket engine assembly (MR-50A). Figure 4 presents the drawing tree of the existing MR-50A engine with those drawings flagged that required revision for the baseline engine. Only 4 of the 28 drawings comprising the MR-50A required revision for the baseline design. Figure 5 is a cutaway of the baseline design.

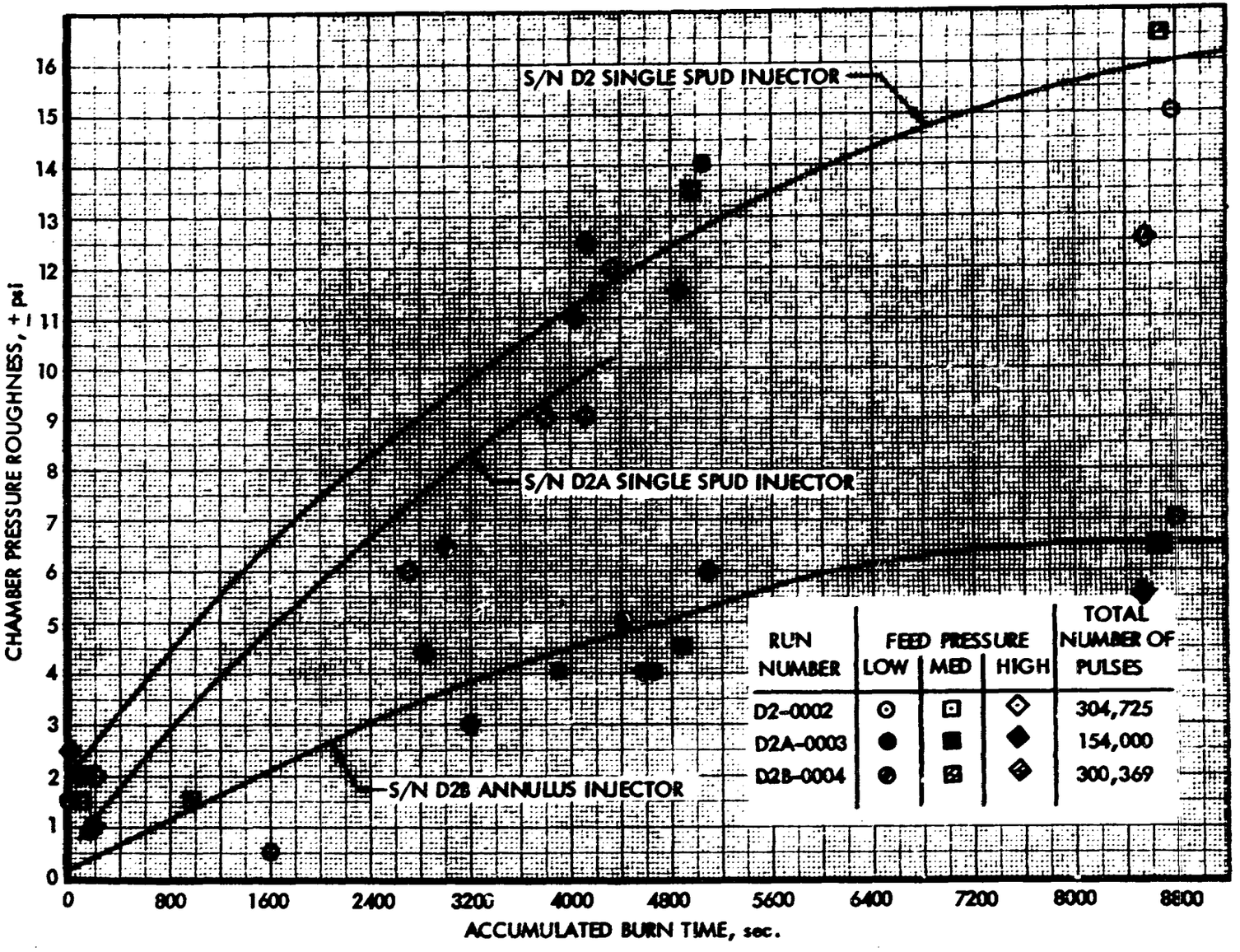

Figure 3. REM-Mono Chamber Pressure Roughness Data

Table II. REM-Mono Thrust Chamber Development

Engine S/N and Test Description	Valve S/N	Injector Configuration	Percent Roughness at 5 lbf at Completion	Total Pulses	Total Burn Time, sec	Comments
D2 Thermal margin (TM)	C507202	Spud	±12.5	304,725	8,745	No boiling
D2A Pulse life test	C507202	Spud	±11.5	154,000	5,563	No boiling
D2B (TM)	C507202	Annulus	± 5.5	300,369	9,766	Boiling
D2C Performance map test	C507202	Spud	±12.0	78,257	3,290	No boiling
D2D (TM)	03	Annulus	± 4.0	28,350	2,964	Boiling
D3 Thrust coefficient test	03	Spud	±15.0	185,000	5,779	No boiling
D4A Pulse life test	03	Spud	±12.0	201,360	5,088	No boiling
			Total	1,098,215	41,195	

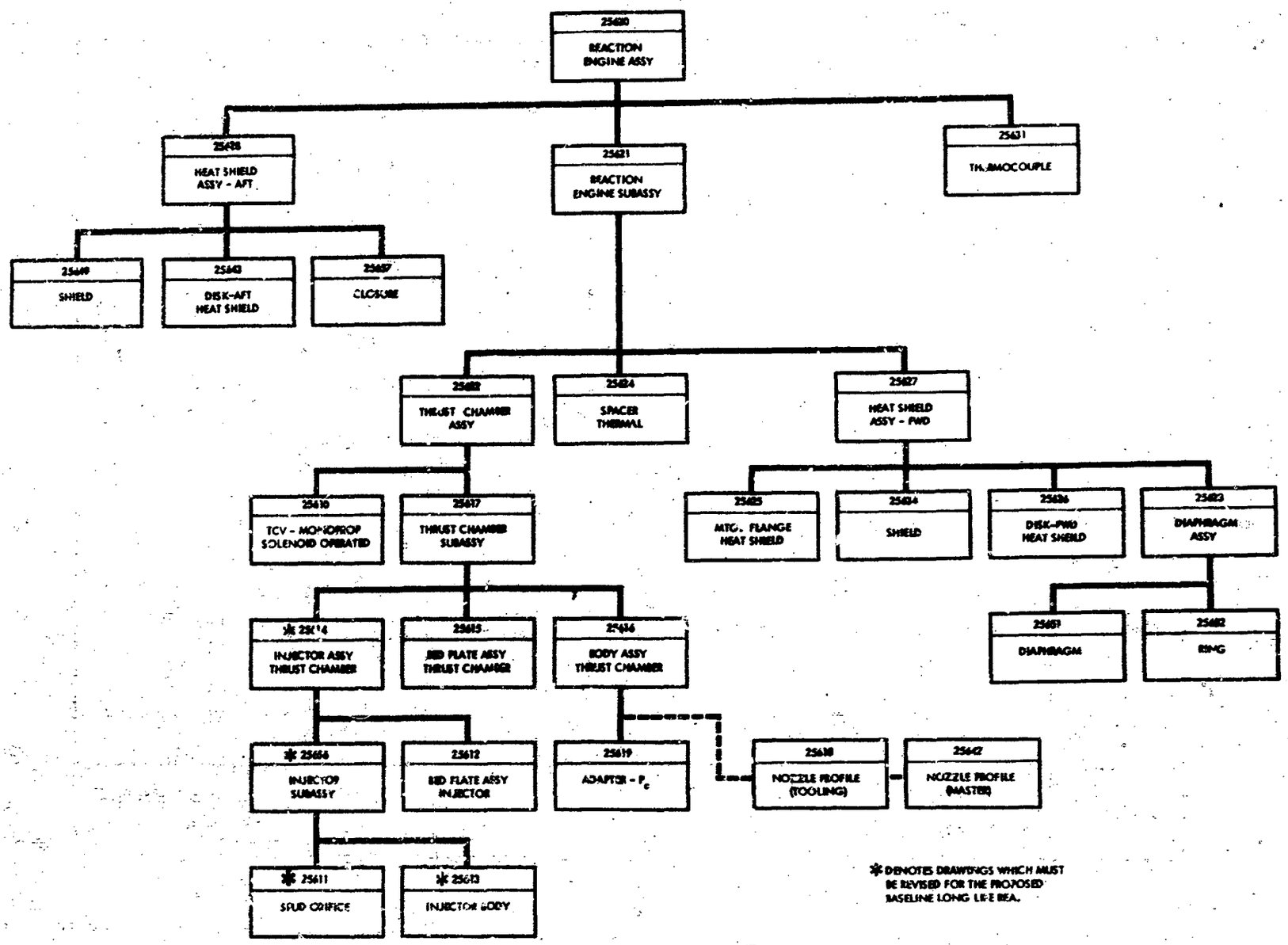

Figure 4. MR-50A Drawing Tree

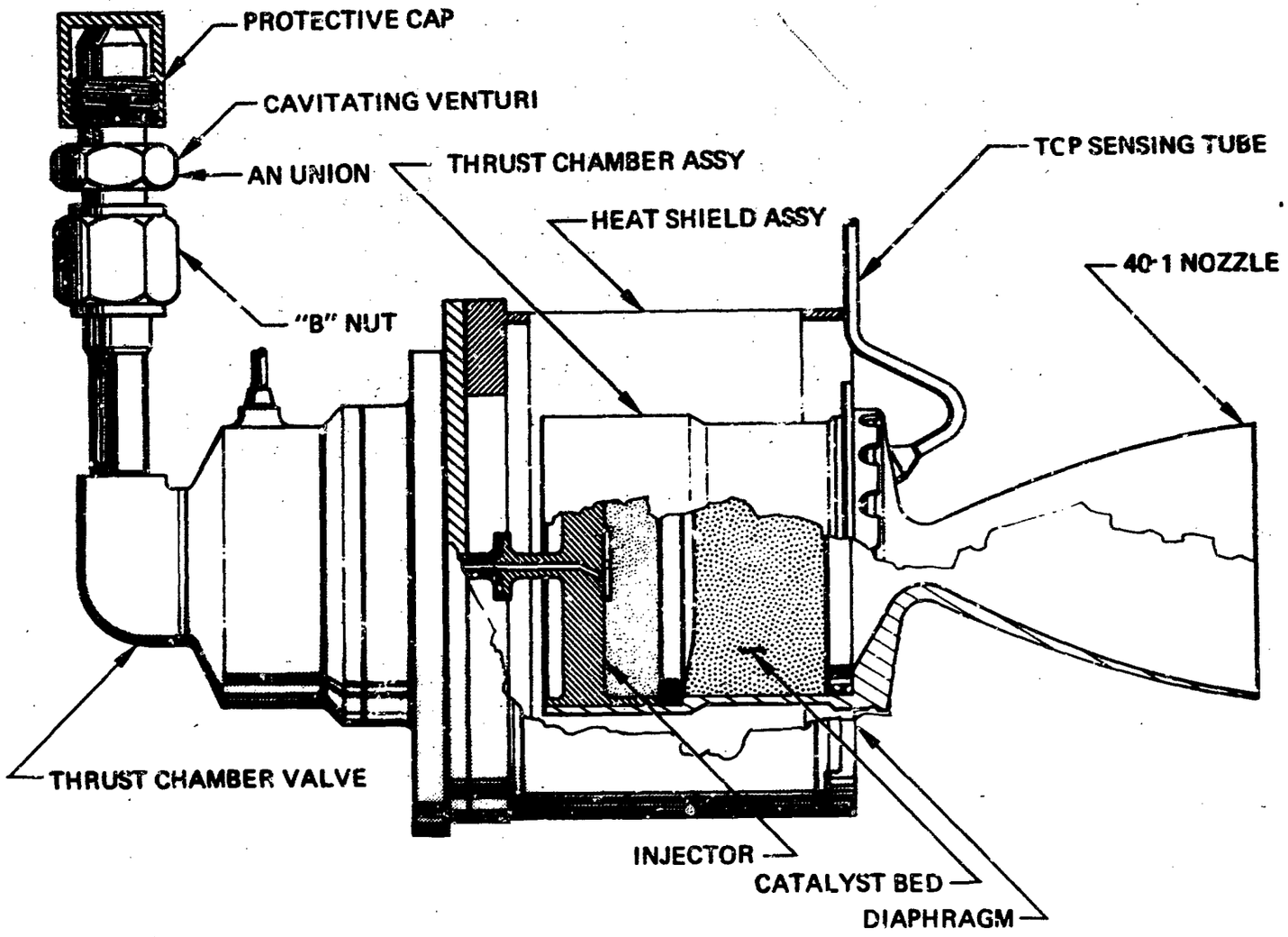

Figure 5. Long-Life Monopropellant Hydrazine Reaction Engine Assembly MR-50C

In order to minimize thrust decay over the specified 3.5 to 1 feed pressure blowdown ratio, a cavitating venturi was substituted for the trim orifice normally used on the MR-50A. Predicted performance of this design is presented in Table III.

The following paragraphs discuss the baseline design in detail with particular emphasis on the injector. The overall engine assembly is the same as the REM-Mono engine described in paragraph 2.1.1. The baseline design differs only in the injector design approach.

Injector Design – The baseline injector design approach is a modification of the REM-Mono injector aimed at increased propellant dispersion over the upper catalyst bed and reduction in the sensitivity of the engine to small catalyst loss and/or settling. In-house research work conducted since the REM-Mono engine was baselined has indicated that any small catalyst loss or settling tends to form a void underneath the injector element. This void can prevent propellant dispersion into the bed and allows the hydrazine to penetrate deeper into the catalyst bed before reacting.

Additional testing has indicated that the above problem may be greatly reduced and/or eliminated by providing greater catalyst bed coverage by the injection element. The baseline injector was aimed at providing improved bed coverage. This rigimesh injection element for the baseline design covers almost three times the cross-sectional area of the catalyst bed, as does the REM-Mono design. Figure 6 presents this baseline injector design together with two alternate designs which provided the same potential dispersion with less holdup (rigimesh) volume.

The injector incorporates a single straight passage feeding three branch passages, through a shallow dispersion cone (countersink) to the rigimesh element. A finer rigimesh material is used (50- by 250-mesh, two layers) as compared to the 12- by 64-mesh material used in the REM-Mono engine. This finer mesh material was chosen for the baseline to provide increased breakup of the propellant into finer and lower momentum streams than does the 12- by 64-mesh material.

Detailed thermal analyses of the baseline and alternate injectors, operating under worst-case thermal duty cycle, are presented in paragraph 2.2.2. As a result of these analyses and thermal margin tests, the final selected Phase I injector design was this baseline design using the REM-Mono 12- by 64-mesh rigimesh material instead of the 50- by 250-mesh material.

Chamber and Nozzle Assembly – The chamber and nozzle assembly consists of the catalyst chamber, nozzle, and chamber pressure tap fitting.

The chamber-nozzle body is a Haynes Alloy No. 25 one-piece machining with a cylindrical lower catalyst bed section and a straight 40:1 contoured nozzle. This material exhibits excellent properties at elevated temperatures and is easy to machine. The entrance to the cylindrical catalyst bed section contains a step on which the intermediate bed plate of the injector assembly bottoms. The chamber section was designed with minimum wall thickness of 0.020 inch. The lower end of the cylindrical portion of the chamber contains a step to which the diaphragm assembly is heliarc welded. The nozzle convergent zone is a 50-degree angle conical section blending into the 0.197-inch-diameter nozzle throat. The nozzle divergent section is RAO contour.

Table III. Predicted Long Life Engine Performance

Parameter	Value								
Feed pressure, psia	350	350	350	225	225	225	100	100	100
Propellant temperature, °F	125	65	40	125	65	40	125	65	40
Pressure drop, psia									
Venturi	174.1	173.4	173.1	92.1	91.4	91.1	18.7	18.0	17.8
Valve	7.5	7.5	7.5	5.0	5.0	5.0	2.4	2.4	2.4
Injector	48.3	48.2	48.1	31.2	31.1	31.1	14.0	14.0	14.0
Upper catalyst bed	8.2	8.4	8.4	6.8	7.0	7.1	4.9	5.0	5.1
Upper screen	5.0	5.1	5.2	4.0	4.1	4.1	2.6	2.7	2.7
Lower catalyst bed	8.5	8.7	8.8	7.1	7.3	7.4	5.1	5.2	5.3
Lower screen	5.8	5.9	6.0	4.6	4.7	4.8	3.1	3.2	3.2
Downstream chamber pressure, psia	92.6	92.8	92.9	74.2	74.4	74.4	49.2	49.5	49.5
Altitude thrust, lbf	5.00	5.01	5.01	3.97	3.99	3.99	2.59	2.61	2.61
Flowrate, lbm/sec	0.02140	0.02175	0.02189	0.01714	0.01744	0.01755	0.01139	0.01162	0.01170
Characteristic exhaust velocity, ft/sec	4297	4236	4211	4292	4231	4206	4282	4222	4197
Thrust coefficient	1.748	1.748	1.748	1.738	1.738	1.738	1.711	1.711	1.711
Specific impulse, lbf-sec/lbm	233.5	230.2	228.8	231.8	228.5	227.2	227.7	224.5	223.2
Ammonia dissociation, %	63.9	63.9	63.9	64.7	64.7	64.6	66.2	66.2	66.1
Molecular weight, lbf/lb moles	12.702	12.706	12.707	12.650	12.654	12.656	12.550	12.555	12.557
Specific heat ratio	1.2907	1.2906	1.2905	1.2924	1.2923	1.2922	1.2957	1.2956	1.2955
Gas temperature, °F	1,617	1,617	1,618	1,606	1,607	1,607	1,585	1,585	1,586

Figure 6. Long-Life Injector Configurations

The injector-to-chamber joint is made by means of meltdown weld. This joint is designed so that the weld joint may be machined away, the injector removed from the chamber, repairs made as required, and the joint then rewelded. This joint has been extensively used on flight engines by RRC.

Catalyst Bed Design – The basic catalyst bed design is identical to the REM-Mono 5-lbf REA. The catalyst bed is a layered bed design consisting of two catalyst particle sizes. The upper 0.25 inch of the catalyst bed contains 25- to 30-mesh ABSG granular catalyst and the lower bed consists of 14- to 18-mesh ABSG granular catalyst 0.65 inch in length. The overall catalyst bed length is 0.9 inch. The catalyst bed diameter is 1.179 inches, which results in a bed loading of 0.02 lbm/in.^{2}-sec at the 5-lbf thrust level.

The upper catalyst bed is retained by an intermediate bed plate of Haynes Alloy 25, which is tack-welded in four places to the injector. The intermediate bed plate is used to provide retention of the upper bed to meet life requirements. The lower catalyst bed is also supported by a Haynes Alloy 25 bed plate. The use of an intermediate bed plate provides compartmentalization of the catalyst bed.

As a result of the catalyst cycling load tests discussed in paragraph 2.3.2, a special 90% attrited 25- to 30-mesh catalyst was substituted for the standard ABSG 25- to 30-mesh catalyst. This catalyst was subjected to the identical processing procedures of the MR-50A REA.

Heat Shield and Support Structure – A high degree of thermal isolation of the thrust chamber is the key to securing high pulse-mode performance at very low duty-cycle operation. Additionally, good thermal isolation is usually desirable to minimize the effect of the reactor upon the spacecraft thermal control system. A limit to the degree of thermal isolation desired is imposed by the need to provide heat for temperature control of valves under cold orbit conditions.

Thermal isolation can be accomplished with conductive insulation, with radiative insulation (shields), or with a combination of the two. In support of the REM-Mono Program, a thermal isolation tradeoff study was run.

Specifically considered was reactor thermal isolation accomplished by maximization of the thermal resistance of support structures (consistent with sound structural design) and by use of either or both Min-K thermal insulation and a radiation shield. The primary function of the Min-K was to help control heat rejection during steady-state operation. At the high temperatures characteristic of steady firing, radiation resistances are low because of the fourth power dependence of emitted radiation. For small-scale hardware, control of steady-state heat rejection is possible simply by using a low-emittance surface on the reactor exterior in combination with a single heat shield around each reactor. The elimination of Min-K (and use of a low reactor emittance) actually results in improved pulse-mode performance at low duty cycle for the present reactor configuration. This results from the fact that radiation "resistances" are high relative to the Min-K resistance for the range of reactor temperatures (500 to 600°F) encountered at minimum duty cycle. At these temperatures, the Min-K increases the radiating area without providing a sufficient conductive resistance to overshadow the resulting tendency for increased radiation loss.

The ineffectiveness of Min-K at a reactor temperature of 500°F is illustrated by the calculations summarized in Table IV. The heat loss is actually increased when Min-K is added to a low emittance reactor. This effect would be even more pronounced if the edge conduction through the stainless steel jacket required to contain the Min-K were taken into account.

Table IV. Insulation Tradeoffs

Basis: Reactor = Cylinder
L = 2.5 inches
D = 0.9 inch
Reactor temperature = 500°F
No insulation edge loss

Insulation	Surface Emittance	Shield (ϵ = 0.03)	Heat Loss
None	0.03	One	1.02 Btu/hr
0.25 inch min-K	0.03	One	1.13 Btu/hr
0.37 inch min-K	0.03	One	1.16 Btu/hr
0.50 inch min-K	0.03	None	2.90 Btu/hr
0.50 inch min-K	0.30	None	9.35 Btu/hr

The low reactor emittance is provided by a plated rhodium surface. Rhodium's characteristic low emittance is not degraded by oxidation such as might occur during sea-level tests. Additionally, it has a high melting point (3,570°F). Diffusion into the base metal at high temperatures as exhibited by gold (melting point 1,950°F), does not occur with this rhodium surface. (Such diffusion must be avoided to prevent degradation of surface emittance with high-temperature exposure.)

From this analysis it is believed that the combination of plating the chamber and using a radiation shield represents the best overall thermal design approach to satisfy most spacecraft applications. Accordingly, this approach was used for the 5-lbf engine on this program.

The engine is mounted by three bolts through tapped holes in the forward heat shield mounting flange. The propellant valve is similarly bolted to this same flange.

The thrust chamber is welded to the propellant valve at the propellant feed tube, and supported at its center of gravity by a 0.005-inch-thick Haynes 25 diaphragm, which is electron-beam-welded to the heat shield. The diaphragm allows for axial displacement of the thrust chamber, because of temperature differentials, while supporting the thrust chamber in the lateral direction.

The heat shield, which also doubles as a structural support for the diaphragm, is an electron-beam-welded assembly consisting of a CRES 304 mounting flange, two CRES 304 diaphragm support flanges, and two 0.003-inch-thick CRES 304 heat shield cans. This assembly mounts to the support cage at the valve interface. Thermal management between the thrust chamber and the valve and support cage is controlled by sizing of the diaphragm and heat shield can.

Propellant Valve – The propellant valve used in the 5-lbf thruster test program is the P/N 5690023-103 normally closed, single soft-seat, long-life solenoid actuated valve manufactured by the Systems Division of Parker-Hannifin Corporation. A cross-sectional view of the valve is shown in Figure 7, and its construction and operation is described in the following paragraphs. This valve has been qualification tested to 1,000,000 cycles for RRC's REM-Mono Block II Program. With this valve, problems inherent in flow and thermal matching to the engine have already been solved, and the engine test program was carried out without risk of compromise due to valve performance.

As shown in Figure 7, the valve consists of the following major elements, with the coil cavity and all external joints being sealed by welding. This valve weighs 0.4 lb maximum.

a. *Valve seat* – The seat is a flat-surfaced Teflon ring swaged into a boss integral with the valve end cap. The seat material is Teflon procured to a Parker material specification which controls its structure, microcleanliness, and physical properties.

b. *Poppet* – The poppet is a free-floating, three-sided, 17-4PH corrosion-resistant steel member, guided by the armature and loaded by the poppet spring. The sealing surface is flat-lapped.

c. *Solenoid Actuator* – The solenoid is a flat-faced axial-air-gap, bipolar-type with both the solenoid shell and armature constructed of type 430F corrosion-resistance steel for good compatibility with N_2H_4 and adequate magnetic performance. The armature is guided and loaded by a 17-7PH Belleville washer in such a way that no sliding contacts occur.

d. *Coil* – The coil consists of HML insulated copper magnet wire wound on a Teflon bobbin, using DC997 varnish. Lead wires are Teflon-insulated and lead wire to magnet wire joints are brazed. The coil is vacuum impregnated and oven-cured.

e. *Filter* – The filter is a 10-micron nominal, 25-micron absolute pleated, woven-wire-disk-type of type 304L corrosion-resistant steel.

2.2 PHASE I ANALYSIS

Phase I analysis efforts were concentrated on evaluating the effects of the injector design modification upon the proven operational capability of the REM-Mono 5-lbf REA. These efforts consisted of injector pressure drop, thermal and stress analysis.

2.2.1 Injector Pressure Drop

Pressure drop data for the REM-Mono design is well documented from test data. This drop is made up of frictional losses in the single feed tube and the loss through the rigimesh itself. The pressure drop in the baseline and both alternate designs is calculated as the sum of pressure drops due to the turn into the branch passages, the flow down the branch passages, the 32-degree turn into the rigimesh section, and the pressure drop due to flow through the rigimesh itself.

Each turn required will result in a pressure drop as given by:

$$\Delta P_{turning} = K_{turning} \frac{\rho V^2}{2g} \qquad (1)$$

where V is the velocity in the supply tube and $K_{turning}$ is a loss constant.

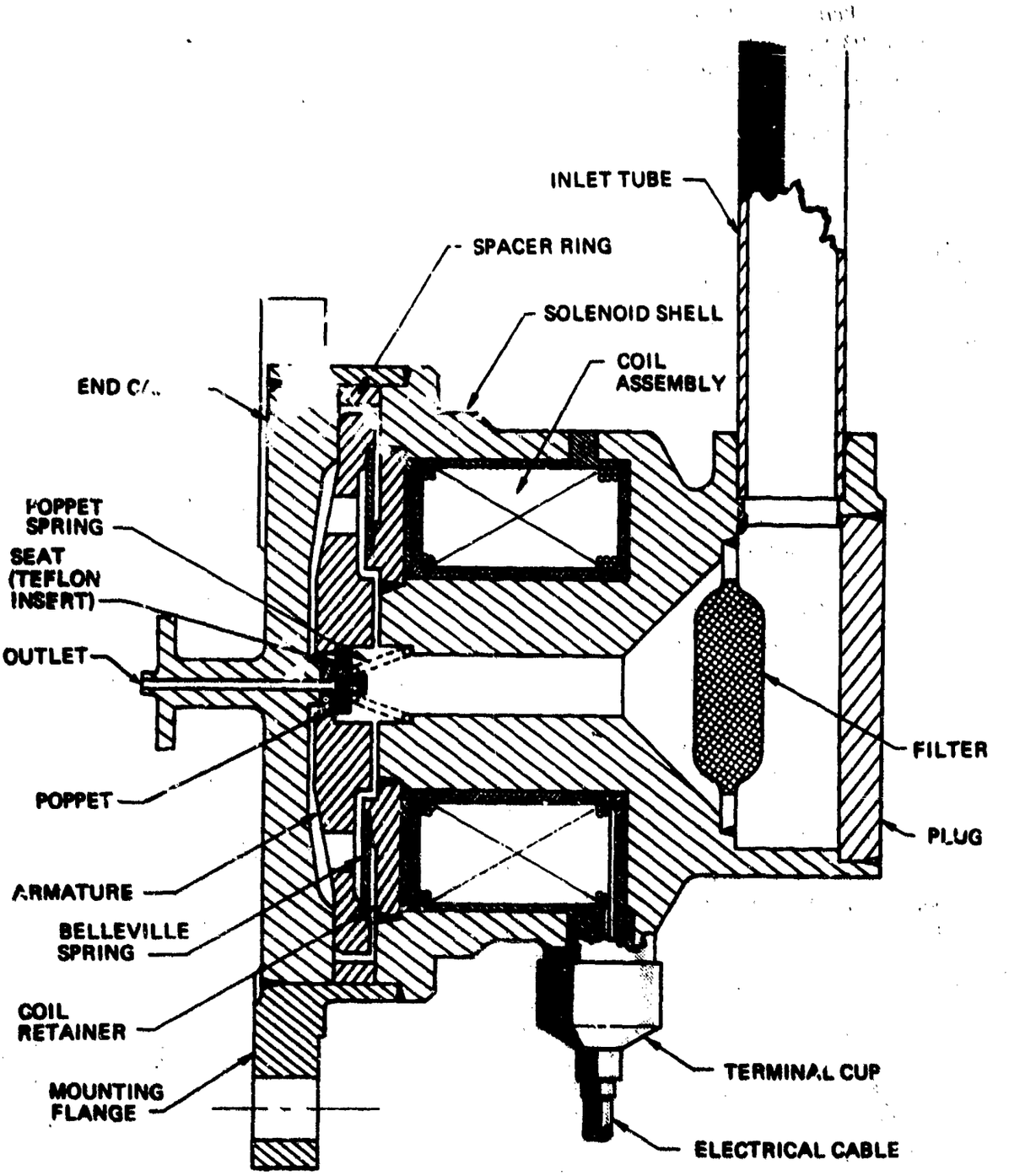

Figure 7. REM-Monopropellant Valve Cross Section

The turning loss constant is given by:

$$K_{turning} = 1.25\left(\frac{\theta}{90}\right)^2 \tag{2}$$

where θ is the turning angle in degrees.

The flow rate rate corresponding to minimum feed pressure and maximum propellant temperature is 0.01139 lbm/sec from Table III. Use of propellant density at the worst case propellant temperature of 125°F, yields a velocity of 27.1 ft/sec in the 0.0355-inch ID feed tube and 28.4 ft/sec in each of the three 0.020-inch ID branch passages. Substitution into the foregoing equations yields:

$\Delta P_{turning}$ feed to branch = 2.5 psi

$\Delta P_{turning}$ branch to rigimesh = 0.8 psi

The frictional pressure drop in the feed tube and branch passages is given by:

$$\Delta P = \left(\frac{2f\rho V^2}{g} \cdot \frac{L}{D}\right) \tag{3}$$

The friction coefficient is given by:

$$f = 0.04\left(R_E\right)^{-0.16} \tag{4}$$

Applying these equations to the subject design results in a frictional pressure drop of 1.9 psi for the 0.387-inch-long feed tube, and 1.5 psi for the 0.147-inch-long branch passages. The pressure drop through the rigimesh is described by the equation:

$$\Delta P = \left(\frac{\dot{\omega}}{C_D' A}\right)^2 \frac{1}{2\rho g} \tag{5}$$

where A is the effective flow area. The pseudo discharge coefficient C_D' varies as the amount of calendering or cold rolling accomplished during the rigimesh manufacturing process. Because of this variability, RRC purchases rigimesh to a specified permeability. The permeability of the REM-Mono rigimish is 3,500 gal/min/ft^2 at a pressure drop of 45 psi. Substitution into equation (5) yields a discharge coefficient for this rigimesh of 0.095. Applying these equations to all three injector designs of Figure 6 results in a rigimesh pressure drop of 7.3 psi.

The 0.060-inch countersink was selected to provide approximately the same rigimesh pressure drop as obtained on the REM-Mono REA. The single countersink on REM-Mono is 0.100 inch, approximately three times larger.

The total injector pressure drop is then calculated as:

ΔP_{inj} = 1.9 + 2.5 + 1.5 + 0.8 + 7.3 = 12.3 psi
at 0.01139 lbm/sec with 125°F propellant

Injector pressure drop as a function of flow rate and propellant temperature is presented in Table III.

2.2.2 Injector Thermal Anaysis

The elimination of two-phase flow blockage is the primary consideration of injector thermal analysis. Two-phase flow blockage does not occur as soon as vapor bubbles begin to form at the fluid boundary. Rather, two-phase flow blockage begins when the bubbles formed at this interface break away from the heated wall and are maintained in the bulk stream. This is referred to as bulk propellant boiling. The formation of bubbles occurs when the wall temperature exceeds the fluid saturation temperature by 10 to 80°F, depending on pressure and flow velocity (Reference 1) whereas bulk propellant boiling occurs when the fluid bulk temperature approaches the saturation temperature.

$$\Delta T_D = \frac{\eta q''}{V_{in}} \tag{6}$$

where:

ΔT_D	=	Difference between fluid bulk temperature and fluid saturation temperature where bubbles detach and choke the flow
q''	=	Heat transfer rate Btu/ft^2 sec
V_{in}	=	Fluid velocity, ft/sec
η	=	Empirical constant, ft^3 °F/Btu - 0.93 + 0.00047 p
p	=	Pressure in psia

Reference 2 presents the results of an experimental investigation that measured heat flux to hydrazine from an electrically heated tube. Boiling heat fluxes of 6 to 16 Btu/in.^{2}-sec were measured at wall temperature between 400 and 500°F, for velocities and pressures similar to those in this design. Because of the constant heat flux nature of that experimental system, the test section would fail when higher heat fluxes were attempted. Lower heat fluxes than the maximum will prevail at all wall temperatures in excess of the "burnout temperature."

During the REM-Mono Program, early testing was concentrated on demonstration of the thermal adequacy of the design approach. To demonstrate that the engine design approach was thermally sound, the engine was operated at varying duty cycles to determine the maximum injector, valve, and feed tube temperatures. Location of pertinent thermocouples used in this testing is shown in Figure 8. Mapping out of the worst-case duty cycle was conducted with ambient temperature propellant. Data from this mapping is summarized in Tables V and VI. This mapping resulted in a worst-case (i.e., maximum injector head temperature) duty cycle of 1 to 2% depending upon the feed pressure. After mapping the worst-case duty cycle with ambient propellant, the engine was operated at worst-case condition with the propellant valve preheated to 250°F and the propellant incrementally heated to 160°F. During operation, all pulse shapes (conducted at both 22 and 200 milliseconds) were completely normal with no signs of thermally related anomalies (i.e., distorted pulse shape).

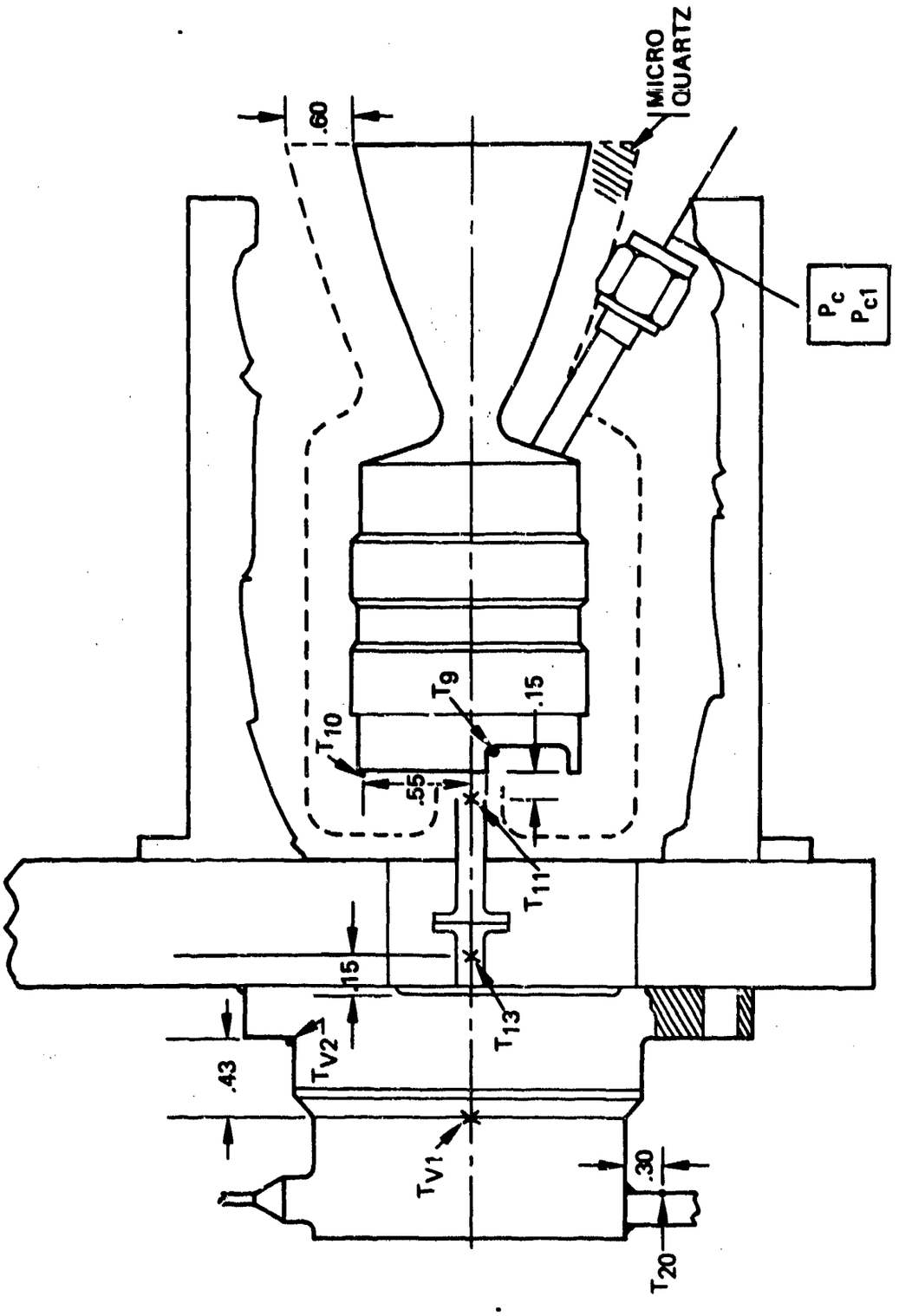

Figure 8. Reactor Thermocouple Locations

Table V. D2-002 Test Data, Worst-Case Duty Cycle Search, Ambient Temperature Conditions
Pulse Width = 0.022 sec Temperature, °F

	Event	T9	T10	T11	T13	TV1	TV2	T20	% Duty Cycle
P_{feed} = 92 psia	201	1,200	1,245	1,020	755	129	140	97	0.5
	202	1,255	1,295	1,030	795	113	126	92	1.0
	203	1,265	1,305	1,085	785	107	117	87	1.5
	204	1,260	1,315	1,075	765	97	114	82	2.0
	205	1,255	1,315	1,060	750	101	110	81	2.5
	206	1,250	1,320	1,045	735	98	108	80	3.0
	207	1,225	1,330	960	695	96	121	85	4.0
	208	1,150	1,295	855	620	90	98	75	5.0
P_{feed} = 183 psia	209	1,240	1,290	1,080	830	115	129	81	0.5
	210	1,265	1,335	1,095	820	101	116	77	1.0
	211	1,250	1,335	1,070	780	96	108	74	1.5
	212	1,230	1,335	1,025	750	92	120	74	2.0
	213	1,195	1,325	970	715	90	101	72	2.6
	214	1,160	1,325	920	690	88	98	72	3.0
	215	1,095	1,320	830	670	86	96	72	4.0
	216	1,050	1,315	780	665	86	95	73	5.0

Table VI. Hot Propellant Margin Test

Psid Psia	Event	T9	T10	T11	T13	TV1	TV2	T20	Pulse Width	% Duty Cycle
91	301	1,235	1,310	1,050	725	91	102	75	0.022	1.97
183	302	1,240	1,335	1,045	765	93	101	91	0.022	1.49
197	303	1,245	1,335	1,065	775	105	115	96	0.022s	1.49
98	304	1,255	1,315	1,085	760	107	146	132	0.022	1.97
102	305	1,330	1,365	1,180	885	254	180	136	0.022	1.97
206	306	1,345	1,400	1,200	955	247	206	145	0.022	1.49
215	307	1,355	1,405	1,220	955	255	217	159	0.022	1.49
107	308	1,330	1,355	1,215	990	250	220	158	0.022	1.97
112	309	1,345	1,370	1,230	990	250	221	164	0.022	1.97
85	310	1,325	1,345	1,230	985	250	224	171	0.022	1.97
224	311	1,365	1,410	1,240	1,030	249	220	169	0.022	1.49
224	312	1,310	1,385	1,150	1,025	250	223	176	0.200	1.50
85	313	1,280	1,305	1,165	955	251	228	171	0.200	2.00

The selected worst case for thermal analysis is a hot environment with the following conditions:

a. Hydrazine enters the valve at 140°F with feed pressure initially 100 psia.

b. The valve/feed tube temperature distribution corresponds to event 306 of Table VI (REM-Mono test results).

c. When wall temperatures are 80°F greater than the saturation temperature of the propellant, nucleate boiling heat transfer applies.

The thermal analysis considers each injector to be comprised of three regions. The first region is the valve holdup volume, and accounts for the relatively long residence time of the propellant in the valve at the low duty cycles which represent the worst-case thermal condition. The second region considers that region from the valve seat to the place where the wall temperature exceeds the saturation temperature by 80°F. The turbulent heat transfer coefficient is calculated from the Seider-Tate equation to characterize this region. In the third region (the remainder of the injector wetted surface and the rigimesh), a heat transfer rate corresponding to the upper limit of nucleate boiling is applied.

Other basic assumptions used in this analysis were:

a. Properties for hydrazine are evaluated at the average pressure for the region of concern based upon the pressure drop analysis of paragraph 2.2.1.

b. Turbulent flow with short tube entrance effects dominates the transfer process in region 2.

c. Pulse-mode propellant consumption is approximately 95% of the product of the pulse width and steady-state flow rate at the feed conditions.

d. A pulse width of 20 milliseconds was used in the analysis, corresponding to the minimum pulse width required of the long life test duty cycle.

In region 1, the propellant residence time in the valve is 39.3 seconds when operating at the conditions stated above. The controlling heat transfer mechanism is conduction from the valve body to the propellant mass and may be represented as:

$$m\, c_p \frac{dT}{dt} = \frac{kA}{L}\left(T_w - T\right) \tag{7}$$

Integration over the residence time interval yields:

$$T_w - T_{out} = \left(T_w - T_{in}\right) \epsilon^{-\frac{kAt}{mc_pL}} \tag{8}$$

where:

t = Residence time, 39.3 seconds

T_w = Constant wall temperature, 217.0°F

T_{in} = Bulk inlet temperature, 125°F

k = Propellant thermal conductivity

m = Propellant mass

c_p = Propellant specific heat

L = Effective conduction length

A = Valve internal surface area

Application of equation (8) gives a propellant temperature of 171°F at the valve exit.

The propellant enters the feed passage, region 2, which has a temperature gradient along its entire length. The feed passage acts as a structural member with valve, feed tube, and injector. The worst-case temperature distribution used for this analysis is presented in Figure 9. Injector propellant inlet pressure is 78.9 psia (from Table III) corresponding to a saturation temperature of 340°F. A wall temperature of 420°F is recorded at 0.074 inches from the valve face on Figure 9.

The bulk propellant temperature increase in region 2 may be determined from the single pass counterflow heat exchanger relationship:

$$(h\pi DL)\frac{\Delta T_a - \Delta T_b}{\ln \Delta T_a/\Delta T_b} = \dot{w} C_p (T_{out} - T_{in}) \qquad (9)$$

where

D = Passage diameter, inches

L = Passage length, inches

ΔT_a = Propellant – wall temperature difference at region 2 exit

ΔT_b = Propellant – wall temperature difference at region 2 inlet

w = Propellant mass flow rate, lbm/sec

C_p = Propellant specific heat, Btu/lbm °F

T_{in} = Propellant inlet temperature, °F

h = Convective heat transfer film coefficient, Btu/in.-hr °F

The Seider-Tate heat transfer film coefficient accounts for the propellant viscosity change due to temperature gradients between the passage wall and hydrazine. The viscosity of hydrazine is predictable up to 720°F, which allows the application of the Seider-Tate relationship in region 2. The empirical formulation is given as:

$$h_c = 0.023\, Re^{-0.2}\, Pr^{-0.667}\left(\frac{\mu_w}{\mu_b}\right)^{-0.14} C_p G \qquad (10)$$

where

Re = Reynolds number

Pr = Prandtl number

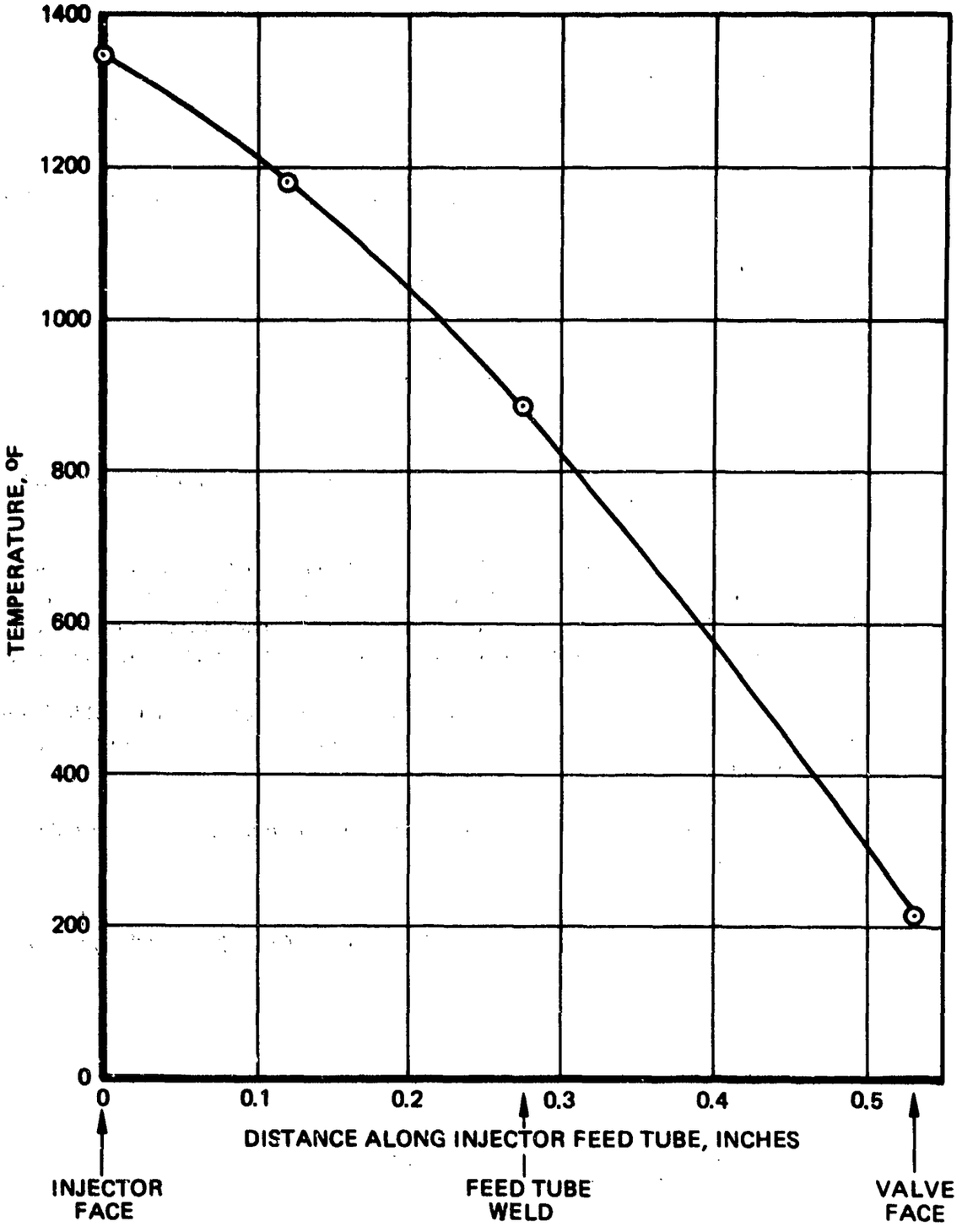

Figure 9. Injector Feed Tube Temperature Distribution Worst-Case Test Results REM-Mono S/N D2, Event 305

μ = Hydrazine viscosity

C_p = Specific heat

G = w/A

A = Passage cross sectional area

w, b = Subscripts denoting evaluation of propellant physical properties at wall and bulk temperatures respectively

Equation (10) may be modified to account for the sharp edge entrance effects of the propellant entering the feed tube. Reference 3 gives the following empirical relationship:

$$h = h_c (1 + F\, D/L) \tag{11}$$

where

F = 3, for short calming section with sharp-edged entrance

h_c = Result of equation (10)

Application of equations (12), (13), and (14) to region 2 results in an exit propellant temperature of 174°F.

Flow conditions in region 3 are considered as follows. A highly subcooled liquid core is separated from a highly superheated wall by a boundary layer. Very small bubbles form in the laminar sublayer and do not detach from the surface. Heat transfer rates characteristic of nucleate boiling are applied, but the cold liquid core "quenches" the process so that vapor blockage does not occur.

Region 3 consists of a) the remainder of the feed tube length, a cylindrical section 0.568-inch long of 0.0355-inch diameter, b) the three branch passages, cylindrical sections 0.147-inch long of 0.020-inch diameter, and c) the rigimesh injection element.

Assuming the upper limit of nucleate boiling applies in region 3, Reference 2 gives the following relationship for the heat transfer rate:

$$q_{ul} = \left[1 - 0.236\left(\frac{P - 675}{675}\right)^2\right]\left[6.9 + 0.246V - T_b\left(0.015 + 2.7 \times 10^{-4}\, V\right)\right] \tag{12}$$

Where:

q_{ul} = Upper limit of nucleate boiling, Btu/in.^{2}-sec

P = Propellant pressure, psia

V = Fluid velocity, ft/sec

T_b = Bulk fluid temperature, °F

For given velocities and pressure, equation (12) may be expressed as:

$$q_{ul} = a - \beta T_b$$

Equating the heat transferred to the fluid, to that stored in the fluid and integrating gives:

$$T_{out} = \frac{1}{\beta}\left[a - (a - \beta T_{in})\, e^{-\frac{\beta \pi D L}{\dot{w} C_p}}\right] \qquad (13)$$

Solving equation (13) for region 3a yields an outlet temperature of 229°F. Repeating for region 3b yields a 22°F rise to a temperature of 251°F.

In order to apply these nucleate boiling heat transfer equations to region 3c it is necessary to define effective flow and surface areas. As discussed in paragraph 2.2.1, an effective flow area had been empirically determined to correspond to the countersink diameter in the injector face. An effective surface area was calculated by an estimation of the amount of flatting of the individual wires during the rigimesh calendering process and subtracting the area where the flats of the two layers are touching. The calculated effective surface areas per square inch of rigimesh material are presented in Table VII for all of the materials tested during Phase I. In order to define flow velocity through the rigimesh, it was necessary to determine an effective flow area porosity. This was defined by recognizing that the pseudo discharge coefficient of equation (5) was equivalent to:

$$C'_D = C_D F_V \qquad (14)$$

where F_V = effective flow area porosity.

Table VII. Rigimesh Characteristics for Thermal Model

Type	Effective Surface Area
2 layer 12 x 64	4.9770 $in.^2/in.^2$
2 layer 50 x 250	5.9689 $in.^2/in.^2$
4 layer 50 x 250	10.9954 $in.^2/in.^2$

Permeability Gal/Min-Ft^2 @ 45 psid	Pseudo Discharge Coefficient	Effective Flow Area Porosity
700	0.019	0.032
1,650	0.045	0.075
3,500	0.095	0.158

Assuming a discharge coefficient of the rigimesh of 0.6 allowed direct calculation of the porosity which is also tabulated on Table VII.

Applying these boundary conditions to equation (13) yields a predicted rigimesh outlet temperature of 277°F. The saturation temperature at this point is 315°F, resulting in a temperature difference of 37°F. Substitution of the rigimesh flow parameters into equation (6) yields a bulk boiling ΔT of 34.2°F, demonstrating that the baseline design would not boil even under these worst-case conditions.

The foregoing thermal model was finalized during Phase I of the program. The preliminary model did not account properly for heat transfer in the rigimesh element. On the basis of this preliminary model, the first thermal design verification tests were conducted on designs, equivalent to the baseline analyzed above, employing two- and four-layer 50- by 250-mesh rigimesh. In order to obtain an equivalent pressure drop with these designs, it was necessary to enlarge the injector face countersink. As discussed further in paragraph 2.3.3, both of these designs gave definite indications of boiling in the vicinity of worst-case operating conditions. The thermal model was subsequently modified to account for rigimesh heat transfer analysis as presented in the foregoing paragraphs. This model yields predicted outlet temperatures of 377°F for the two-layer and 446°F for the four-layer rigimesh, which correlates with the observed boiling.

2.2.3 Rigimesh Stress Analysis

Since the only structural difference between the REM-Mono 5-lbf REA and the Long-Life REA was the rigimesh injection element, stress analysis was limited to this area. Table VIII summarizes the results of this analysis with comparative data for the REM-Mono design (case 1). All calculations are for maximum surge-pressure across the rigimesh corresponding to hot pulsing operation. Table VIII shows that it is necessary to use a center support in conjunction with the REM-Mono two-layer, 12- by 64-mesh rigimesh to maintain the same type of safety factors employed on the REM-Mono design. Case 4, which evaluates further support for the element, shows insignificant gain over the relatively inexpensive center support. Case 5 predicts imminent failure for the 50- by 250-mesh rigimesh without a center support, which condition was verified by test as discussed in paragraph 2.3.3. This result validated the simplified analytical techniques used in the analysis.

2.3 PHASE I TESTS

The Phase I test effort was divided into two areas, supporting research and conceptual evaluation (development) tests. Under the supporting research activities, test series were conducted on material nitriding and catalyst strength both static and cycling. Development testing included thermal margin and cold-start tests in addition to an abbreviated life test on the final Phase I design.

2.3.1 Nitriding

Five candidate materials for use in monopropellant hydrazine rocket engines were subjected to a nitriding test. A schematic of the test setup is shown in Figure 10. The setup was first run with just the specimen holders to determine the minimum flow rate of NH_3 to achieve 50 to 60% dissociation. Each test run included a Hastelloy X specimen to verify test conditions. The samples were maintained at 1,800°F for 6 hours in the dissociating ammonia environment, with gas samples

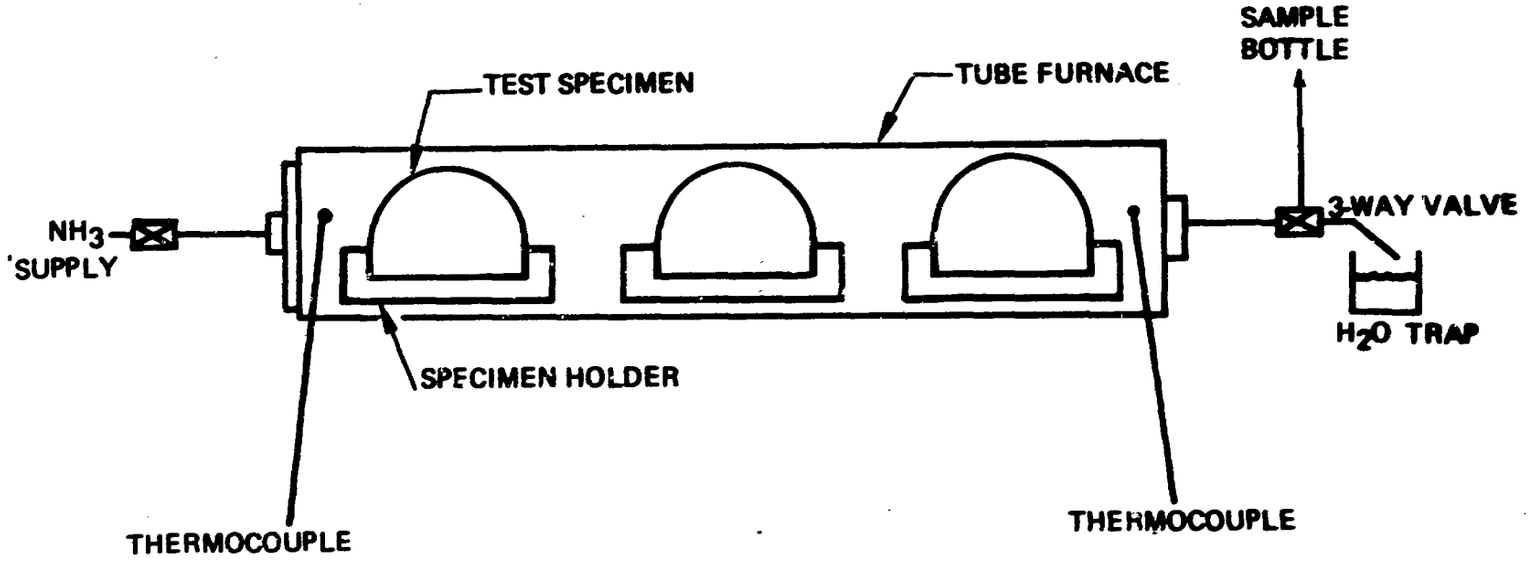

Figure 10. Material Nitriding Investigation Test Schematic

taken at 1, 3 and 6 hours to verify satisfactory dissociation. Table IX lists the five materials tested together with their average composition.

Table VIII. Rigimesh Injector Element Stress Analysis (Worst-Case Conditions 350 psid)

Case	Description	Maximum Radial Stress SR, psi	Yield Stress @ 600°F*	
			N-155, ksi	L-605,ksi
1	REM-Mono	2,917	21.2	24.6
2	Baseline with 4 lyr 12 x 64	8,102	21.2	24.6
3	Case 2 with center support	3,785	21.2	24.6
4	Case 2 with 4 support posts	3,742	21.2	24.6
5	Baseline with 4 lyr 50 x 250	33,897	21.2	24.6
6	Case 5 with center support	15,837	21.2	24.6
7	Alternate No. with 2 lyr 50 x 250 (annulus)	6,371	16.3	18.9
8	Alternate No. 2 with 2 lyr 12 x 64	1,296	21.2	24.6
9	Alternate No. 2 with 4 lyr 50 x 250	5,423	21.2	24.6
10	Alternate No. 2 with 2 lyr 50 x 250	21,694	21.2	24.6

*Extrapolated values

Table IX. Nitriding Test Specimen Chemical Composition

Alloy	Chemical Composition – % By Weight											
	C	Mn	Si	Cr	Ni	Co	Mo	W	Cb	Fe	Ti	Al
Hastelloy B	0.08	1.0	1.0	15.5	Balance	2.5	16.0	3.7		5.5		
L-605	0.10	1.5	0.5	20.0	10.0	Balance		15.0				
Hastelloy C	0.05	1.0	1.0	1.0	Balance	2.5	28.0			5.0		
Inconel 718	0.04	0.2	0.3	18.6	Balance		3.1		5.0	18.5	0.9	0.4
Hastelloy X	0.10	0.5	0.5	22.0	Balance	1.5	9.0	0.6		18.5		

Following this prestressed exposure to the nitriding environment, each test specimen was subjected to a Rockwell hardness test and a free bend test, and a polished section was photomicrographed. Table X presents the results of each of these tests on the specimen. Prior to the nitriding test, all specimens would withstand a 180-degree bend without fracture. The nitriding depth is that observable from the photomicrographs. The following paragraphs present the photomicrographic analysis of each of the materials tested.

Table X. Nitriding Investigation Results

Alloy Tested	Free Bend*	Hardness R 15N	Depth of Nitriding (inches)
Hastelloy B	180°	66.3	0.005
L 605	135°	72.8	0.006
Hastelloy C	85°	72.2	0.009
Inconel 718	52°	68.1	0.009
Hastelloy X	9°	68.3	0.014

*Degrees free bend to failure

Hastelloy X – Hastelloy X was assumed to have a fair resistance to nitriding and was selected for the control specimens to be run with each test. The test results indicate that it is very susceptible to nitriding and was the least resistant of the alloys tested. Figures 11 through 13 show the photomicrographs from each of the three test specimens. These photos show the diffusion of nascent nitrogen to progress quite rapidly at the grain boundaries of Hastelloy X. Metal nitrides first form at the grain boundaries which then grow until the entire grain is converted into a metal nitride complex. Figure 11 shows a condition very similar to incipient melting at the grain boundary (it could be assumed that as the composition changed, the melting temperature is lowered and a molten phase may form). The advance of nitride reactions along grain boundary paths is much greater than that of other materials tested.

Inconel 718 – The nitriding of Inconel 718 differs from that of Hastelloy X in that diffusion occurs through grains rather than along grain boundaries. As shown in Figures 14 and 15, diffusion probably advances along structural planes within the grains. This type of nitriding is somewhat slower, but the depth that has occurred is greater than that for other alloys tested. Several distinct layers of nitride reactions can be observed in Figure 14. These layers range from a complex nitride layer at the surface to a barely evident precipitation of particles toward the center of the test specimen.

Hastelloy C – Hastelloy C does not appear to be as sensitive to nitriding as Hastelloy X or Inconel 718. Referring to Table IX, Hastelloy C has the highest molybdenum content of the alloys tested. Molybdenum is reported to be susceptible to the formation of plate-like nitrides at grain boundaries. If so, this would explain the distinct appearance of grains throughout the specimen as shown in Figure 16.

L605 (Haynes Alloy No. 25) – The microstructure of L605 as shown in Figure 17 indicates a surface layer nitride reaction and a small amount of diffusion along grain boundaries. It is also quite possible that the particles (salt and pepper) throughout the specimen are nitride precipitates. Unnitrided specimens of L605 generally exhibit a typical solid solution microstructure with only a small amount of secondary precipitation.

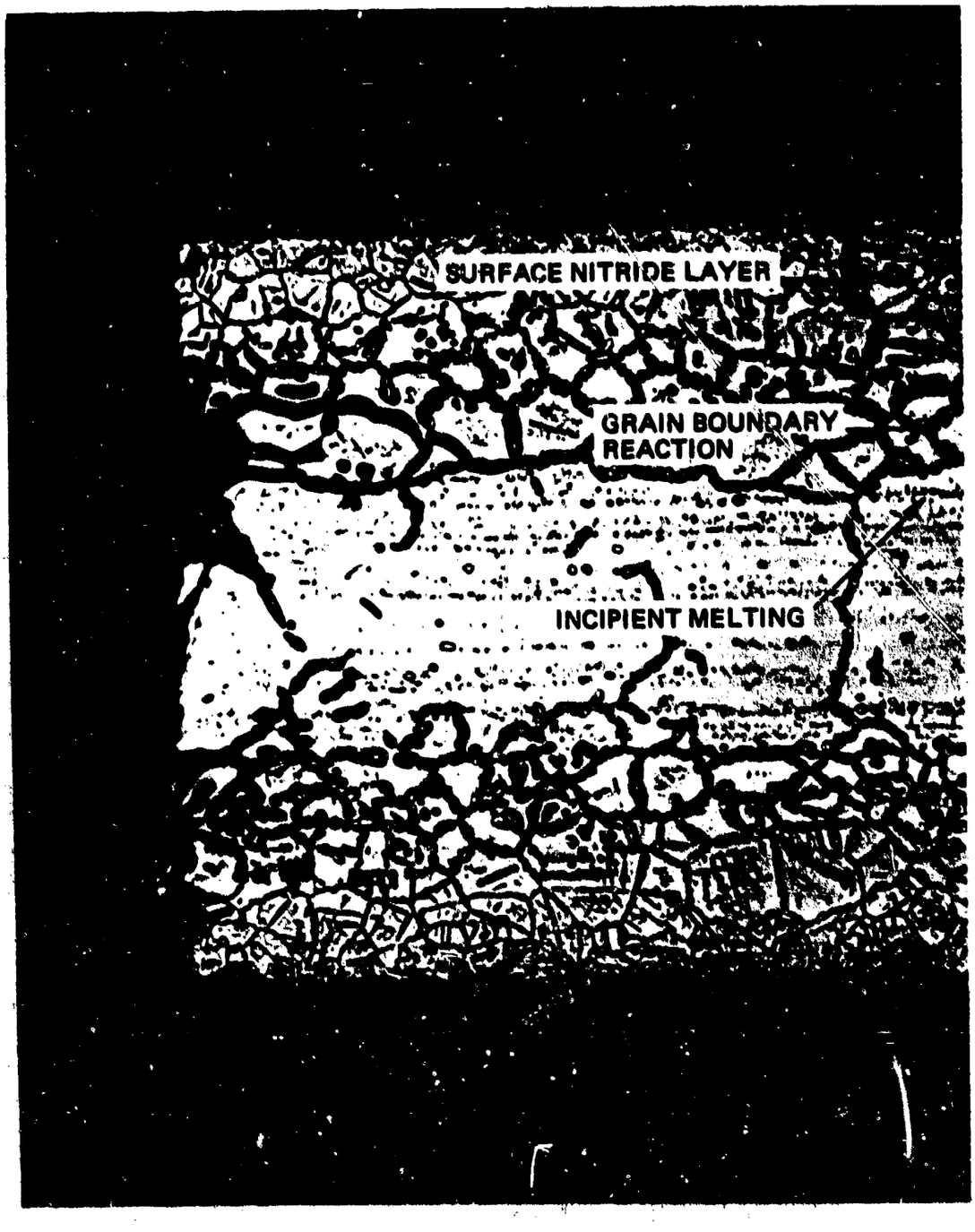

Figure 11. Photomicrograph (100X) Hastelloy X – Test 4

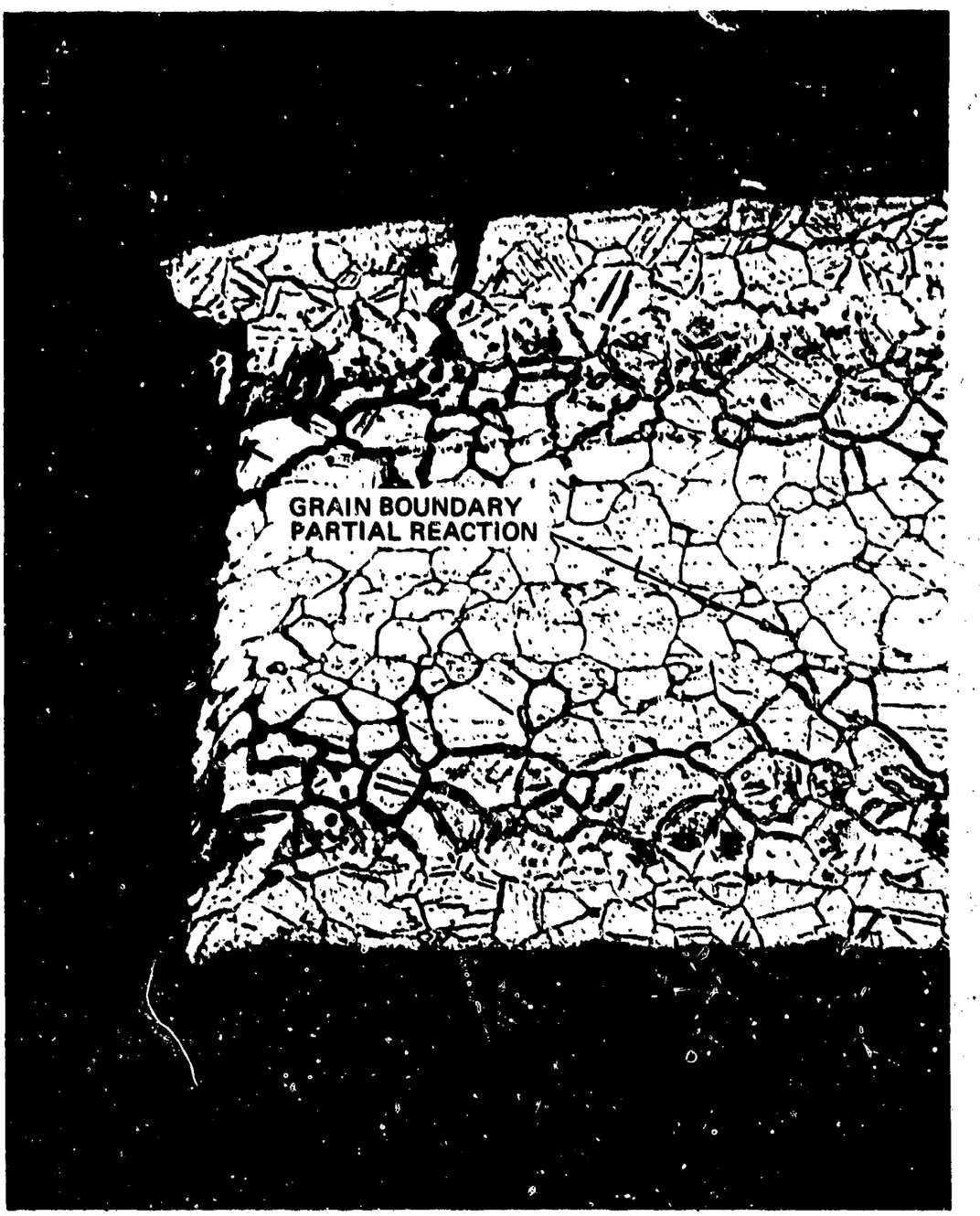

Figure 12. Photomicrograph (100X) Hastelloy X – Test 2

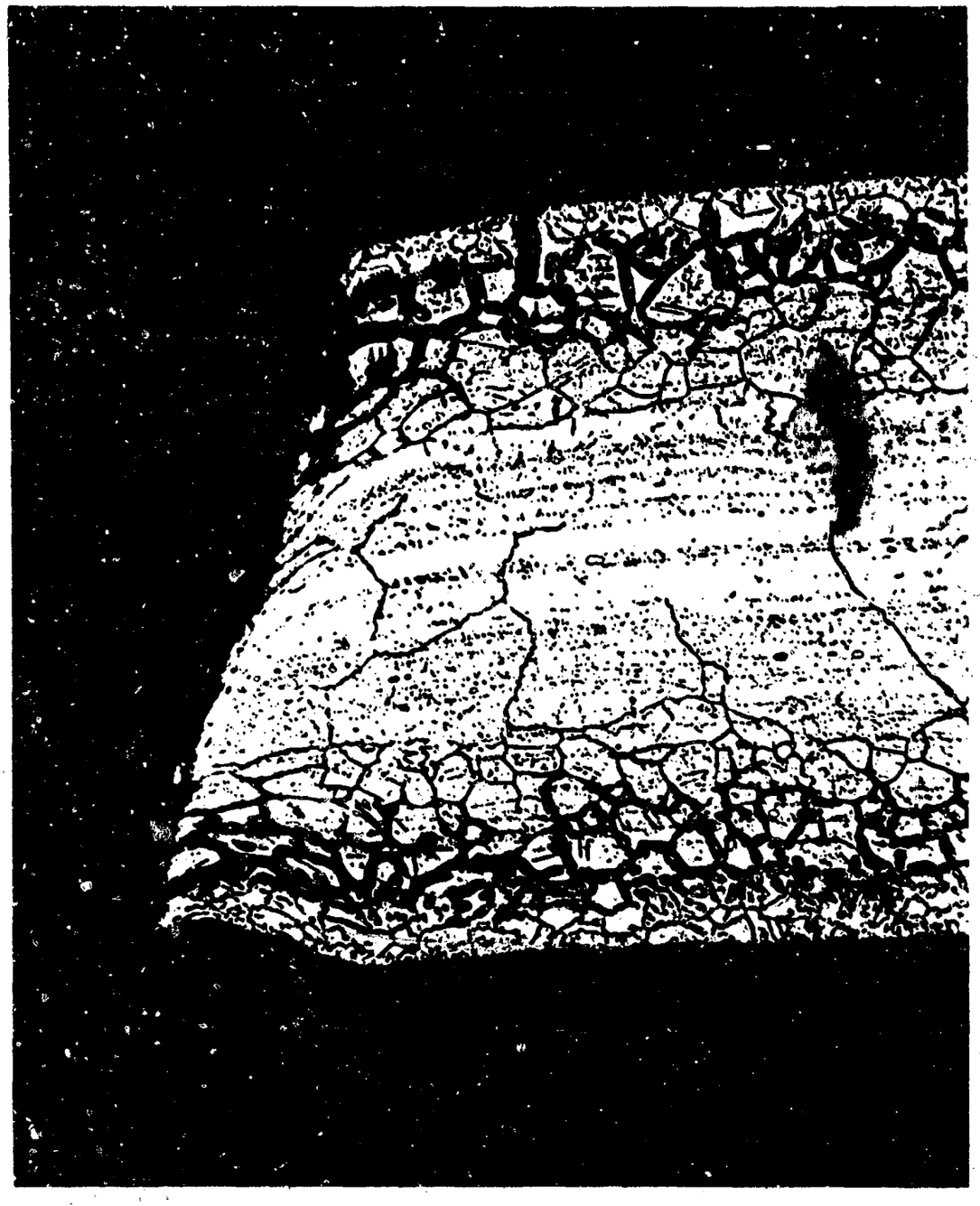

Figure 13. Photomicrograph (100X) Hastelloy X – Test 3

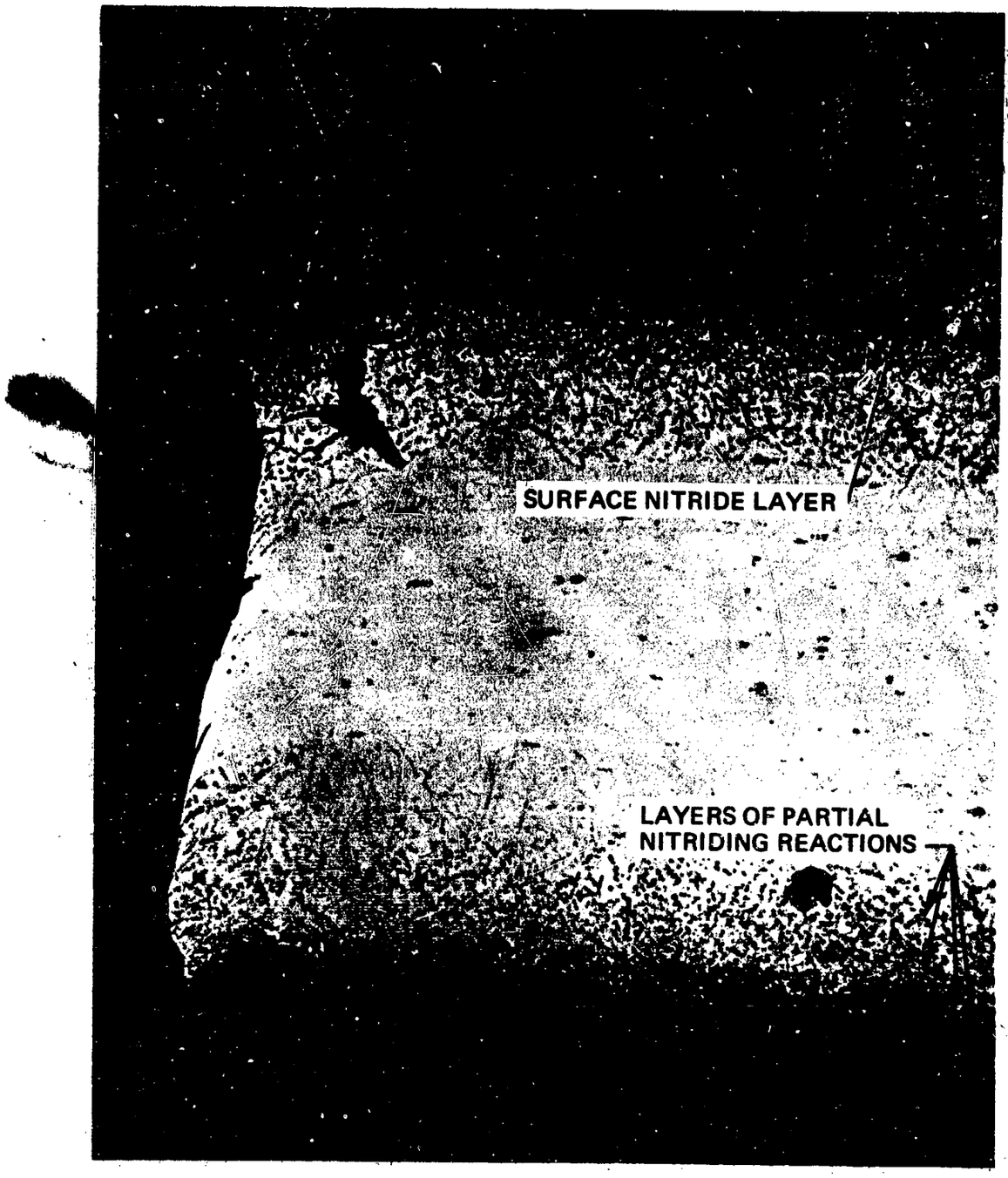

Figure 14. Photomicrograph (100X) Inconel 718 – Test 4

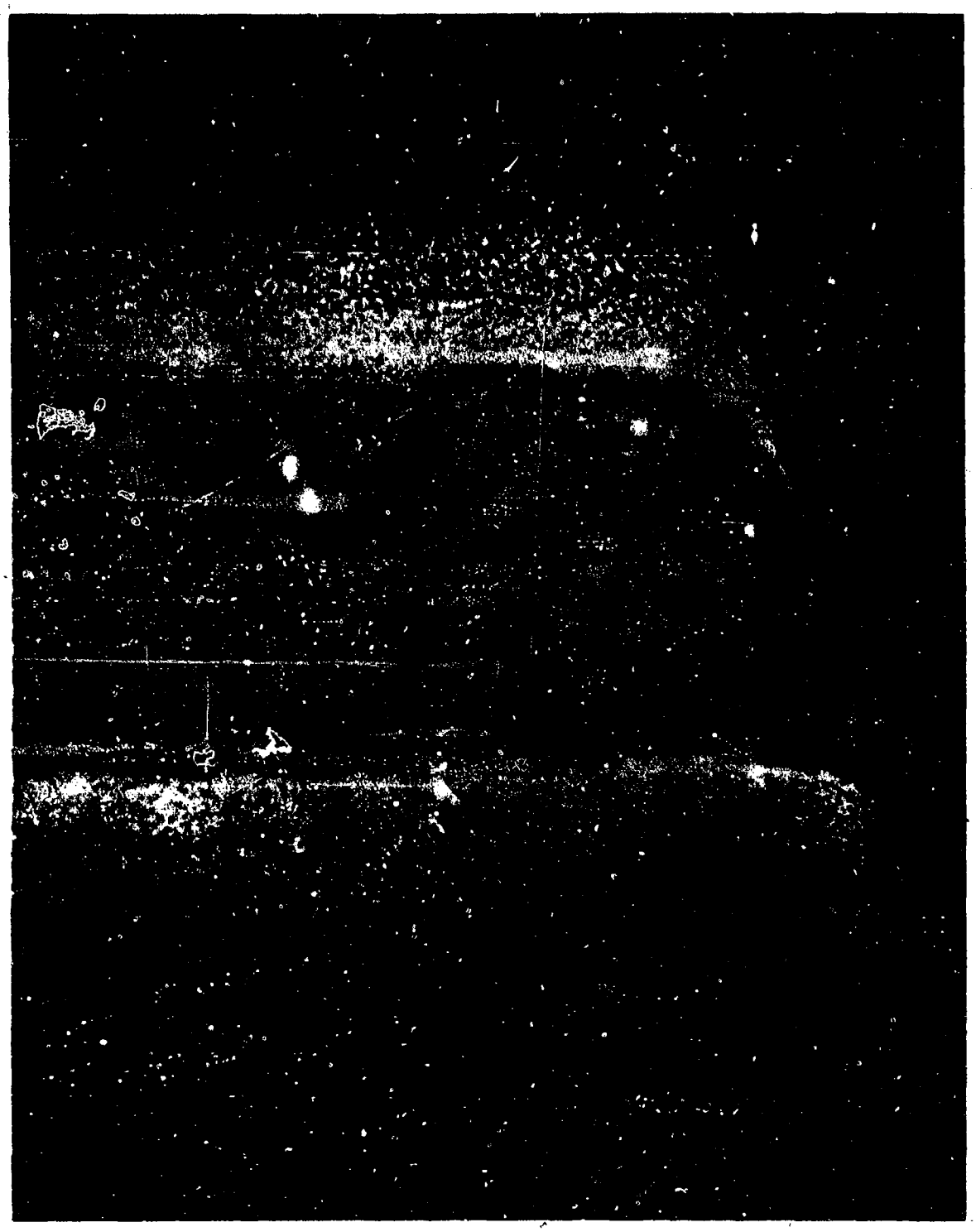

Figure 15. Photomicrograph (100X) Inconel 718 – Test 2

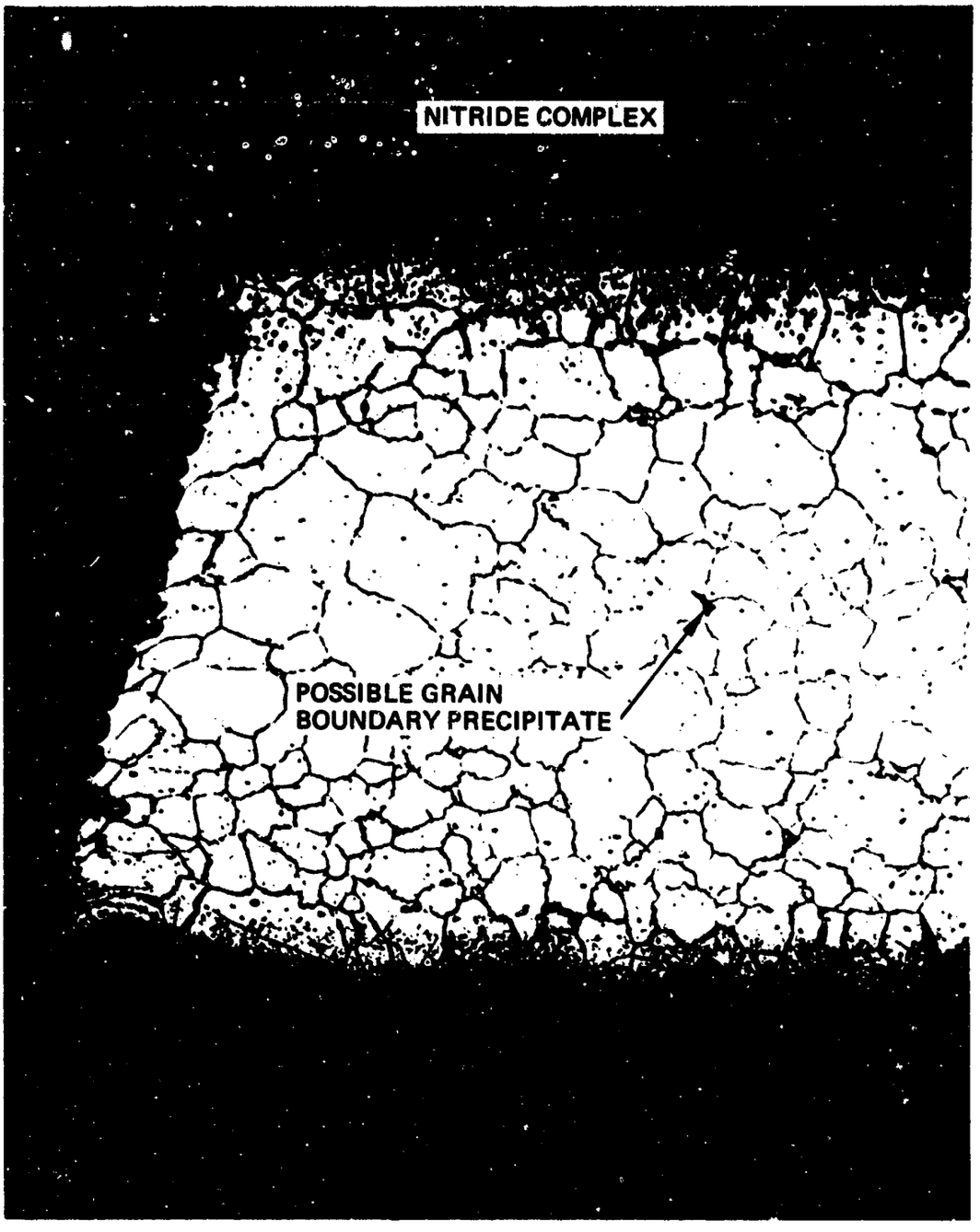

Figure 16. Photomicrograph (100X) Hastelloy C – Test 3

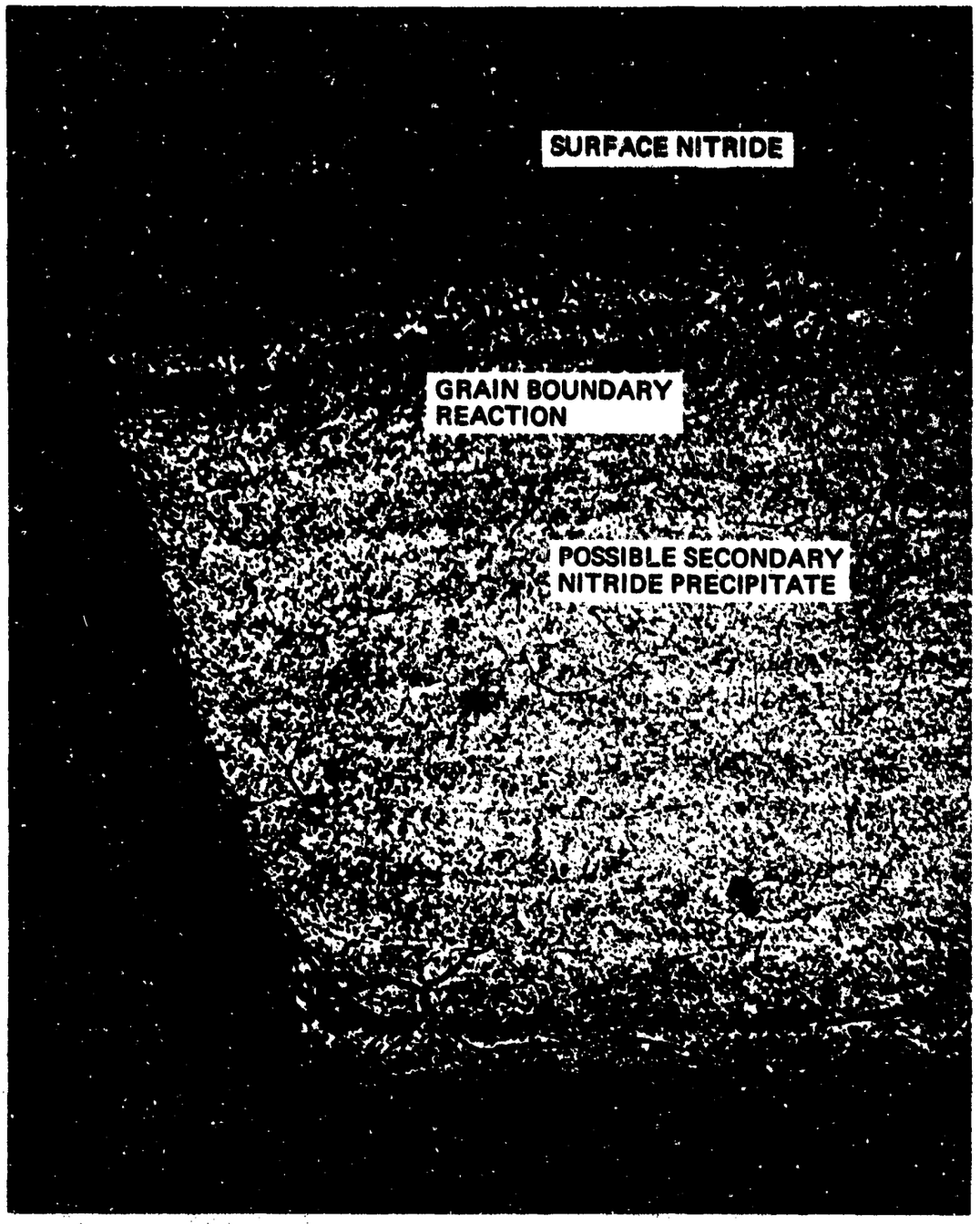

Figure 17. Photomicrograph (100X) L605 – Test No. 3

Hastelloy B – Hastelloy B appeared to have the best resistance to nitriding of the alloys tested. Nitride reactions do occur both in the grain boundaries and along structural planes of the grain. The depth of nitriding is about the same for both grain and grain boundary. It should be further noted that after the nitriding test, the test specimens would withstand a full 180-degree bend without fracture, and cracking was limited to the nitride layer. Figures 18 and 19 exhibit the nitride reaction for Hastelloy B resulting from this test.

These tests show Hastelloy B to be more nitride resistant than the other high-temperature alloys tested. The results of this test identify some chemical constituents which are undesirable in this environment (iron, for example) and thus have identified other materials which should be studied (TZM, Inconel 713, etc.).

Injector S/N 2 – Teardown of REA S/N 2 following the thermal design verification test revealed a failure of the rigimesh injection element as shown in Figure 20. This 0.5-inch-diameter element used 4-layer N-155 50- by 250-mesh rigimesh. Examination revealed extensive nitriding over the complete surface.

In order to determine if Haynes 25 by 50 by 250-mesh rigimesh could withstand the long-life duty cycle, a REM-Mono injector was sectioned and photomicrographed. The injector used (S/N 009) had been used on the active pitch position of prequalification REM S/N 0001A. During REM-Mono prequalification testing this engine had delivered 18,914 lbf-sec total impulse while accumulating 172,779 pulses. Photomicrographic comparison at 100 X magnification of this injector's rigimesh element and the element from the long-life injector S/N 2 is presented in Figure 21. The relative wire sizes between the two meshes are 0.004 inch minimum for 50 by 250 mesh and 0.016 inch minimum for 12 by 64 mesh. The photomicrographs reveal complete nitriding of the N-155 50- by 250-mesh material used in S/N 2, and a nitriding layer approximately 0.0004 inch on the H-25 12- by 64-mesh material used on REM-Mono. The Long-Life Program requires a burn time approximately ten times that of REM-Mono. Thus, if a worst-case assumption is made that the nitriding depth is linear with time, an end-of-life depth of 0.004 inch would occur with Haynes 25.

This study concluded therefore that Haynes 25, 50- by 250-mesh rigimesh would be satisfactory for the REM-Mono life requirements and consequently most satellite applications. For the Long-Life Program, however, the probability of excessive nitriding of a 0.004-inch-diameter wire precluded the use of 50- by 250-mesh rigimesh.

In summary, the nitriding tests indicate Hastelloy B to be a superior material for nitride resistance with Haynes 25 a close second. Because of the closeness of Haynes 25 to Hastelloy B in nitriding resistance, it was retained as the material for the thrust chamber body, bed plates, bed plate screens, and the injection element. Because of the lower operating temperature of the injector, Inconel 600 was used, although subsequent life tests indicate that an optimum material should have been selected.

2.3.2 Catalyst Strength

Nonflow cycle tests were conducted to verify the catalyst preload design criteria. The first test series was made up of static catalyst loading tests to evaluate the effects of catalyst overpack and

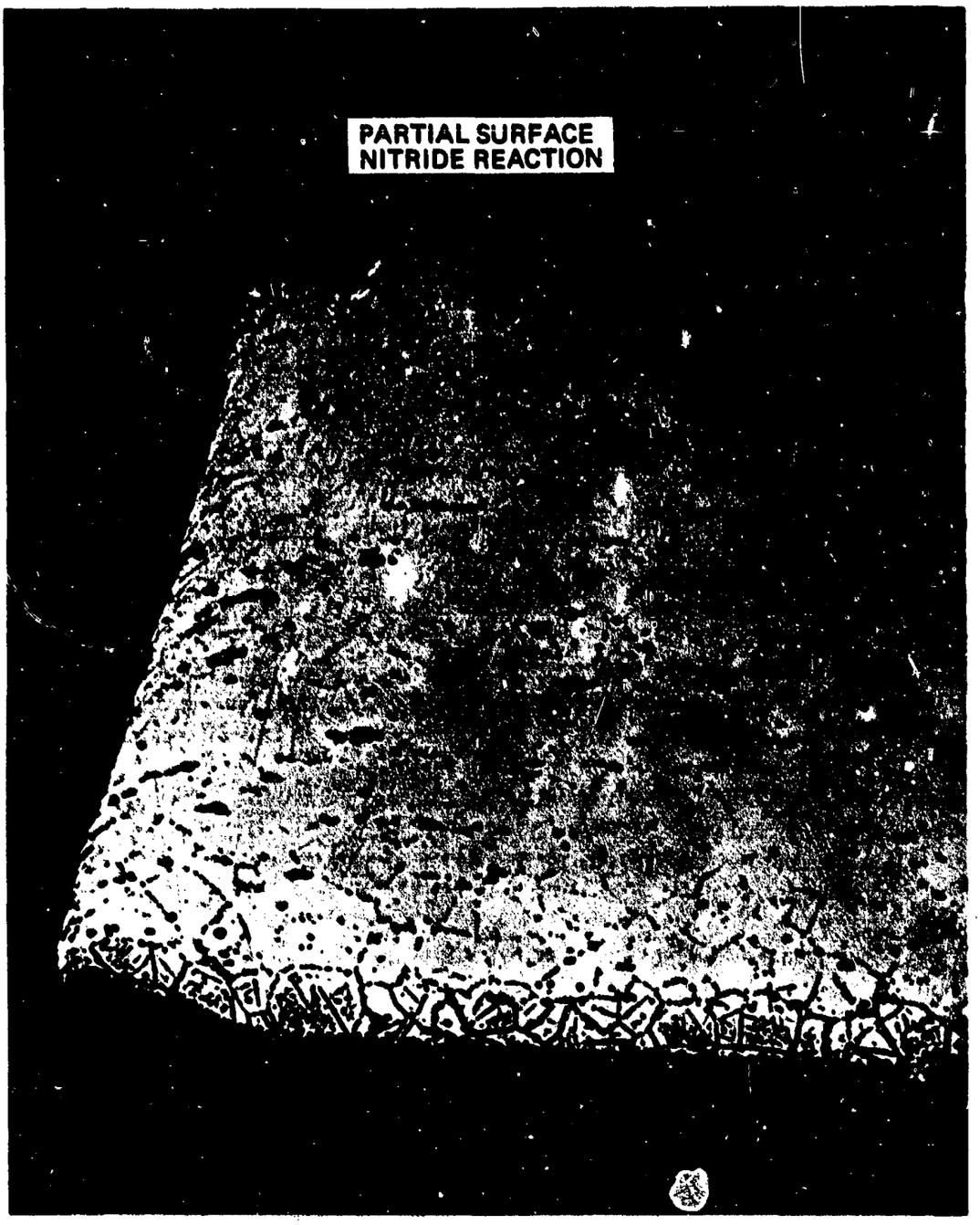

Figure 18. Photomicrograph (100X) Hastelloy B – Test 2

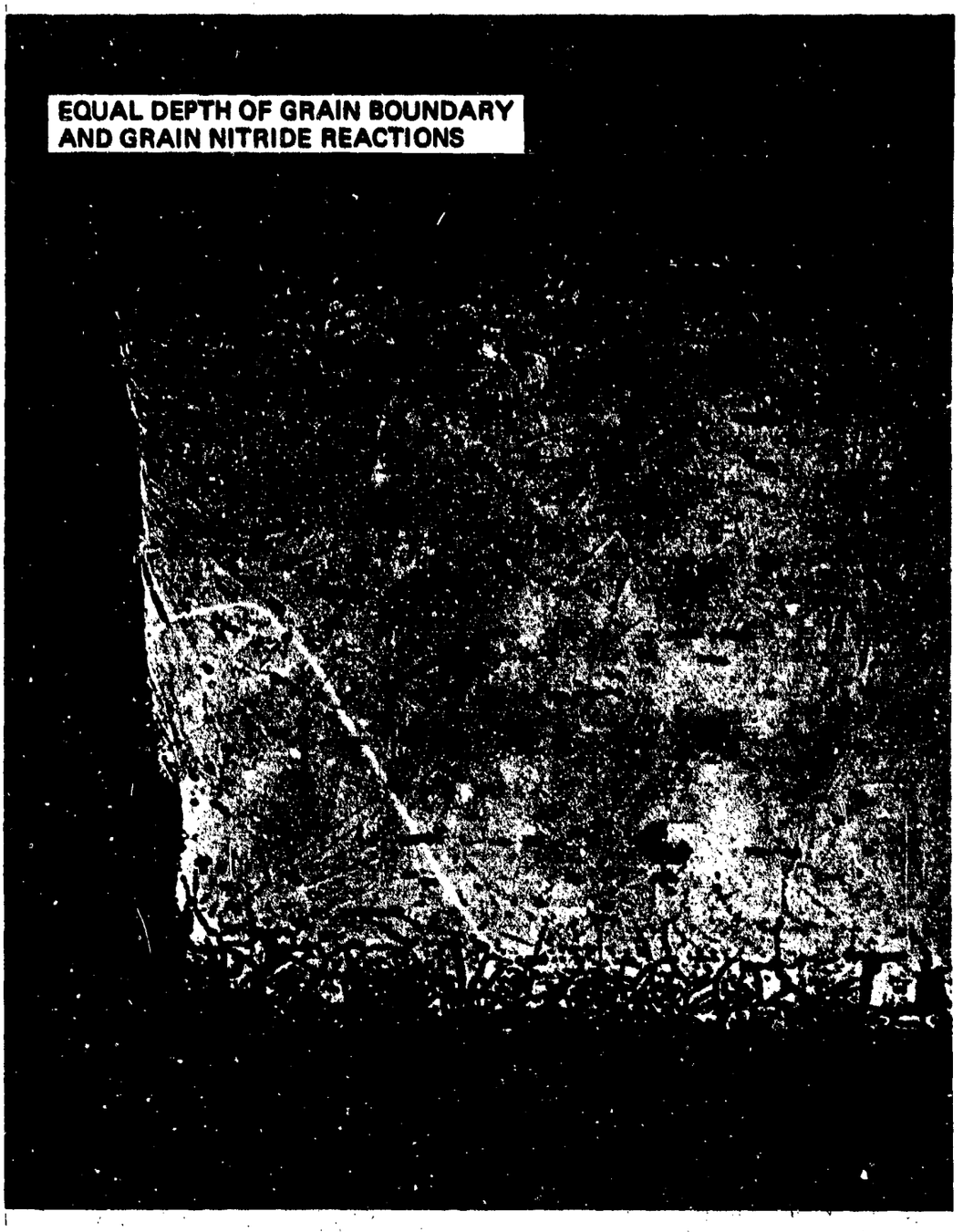

Figure 19. Photomicrograph (100X) Hastelloy B — Test 4

BODY WITHOUT MAGNIFICATION

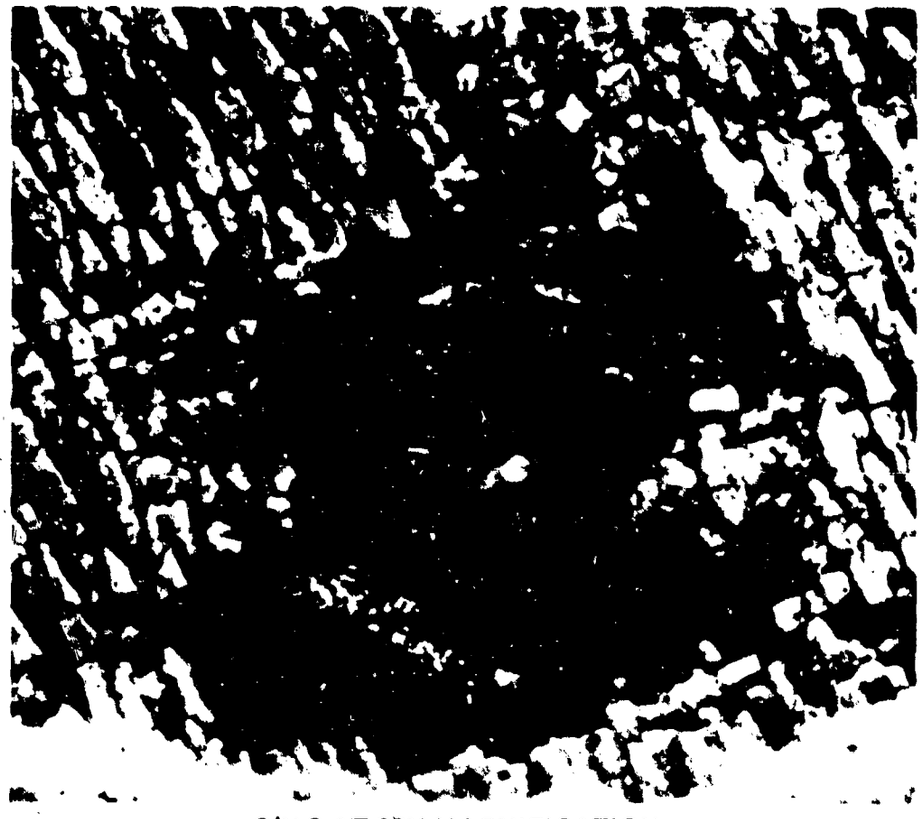

S/N 2 AT 23X MAGNIFICATION

Figure 20. Long-Life Injector S/N 2 after Thermal Design Verification Test

SECTION OF S/N 2 AT 100X MAGNIFICATION

Figure 21. Comparison of Long-Life and REM-Mono Injector Elements

SECTION OF REM-MONO PREQUALIFICATION INJECTOR S/N 009 AFTER LIFE TEST AT 100X MAGNIFICATION

Figure 21 (Concluded). Comparison of Long-Life and REM-Mono Injector Elements

differential thermal expansion upon the catalyst. Maximum loads as determined from this static test series were used for a series of catalyst cycling load tests to assess the catalyst strength capability.

Static Tests – The static load catalyst test setup is schematically shown in Figure 22. A 6-gram sample of 25- by 30-mesh catalyst was loaded into the specimen holder which is 1 inch inside diameter. This closely simulates the injector assembly of the Long-Life REA (1.179 inch ID). The specimen was packed by vibration for 5 minutes with 20 psi preload on the mandrel. Each specimen was incrementally loaded with the deadweight tester to determine the actual pressures corresponding to calculated length changes. Dimensionless deflection as a function of applied pressure from the first nine tests is presented in Figure 23. For the first seven tests each specimen was subjected to sufficient pressure to deflect 0.0085 inch. Subsequently an additional deflection of 0.006 inch was achieved to simulate the effect of the catalyst reaching thermal equilibrium with the thrust chamber walls still cold. In order to normalize the data for the length differences, the data is presented as dimensionless deflection. Test numbers 1 through 5 were conducted by incremental loading and unloading of the specimen in 20 psi steps. This test procedure yielded as many as 60 cycles of loading on test 4. In order to eliminate any effects of this cyclic loading, tests 6 and 7 were steadily loaded and unloaded. As shown in Figure 23, the test procedure does cause a slight shift in the curve shape but has negligible effect on the permanent deflection. Tests 1, 2, 3 and 6 were conducted on virgin catalyst processed per REM-Mono specification MS-0110, whereas tests 5 and 7 used that portion of catalyst from previous tests that was retained on a 30-mesh sieve. Test 4 was unique in that the catalyst from test 3 was not removed from the holder, the final length measured on test 3 being used as the initial length (L_O) for test 4.

The average permanent deflection of the virgin samples is calculated from the average dimensionless deflection of 0.0266 combined with the average initial length of 0.300 inch to yield 0.008-inch deflection. Combining this with the 0.0085-inch overpack and 0.006-inch catalyst thermal growth indicates that the catalyst is capable of 0.0065-inch recovery. The chamber thermal growth calculations indicate a worst-case equivalent length change of 0.0087 inch, which, for a 0.0085-inch overpack, results in a void in the upper bed of 0.0022 inch equivalent length during steady-state operation. Tests 5 and 7 were conducted to see if one pressure cycle would weed out the weak particles. The results shown on Figure 23 with a relatively high permanent deflection indicate conversely that some weakening has occurred due to the previous stress cycle.

In order to limit the potential void volume in the upper catalyst bed additional tests were conducted at different overpacks. Test results are included on Figure 23. Test number 8 simulated an overpack of 0.003 inch which was loaded additionally to the predicted catalyst thermal growth of 0.006 inch and relaxed for a permanent dimensionless deflection of 0.011. With an average specimen initial length of 0.300 inch, this corresponds to a permanent deflection of 0.0033 inch. Combining this with the 0.003-inch overpack and 0.006-inch catalyst thermal growth indicates that the catalyst is capable of 0.0059-inch recovery. This results in an apparent void under hot wall conditions of 0.003 inch as compared to 0.0022 inch with the 0.0085-inch overpack. However, as shown on Figure 23, the maximum loading pressure applied to the catalyst bed is reduced from 920 psi with the 0.0085-inch overpack to 640 psi for the 0.003-inch overpack, with a corresponding improvement in percent survivors from 84.3 to 97.7. In view of the extremely small void equivalent length change as compared to the significant reduction in catalyst loads, the 0.003-inch overpack was selected as baseline for the Long-Life Engine Program.

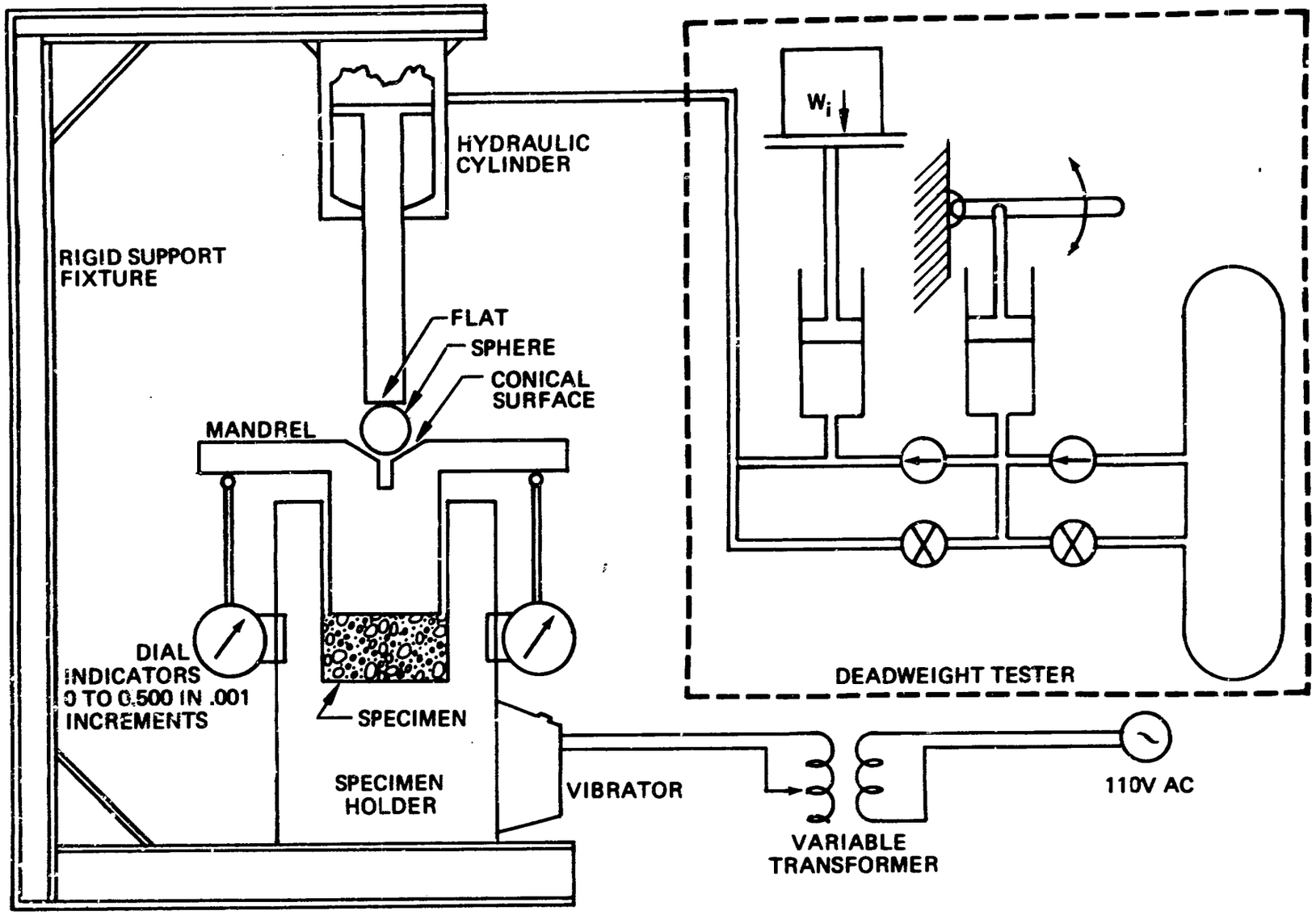

Figure 22. Catalyst Crush Test Setup

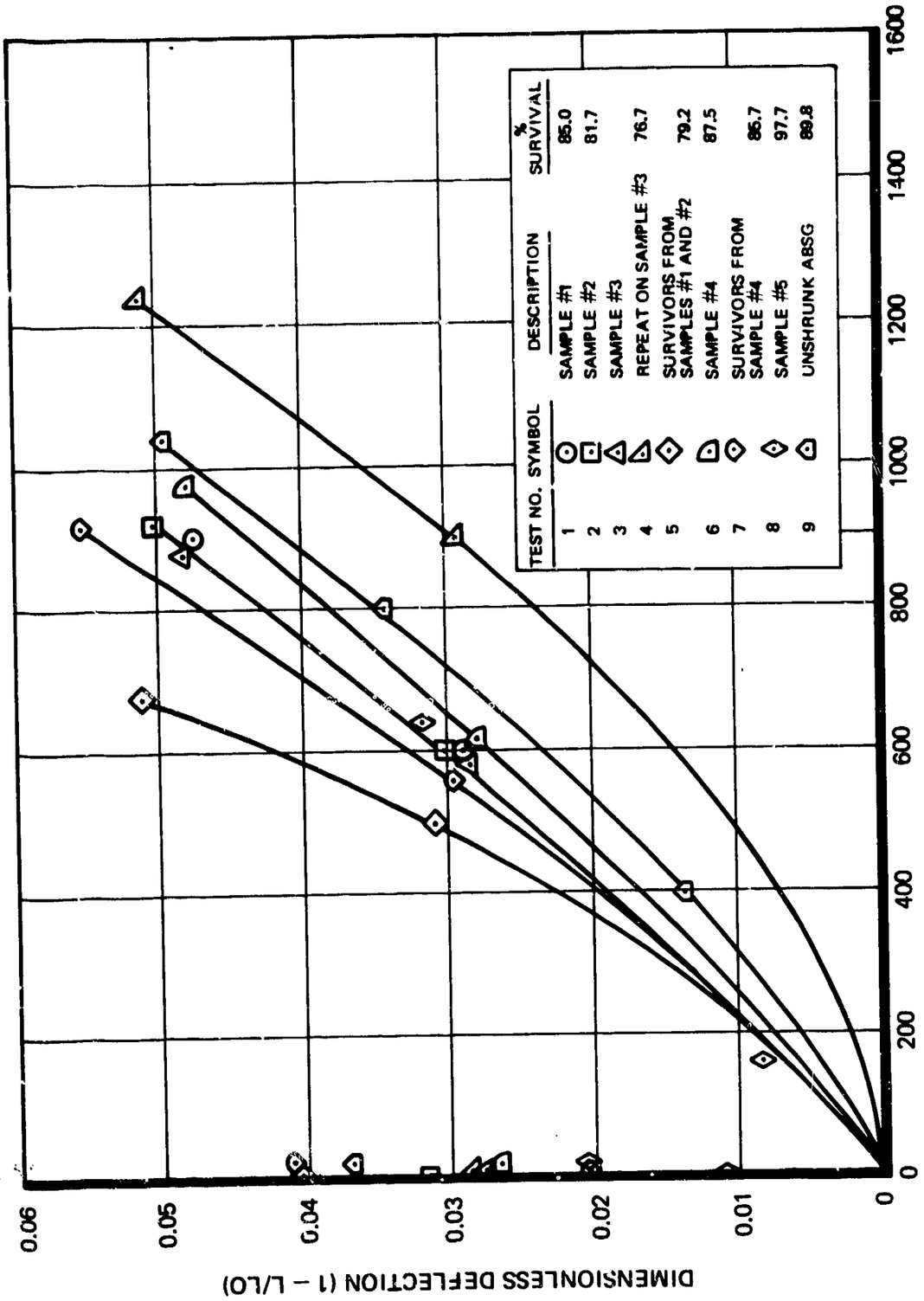

Figure 23. Catalyst Strength – Static Test Results

Test 9 was a repeat of test number 6 on a sample of untreated catalyst (as received from Shell Development Company). The purpose of this test was to determine if RRC's processing of the catalyst had any effect on strength. As shown on Figure 23 the only appreciable difference is permanent deflection with the unshrunk catalyst significantly higher. The test indicates that RRC processing is not at all detrimental to catalyst strength.

A special sample of 90% water attrited Shell 405 ABSG catalyst was obtained from AFRPL and samples were subjected to this static load test. Test results are summarized on Figure 24. For comparison purposes the results of test number 8 are also included; this test was conducted on REM-Mono type catalyst (50% attrited). As shown on the figure there is a significant difference in load carrying capability with the 90% attrited catalyst as compared to the 50% attrited. The effect of shrinking this 90% attrited catalyst does not appreciably effect the load carrying capacity or permanent deflection as shown on Figure 24. This same characteristic was demonstrated on the 50% attrited catalyst on Figure 23.

Cycling Tests – Simulated catalyst beds were subjected to cycling load tests to determine the effects of mechanical loads, predicted during test firings, on the physical properties of the catalyst. The schematic of the catalyst cycling test apparatus is presented in Figure 25. On the basis of the static load test results, the load was cycled between 0 and 640 psig at a rate of one cycle per minute with pressure rise and decay times less than 1 second each. Three samples were taken of each catalyst type tested and subjected to 1, 10 and 100 cycles.

Samples of the REM-Mono catalyst as well as shrunk and unshrunk 90% attrited catalyst were subjected to this test series. Test results are tabulated in Table XI. As shown on the table the 90% attrited catalyst significantly improves the permanent deflection and percent survivors at the 100-cycle data point. These values were converted into an effective hot bed void length in the upper bed by assuming that all fines smaller than 50 mesh would pass through the upper bed plate screen and combining this with the permanent deflection. This data is plotted in Figure 26. As a result of these tests the 90% water attrited Shell 405 ABSG catalyst was selected for the baseline long life engine.

2.3.3 Thermal Margin Tests

REA's fabricated with each of the candidate injector designs were subjected to a thermal design verification test. This test was designed to determine the ability of the REA to operate successfully while being fired at worst-case thermal duty cycle. The test installation schematic is shown in Figure 27; for this test series the cryogenic target and REA force cooler were not used. The test instrumentation list is presented on Table XII and REA thermocouple instrumentation locations are shown on Figure 28.

Test number 1 was conducted with REA S/N 2 which incorporated the 0.5-inch-diameter single spud injector element fabricated from four-layer 50- by 250-mesh N-155 rigimesh. At the completion of the sequence series which searched for the worst-case duty cycle, injector boiling was indicated by the quick-look data. The test series was partially repeated at maximum feed pressure conditions (350 psia). Pulse peak chamber pressure and ignition delay for each of these sequences is presented on Table XIII, and peak chamber pressure is plotted as a function of duty cycle on Figure 29. The complete test series was repeated with the inlet propellant temperature decreased from 140

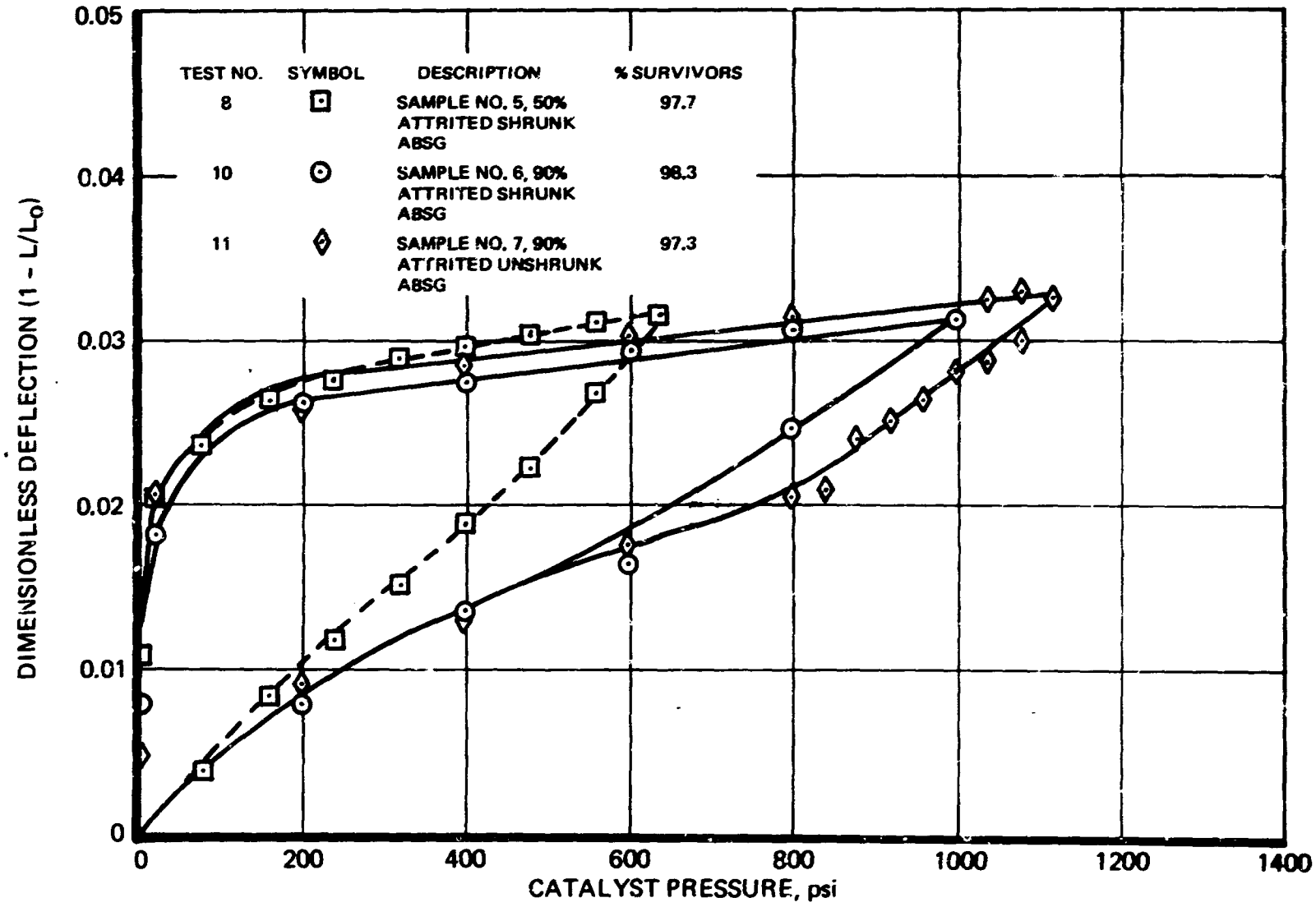

Figure 24. Catalyst Static Load Test Results

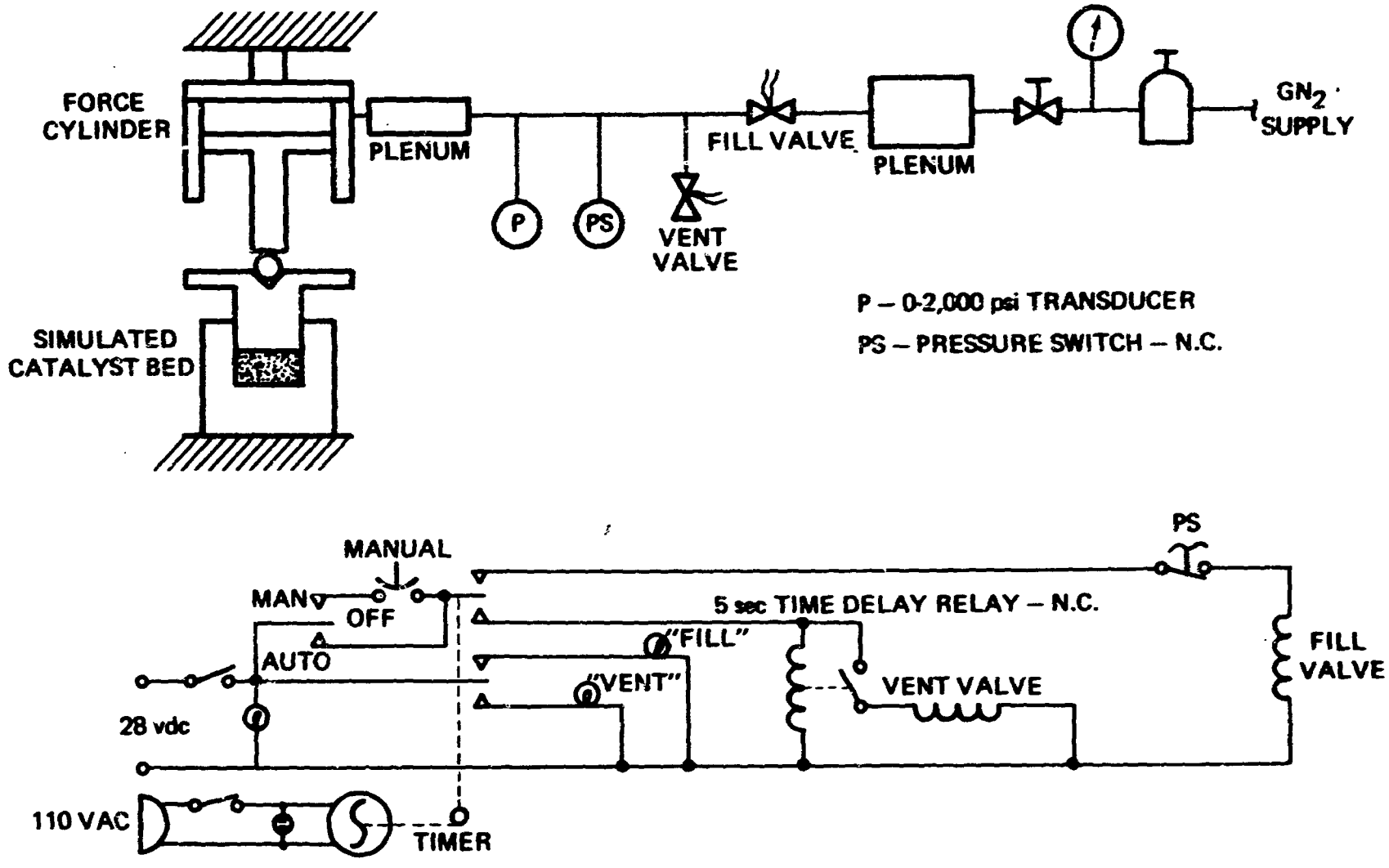

Figure 25. Catalyst Cycling Test Apparatus

Table XI. Catalyst Cycling Load Test Results

Sample Type	Sample No.	No. of Cycles	Loaded Length (inches)	1st Cycle Deflec. (inches)	Last Cycle Deflec.	Perm. Deflec. (inches)	Screening Distribution – Weight			
							% 30 Mesh	% 40 Mesh	% 50 Mesh	% <50 Mesh
25-30 Mesh Shell 405 Carrier 50% Water Attrited Shrunk-	1	1	0.3128	0.0127	—	0.0060	97.6	2.0	0.2	0.2
	2	10	0.3191	0.0183	0.0263	0.0168	87.8	8.5	0.8	2.9
	3	100	0.3201	0.0181	0.0457	0.0274	61.9	18.9	5.7	13.5
25-30 Mesh Shell 405 Carrier 90% Water Attrited Unshrunk-	4	1	0.3026	0.0072	—	0.0012	98.4	1.0	0.5	0.1
	5	10	0.2983	0.0065	0.0080	0.0019	98.4	1.3	0.2	0.1
	6	100	0.3016	0.0070	0.0143	0.0070	91.3	5.8	1.2	1.7
25-30 Mesh Shell 405 Carrier 90% Water Attrited Shrunk-	7	1	0.3036	0.0078	—	0.0012	99.1	0.6	0.1	0.2
	8	10	0.3088	0.0080	0.0099	0.0025	99.3	0.5	0.1	0.1
	9	100	0.3085	0.0090	0.0170	0.0105	88.9	6.1	2.5	2.5

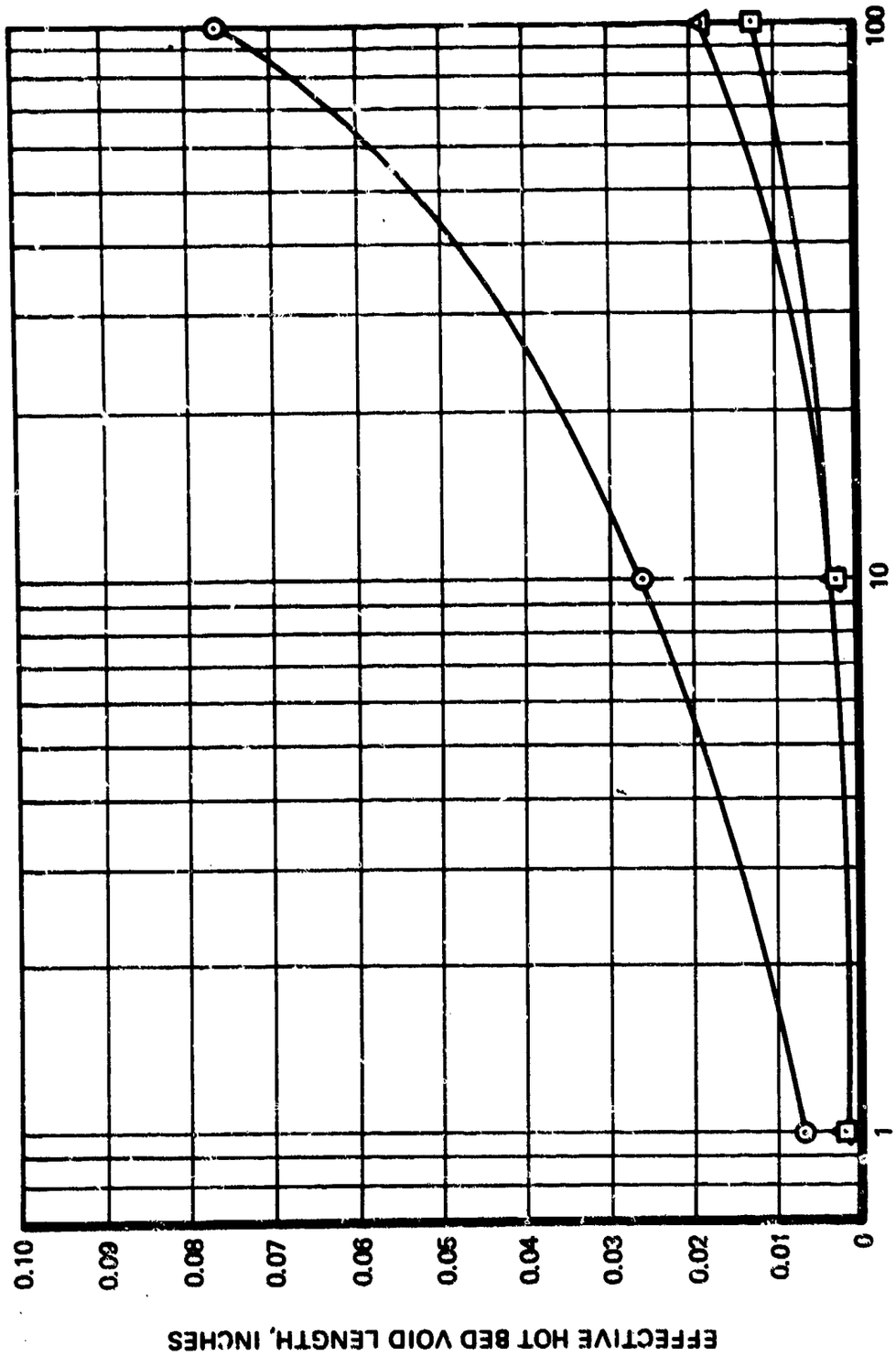

Figure 23. Catalyst Cycling Load Test Results

11023-67D

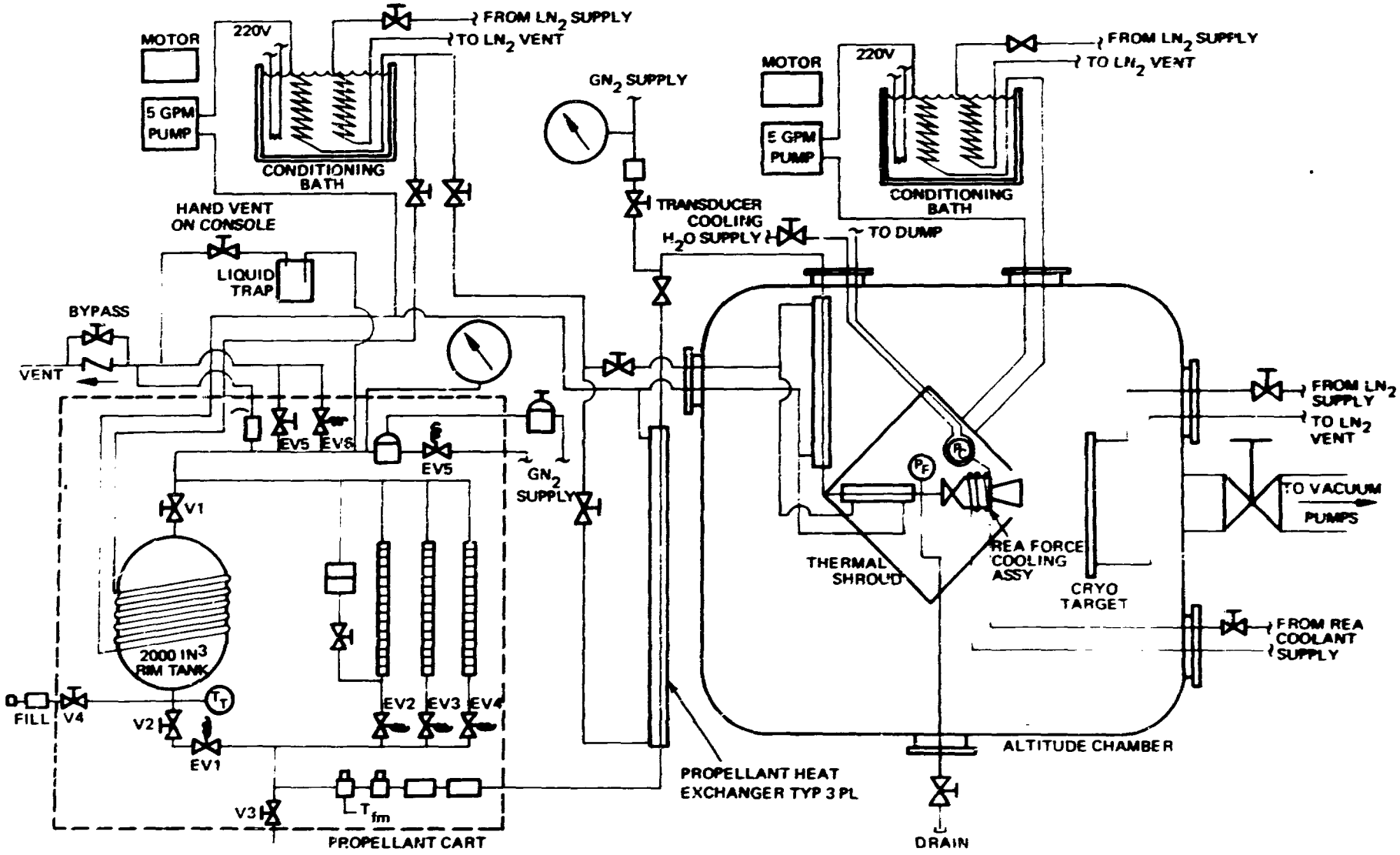

Figure 27. REA Altitude Test Setup

Table XII. Thermal Design Verification Test - Instrumentation List

Parameter	Symbol	Range	Recording Method		
			Dymec	Strip Chart	Osc
Chamber pressure	P_{c1}	0–150 psia	X	X	X
Chamber pressure	P_{c2}	0–150 psia	X	X	X
Feed pressure	P_f	0–500 psig	X	X	X
Test cell pressure	P_a	0–0.5 psia	X		X
TCV temperature	T_{v1}	0–10 mv	X		
TCV temperature	T_{v2}	0–10 mv	X		
Feed tube temperature	T_{ft1}	0–100 mv	X		
Feed tube temperature	T_{ft2}	0–100 mv	X		
Feed tube temperature	T_{ft3}	0–100 mv	X		
Injector temperature	T_{h1}	0–100 mv	X		
Injector temperature	T_{h2}	0–100 mv	X		
Injector temperature	T_{h3}	0–100 mv	X		
Chamber wall temperature	T_{w1}	0–100 mv	X		
Chamber wall temperature	T_{w2}	0–100 mv	X		
Chamber wall temperature	T_{w3}	0–100 mv	X		
Nozzle temperature	T_{nc}	0–100 mv	X	X	
Propellant temperature	T_{fi}	0–10 mv	X	X	
Flowmeter temperature	T_{fm}	0–10 mv	X		
Shroud temperature	T_{ts}	0–10 mv	X	X	
Fuel flow	$\dot{w}_1$	0–1 KHz	X		X
Fuel flow	$\dot{w}_2$	0–1 KHz	X		X
Time reference	Hz	500 ± 1 Hz	X		X
TCV voltage	V_e	0–30 vdc			X
TCV current	V_i	0–1 adc			X

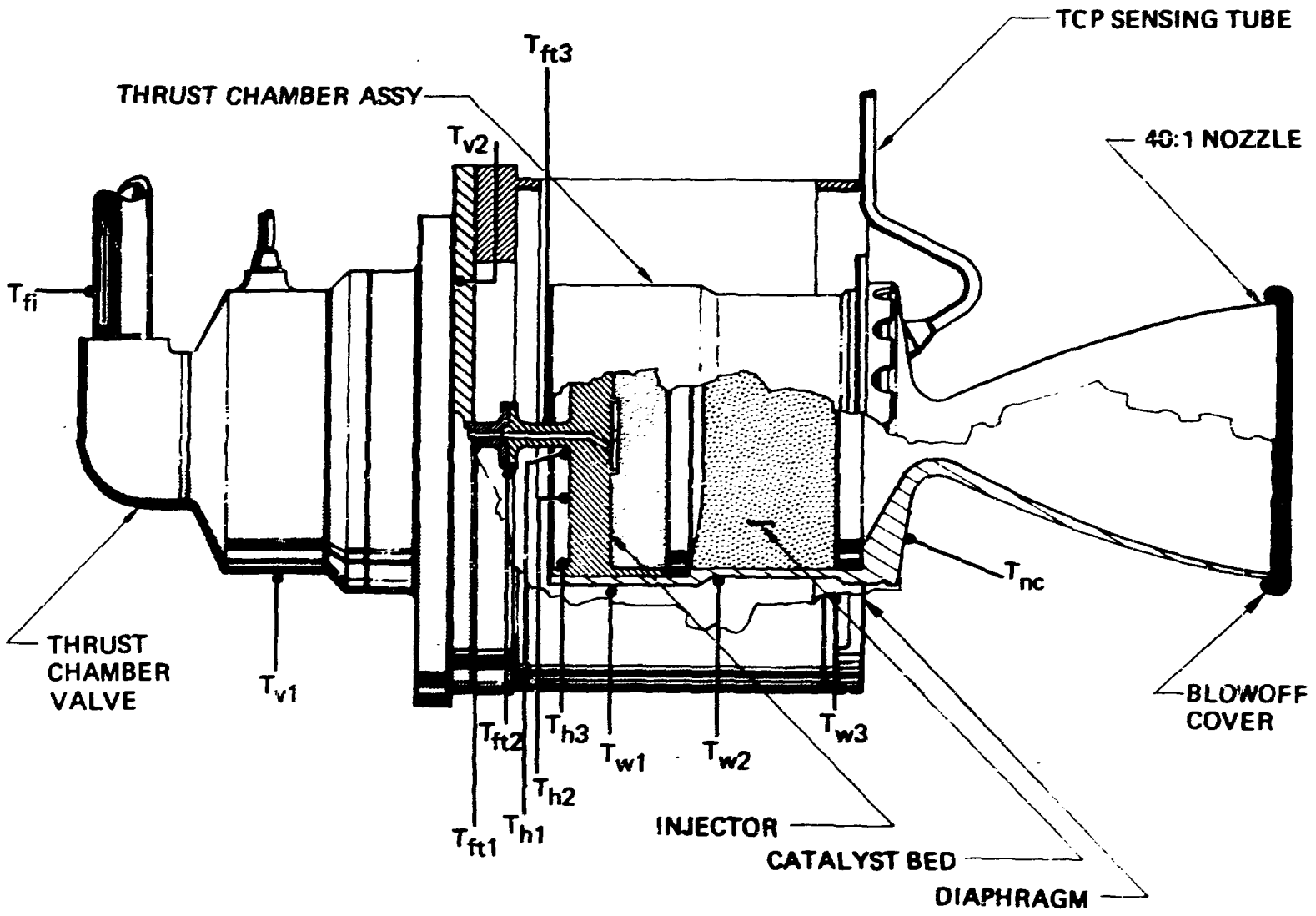

Figure 28. Reaction Engine Assembly Long-Life Test Thermocouple Locations

Table XIII. Long Life REA Development Ignition Delay & Peak Chamber Pressure for TDVT S/N 2 Test 1

P_f = 100 psia

T_p = 140°F

Sequence No.	Duty Cycle	t_i ~ms	P_c (1st Pulse)	P_c (Equilibrium)
1-1	0.020/1.980	22	9	15
1-2	0.020/.980	10	17	12
1-3	0.020/.480	10	16	10
1-4	0.050/.950	10	17	12
1-5	0.050/1.950	9	17	11
1-6	0.050/2.450	9	16	12
1-7	0.050/3.280	9	19	12
1-8	100/—	9	N/A	40

P_f = 350 psia

T_p = 140°F

Sequence No.	Duty Cycle	t_i ~ms	P_c (1st Pulse)	P_c (Equilibrium)
1-1H	0.020/1.980	9	51	38
1-2H	0.020/.980	9	48.9	39.0
1-3H	0.020/.480	10	49.8	41.4
1-4H	0.050/.950	9	75.9	75.0
1-5H	0.050/1.950	N/A	N/A	N/A
1-6H	0.050/2.450	N/A	N/A	N/A
1-7H	0.050/3.280	N/A	N/A	N/A
1-8H	100/—	3	N/A	99.0

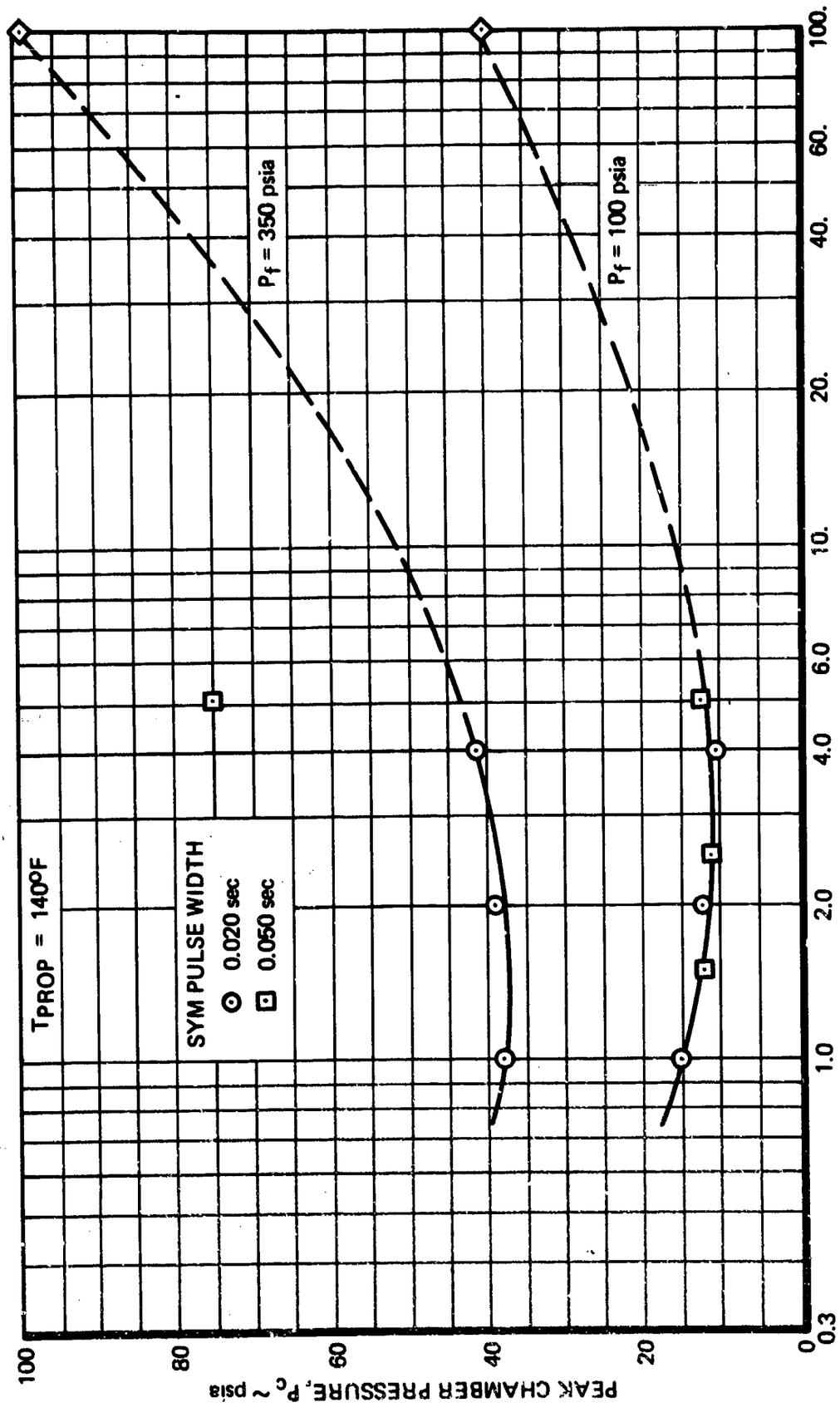

Figure 29. Peak Chamber Pressure for TDVT – S/N 2, Test 1

to 125°F. The results of this test are presented in Table XIV and plotted on Figure 30. During the last sequence of this test series (1-8Ha) a sharp dropoff in steady-state chamber pressure occurred 50 seconds into the run. Engine disassembly revealed that this was due to a failure of the rigimesh injection element. Figure 20 shows the element after firing; this figure includes a photograph at 23 X magnificaton which shows severe nitriding and stress cracks.

Although the N-155 material had been successfully employed as an interim design on another RRC engine, its high iron content makes it much more susceptible to nitriding than Haynes 25 (see paragraph 2.3.1).

On the basis of the test results on the single spud injector and revised thermal analyses, it was apparent that the two-layer 50- by 250-mesh rigimesh in the annulus injector would fail. However, since the REA was already assembled and it would provide a checkpoint on the thermal model, RRC conducted the TDVT test on the annulus injector. Pulse peak chamber pressure and ignition delay for each of the sequences is also presented on Table XIV, with peak chamber pressure plotted as a function of duty cycle on Figure 31. It is obvious from this data that injector boiling did occur at the low feed pressure in correlation with the final thermal model (see paragraph 2.2.2).

Inspection of the rigimesh element following disassembly revealed hairline cracks in the fine wires over each of the three branch passages with a permanent deflection of 0.001 inch.

As a consequence of these TDVT tests and nitriding test evaluations, the 50- by 250-mesh rigimesh was eliminated from further consideration for the long-life application. Injectors S/N 3 and 4 were fabricated on the basis of the use of 12- by 64-mesh rigimesh using alternate No. 2 and the baseline injector configurations respectively (see Figure 6). Because of the simplicity of the baseline injector design, injector S/N 4 was completed first and subjected to the TDVT test series. Pulse peak chamber pressure and ignition delay for each of these sequences is presented on Table XV, and peak chamber pressure is plotted as a function of duty cycle on Figure 32. There was no evidence of boiling throughout the test, and the steady-state sequence (1-8) was extremely smooth with nominal chamber pressure oscillations less than ±1 psi. Temperatures for this run are tabulated for each sequence on Table XVI.

As a result of these tests, this design was selected as baseline and work was stopped on the three speed design (S/N 3).

2.3.4 Cold Start Test

A cold-start test series was conducted on the design selected from the thermal design verification test series. This test duty cycle, shown on Table XVII, incorporated a 65°F baseline duty cycle, which was conducted before and after the cold-start test series. Forty-two, 10-second-duration cold starts were conducted at maximum inlet pressure with both the engine and propellant at 40°F. During assembly and test of the cold-start REA, a nonfiring thrust chamber was assembled with fresh catalyst, subjected to identical handling, and exposed to the same external atmosphere in order to isolate the effects of cold starts upon catalyst characteristics. The test setup was as shown on Figure 27.

Table XIV. Long Life REA Development Ignition Delay & Peak Chamber Pressure for TDVT S/N 2 Test 2

P_f = 100 psia

T_p = 125°F

Sequence No.	Duty Cycle	t_i ~ms	P_c (1st Pulse)	P_c (Equilibrium)
1-1a	0.020/1.980	19	17.7	19.2
1-2a	0.020/.980	14	14.6	26.7
1-3a	0.020/.480	10	24.0	27.0
1-4a	0.050/.950	8	30.9	33.9
1-5a	0.050/1.950	7	31.5	32.4
1-6a	0.050/2.450	9	31.5	32.7
1-7a	0.050/3.280	8	30.0	32.4
1-8a	100/—	9	29.5	40.2

P_f = 350 psia

T_p = 125°F

Sequence No.	Duty Cycle	t_i ~ms	P_c (1st Pulse)	P_c (Equilibrium)
1-1Ha	0.020/1.980	8	54.3	69.3
1-2Ha	0.020/.980	8	60.3	75.9
1-3Ha	0.020/.480	8	64.5	79.2
1-4Ha	0.050/.950	8	88.5	96.0
1-5Ha	0.050/1.950	9	86.4	92.4
1-6HA	0.050/2.450	9	76.5	92.4
1-7Ha	0.050/3.280	8	82.5	87.9
1-8Ha	100/—	11	87.0	87.0

Table XIV. Long-Life REA Development Ignition Delay and Peak Chamber Pressure for TDVT S/N 1 Test 3 (Concluded)

P_f = 100 psia
T_p = 125°F

Sequence No.	Duty Cycle On/Off Time Seconds	t_i ~ms	P_c, psia (1st Pulse)	P_c, psia (Equilibrium)
1–1	0.020/1.980	26	9.8	8.3
1–2	0.020/0.980	11	8.7	4.8
1–3	0.020/0.480	12	6.3	5.4
1–4	0.050/0.950	11	33.9	5.7
1–8	100/	12		31.8

P_f = 350 psia
T_p = 125°F

Sequence No.	Duty Cycle On/Off Time Seconds	t_i ~ms	P_c, psia (1st Pulse)	P_c, psia (Equilibrium)
1–1	0.020/1.980	11	35.7	32.7
1–4	0.050/0.950	10	55.5	68.4
1–5	0.050/1.950	10	59.7	63.7
1–6	0.050/2.450	11	58.5	62.1
1–7H	0.050/3.280	10	59.1	62.1
1–8H	100/	10		78.8

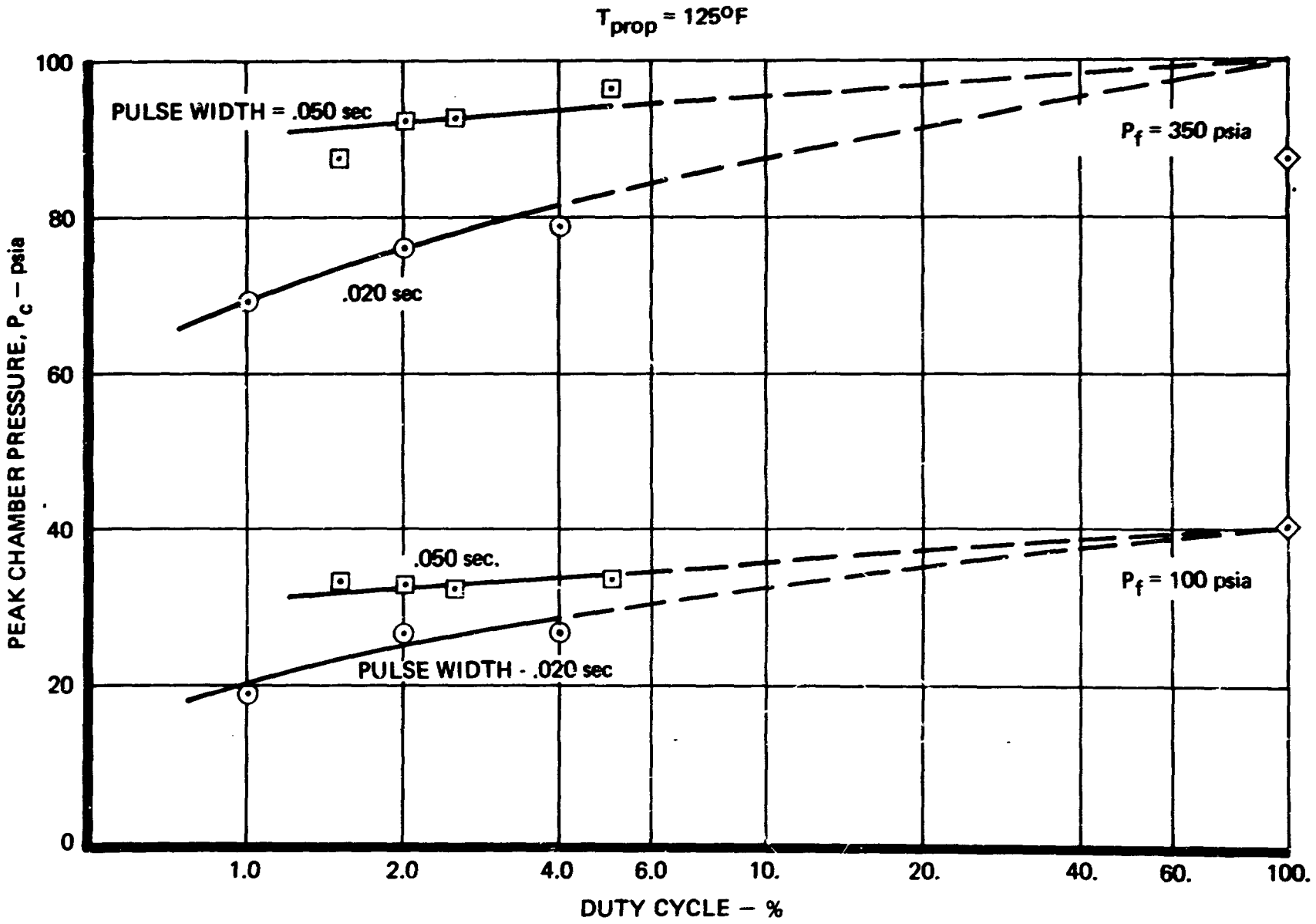

Figure 30. Peak Chamber Pressure for TDVT S/N 2 Test 2

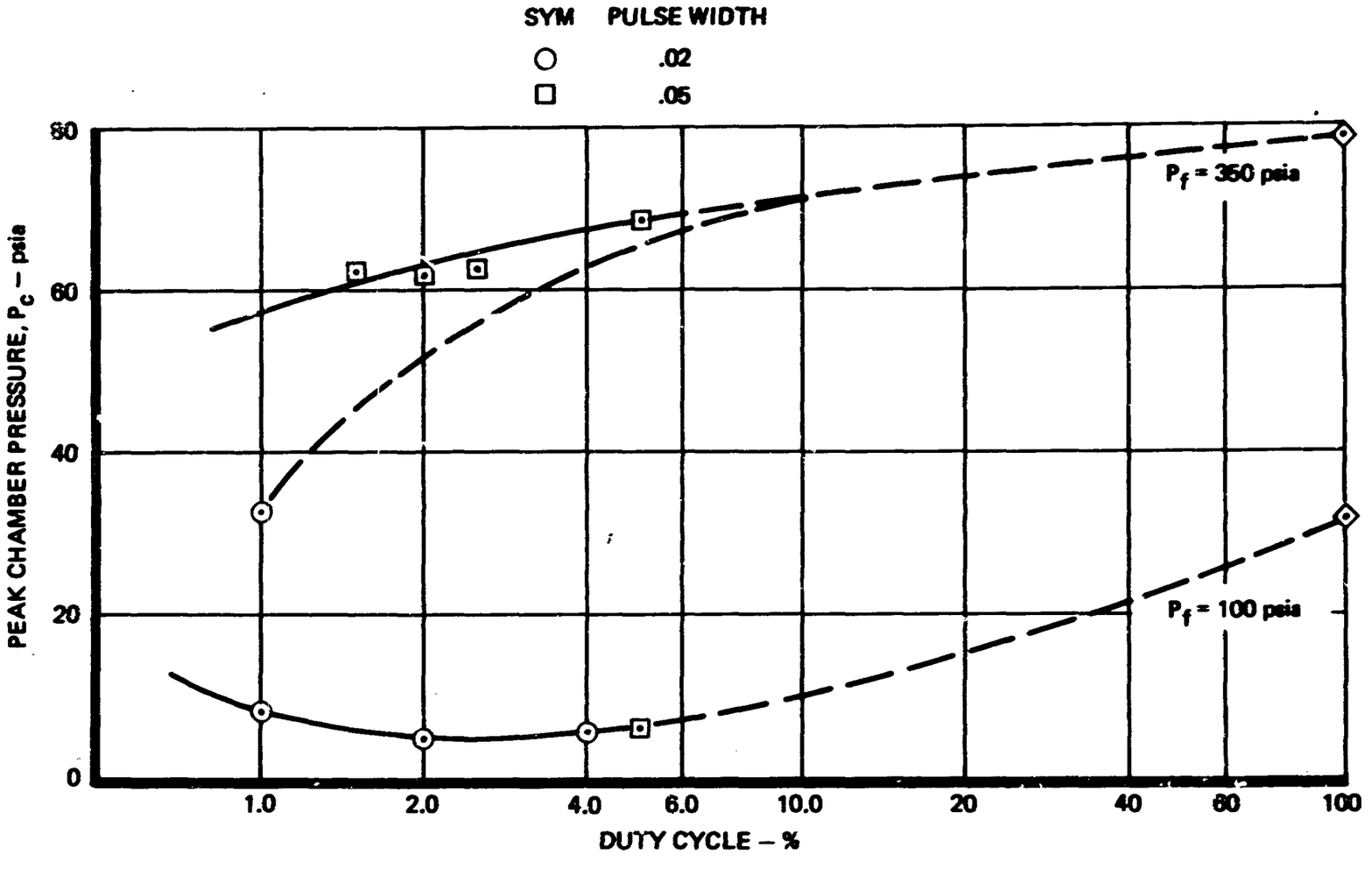

Figure 31. Peak Chamber Pressure for TDVT, S/N 1 Test 3 T_{prop} = 125°F

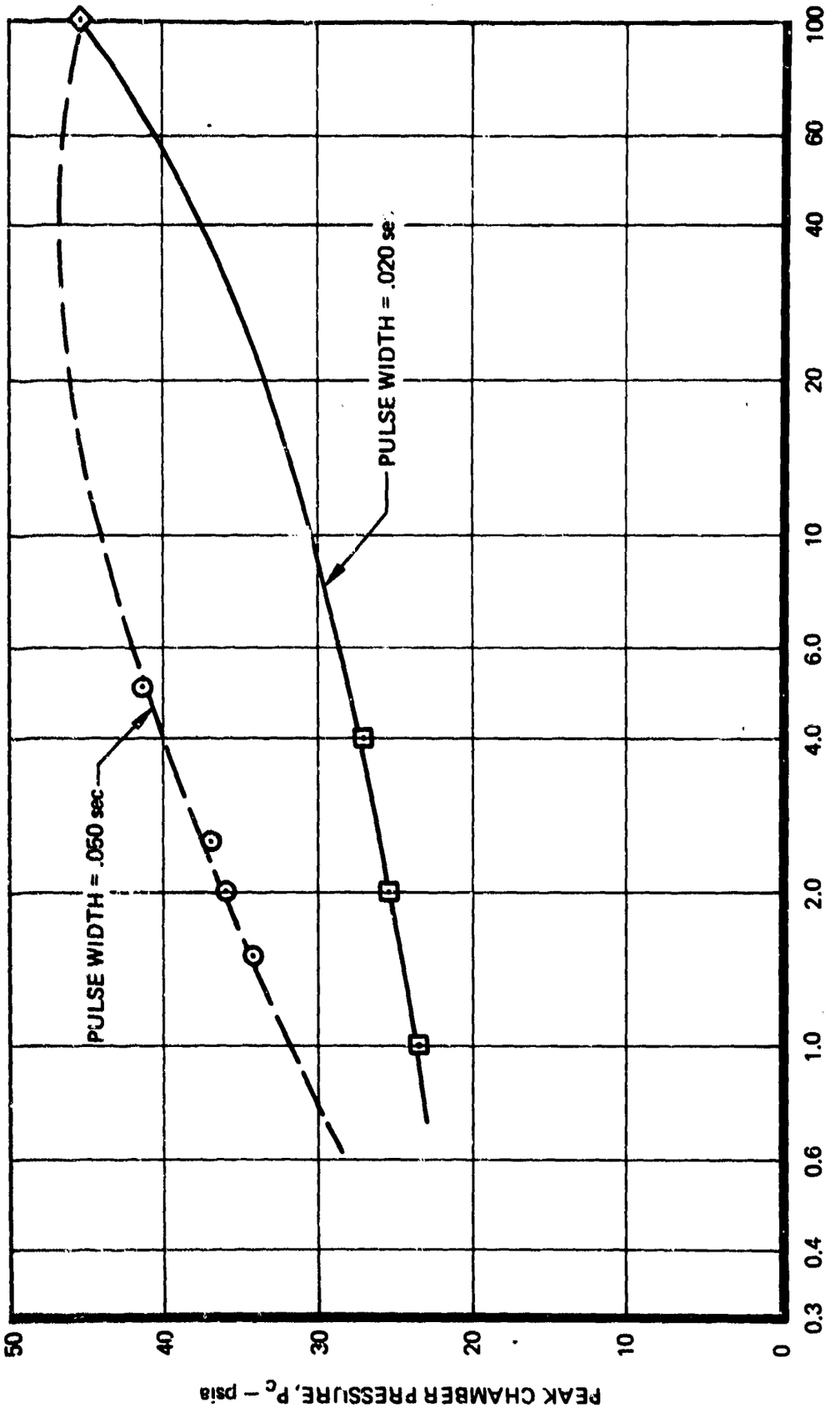

Figure 32. Peak Chamber Pressure for TDVT Run No. 4
S/N 4 P_{feed} = 100 psia T_{prop} = 125°F

Table XV. Long-Life REA Development Ignition Delay and Peak Chamber Pressure for TDVT S/N 4 Test 4

P_f = 98 psia

T_p = 125°F

Sequence No.	Duty Cycle On/Off Time Seconds	t_i ~ms	P_c (1st Pulse)	P_c (Equilibrium)
1–1	0.020/1.980	22	11.7	24.0
1–2	0.020/0.980	12	19.8	25.5
1–3	0.020/0.480	11	22.5	27.9
1–4	0.050/0.950	10	34.5	38.4
1–5	0.050/1.950	9	33.8	36.0
1–6	0.050/2.450	12	32.4	36.0
1–7	0.050/3.280	12	33.0	33.6
1–8	100/	11	N/A	45.0

Cold Start Test Results – Pulse-mode data from the first baseline test series is summarized in Table XVIII. Each of these sequences was started with the REA and propellant at 65°F and consisted of 100 pulses.

Following this initial baseline test, 42 successive cold starts were fired on the REA. Each 10-second steady-state burn was started with both the REA and propellant at 40°F. Test data is summarized in Table XIX. Data from those sequences for which ignition delay is not available are due to an overexposure on the oscillograph. This was repaired for subsequent runs by adding additional automatic leader to the oscillograph before the first pulse. As required by the work statement, the REA start temperatures were obtained by allowing the REA to cool naturally for 1 hour followed by force cooling for no more than 30 minutes. Forced cooling was accomplished by the blowing of nitrogen down the sides of the thrust chamber. This nitrogen increased the vacuum chamber ambient pressure from the normal 10 microns to 400 microns and thus allowed conduction from the REA to the 40°F thermal shroud and the -300°F cold target. The nitrogen gas was premixed with 1% hydrogen to eliminate any posibility of oxygen diffusing to the warm catalyst and damaging it by the formation of irridium dioxide.

The long ignition delays and associated pressure spikes observed on the first six cold starts were obviously detrimental to engine operation. Therefore, an investigation was conducted into the possible causes by changing the cooldown procedure. On Sequence 2-28 the REA was allowed to cool naturally for 2 hours before force cooling was applied. The natural cool time was extended to 3 hours for sequences 2-29 and 2-30. On sequences 2-31, 2-32, 2-34, 2-35 and 2-36 the REA was allowed to cool naturally to 200°F (approximately 2 hours) and the purge gas changed to gaseous nitrogen only. Sequence 2-33 corresponded to a weekend hold with no force cooling at all.

Table XVI. TDVT Run 4

Sequence No.	T_{v1}	T_{v2}	T_{ft1}	T_{ft2}	T_{ft3}	T_{h1}	T_{h2}	T_{h3}	T_{w1}	T_{w2}	T_{w3}	T_{nc}
1-1	175	251	394	615	950	1,018	1,108	1,037	1,065	1,033	859	806
1-2	170	265	379	484	1,009	1,118	1,218	1,126	1,166	1,130	960	904
1-3	165	269	388	425	1,021	1,167	1,283	1,177	1,227	1,195	1,037	980
1-4	172	282	409	467	1,022	1,173	1,299	1,195	1,248	1,231	1,080	1,022
1-5	189	288	446	613	1,016	1,115	1,229	1,130	1,172	1,148	982	923
1-6	192	287	455	634	988	1,084	1,193	1,100	1,140	1,116	948	891
1-7	198	283	435	641	957	1,045	1,146	1,061	1,100	1,076	909	853
1-8	149	285	294	238	254	378	886	1,105	1,271	1,396	1,299	1,266

Table XVII. Cold Start Test Duty Cycle

Seq. No.	Pulse Width-Sec	Off Time-Sec	No. of Pulses	Feed Pressure	Propellant Temp.	Shroud Temp.	Target Temp.
2-1	0.020	0.980	100	100	65	65	65
2-2	0.020	0.480	100	100	65	65	65
2-3	0.050	0.950	100	100	65	65	65
2-4	0.050	0.450	100	100	65	65	65
2-5	0.100	0.900	100	100	65	65	65
2-6	0.150	0.850	100	100	65	65	65
2-7	10.000	—	1	100	65	65	65
2-8	0.020	0.980	100	225	65	65	65
2-9	0.020	0.480	100	225	65	65	65
2-10	0.050	0.950	100	225	65	65	65
2-11	0.050	0.450	100	225	65	65	65
2-12	0.100	0.900	100	225	65	65	65
2-13	0.150	0.850	100	225	65	65	65
2-14	10.000	—	1	225	65	65	65
2-15	0.020	0.980	100	350	65	65	65
2-16	0.020	0.480	100	350	65	65	65
2-17	0.050	0.950	100	350	65	65	65
2-18	0.050	0.450	100	350	65	65	65
2-19	0.100	0.900	100	350	65	65	65
2-20	0.150	0.850	100	350	65	65	65
2-21	10.000	—	1	350	65	65	65
2-22	10.000	—	1	350	40	40	-320
2-23 through 2-63	Repeat Seq. No. 2-22						

Table XVII. Cold Start Test Duty Cycle (Concluded)

Seq. No.	Pulse Width-Sec	Off Time-Sec	No. of Pulses	Feed Pressure	Propellant Temp.	Shroud Temp.	Target Temp.
2-64	0.020	0.980	100	350	65	65	65
2-65	0.020	0.480	100	350	65	65	65
2-66	0.050	0.950	100	350	65	65	65
2-67	0.050	0.450	100	350	65	65	65
2-68	0.100	0.900	100	350	65	65	65
2-69	0.150	0.850	100	350	65	65	65
2-70	10.000	—	1	350	65	65	65
2-71	0.020	0.980	100	225	65	65	65
2-72	0.020	0.480	100	225	65	65	65
2-73	0.050	0.950	100	225	65	65	65
2-74	0.050	0.450	100	225	65	65	65
2-75	0.100	0.900	100	225	65	65	65
2-76	0.150	0.850	100	225	65	65	65
2-77	10.000	—	1	225	65	65	65
2-78	0.020	0.980	100	100	65	65	65
2-79	0.020	0.480	100	100	65	65	65
2-80	0.050	0.950	100	100	65	65	65
2-81	0.050	0.450	100	100	65	65	65
2-82	0.100	0.900	100	100	65	65	65
2-83	0.150	0.850	100	100	65	65	65
2-84	10.000	—	1	100	65	65	65

NOTE: At the completion of each sequence the REA will be allowed to cool for 1 hr. and then will be force cooled to the shroud temp in 30 min.

Table XVIII. Cold Start Test Baseline Pulse Mode Data

Seq. No.	Feed Pressure ~psia	Duty Cycle	First Pulse		Equilibrium Pulse				Peak P_c ~psia
			τ_{ign} ~msec	Peak Pc ~psia	$\tau_{1\%}$ ~msec	I_{bit} ~lbf-sec	Centroid ~ sec.	I_{sp} ~lbf-sec/lbm	
2-1	100	0.02/.98	32	4.7	9	0.0336	0.034	119.4	27.0
2-2	100	0.02/.48	110	2.4	9	0.0381	0.041	138.9	25.0
2-3	100	0.05/.95	74	16.8	9	0.1002	0.047	197.6	35.0
2-4	100	0.05/.45	61	26.4	9	0.1097	0.053	202.3	36.0
2-5	100	0.10/.90	NA	48.9	9	0.2203	0.074	219.6	38.0
2-6	100	0.15/.85	103	80.4	9	0.3342	0.098	219.1	39.0
2-8	100	0.02/.98	95	10.8	9	0.0321	0.036	150.5	24.0
2-9	225	0.02/.48	82	60	9	0.0547	0.038	163.1	51.0
2-10	225	0.05/.95	NA	NA	9	0.1697	0.046	201.1	69.0
2-11	225	0.05/.45	68	23.7	9	0.1724	0.051	216.6	70.0
2-12	225	0.10/.90	86	71.1	9	0.3515	0.072	225.2	63.0
2-13	225	0.15/.85	70	120.9	10	0.5446	0.099	222.9	66.0
2-15	350	0.02/.98	92	12.9	9	0.0638	0.035	179.7	53.0
2-16	350	0.02/.48	93	7.2	8	0.0625	0.038	182.2	51.0
2-17	350	0.05/.95	63	34.2	10	0.2113	0.047	221.3	75.0
2-18	350	0.05/.45	NA	NA	NA	NA	NA	NA	NA
2-19	350	0.10/.90	73	147.0	10	0.4559	0.073	228.2	81.0
2-20	350	0.15/.85	82	160.5	10	0.6930	0.099	225.4	83.0

Table XIX. Cold-Start Test

Sequence No.	Sign ~ msec	P_c, Spike ~ psia	P_c, Equilibrium ~ psia	Roughness ~ ±psid
2-22	NA	NA	83.0	2.0
2-23	NA	NA	84.0	1.5
2-24	83	195.6	83.4	1.5
2-25	86	231	82.5	2.0
2-26	72	225	83.1	2.0
2-27	68	214.8	83.4	1.5
2-28	87	274.5	83.4	2.0
2-29	88	267.6	82.5	2.7
2-30	125	300+	81.6	2.7
2-31	83	186.3	83.4	1.5
2-32	88	182.4	83.4	2.7
2-33	98	300+	81.6	2.0
2-34	70	159	82.5	2.7
2-35	62	180	82.5	2.7
2-36	60	203	81.9	3.0
2-37	80	255	83.4	2.0
2-38	55	228	83.1	2.7
2-39	100	300+	83.1	3.0
2-40	70	177	83.7	3.0
2-41	70	182	83.7	3.8
2-42	80	242	83.4	3.8
2-43	90	249	82.8	3.8
2-44	88	258	82.5	3.0
2-45	55	229.5	83.4	4.0
2-46	60	193.5	83.7	4.5
2-47	56	198	83.7	6.0
2-48	65	207	84.0	6.0
2-49	56	214.5	83.4	6.0
2-50	62	222	83.4	5.3
2-51	50	241.5	84.0	6.0
2-52	NA	247.5	82.5	7.8
2-53	68	240	82.5	7.0
2-54	70	231	81.9	7.8
2-55	90	286	82.5	6.0
2-56	65	259.5	82.5	7.5
2-57	77	265	83.4	6.5
2-58	90	300+	83.7	7.0
2-59	78	264	82.8	7.0
2-60	73	214	81.6	7.5
2-61	75	181.5	84.0	8.25
2-62	77	225	83.4	7.0
2-63	72	222	83.4	8.25

Sequences 2-37, 2-38 and 2-39 duplicated this natural cooldown with the shroud temperature decreased to 20°F to aid in cooling. All of these variations had no appreciable effect on the ignition delay, so the test was completed with the original 1.5-hour cool down of the test plan. It is postulated that a void formed in the upper bed as a result of the first six "hard" starts, and such a void would consistently cause subsequent hard starts independent of catalyst conditioning.

As shown on Table XIX, the engine chamber pressure roughness increased throughout the test series. This is graphically presented in Figure 33, which also shows sequence 2-47 (pulse number 1829) to be the first data point beyond the work statement goals on roughness.

Pulse-mode data from the last baseline test series is summarized in Table XX. Table XXI presents all baseline steady-state performance data. All steady-state runs were of 10 second duration; consequently the performance as tabulated does not reflect complete thermal equilibrium conditions. Pre- and post-cold-start baseline pulse-mode data is compared in Table XXII.

As noted thereon, there are only two instances of impulse-bit reproducibility outside the work statement goal although almost all centroid repeatability is outside the limits.

In-house Cold Start Test Results – As part of in-house testing, a REM-Mono thrust chamber assembly was subjected to a series of extended steady-state firings at low temperature conditions. Table XXIII summarizes pertinent start transient data from the test series. The fact that this engine could be started at 40°F bed temperature with 40°F propellant (tests 4 and 5) with relatively short ignition delays and small spikes was in conflict with the test data obtained in long-life cold start test series. A comparison of facility equipment and techniques used on the in-house tests which differed from the long-life tests isolated two significant items. First, the in-house test did not use a cold target to simulate deep space. Secondly, no attempt was made to force-cool the in-house tests; the REA was allowed to cool naturally at vacuum conditions (approximately 10 microns). It was therefore determined at a technical program review meeting with AFPCO that the life test duty cycle be revised so as to delete the cold target and force-cooling and repeat 25 of the cold starts.

Two potential explanations of why these test facility differences and/or longer periods between tests could be causing the shift in ignition delay are discussed in the following paragraphs.

a. *Gas Poisoning* – Rocket Research Corporation has documented many cases of ammonia (and/or hydrogen) poisoning a catalyst bed. It has been postulated that the ammonia occupies active catalytic sites and thereby significantly reduces the catalyst activity. The normal ammonia produced by a firing is driven off in vacuum by the elevated temperature of the catalyst (i.e., degree of poisoning depends upon time temperature cooldown history). If this ammonia remains in the catalyst bed at low temperatures, it is extremely difficult to remove. The immediate presence of a cold target (-300°F) in the vacuum tank will freeze some of the ammonia in the exhaust gas products. This ammonia will sublime during the cool-down period, allowing ammonia molecules to enter a cool bed.

b. *Quenching* – The procedure used for force cooling the REA could cause condensation of entrapped gases within the catalyst particles. Additionally, the 1% H_2 added to the purge N_2 could enter the cool catalyst bed and be adsorbed on active sites.

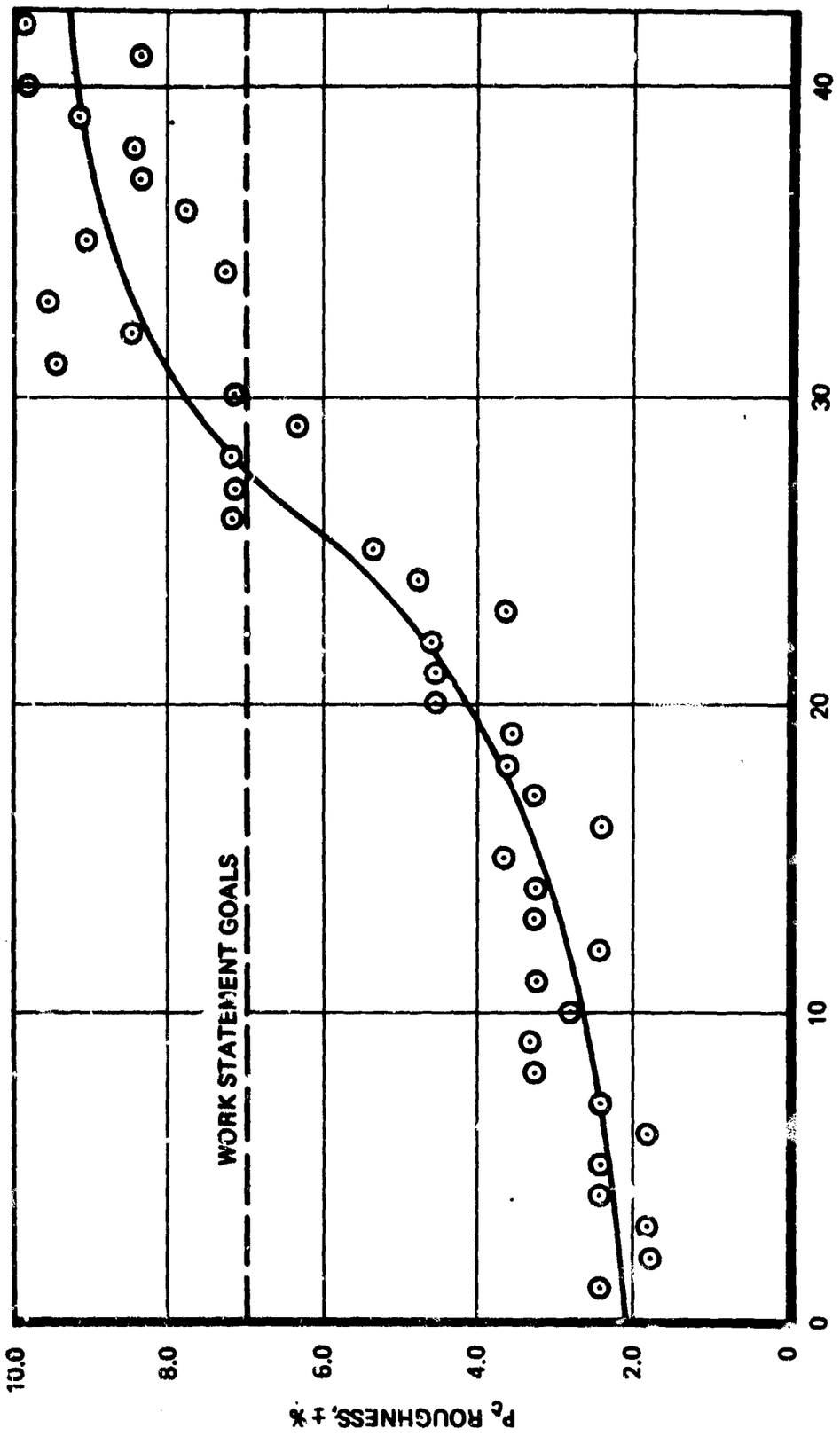

Figure 33. 10^6 Cycle Program Cold Start Test

Table XX. Cold Start Test Baseline Pulse Mode Data

Sequence Number	Feed Pressure ~ psia	Duty Cycle	First Pulse		Equilibrium Pulse				Peak Pc ~ psia
			$I_{1\%}$ ~ msec	Peak Pc ~ psia	$I_{1\%}$ ~ msec	I_{bit} ~ lbf-sec	Centroid ~ sec	I_{sp} ~ lbf-sec/lbm	
2-64	350	0.02/.98	19	13.5	NA	NA	NA	NA	62.0
2-65	350	0.02/.48	105	7.2	10	0.0589	0.050	153.7	63.0
2-66	350	0.05/.95	66	57.9	10	0.2174	0.053	203.8	90.0
2-67	350	0.05/.45	60	53.7	10	0.2161	.062	204.7	90.0
2-68	350	0.10/.90	55	99.9	10	0.4457	0.080	NA	81.0
2-69	350	0.15/.85	58	103.2	10	0.6809	0.104	222.2	84.0
2-71	225	0.02/.98	60	8.1	10	0.0449	0.054	156.3	25.0
2-72	225	0.02/.48	69	5.7	16	0.0444	0.056	151.9	25.0
2-73	225	0.05/.95	47	43.5	10	0.1648	0.060	188.3	63.0
2-74	225	0.05/.45	60	33.6	10	0.1597	0.087	203.4	63.0
2-75	225	0.10/.90	50	78.6	10	0.3461	0.087	218.5	63.0
2-76	225	0.15/.85	61	63.6	10	0.5316	0.112	221.0	66.0
2-78	100	0.02/.98	77	7.8	10	0.0400	0.098	129.4	9.0
2-79	100	0.02/.48	63	5.1	10	0.395	0.139	116.9	10.0
2-80	100	0.05/.95	56	27.3	10	0.1049	0.126	196.5	27.0
2-81	100	0.05/.45	55	31.5	10	0.1013	0.123	189.7	30.0
2-82	100	0.10/.90	57	33.9	9	0.2190	0.114	223.8	31.0
2-83	100	0.15/.85	50	39.3	9	0.3132	0.128	220.5	33.0

Table XXI. Cold-Start Test Baseline Steady-State Data S/N 4 REA

Sequence No.	Pfeed ~ psia	τ1% ~ msec	τ90% ~ msec	τ10% ~ msec	P_c ~ psia	F ~ lbf	I_{sp} ~ sec	Roughness ~ ±psid
2-7	102	71	1,432	43	41.0	2.118	201.1	1.0
2-14	225	71	1,180	NA	66.2	3.500	214.2	1.0
2-21	350	78	1,280	39	82.7	4.411	215.1	2.0
2-70	351	50	1,580	50	84.0	4.505	219.2	12.0
2-77	225	50	2,170	50	67.8	3.605	218.9	10.5
2-84	101	40	2,970	62	35.1	1.802	205.0	10.5

The effect of force-cooling increased the vacuum tank pressure from the nominal 10 microns to 400 microns. At this pressure conductive heat losses to the target become significant and cause rapid cooling. If the walls of the thrust chamber cool much more rapidly than the catalyst particles, differential thermal contraction could cause catalyst breakup.

Catalyst Evaluation Test Results – During buildup of REA S/N 4 for the cold-start test series, a sample REA was also built up and subjected to the same handling and test procedures with the exception of firing. Both REA's were disassembled following the test series and catalyst evaluation tests conducted. Prior to disassembly X-rays were taken of the catalyst bed on the fired REA (S/N 4). An X-ray is presented in Figure 34 which shows a relatively large void in the upper (25- to 30-mesh) catalyst bed. This void was substantiated on teardown as 11.9% weight loss in the upper bed. The lower bed of 14 to 18 mesh had an indicated 2.5% weight loss as a result of the cold start test series.

Catalyst from both the fired and unfired REA's was sieved and weighed to determine size distribution and subjected to a crush strength test. Results of these tests are shown in Table XXIV together with the crush strength requirements of RRC-MS-0110 Acceptance Test Procedure. It is apparent from this data that the upper catalyst bed was damaged by the start spikes associated with cold starts. The crush strength requirements are established for a 6-gram sample of catalyst. Since only 5 grams of fired 25- to 30-mesh catalyst were remaining, both fine-mesh crush tests were conducted on 5-gram samples. Comparision of the fired and unfired crush strength data for both the 14- to 18- and 25- to 30-mesh catalysts indicates a trend toward weakening as a result of firing.

All samples were further subjected to hydrogen chemisorption tests to determine the active metal surface area. This measurement has been determined to be an excellent indication of catalyst activity. Test results are tabulated on Table XXV together with data from virgin (as received) and fresh-shrunk catalyst samples. The prefiring thermal treatment procedure stabilizes the active metal surface area of the virgin catalyst and subsequent reduction as a result of firing is minimal.

Table XXII. Cold-Start Test Baseline Pulse Mode Comparison

Duty Cycle	Pfeed ~ psia	Mean I_{bit} ~ lbf-sec	Spread ±lbf-sec	Spread ±%	Work Statement Goal ±%	Mean Cent. ~ sec	Spread ±sec	Spread ±%	Work Statement Goal
0.02/0.98	100	0.0368	0.0032	8.7	10.0	0.066	0.032*	48.5	5.0 ms
0.02/0.48	100	0.0388	0.0007	1.8		0.090	0.049*	54.4	
0.05/0.95	100	0.1026	0.0024	2.3	7.0	0.087	0.040	46.0*	5.0%
0.05/0.45	100	0.1055	0.0042	4.0		0.088	0.035	39.8*	
0.10/0.90	100	0.2197	0.0007	0.3		0.094	0.020	21.3*	
0.15/0.85	100	0.3237	0.0105	3.2		0.113	0.015	13.3*	
0.02/0.98	225	0.0385	0.0064	16.6*	10.0	0.045	0.009*	20.0	5.0 ms
0.02/0.48	225	0.0496	0.0052	10.5*		0.047	0.009*	19.1	
0.05/0.95	225	0.1673	0.0025	1.5	7.0	0.053	0.007	13.2*	5.0%
0.05/0.45	225	0.1661	0.0064	3.9		0.069	0.018	26.1*	
0.10/0.90	225	0.3488	0.0027	0.8		0.080	0.008	10.0*	
0.15/0.85	225	0.5381	0.0065	1.2		0.106	0.007	6.6*	
0.02/0.98	350	NA	NA	NA	10.0	NA	NA	NA	5.0 ms
0.02/0.48	350	0.0607	0.0018	3.0		0.044	0.006*	13.6	
0.05/0.95	350	0.2144	0.0031	1.4	7.0	0.050	0.003	6.0*	5.0%
0.05/0.45	350	NA	NA	NA		NA	NA	NA	
0.10/0.90	350	0.4508	0.0051	1.1		0.077	0.004	3.9	
0.15/0.85	350	0.6870	0.0061	0.9		0.102	0.003	2.9	

*Outside of specification limits

Table XXIII. Summary of Steady-State Test Ignition Data REA S/N RAE-001

Test No.	Initial Propellant Temperature, °F	Initial Catalyst Bed Temperature, °F	Ignition Delay Time, ms*	Maximum Pressure on Start, psia	Steady-State Chamber Pressure, psia
151811-001	50	65	20	110	110
151811-002	40	60	20	105	105
151811-003	40	49	40	117	71
151811-004	38	41	20	31	35
151811-005	36	40	40	200	105

*Time from valve open to chamber pressure start rise

Samples of the fired and unfired catalysts together with dry-shrunk catalyst were analyzed for total surface area and pore size distribution by the BET apparatus, and active metal content by iridium spectrochemical analysis. Results of measuring the active metal content by iridium spectrochemical analysis are presented in Table XXVI. Although the measured values of the fired catalyst are significantly less than "as manufactured" specification values (≥30.0%), the unfired catalyst sample shows the same result. Personnel at Shell Development Company (SDC) were contacted regarding the validity of these measurements. These discussions revealed that SDC has had similar results with the method on catalyst known to contain 30% iridium. As a result of these problems, SDC has developed a gravinometric analysis technique which is in excellent agreement with manufacturing data. On the basis of compared results, SDC claims that a spectrochemical analysis can be no better than ±10% whereas the gravinometric method is accurate to ±0.1%. Shell Development Company did propose to conduct a gravinometric analysis on this catalyst; however, in view of expense and schedule RRC deleted this test with AFPCO concurrence.

Also presented on Table XXVI are the total BET surface area and median pore radium determined by nitrogen adsorption analysis. Tables XXVII and XXVIII compare the BET determined pore size distributions for each of the catalysts studied. On the basis of the data presented in these three tables, no obvious catalyst pore size changes occurred as a result of the forty-two 65°F starts and forty-two 40°F starts which this fired catalyst was exposed.

2.3.5 Abbreviated Life Test

In view of the cold-start test results discussed above, the abbreviated life-test duty cycle of the work statement was modified, with AFPCO concurrence, to demonstrate REA performance over a series of 25 cold starts without the aid of artificial cooling techniques. The cryogenic target and REA force-cooling assembly were removed from the test setup shown in Figure 27. The abbreviated life-test duty cycle is presented in Table XXIX.

REA S/N 5 – The duty cycle of Table XXIX was initiated on REA S/N 5. Pulse-mode data from the baseline test is summarized in Table XXX. Table XXIX modified the baseline duty cycle so that

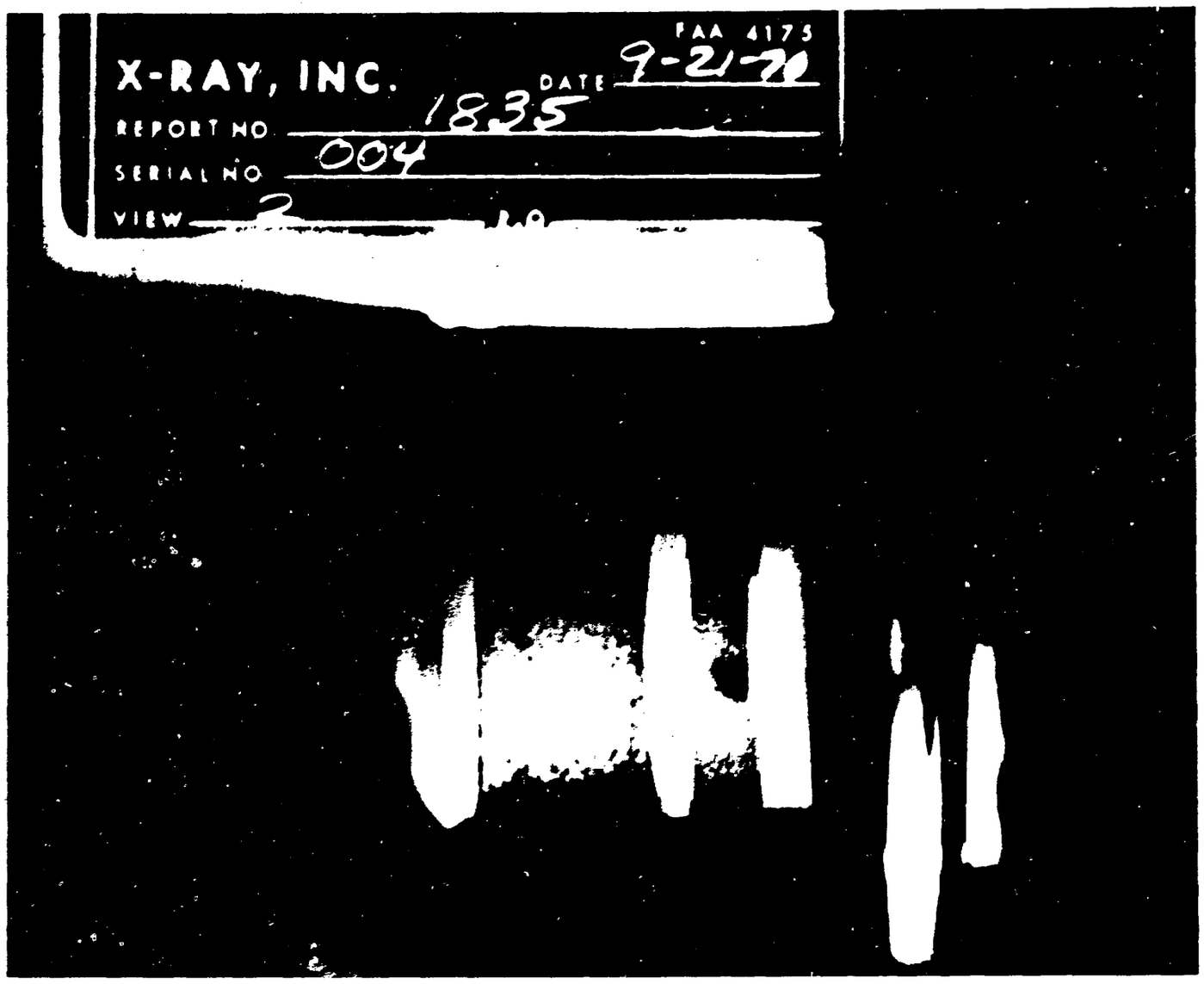

Figure 34. X-Ray of REA S/N 4 Following Cold-Start Test Series

Table XXIV. Catalyst Evaluation Test Results

	Size Distribution (1) 25 - 30 Mesh % by Weight			
	30 Mesh	40 Mesh	50 Mesh	Fines
Fired sample	79.48	10.01	3.04	7.47
Unfired sample	97.80	1.84	0.15	0.21

	Size Distribution (1) 14 - 18 Mesh % by Weight			
	18 Mesh	25 Mesh	50 Mesh	Fines
Fired sample	93.85	3.06	3.00	1.09
Unfired sample	96.63	2.23	0.91	0.23

	Crush Strength Test Results 25-30 Mesh		
	Dimensionless Deflection at 1000 psi	Dimensionless Recovery at 20 psi	Weight % <30 Mesh After Test
Fired sample	0.105	0.0209	70.0
Unfired sample	0.0725	0.0155	82.5
MS-0110 ATP	<0.100	>0.015	>75

	14 - 18 Mesh		
	Dimensionless Deflection at 1000 psi	Dimensionless Recovery at 20 psi	Weight % <18 Mesh After Test
Fired sample	0.120	0.0171	54.7
Unfired sample	0.113	0.0205	59.5
MS-0110 ATP	<0.180	>0.015	>55

(1) Percent retained on indicated mesh size screen

Table XXV. Hydrogen Chemisorption Test Results

25–30 Mesh	
50% attrited as received (average)	390 μ moles/gram
50% attrited after shrinkage (average based on O_2 chemisorption)	147 μ moles/gram
90% attrited as received	356 μ moles/gram
90% attrited after shrinkage	154 μ moles/gram
90% attrited from cold-start REA	163 μ moles/gram
90% attrited from sample REA	155 μ moles/gram
50% attrited from REM-Mono qual S/N 1001 SY REA	122.6 μ moles/gram
14–18 Mesh	
As received (average)	400 μ moles/gram
After shrinkage (average based on O_2 chemisorption)	135 μ moles/gram
Cold-start REA	139 μ moles/gram
Sample REA	144 μ moles/gram

Table XXVI. Catalyst Evaluation Test Results

	Active Metal Analysis (% Iridium)	
	25–30 Mesh	14–18 Mesh
Fired sample	25.6	26.1
Unfired sample	26.5	27.1

	Nitrogen Adsorption Analysis			
	25–30 Mesh		14–18 Mesh	
	BET Area m^2/g	Medium Pore Radius A°	BET Area m^2/g	Medium Pore Radium A°
As received after shrinking	47.9	56.4	38.8	75.6
Unfired sample	49.2	57.6	42.3	70.1
Fired sample	48.8	58.9	48.1	67.8

Table XXVII. Pore Size Distribution 25-30 Mesh Catalyst

Pore Radius A°	Volume – Percent			Area – Percent		
	As Received and Shrunk	Unfired Sample	Fired Sample	As Received and Shrunk	Unfired Sample	Fired Sample
300 - 250	2.8	2.8	2.8	0.5	0.5	0.5
250 - 200	4.5	4.9	5.1	1.0	1.1	1.1
200 - 150	6.0	6.5	6.6	1.7	1.9	1.9
150 - 100	9.2	9.9	10.0	3.8	4.0	4.1
100 - 90	3.2	3.4	3.6	1.7	1.8	1.9
90 - 80	4.8	4.9	5.4	2.8	2.8	3.2
80 - 70	7.0	6.7	6.4	4.5	4.3	4.3
70 - 60	9.2	8.6	9.1	7.0	6.6	7.0
60 - 50	10.2	10.2	9.9	9.1	9.1	9.0
50 - 45	6.5	5.8	6.0	6.7	5.9	6.3
45 - 40	6.9	6.4	6.4	8.0	7.4	7.5
40 - 35	6.8	6.5	6.4	8.9	8.5	8.5
35 - 30	6.3	6.2	6.2	9.4	9.3	9.4
30 - 25	6.8	6.9	6.3	12.1	12.2	11.4
25 - 20	5.9	5.7	5.8	12.8	12.4	12.8
20 - 15	3.8	4.5	4.0	10.0	12.2	11.1
15 - 10	0.0	0.0	0.0	0.0	0.0	0.0
10 - 7	0.0	0.0	0.0	0.0	0.0	0.0

Table XXVIII. Pore Size Distribution 14 - 18 Mesh Catalyst

Pore Radius A°	Volume – Percent			Area – Percent		
	As Received and Shrunk	Unfired Sample	Fired Sample	As Received and Shrunk	Unfired Sample	Fired Sample
300 - 250	3.2	3.4	3.3	0.7	0.7	0.6
250 - 200	5.8	5.0	4.5	1.6	1.3	1.1
200 - 150	7.7	7.3	6.7	1.8	2.5	2.1
150 - 100	16.1	14.0	14.2	8.3	6.8	6.3
100 - 90	5.7	4.8	4.6	3.7	2.9	2.5
90 - 80	7.7	7.2	6.8	5.6	4.9	4.3
80 - 70	8.4	8.4	8.3	6.9	6.4	5.9
70 - 60	9.3	9.7	9.3	8.9	8.7	7.6
60 - 50	9.3	9.5	8.8	10.5	10.0	8.5
50 - 45	4.8	5.2	4.9	7.0	7.0	6.0
45 - 40	4.8	5.2	4.9	7.0	7.0	6.0
40 - 35	4.7	5.0	5.0	7.7	7.7	7.1
35 - 30	4.1	4.5	4.6	7.9	8.0	7.5
30 - 25	3.8	4.7	4.6	8.5	9.8	8.8
25 - 20	3.5	4.0	4.0	9.6	10.3	9.4
20 - 15	1.2	2.1	4.1	3.9	6.4	12.6
15 - 10	0.0	0.0	1.1	0.0	0.0	3.8
10 - 7	0.0	0.0	0.0	0.0	0.0	0.0

Table XXIX. Life Test Duty Cycle

Sequence No.	Pulse Width sec	Off Time sec	Number of Pulses	Feed Pressure psia	Cumulative Pulses	Shroud Temp °F	Initial REA Temp °F
3-1	0.020	0.980	100	100	100	65	65
3-2		0.480	100	100	200	65	–
3-3	0.050	0.950	100	100	300	65	–
3-4	0.050	0.450	100	100	400	65	–
3-5	0.100	0.900	100	100	500	65	–
3-6	0.150	0.850	100	100	600	65	–
3-7	10.000	–*	1	100	601	65	–
3-8	0.020	0.980	100	225	701	65	65
3-9	0.020	0.480	100	225	801	65	–
3-10	0.500	0.950	100	225	901	65	–
3-11	0.050	0.450	100	225	1,001	65	–
3-12	0.100	0.900	100	225	1,101	65	–
3-13	0.150	0.850	100	225	1,201	65	–
3-14	10.000	–*	1	225	1,202	65	–
3-15	0.020	0.980	100	350	1,302	65	65
3-16	0.020	0.480	100	350	1,402	65	–
3-17	0.050	0.950	100	350	1,502	65	–
3-18	0.050	0.450	100	350	1,602	65	–
3-19	0.100	0.900	100	350	1,702	65	–
3-20	0.150	0.850	100	350	1,802	65	–
3-21	10.000	–*	1	350	1,803	65	–
3-22	10.000	–*	1	350	1,804	40	40
3-23 thru 3-46	Repeat sequence 3-22		24	350	1,828	40	40
3-47 thru 3-67	Repeat sequences 3-1 through 3-21		1,803	–	3,631	–	–

*Off time is that required to reach next sequence initial REA temperature without force cooling.

Table XXX. Abbreviated Life Test Baseline Pulse Mode Data REA S/N 5

			First Pulse		Equilibrium Pulse			
Sequence Number	Feed Pressure ~ psia	Duty Cycle	* $\tau_{1\%}$ ~ msec	Peak Pc ~ psia	$\tau_{1\%}$ ~ msec	I_{bit} ~ lbf-sec	Centroid ~ sec	I_{sp} ~ lbf-sec/lbm
3 - 1	100	0.02/.98	31	9.3	11	0.0395	0.050	NA
3 - 2	100	0.02/.48			11	0.0516	0.053	NA
3 - 3	100	0.05/.95			11	0.1150	0.056	202.1
3 - 4	100	0.05/.45			10	0.1241	0.056	218.1
3 - 5	100	0.10/.90			10	0.2382	0.078	215.8
3 - 6	100	0.15/.85			10	0.3532	0.106	217.8
3 - 8	225	0.02/.98	29	11.4	10	.0571	0.042	136.9
3 - 9	225	0.02/.48			10	0.0657	0.040	163.4
3-10	225	0.05/.95			9	0.1771	0.051	216.4
3-11	225	0.05/.45			9	0.1745	0.054	214.9
3-12	225	0.10/.90			9	0.3526	0.076	215.5
3-13	225	0.15/.85			9	0.5230	0.102	199.8
3-15	350	0.02/.98	44	11.7	**NA	NA	NA	NA
3-16	350	0.02/.48			8	0.0868	0.036	205.7
3-17	350	0.05/.95			8	0.2217	0.048	216.1
3-18	350	0.05/.45			8	0.2120	0.052	210.3
3-19	350	0.10/.90			8	0.4571	0.075	218.7
3-20	350	0.15/.85			8	0.6725	0.101	200.3

* All times measured from valve signal
1T of chamber pressure defined as ignition delay

** NA – data not available – lost in recording

only the first duty cycle at each feed pressure is started at 65°F REA. Propellant temperature is conditioned at 65°F throughout the complete test. Consequently, first pulse data is only presented for these 65°F sequences. Steady-state baseline data is presented in Table XXXI and shows chamber pressure roughness above the work statement goals at the high feed pressure. At this point it was decided to terminate the test and determine the cause of excessive roughness. Before removal of the REA, however, a series of cold starts was conducted to verify the effect of facility and technique changes that had been incorporated as a result of the cold-start test series conducted on REA S/N 4. Data from these five cold starts (40°F REA with 40°F propellant) is tabulated in Table XXXII. As shown on this table, the ignition delay and spike chamber pressure are significantly less than observed on REA S/N 4 (Table XIX).

Table XXXI. Abbreviated Life Test Baseline Steady-State Data REA S/N 5

Sequence No.	P_{feed} ~ psia	τ1% ~ msec	τ90% ~ msec	τ10% ~ msec	P_c ~ psia	F ~ lbf	I_{sp} ~ sec	Roughness	
								~ ±psid	~ ±%
3-7	97	10	46	49	42.5	2.23	197.1	2.0	4.7
3-14	217	9	31	40	68.1	3.65	226.2	4.5	6.6
3-21	341	9	82	42	84.6	4.57	225.9	6.0	7.1

Table XXXII. Abbreviated Life Test REA S/N 5

Sequence No.	τ_{ign} ~ msec	P_c, Spike ~ psia	P_c, Equilibrium ~ psia	Roughness ~ ±psid
3–22	20	93	83.0	9.0
3–23	40	148	84.0	7.5
3–24	30	86	84.0	8.0
3–25	40	130	83.0	8.0
3–26	40	129	83.0	10.0

Post-test X-rays of REA S/N 5 were almost idential with those of REA S/N 4 presented in Figure 34, the exception being that the void area appeared slightly smaller on REA S/N 5. REA disassembly, however, did reveal that the intermediate bed plate had been deflected in the center approximately 0.020 inch. Since this bed plate had been used on two previous REA's (S/N 3 TDVT and S/N 4 cold-start tests) and had not been checked for flatness prior to assembly into REA S/N 5, it was considered to be the cause of the void in the upper catalyst bed. Upper catalyst bed packing is accomplished by use of a flat packing tool, and final overpack measurements are verified by use of the intermediate bed plate. Therefore, no provision exists to accommodate a deflected bed plate.

The injector subassembly (P/N 26235-302-11, S/N 2) was cleaned and flow calibrated. This calibration showed no significant change from the flow calibration prior to REA S/N 5 assembly.

REA S/N 6 – REA S/N 6 was assembled by use of injector subassembly S/N 2 from REA S/N 5 and a new intermediate bed plate. The REA was subjected to the abbreviated life test of Table XXIX. Pulse-mode data from the first baseline test is summarized in Table XXXIII. Following this initial baseline test, 26 successive cold starts were fired on the REA. Each 10-second steady-state burn was started with both the REA and propellant at 40°F. As discussed above, all cooling was natural and the -300°F cold targets were eliminated from the installation. Pertinent data from each of these cold starts is presented in Table XXXIV. Figure 35 graphically presents ignition delay as a function of cool down time and shows a distinct trend toward shorter ignition delays with increasing cool-down times. Also shown on this figure is in-house data from a Transtage 27-lbf REA which was tested under identical conditions; the correlation as shown on Figure 35 is excellent. This phenomenon is consistent with an adsorbed gas model as described in paragraph 2.3.4 (item a. under *In-house Cold Start Test Results*), since the longer time available for outgassing yields shorter ignition delays. Figure 36 is a plot of ignition delay and spike peak chamber pressure showing a very strong correlation.

Following the 26 cold starts the baseline duty cycle was repeated with pulse-mode data as summarized in Table XXXV. Table XXXVI compares steady-state data from both baseline tests, and Table XXXVII compares the pulse-mode data to the work statement goals. As shown on Table XXXVII, there are three instances of "out of work statement goals" centroid repeatibility as compared to only three instances within goals on REA S/N 4 (see Table XXII). This improvement in operation, coupled with the improved roughness characteristics shown in Figure 37, indicates that the facility and technique modification incorporated into the cold-start tests of REA S/N 6 did eliminate the majority of the overstress test conditions.

REA S/N 6 – Extended Life Test – Following the abbreviated life test on REA S/N 6, an extended life test was conducted in accordance with the duty cycle presented in Table XXXVIII. The catalyst bed degradation caused by the previous 26 cold starts, as evidenced by the steady-state roughness of baseline number 2, led to rapid deterioration as a result of pulsing. Figure 38 compares the low feed pressure pulse shapes for the four baseline pulse widths. As shown on this figure, considerable pulse shape distortion was evident by baseline number 4 (106,000 pulses), and the test was subsequently terminated at 258,000 pulses. Figures 39 through 41 present baseline pulse mode impulse bit as a function of baseline number for all six pulse duty cycles for the three feed pressure conditions respectively. As shown on these figures, the delivered impulse bit is very repeatable in spite of the distortion shown on Figure 38. Impulse bit and centroid repeatability for all five baseline tests are summarized in Table XXXIX. Although only seven of the eighteen duty cycles meet the work statement impulse bit repeatability goals, all but two of the duty cycles have spreads less than 15%. The centroid data presented on Table XXXIX shows the effect of pulse shape distortion with no duty cycle within the work statement goals. This is graphically shown in Figures 42 through 44 which present centroid as a function of baseline number and feed pressure.

Steady-state roughness as a function of pulse number is plotted on Figure 45. Steady-state thrust is presented on Figure 46. Although the roughness does significantly increase as the test progressed at mid and high feed pressure, mean steady-state thrust was very stable with a maximum spread of 3.5% at the low feed pressure conditions.

Table XXXIII. Abbreviated Life REA S/N 6 Baseline Pulse Mode Data

			First Pulse		Equilibrium Pulse			
Sequence Number	Feed Pressure ~ psia	Duty Cycle	* $\tau_{1\%}$ ~ msec	Peak Pc ~ psia	$\tau_{1\%}$ ~ msec	I_{bit} ~ lbf-sec	Centroid ~ sec	I_{sp} ~ lbf-sec/lbm
3 - 1	100	0.02/.98	29	13.5	10	0.0430	0.041	140.0
3 - 2	100	0.02/.48			9	0.0482	0.040	171.6
3 - 3	100	0.05/.95			9	0.1178	0.053	215.4
3 - 4	100	0.05/.45			9	0.1280	0.051	241.0
3 - 5	100	0.10/.90			9	0.2443	0.075	234.5
3 - 6	100	0.15/.85			9	0.3646	0.100	230.3
3 - 8	225	0.02/.98	29	9.9	9	0.0658	0.035	150.2
3 - 9	225	0.02/.48			9	0.0798	0.035	175.7
3-10	225	0.05/.95			9	0.1882	0.047	205.0
3-11	225	0.05/.45			9	0.1959	0.050	214.9
3-12	225	0.10/.90			NA	NA	NA	NA
3-13	225	0.15/.85			9	0.6554	0.098	221.7
3-15	350	0.02/.98	112	5.7	9	0.0894	0.033	189.4
3-16	350	0.02/.48			9	0.1102	0.034	218.6
3-17	350	0.05/.95			9	0.2748	0.048	226.4
3-18	350	0.05/.45			9	0.2524	0.047	239.0
3-19	350	0.10/.90			9	0.4887	0.071	230.2
3-20	350	0.15/.85			9	0.7570	0.099	224.4

*NA – data not available – lost in recording

Table XXXIV. Abbreviated Life Test REA S/N 6 Cold Start Series

Sequence Number	$\tau_{1\%}$ ~ msec	Pc, Spike ~ psia	Pc, Equilib. ~ psia	Roughness ~ ± psid	Cool Time ~ hours
3-22	55	121	84	3.0	13.0
3-23	81	146	84	1.5	11.0
3-24	78	172	85	3.0	12.0
3-25	90	139	84	3.0	11.0
3-26	90	158	84	4.0	6.0
3-27	54	117	84	3.0	9.0
3-28	85	153	85	3.0	9.0
3-29	85	144	84	2.0	5.6
3-30	24	50	84	2.0	62.0
3-31	49	105	84	3.0	8.5
3-32	19	50	84	3.0	11.0
3-33	22	35	84	2.0	14.0
3-34	24	43	84	1.5	10.0
3-35	50	96	84	2.0	7.6
[illegible]	50	121	84	3.0	7.5
3-37	47	97	84	3.0	9.0
3-38	50	100	84	3.0	12.0
3-39	31	54	84	3.0	15.1
3-[illegible]	50	114	84	2.0	9.0
3-41	23	43	84	1.5	65.0
3-42	47	96	84	2.0	7.7
3-43	26	46	84	3.0	11.5
3-44	48	95	84	2.0	12.3
3-45	30	37	84	3.0	13.7
3-46	NA	NA	NA	NA	13.0
3-46R	25	39	84	3.0	11.0

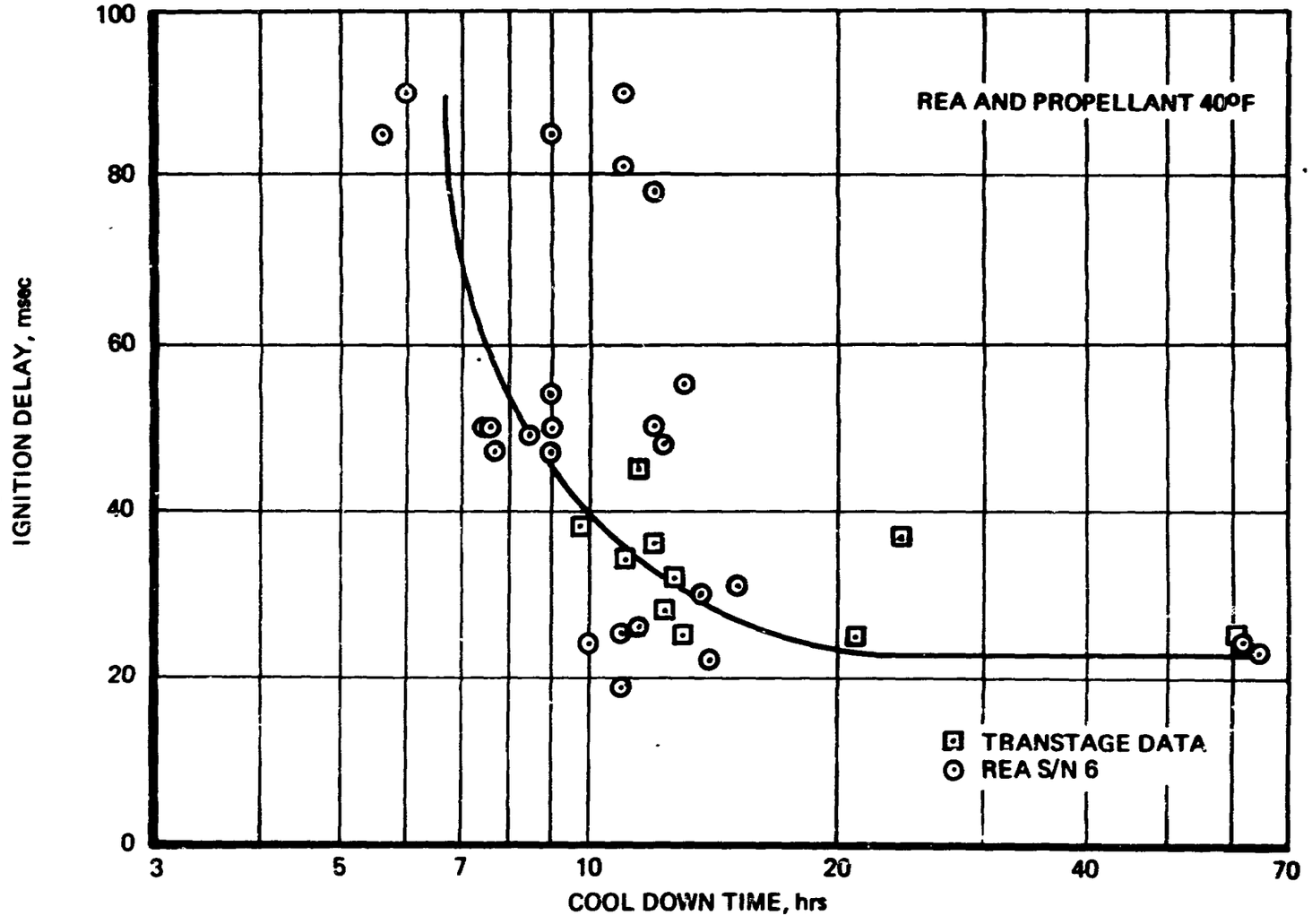

Figure 35. Abbreviated Life Test REA S/N 6 Cold Start Data

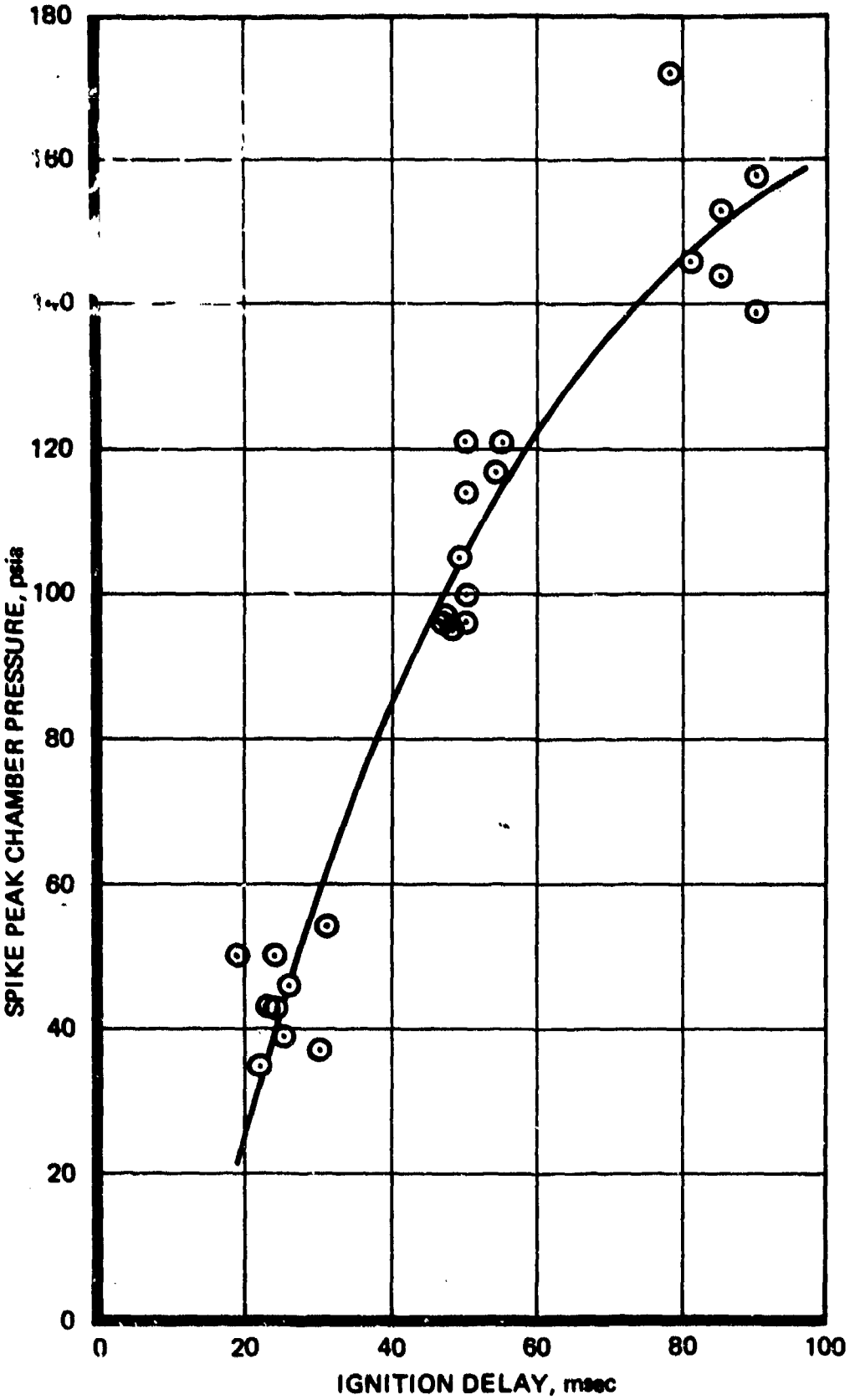

Figure 36. Abbreviated Life Test REA S/N 6 Ignition Delay Versus Peak Chamber Pressure

Table XXXV. Abbreviated Life Test REA S/N 6 Baseline Pulse Mode Data

			First Pulse		Equilibrium Pulse			
Sequence Number	Feed Pressure ~ psia	Duty Cycle	* $\tau_{1\%}$ ~ msec	Peak Pc ~ psia	$\tau_{1\%}$ ~ msec	I_{bit} ~ lbf-sec	Centroid ~ sec	I_{sp} ~ lbf-sec/lbm
3-47	100	0.02/.98	36	9	10	0.0424	0.053	151.3
3-48	100	0.02/.48			10	0.0460	0.050	164.3
3-49	100	0.05/.95			10	0.1170	0.058	217.0
3-50	100	0.05/.45			9	0.1201	0.059	227.5
3-51	100	0.10/.90			9	0.2261	0.080	224.7
3-52	100	0.15/.85			9	0.3328	0.104	225.2
3-54	225	0.02/.98	60	10.8	9	0.0611	0.043	144.5
3-55	225	0.02/.48			9	0.0760	0.044	169.6
3-56	225	0.05/.95			9	0.2040	0.054	221.3
3-57	225	0.05/.45			NA	0.2117	NA	226.9
3-58	225	0.10/.90			9	0.3982	0.077	227.0
3-59	225	0.15/.85			9	0.5958	0.104	224.5
3-61	350	0.02/.98	86	8.7	10	0.0865	0.040	183.3
3-62	350	0.02/.48			9	0.1066	0.042	218.0
3-63	350	0.05/.95			9	0.2575	0.051	223.7
3-64	350	0.05/.45			9	0.2531	0.051	226.6
3-65	350	0.10/.90			9	0.4943	0.075	223.8
3-66	350	0.15/.85			10	0.7381	0.100	220.5

Table XXXVI. Abbreviated Life Test Baseline Steady-State Data S/N 6 REA

Sequence No.	P_{feed} ~ psia	$\tau 1\%$ ~ msec	$\tau 90\%$ ~ msec	$\tau 10\%$ ~ msec	P_c ~ psia	F ~ lbf	I_{sp} ~ sec	Roughness ~ ±psid
3-7	94	8	53	53	43.8	2.299	218.0	1.5
3-14	214	8	34	40	67.5	3.619	221.7	1.5
3-21	340	8	68	45	84.9	4.585	224.6	3.0
3-53	95	10	155	57	41.1	2.146	215.9	3.0
3-60	210	8	28	45	66.5	3.562	225.8	6.0
3-67	335	8	71	46	84.9	4.588	229.0	7.0

REA S/N 6 Disassembly – Post-test X-rays of REA S/N 6 revealed a void in the upper catalyst bed under the rigimesh injection element. The void was not centered under the element but rather biased toward one side of the element. This condition was verified upon removing the intermediate bed plate when a local void was observed (approximately 6.5% by volume) on one side of the catalyst bed. The position of the void relative to the injector was marked for further study of the injector on the water flow bench. Catalyst weights revealed an 8% weight loss in the 25- to 30-mesh upper bed and no loss in the 14- to 18-mesh lower bed. Both screens on the intermediate bed plate were loose and the upper screen was badly nitrided with a burnt appearance in the area of the void. Although there were broken wires in the nitrided area, the holes thus formed were of insufficient size to allow the migration of catalyst from the upper to the lower catalyst bed. This conclusion was further substantiated by the fact that no catalyst was found in the holes of the intermediate bed plate.

A microscopic examination of the rigimesh injection element revealed excellent appearance, with no apparent nitriding. Post-test water flow showed a flow maldistribution, however, with excessive flow in the region of the void. Further disassembly of the injector revealed that the rigimesh orientation was different than injector S/N 001 which had been used in REA S/N 4. The rigimesh material is composed of two layers of 12- by 64-mesh screen which are calendered together. The warp wires (12 per inch) of each layer are oriented at 90 degrees during manufacture. The warp wires on the side of the rigimesh which propellant first contacts are drawn to scale in Figure 47, which shows the discrepancy of alignment between S/N 001 and 002. This misalignment was precluded on later injector assemblies by the addition of a scribe line across the injector face (location S on Figure 47) which was aligned with the visible warp wire during assembly. This, combined with additional visual flow checks during assembly water flow calibration and additional alignment checks before packing the upper catalyst bed, ensured that all subsequent injectors had the same operating characteristics as injector S/N 001.

Venturi Flow Testing – Figure 48 is a tracing of chamber pressure on REA S/N 6 during its first baseline pulse-mode operation. The shift in steady-state chamber pressure shown on this figure was also noted on REA S/N 5, although generally on both REA's the shift did not occur during the pulse as shown, but rather from one pulse to the next. When this phenomenon was noted on REA S/N 5, it was also noted that propellant flow rate changed proportionally to chamber pressure

Table XXXVII. Abbreviated Life Test REA S/N 6 Baseline Pulse Mode Comparison

Duty Cycle	P_{feed} ~ psia	Mean I_{bit} ~ lbf-sec	Spread ±lbf-sec	Spread ± %	Work Statement Goal ± %	Mean Cent. ~ sec	Spread ± sec	Spread ± %	Work Statement Goal
0.02/.98	100	0.0427	0.0003	0.7	10.0	0.047	0.006*	12.8	5.0 ms
0.02/.48	100	0.0471	0.0011	2.3		0.045	0.005	11.1	
0.05/.95	100	0.1174	0.0004	0.3	7.0	0.056	0.003	4.5	5.0 %
0.05/.45	100	0.1241	0.0040	3.2		0.055	0.004	7.3*	
0.10/.90	100	0.2352	0.0091	3.9		0.078	0.003	3.2	
0.15/.85	100	0.3487	0.0159	4.6		0.102	0.002	1.9	
0.02/.98	225	0.0635	0.0024	3.7	10.0	0.039	0.004	10.3	5.0 ms
0.02/.48	225	0.0779	0.0019	2.4		0.040	0.005	11.4	
0.05/.95	225	0.1961	0.0079	4.0	7.0	0.051	0.004	6.9*	5.0 %
0.05/.45	225	0.2038	0.0079	3.9		0.050	NA	NA	
0.10/.90	225	0.3982	NA	NA		0.077	NA	NA	
0.15/.85	225	0.6256	0.0298	4.8		0.101	0.003	3.0	
0.02/.98	350	0.0880	0.0015	1.6	10.0	0.037	0.0045	9.6*	5.0 ms
0.02/.48	350	0.1084	0.0018	1.7		0.038	0.004	10.5*	
0.05/.95	350	0.2662	0.0087	3.3	7.0	0.050	0.002	3.0	5.0 %
0.05/.45	350	0.2528	0.0004	0.1		0.049	0.002	4.1	
0.10/.90	350	0.4915	0.0028	0.6		0.073	0.002	2.7	
0.15/.85	350	0.7476	0.0095	1.3		0.100	0.001	0.5	

*Outside of Work Statement Goals

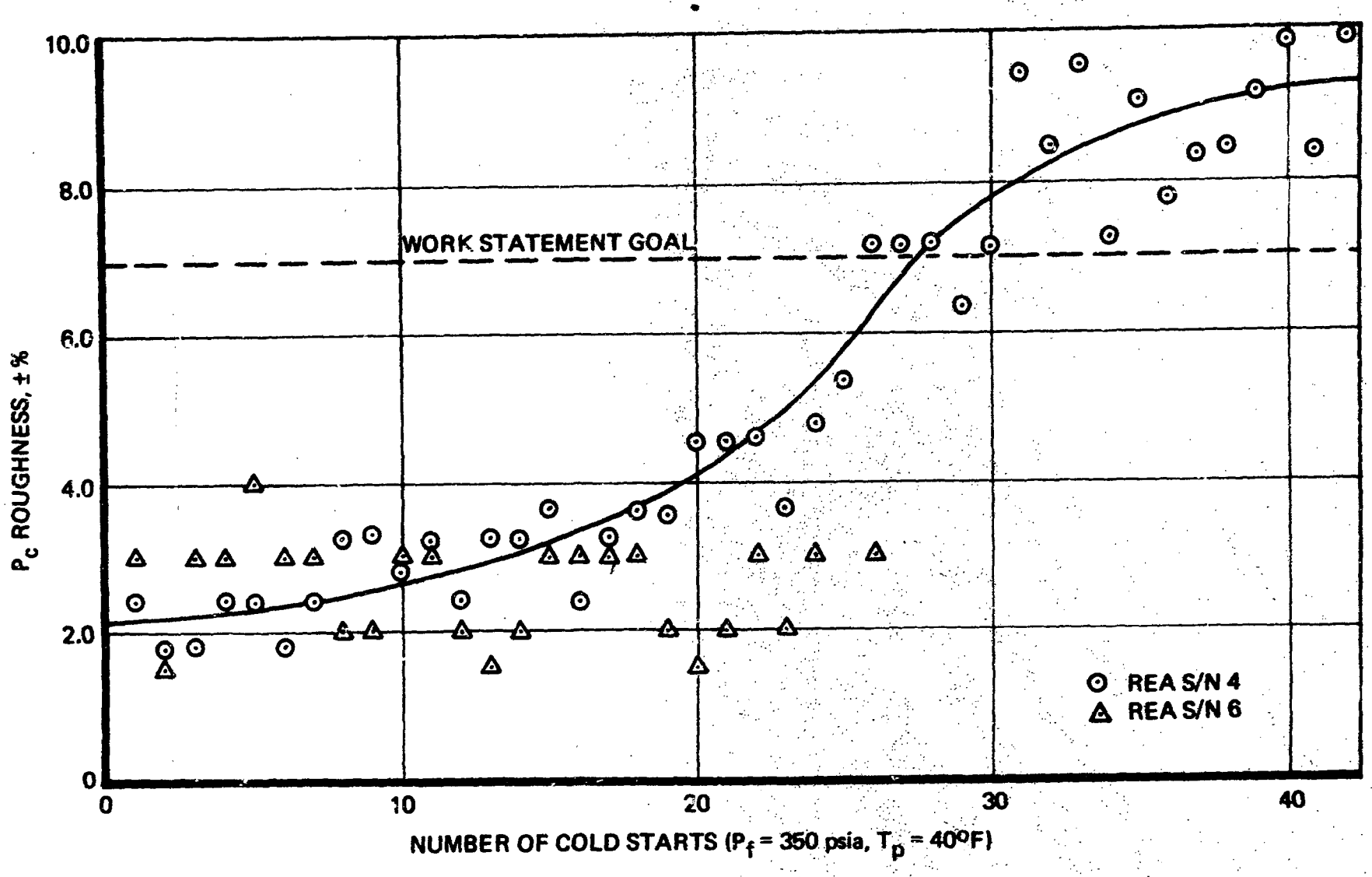

Figure 37. 10^6 Cycle Program Cold Start Test

11046-33

Table XXXVIII. Extended Life Test Duty Cycle REA S/N 6

Sequences 3-1 through 3-67 – Abbreviated life test per TPL 0147, Revision B
Sequences 3-68 through 3-74 – Duty cycle M at P_{feed} = 350 psia
Sequences 3-75 through 3-95 – Baseline No. 3
Sequences 3-96 through 3-158 – Repeat duty cycle N three times
Sequences 3-159 through 3-179–Baseline No. 4
Sequences 3-180 through 3-410–Repeat duty cycle N eleven times
Sequences 3-411 through 3-417–Repeat duty cycle M at P_{feed} = 100 psia
Sequences 3-418 through 3-428–Baseline No. 5

DUTY CYCLE M

Sequence	On Time msec	Off Time msec	Number of Pulses
a	20	980	3,200
b	20	480	3,200
c	50	950	1,300
d	50	450	1,300
e	100	900	600
f	150	850	400
g	60,000	Steady State	1

DUTY CYCLE N

Sequence	Propellant Temperature, °F	Feed Pressure, psia	Duty Cycle
a	65	350	M
b	65	225	M
c	65	100	M

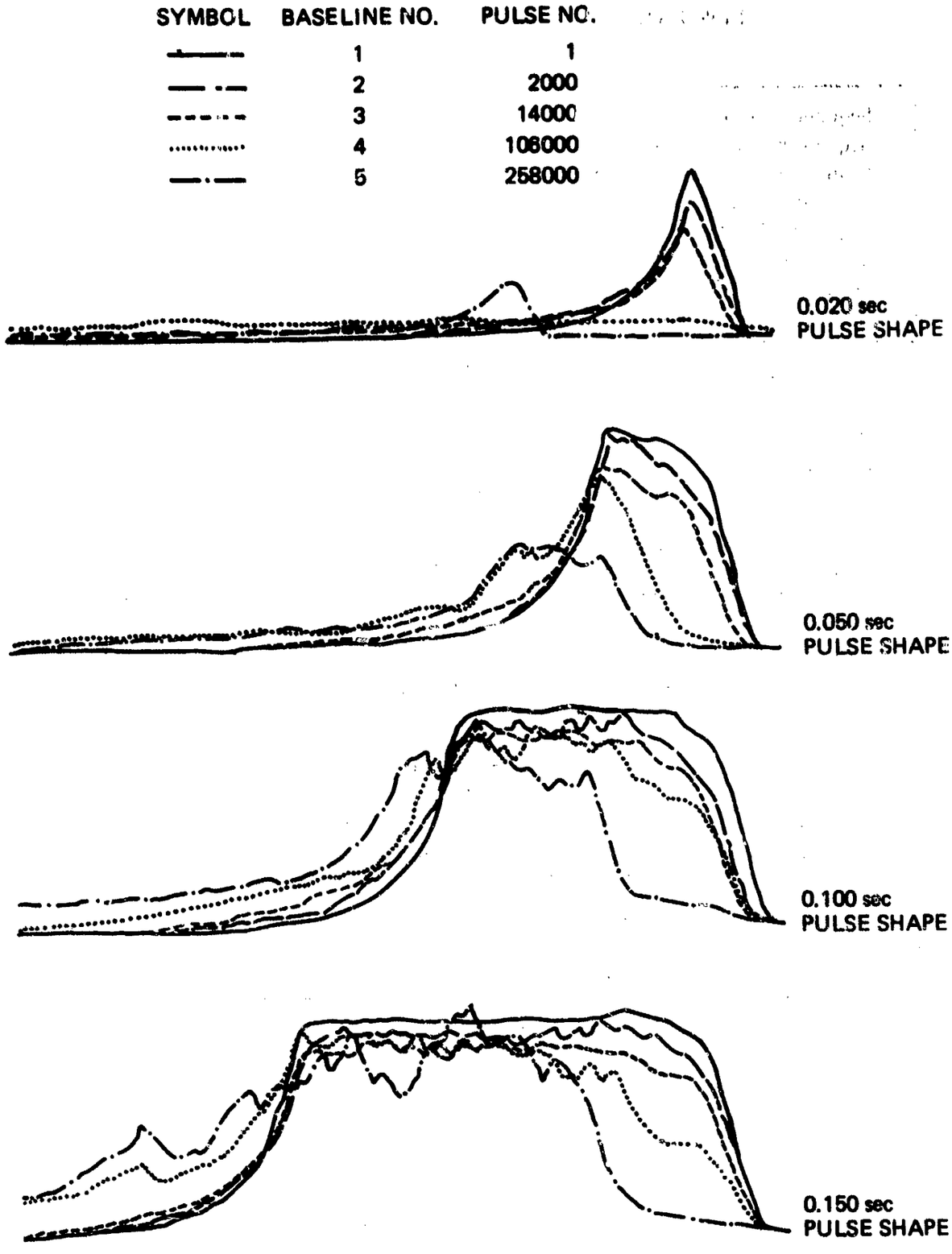

Figure 38. Extended Life Test Pulse Comparison
REA S/N 6 at P_{feed} = 100 psia

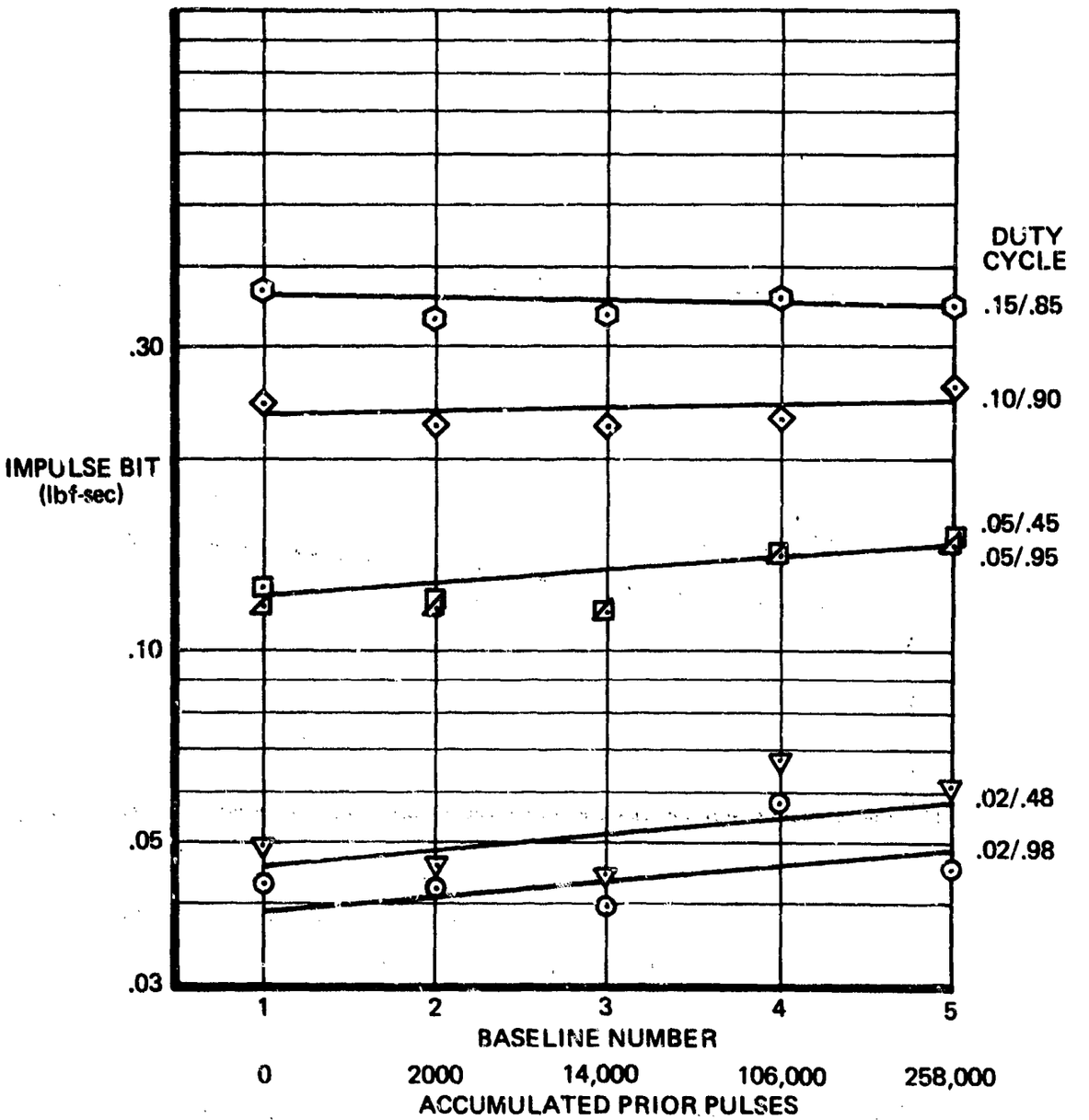

Figure 39. Extended Test REA S/N 6 Low Feed Pressure (100 psia)

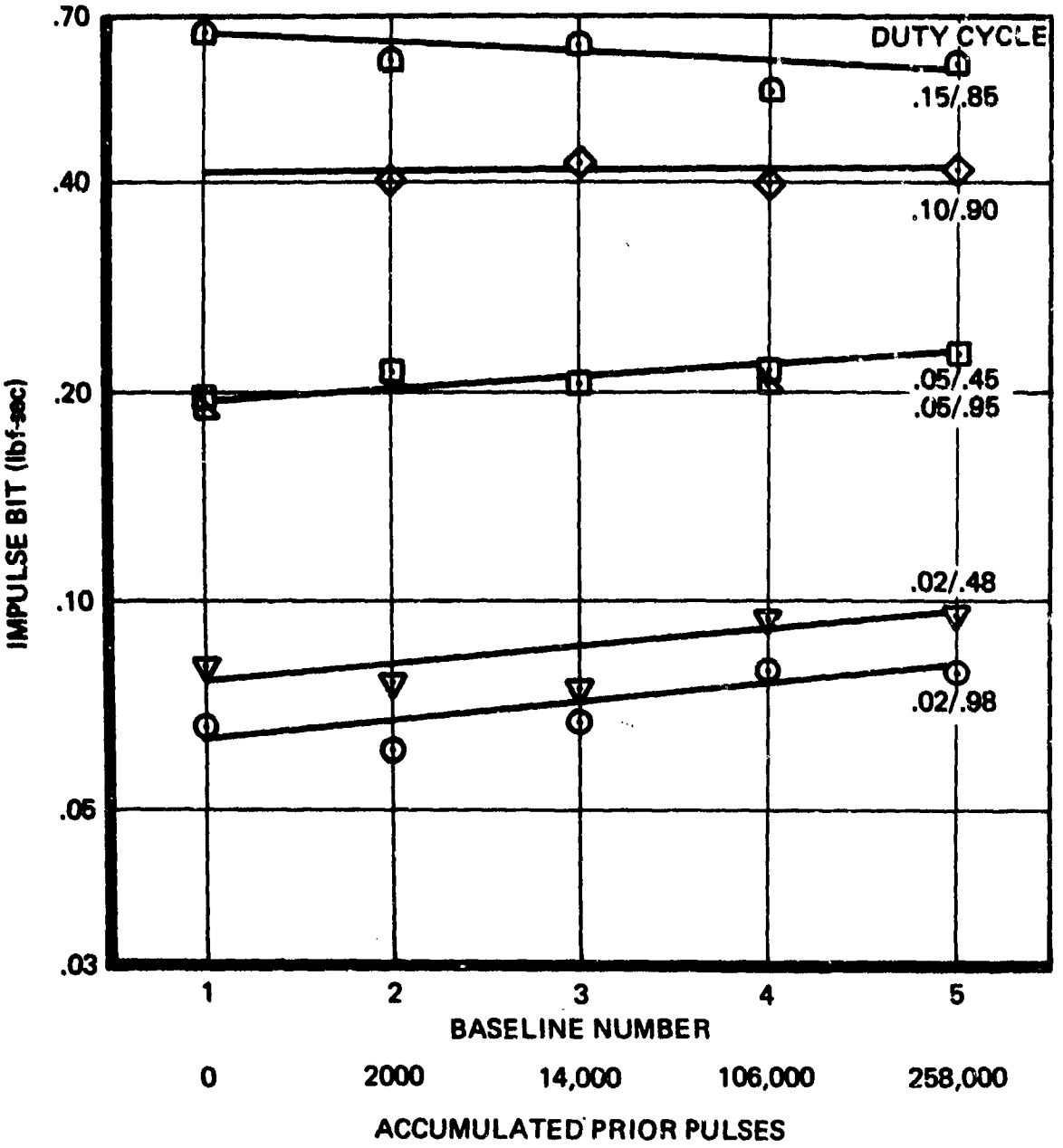

Figure 40. Extended Life Test REA S/N 6 Mid-Feed Pressure (225 psia)

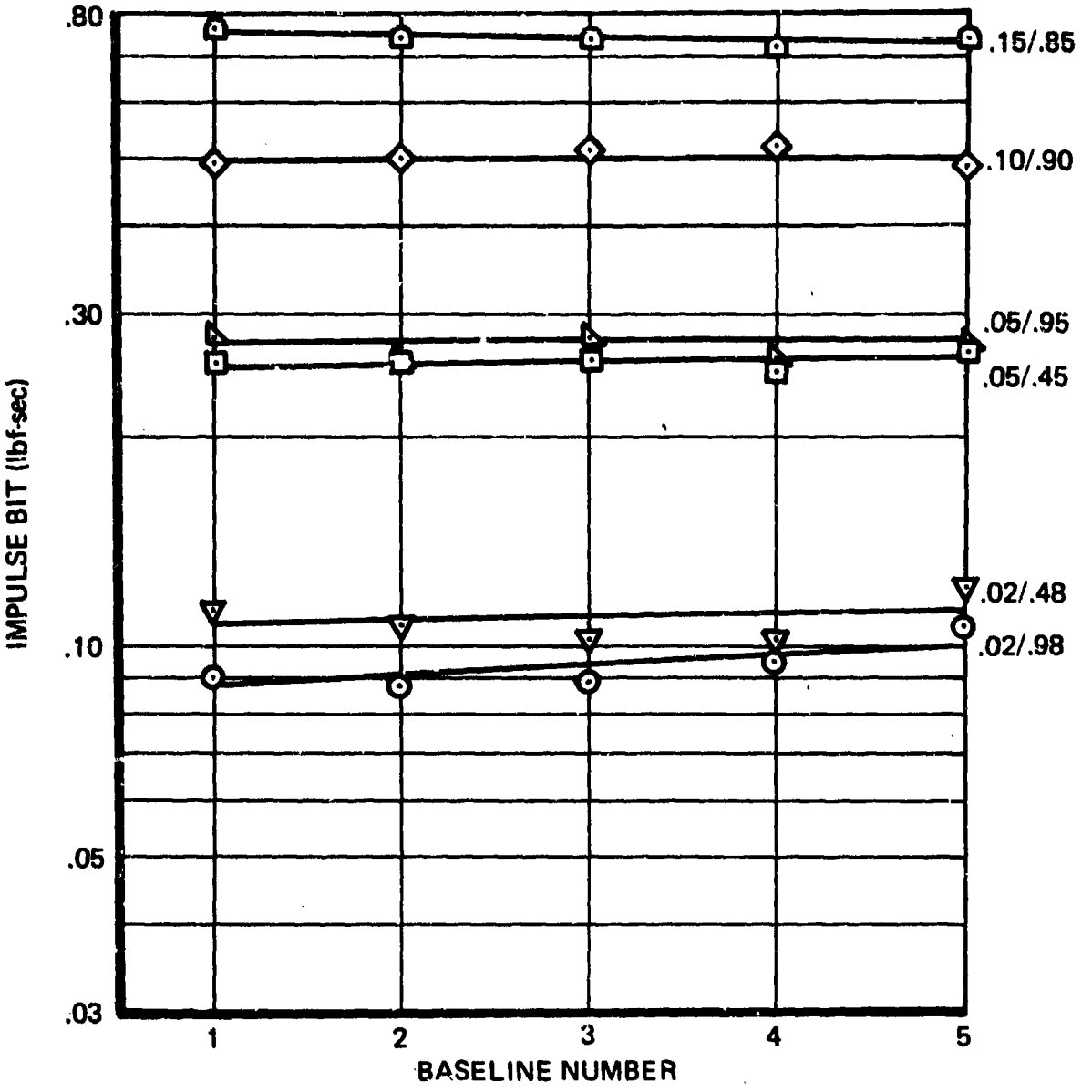

Figure 41. Extended Life Test REA S/N 6 High Feed Pressure (350 psia)

Table XXXIX. Extended Life Test REA S/N 6 Baseline Pulse Mode Comparison (No. 1 through No. 5)

Duty Cycle	P_{feed} ~psia	Mean I_{bit} ~lbf-sec	Spread ± lbf-sec	Spread ± %	Work Statement Goal ± %	Mean Cent. ~ sec	Spread ± sec	Spread ± %	Work Statement Goal
0.02/.98	100	0.0458	0.0091	19.9*	10.0	0.124	0.127*	102.3	5.0 ms
0.02/.48	100	0.0533	0.0113	21.2*		0.103	0.073*	70.6	
0.05/.95	100	0.1270	0.0165	13.0*	7.0	0.102	0.064	62.4*	5.0 %
0.05/.45	100	0.1317	0.0169	12.8*		0.098	0.062	63.4*	
0.10/.90	100	0.2377	0.0180	7.6*		0.112	0.064	56.9*	
0.15/.85	100	0.3463	0.0159	4.6		0.133	0.045	33.8*	
0.02/.98	225	0.0703	0.009	12.8*	10.0	0.157	0.153*	97.6	5.0 ms
0.02/.48	225	0.0839	0.0102	12.1*		0.103	0.097*	93.9	
0.05/.95	225	0.2053	0.0197	9.6*	7.0	0.102	0.064	62.4*	5.0 %
0.05/.45	225	0.2104	0.0154	7.3*		0.085	0.039	45.2*	
0.10/.90	225	0.4086	0.0140	3.4		0.123	0.035	28.5*	
0.15/.85	225	0.6014	0.0564	9.4*		0.128	0.030	23.0*	
0.02/.98	350	0.0934	0.0108	11.5*	10.0	0.111	0.136*	122.1	5.0 ms
0.02/.48	350	0.1084	0.0097	8.9		0.102	0.080*	78.1	
0.05/.95	350	0.2687	0.0097	3.6	7.0	0.084	0.063	75.0*	5.0 %
0.05/.45	350	0.2552	0.0083	3.2		0.072	0.033	45.6*	
0.10/.90	350	0.4998	0.0179	3.6		0.101	0.040	39.2*	
0.15/.85	350	0.7379	0.0180	2.4		0.116	0.023	19.9*	

*Outside of Work Statement Goals

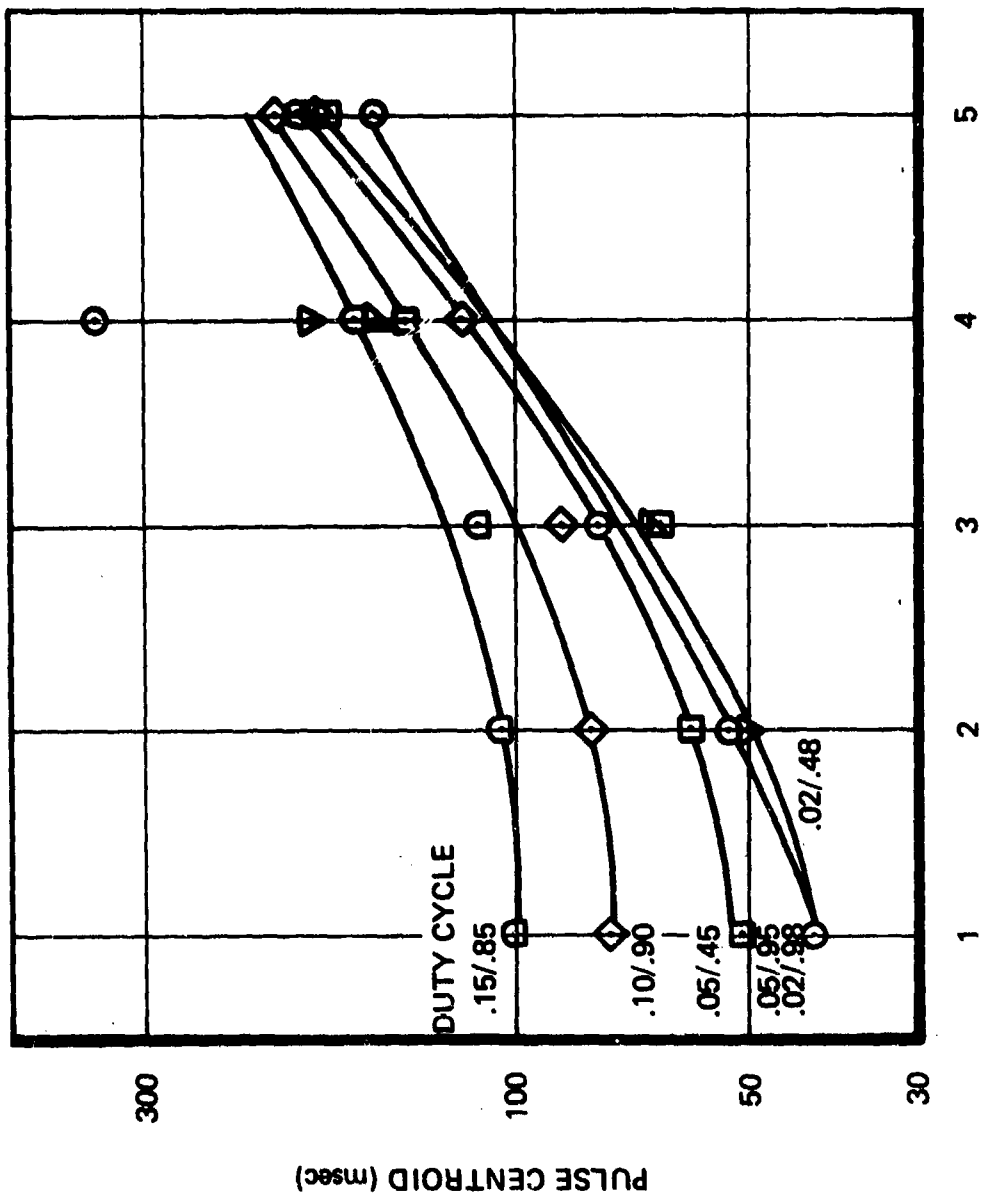

Figure 42. Extended Life Test REA S/N 6 Low Feed Pressure (100 psia)

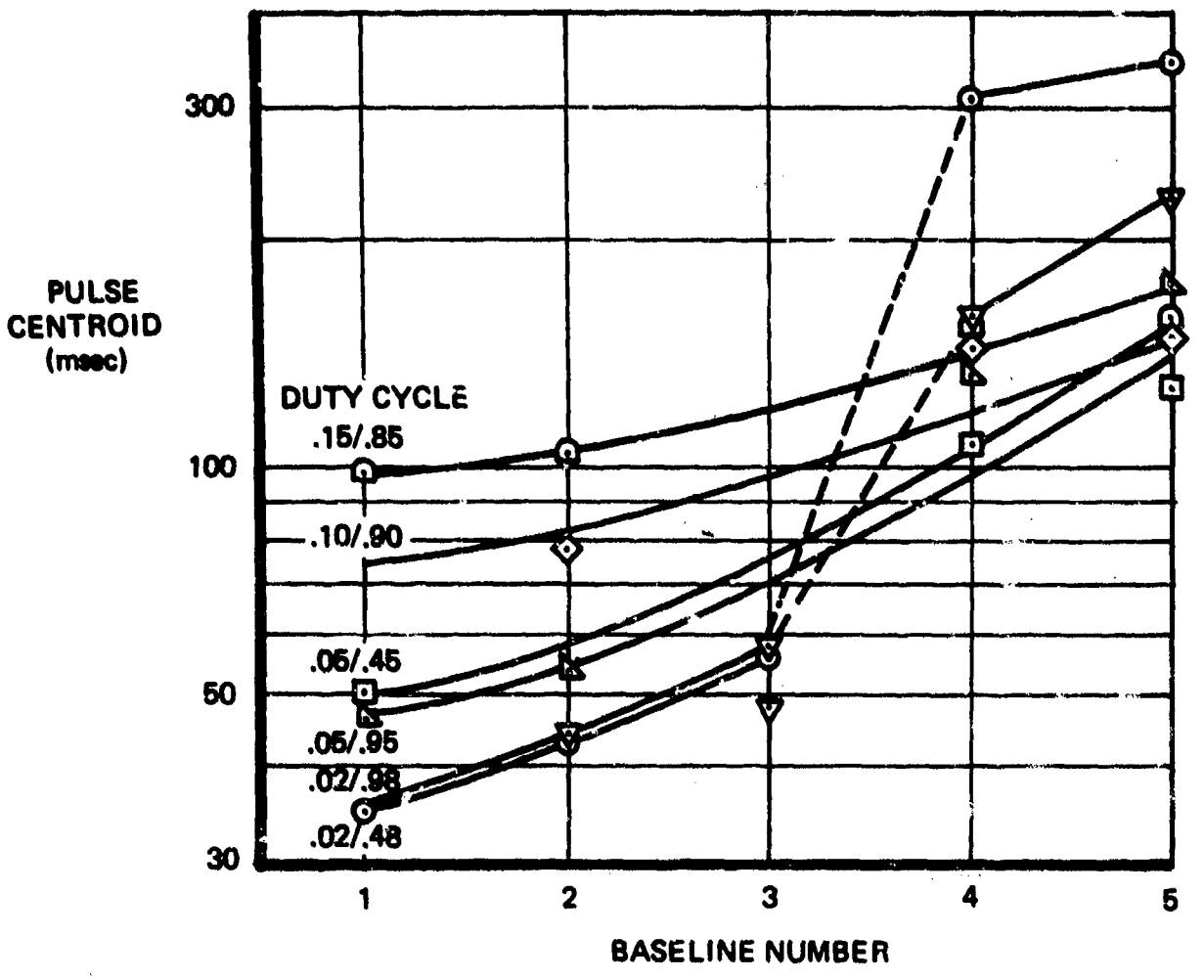

Figure 43. Extended Life Test REA S/N 6 Mid-Feed Pressure (225 psia)

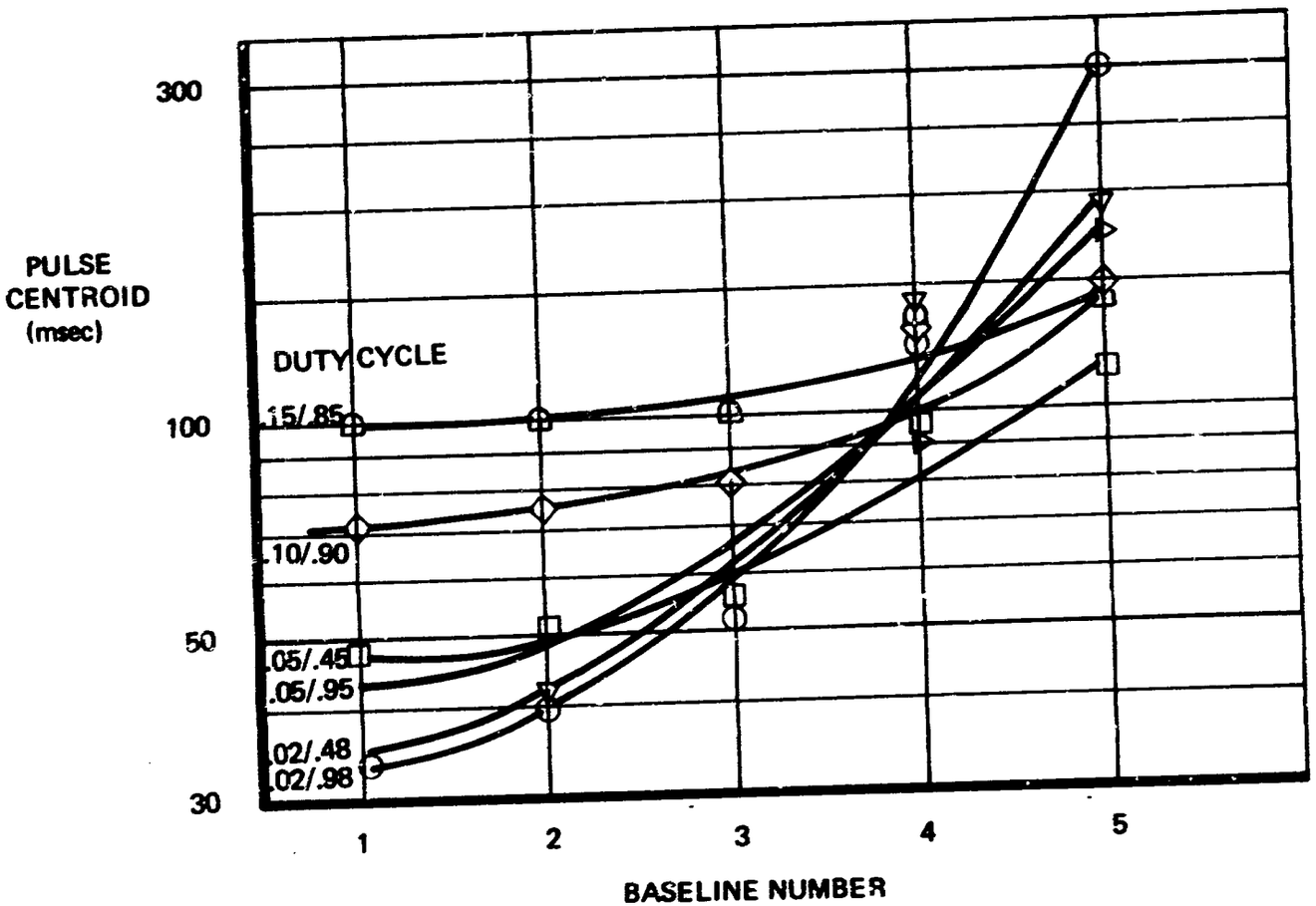

Figure 44. Extended Life Test REA S/N 6 High Feed Pressure (350 psia)

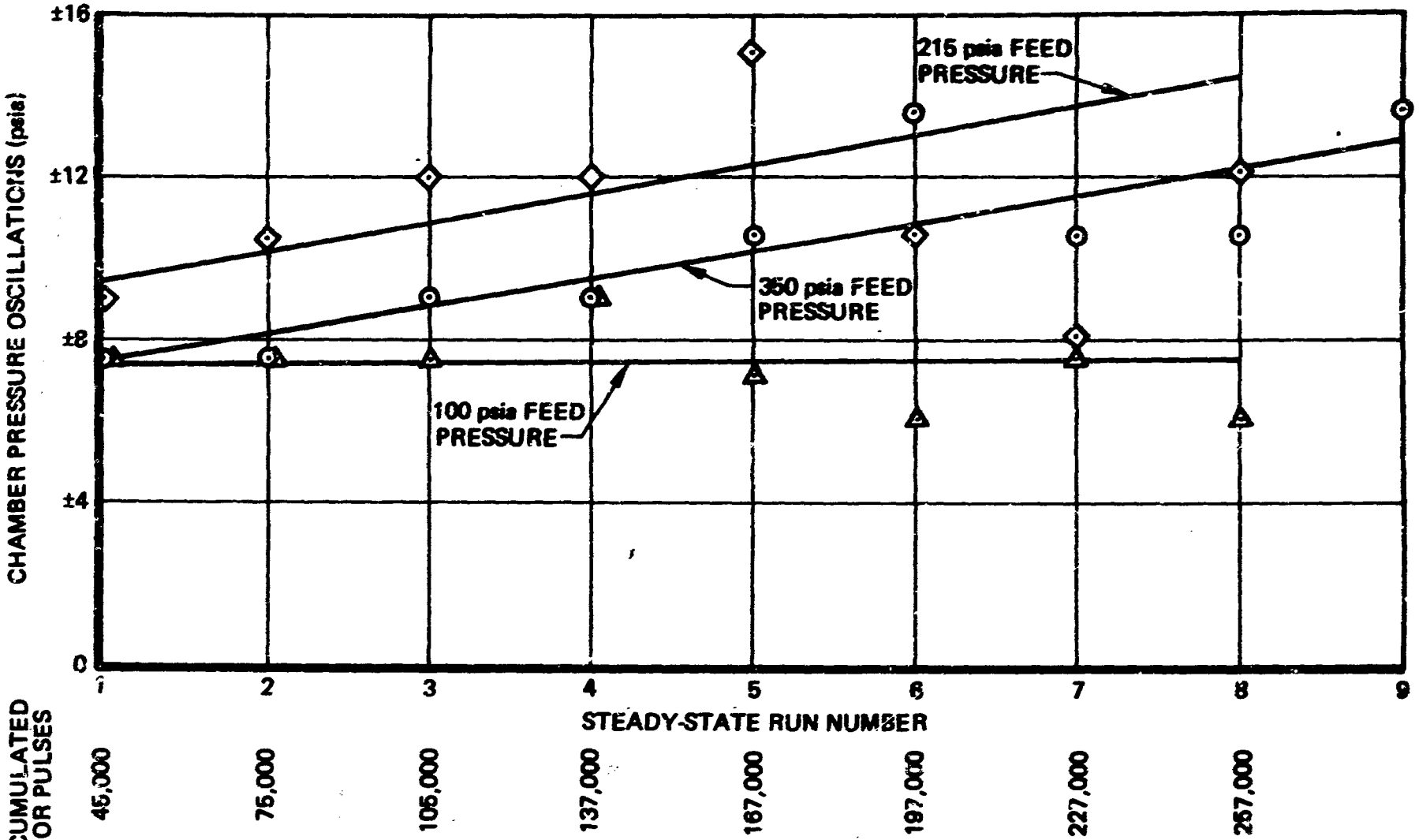

Figure 45. Extended Pulsing Life Test Steady-State Performance Comparison
60-Second Tests

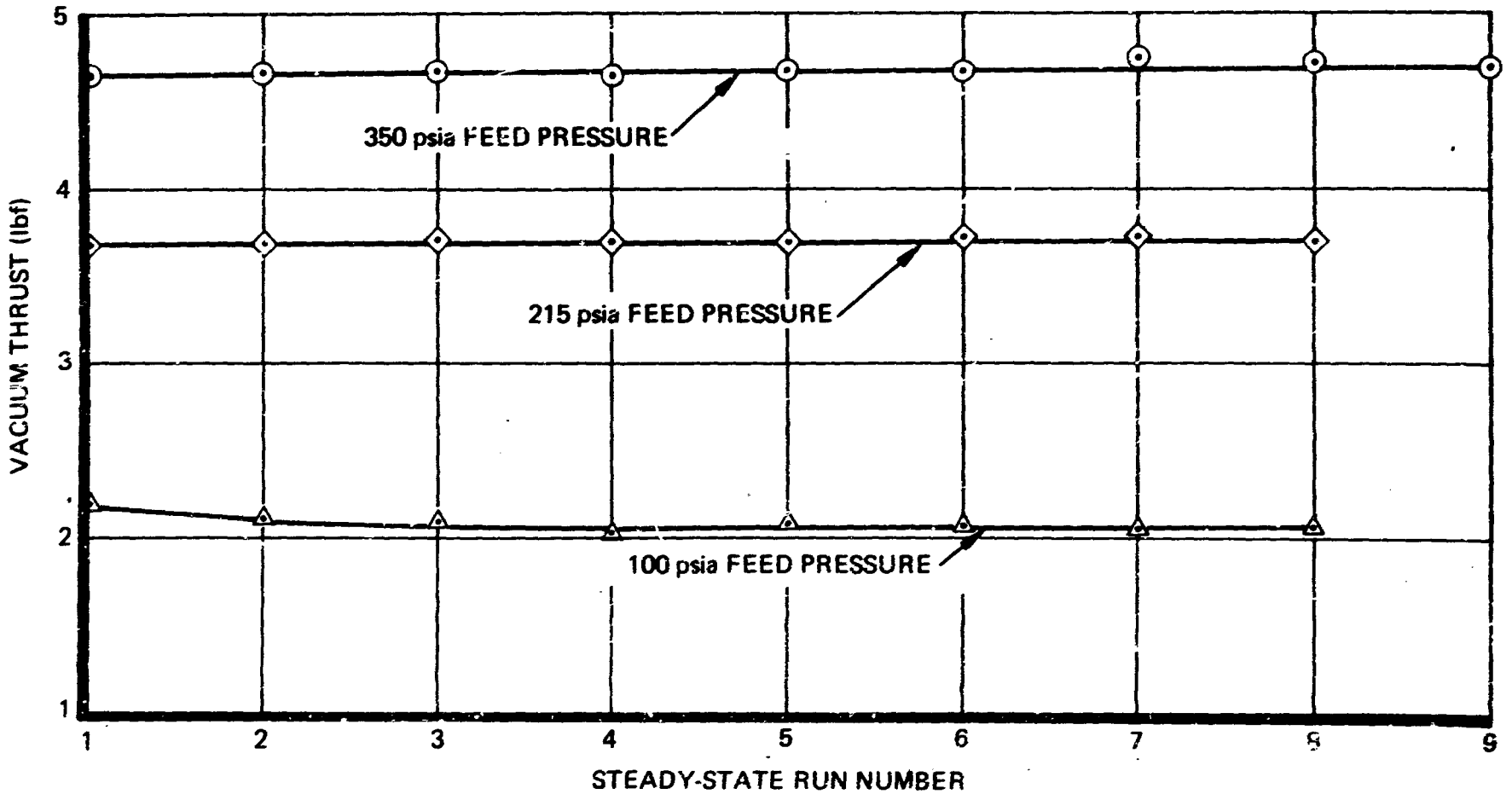

Figure 46. Extended Pulsing Life Test Steady-State Performance Comparison – 60 Second Tests

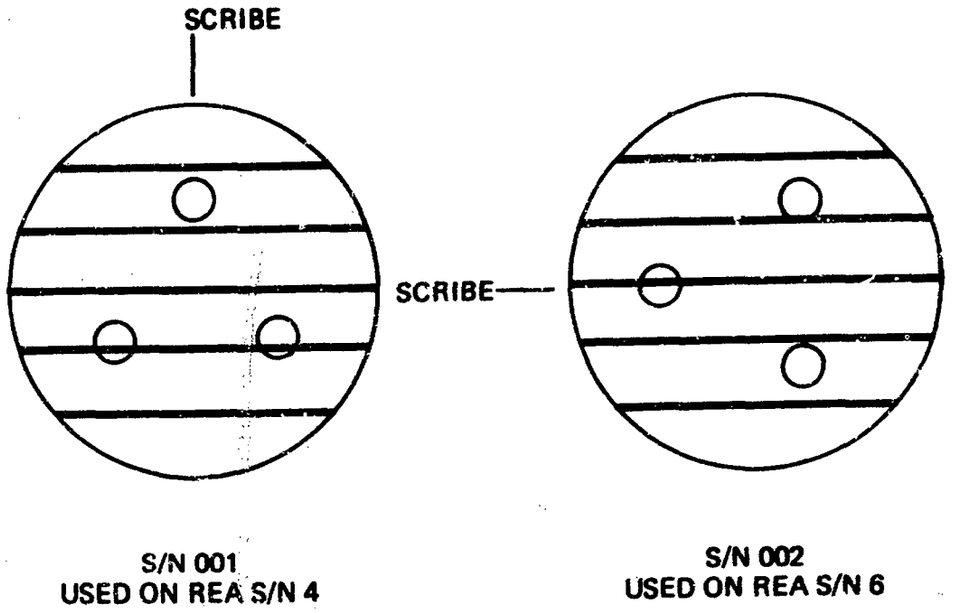

Figure 47. Injector Subassembly 26235-302-11 – Rigimesh Warpwire Alignment Comparison

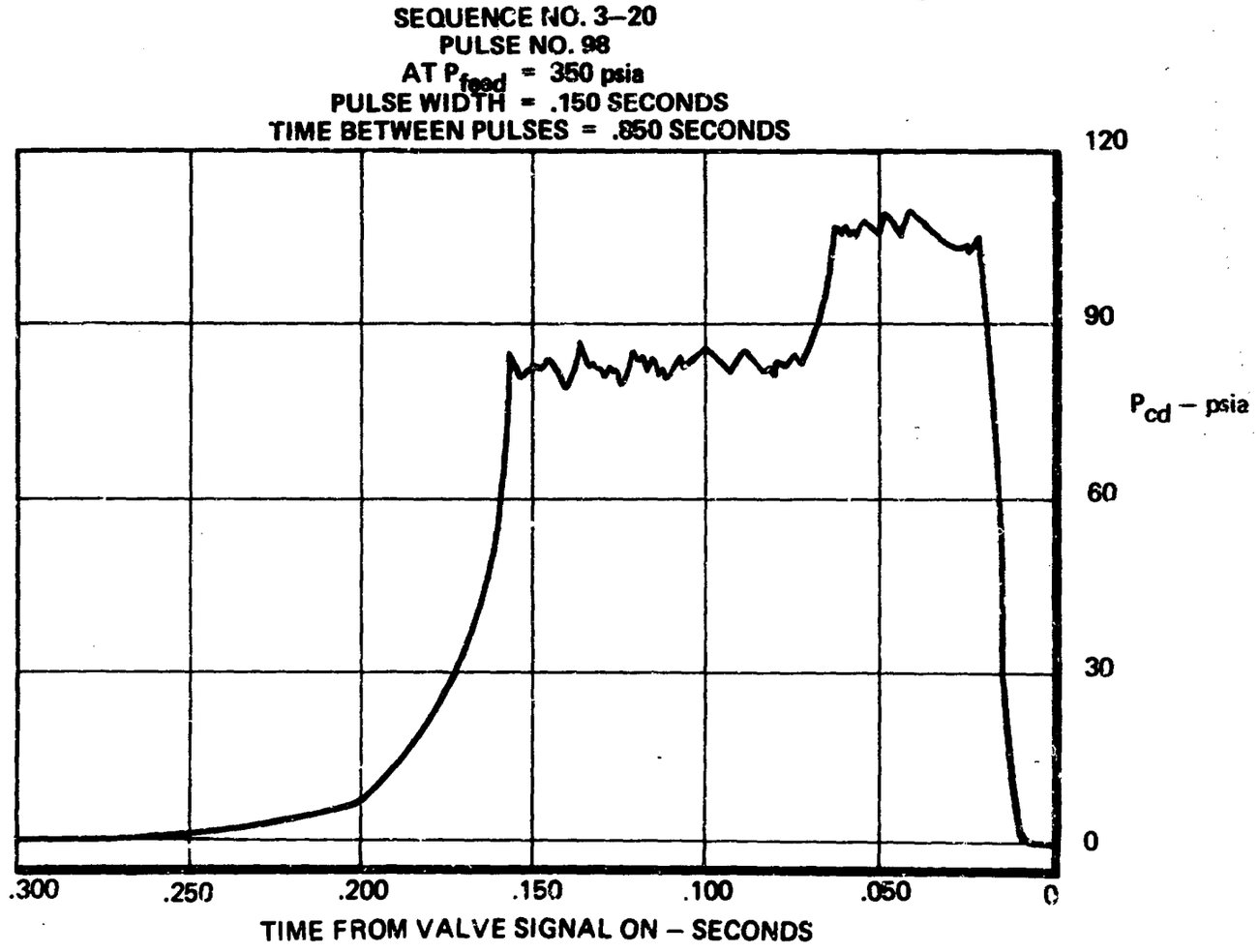

Figure 48. DISTORTED PULSE TRACE – ABBREVIATED LIFE TEST REA S/N 6

indicating a change in venturi flow characteristics. During the disassembly of REA S/N 5 and assembly of REA S/N 6, a series of flow tests was conducted with the venturi in an attempt to verify this unstable operation.

Figure 49 presents the steady-state flow calibration data for the subject venturi. Extensive data was obtained in the area of incipient cavitation showing far different characteristics than the sudden break usually assumed. The equilibrium cavitation flow rate values shown on the figure are in excellent agreement with the manufacturers. The projections of these equilibrium values to the noncavitating flow curve yield recovery values equivalent to the manufacturers claim (80 + %). However, the region between noncavitation and full cavitation is unstable. The effect of this on pulse-mode flow rate was demonstrated on the flow bench by addition of a simulated propellant valve to the downstream side of the venturi. With this test arrangement pulse mode and steady-state flow overshoots were demonstrated at various duty cycles with as much as 9.0% increase over nominal flow maintained for periods as long as 5 seconds. Various techniques of improving entrance flow conditions were evaluated in an attempt to eliminate the condition, but to no avail. It was apparent that the venturi would have to be polished extensively to correct this problem; however, since this would have changed the stable operating point and it was desirable that REA S/N 6 performance be compared with S/N 4 and 5, it was determined that REA S/N 6 be tested with the venturi as is.

2.4 PHASE I FINAL DESIGN

Figure 50 presents a schematic of the MR-50C REA which represents the Phase I final design. The final design is identical to the REM-Mono MR-50 REA except for the following five areas.

2.4.1 Catalyst

The upper catalyst bed uses 90% attrited 25- to 30-mesh Shell 405 catalyst, as compared to 50% attrited in REM-Mono. This selection was based upon the catalyst strength test results discussed in paragraph 2.3.2.

2.4.2 P_c Tube Adapter

As shown on Figure 50, the MR-50C REA incorporates an AN fitting on the chamber pressure tap. The REM-Mono REA uses a brazed junction to the pressure transducer.

2.4.3 Injector

On the basis of the thermal design verification test results, the MR-50C injector uses a 0.5-inch-diameter, 12- by 64-mesh, two-layer, Haynes 25 rigimesh injector spud. This spud outside diameter is welded to the injector face and retained in the center with a 0.060-inch-diameter tack weld. Propellant is supplied to this spud from three 0.020-inch-diameter branch passages which join in a single 0.0355-inch feed tube from the propellant valve. The REM-Mono injector uses a 0.3-inch-diameter spud of the same rigimesh material which is supplied with propellant from a single 0.0355-inch feed tube.

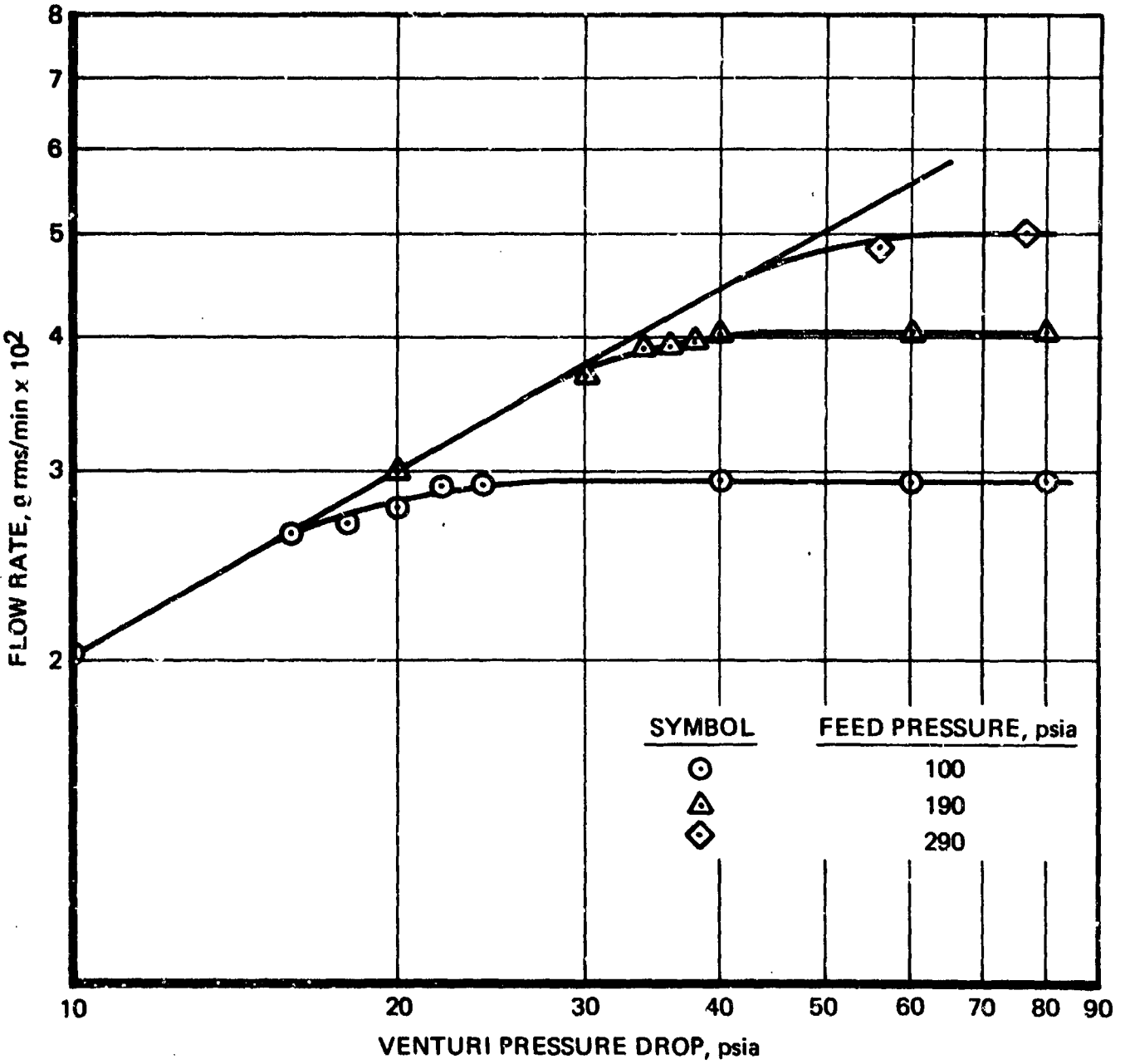

Figure 49. Flow Calibration Fox Venturi, P/N 61028-4R, S/N 154

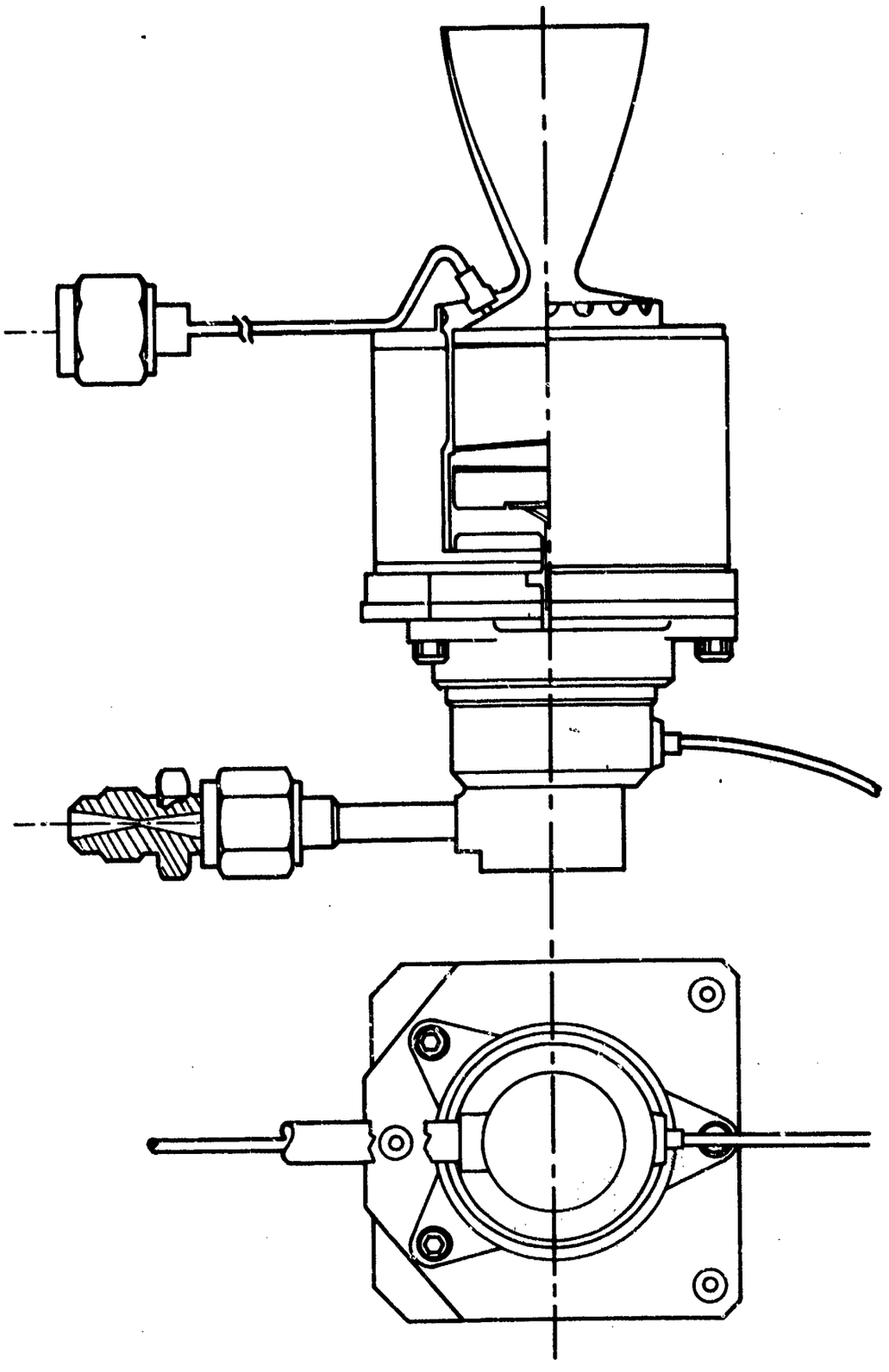

Figure 50. Long-Life Monopropellant Hydrazine Rocket Engine Assembly (MR-50C)

11046-65

2.4.4 Propellant Interface

As shown on Figure 50, the propellant interface is a 0.25-inch MS union which internally incorporates a cavitating venturi. The venturi is sized to deliver 5-lbf flow rate at 250 psia feed pressure. The REM-Mono propellant inlet is a 0.25-inch CRES 304 tube prepared for brazing. REM-Mono uses a trim orifice to deliver 5 lbf at a feed pressure of 194 psia.

2.4.5 Thermal Control Surfaces

The MR-50C does not incorporate an aft heat shield or thrust chamber thermal control plating as incorporated on the REM-Mono. These refinements of REM-Mono were required to meet very tight performance requirements while tied to a REM heat sink. Their cost and complexity were not justified by the performance gain when this heat sink was removed. Should additional performance be required, these concepts have been fully qualified on the REM-Mono Program. The forward heat shield represents a structural as well as thermal control device and is identical for REM-Mono and MR-50C.

The REM-Mono propellant valve is painted with Sicon R black paint on vehicle-exposed surfaces and aluminum paint on thrust-chamber-exposed surfaces. This thermal control is required to minimize heater power necessary to maintain the valve above freezing under worst-case cold-orbit conditions. Since there was no detailed spacecraft definition for the MR-50C REA, these thermal control paint patterns were not employed.

2.5 PHASE IA TESTS

A technical program review held at AFRPL following the completion of Phase I resulted in the revision of the statement of work so as to replace Phase I with Phase IA. The Phase IA revision included simultaneous testing of a) a flight-type 5-lbf REA (Phase I final design) to a 1,000,000-cycle duty cycle which included 42 cold starts (REA and propellant at 40°F) and b) a cold-start catalyst evaluation test series which investigated the effects of cold starts on catalyst attrition. The selection of 42 cold starts for the 1,000,000-cycle test program represented a compromise between total test time/cost and the established cool down procedures (see paragraph 2.3.4) which consume considerable test time.

2.5.1 Life Cycle Test

A flight-type REA, S/N 7, was fabricated and assembled to the Phase I final design configuration (RRC drawing 25820). This REA was installed in vacuum chamber No. 5 at the RRC vacuum test facility. A schematic diagram of this portion of the facility is illustrated in Figure 51. Figure 52 presents the overall propellant feed and thermal conditioning system used in this test setup. The test instrumentation list is summarized in Table XL.

The primary data system for the life test base point tests was the Monsanto Digital Data System. Backup for the primary system and recording of data during the balance of the testing was provided by a Dymec Digital Data system (slow scan), a Cimron Digital Data System (slow scan), oscillograph recorders, and strip chart recorders.

An electronic control system was used to provide the necessary manual and semiautomatic control signals to enable the control and operation of all the systems required during the test. The majority

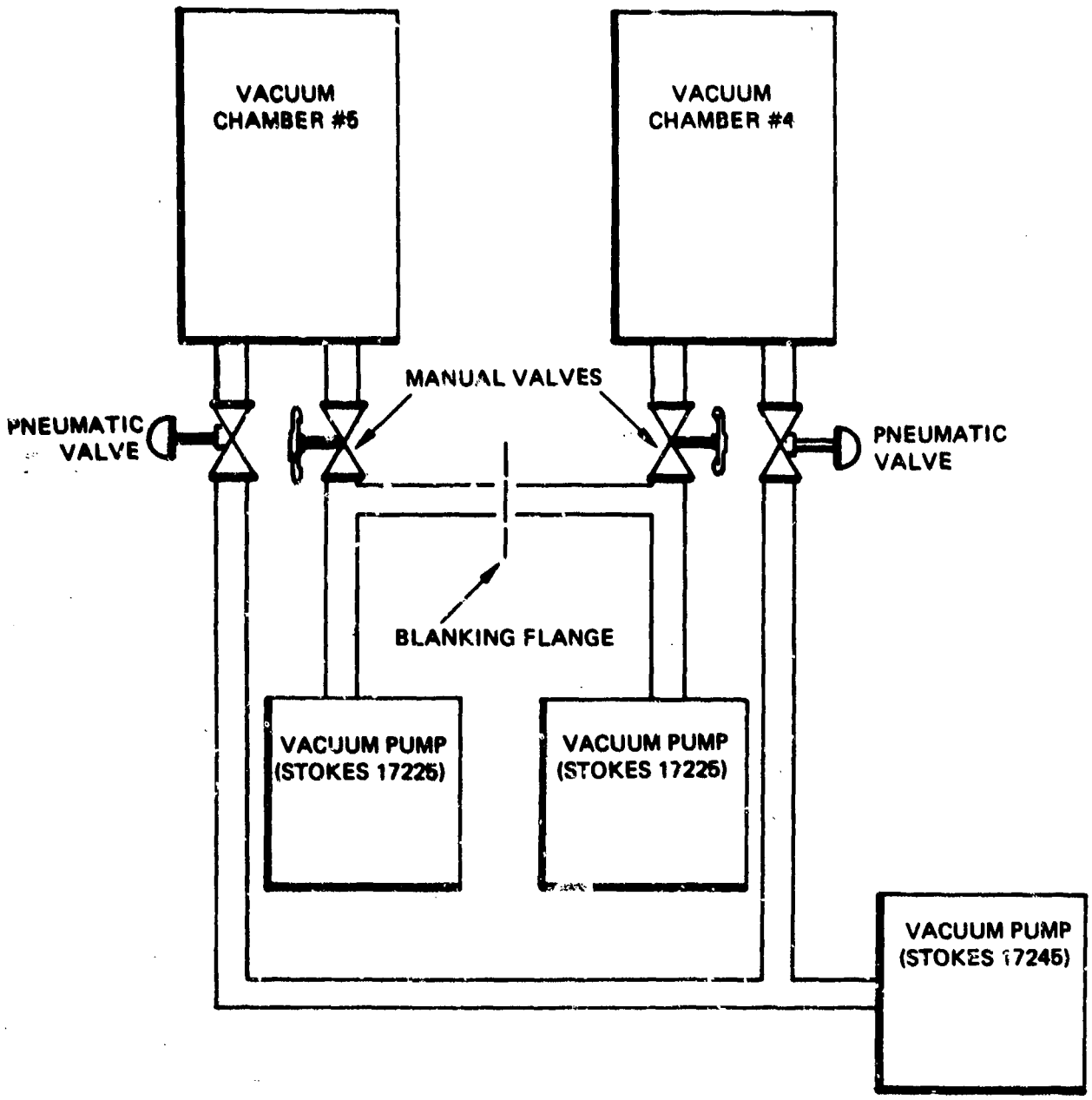

Figure 51. Altitude Test Facility

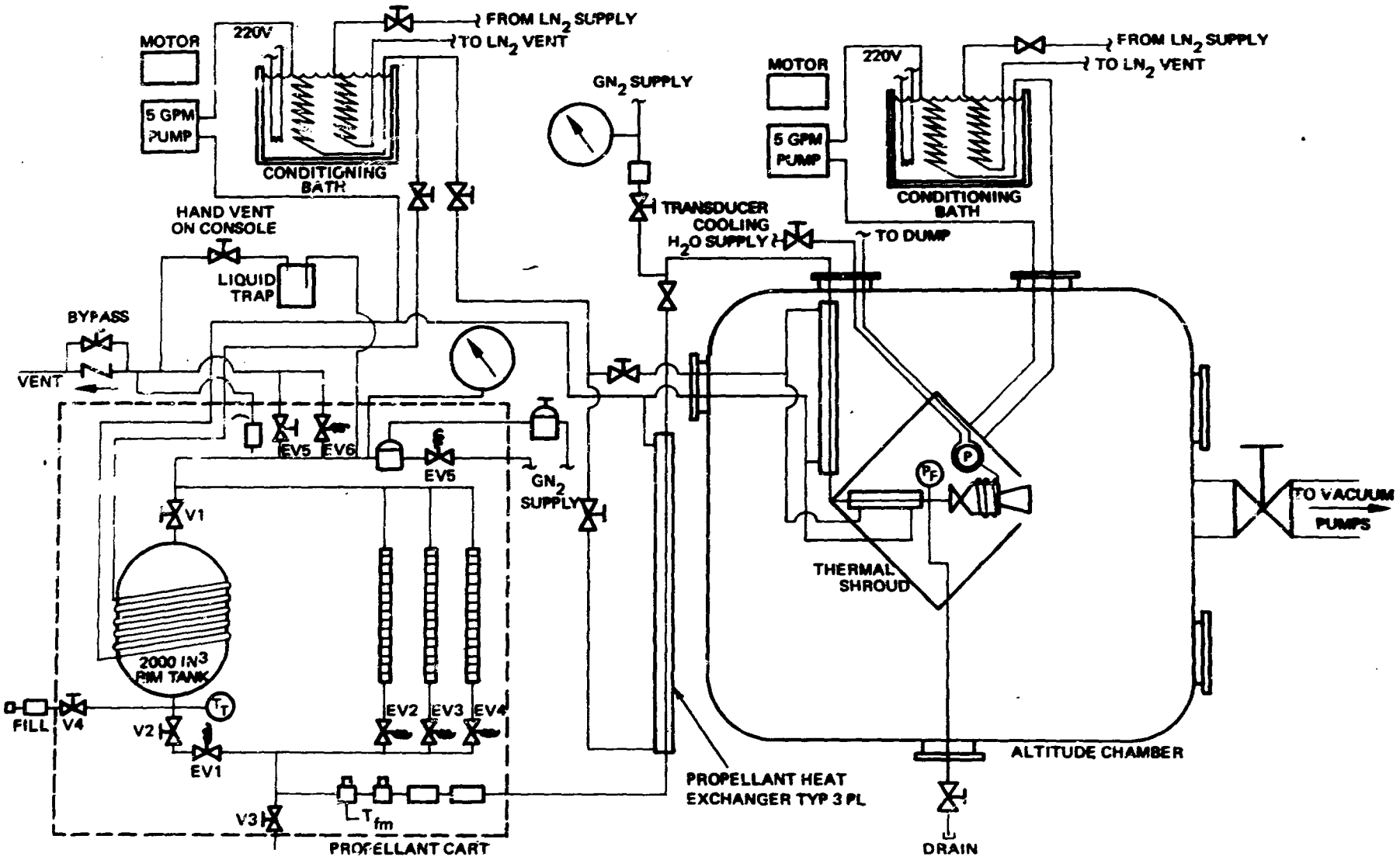

Figure 52. Propellant Feed System and Thermal Conditioning System

Table XL. Life Cycle Test Instrumentation List – Abbreviated Life Test

Parameter	Symbol	Range	Recording Method				
			Dymec	Cimron	Monsanto*	Osc	Strip Chart
Chamber pressure	P_{c1}	0–150 psia	X		X	X	X
Chamber pressure	P_{c2}	0–150 psia	X		X	X	X
Feed pressure	P_f	0–500 psig	X		X	X	X
Test cell pressure	P_a	0–0.5 psia	X		X	X	
TCV temperature	T_v	0–10 mv		X			
Chamber wall temperature	T_{w1}	0–100 mv		X	X		
Chamber wall temperature	T_{w2}	0–100 mv		X	X		
Nozzle temperature	T_{nc}	0–100 mv		X	X		X
Propellant temperature	T_{fi}	0–10 mv		X	X		X
Flow meter temperature	T_{fm}	0–10 mv		X	X		
Shroud temperature	T_{ts}	0–10 mv		X			X
Fuel flow	$\dot{w}_1$	0–1 KHz	X		X	X	
Fuel flow	$\dot{w}_2$	0–1 KHz	X		X	X	
TCV voltage	V_e	0–30 vdc			X	X	
TCV current	V_i	0–1 adc			X	X	
Time reference	Hz	500 ± 1 Hz	X			X	

*Base point tests only

of the operations are controlled by the Tally tape system once the test is initiated. The tape controls turning the oscillograph on and off, opening and closing the propellant valves, starting and stopping the Monsanto digital data acquisition system, and sequencing the propellant cart valves between main tank and sight glass supplies. Manual operations required are setting the oscillograph speed, turning on the strip charts (at start of test), setting the feed pressure, and taking sight glass readings on the closed-circuit television system. The valve driver circuit (suppression circuit) schematic diagram is illustrated in Figure 53. This suppression circuit limits back EMF to 56 volts.

The test duty cycle, feed pressure, thermal conditions and start temperatures are shown in Table XLI.

The life cycle test was initiated on REA S/N 7 on February 16, 1971. Testing was terminated on March 19, 1971, after the accumulation of 509,057 pulses with a cumulative total impulse of 107,635 lbf-sec. Testing was in accordance with Table XLI from sequences 4-1 through 4-60. All pulses had been conducted with 40°F propellant except for the five baseline tests which had been conducted at 65°F (total of 9,015 pulses). During the preceding testing the REA had been fired 22 times from an initial bed temperature of 40°F. Additionally each baseline includes three starts from initial bed temperature of 65°F.

Chamber pressure pulse shapes for each of the five baselines are compared in Figure 54. As shown on this figure the pulse shape distortion after 500,000 cycles is severe and the test was consequently discontinued on the basis of agreement between AFPCO and RRC. Baseline pulse mode performance for this REA is summarized in Tables XLII and XLIII. Average impulse bit for the last 10 pulses of each duty cycle noted is presented together with the spread for those pulses. Impulse bit at the low feed pressure is plotted as a function of pulse number on Figure 55. Data is presented for each of the five baselines conducted during the 500,000 pulses. The degradation noted in pulse shape and steady state performance of baseline 6 in Figure 54 is further dramatized on Table XLII. Table XLIII presents centroid (time from valve signal to 50% impulse delivered) and specific impulse data for the same pulses. Centroid repeatability for all but the 0.020-second pulse widths is extremely repeatable through the first 250,000 pulses as graphically displayed in Figure 56. It is significant to note that centroid is unaffected by feed pressure and therefore, the overall average centroid is presented in Figure 56.

Figure 57 presents oscillograph tracings of all steady-state start transients at the minimum feed pressure with 40°F propellant. It is obvious from these analyses that the REA suffered a gross failure between sequences 4-46 and 4-52. Tailoff overlays from the same sequences shown in Figure 58 correlate with this conclusion. The test duty cycle (Table XLI) shows that these two sequences correspond to 398.243 and 458,249 cumulative pulses. The REA's demonstrated life capability is therefore approximately 400,000 pulses, corresponding to more than 80,000 lbf-sec total impulse delivered.

Steady-state performance from each of the five baseline runs is presented in Table XLIV. Steady-state thrust and specific impulse are plotted as a function of pulse number on Figures 59 and 60, respectively. This data also correlates with the distortion noted on pulse shape at 500,000.

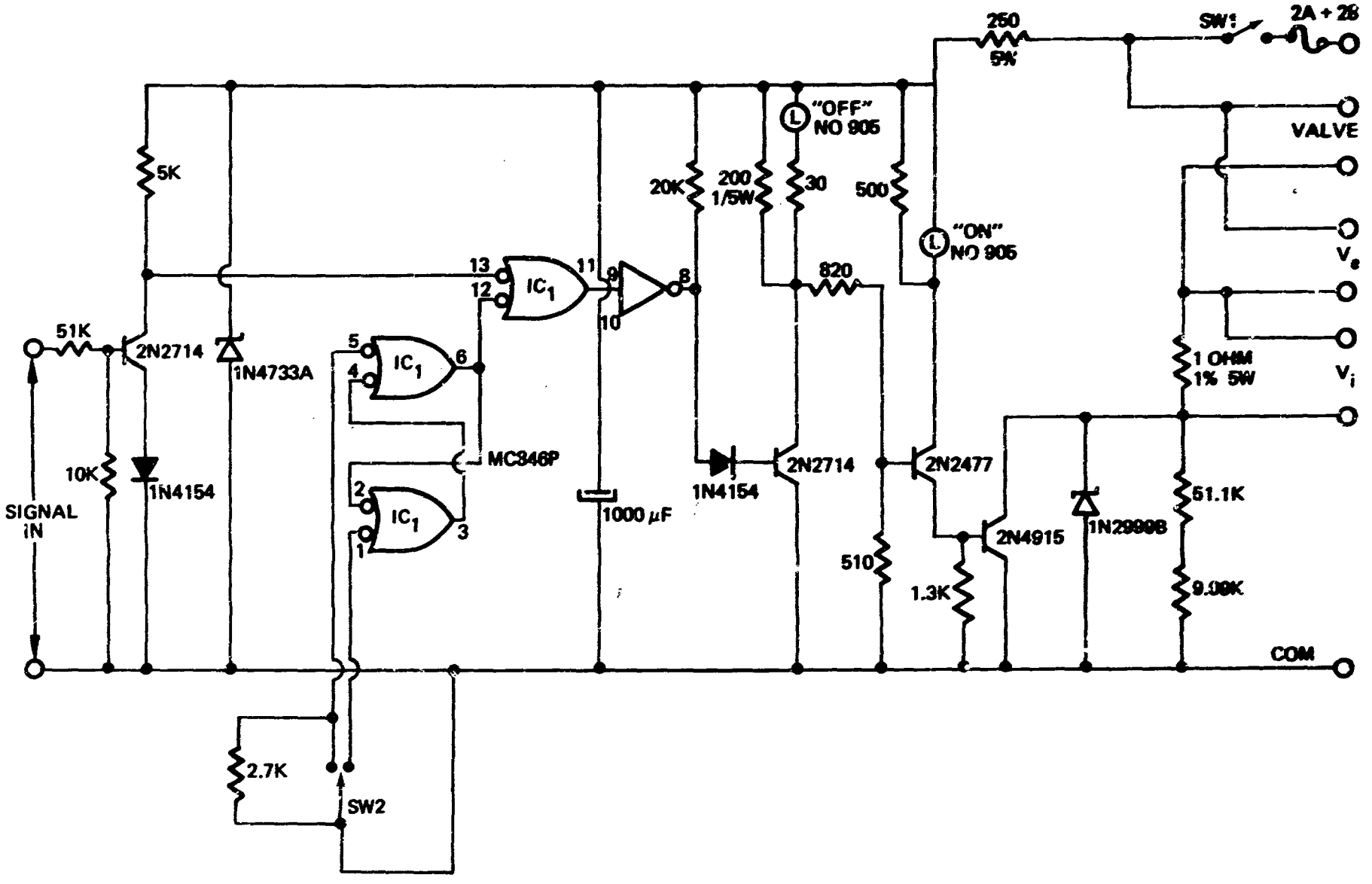

11024-51

Figure 53. Thrust Chamber Valve Driver/Suppression Circuit
Rocket Research Corporation

Table XLI. Abbreviated Life Test Duty Cycle

BASE POINT DUTY CYCLE (BL)

Subsequence No.	On Time ms	Off Time ms	Number of Pulses	Catalyst Bed Start Temperature	Frequency
a	20	980	100	65°F	1 cps
b	20	480	100	–	2 cps
c	50	950	100	–	1 cps
d	50	450	100	–	2 cps
e	100	900	100	–	1 cps
f	150	850	100	–	1 cps
g	10,000	–	1	–	Steady state

DUTY CYCLE A

Sequence No.	On Time ms	Off Time ms	Number of Pulses	Frequency
a	20	980	1,200	1 cps
b	20	480	3,200	2 cps
c	50	950	1,300	1 cps
d	50	450	1,300	2 cps
e	100	900	1,800	1 cps
f	150	850	1,200	1 cps
g	60,000	–	1	Steady state

DUTY CYCLE C

a	50	450	27,000	2 cps

Table XLI. Abbreviated Life Test Duty Cycle (Continued)

Sequence No.	Duty Cycle	Propellant and Shroud Temperature °F	40°F Catalyst Bed Start on Subsequence No.	Feed Pressure psia
4-1	BL	65	None	100
4-2	BL	65	None	225
4-3	BL	65	None	350
4-4	A	40	a	100
4-5	BL	65	None	100
4-6	BL	65	None	225
4-7	BL	65	None	350
4-8	C	40	a	100
4-9	C	40	a	225
4-10	C	40	a	350
4-11	A	40	a	225
4-12	BL	65	None	100
4-13	BL	65	None	225
4-14	BL	65	None	350
4-15	A	40	None	350
4-16	A	40	c	100
4-17	A	40	None	225
4-18	A	40	c	350
4-19	A	40	None	100
4-20	A	40	c	225
4-21	A	40	None	350
4-22	A	40	b	100
4-23	A	40	None	225
4-24	A	40	a	350
4-25	A	40	None	100
4-26	A	40	None	225
4-27	A	40	g	350
4-28	A	40	None	100
4-29	A	40	b	225
4-30	BL	65	None	100
4-31	BL	65	None	225
4-32	BL	65	None	350
4-33	A	40	None	350
4-34	A	40	e	100
4-35	A	40	None	225
4-36	A	50	b	350
4-37	A	40	None	100

Table XLI. Abbreviated Life Test Duty Cycle (Continued)

Sequence No.	Duty Cycle	Propellant and Shroud Temperature °F	40°F Catalyst Bed Start on Subsequence No.	Feed Pressure psia
4-38	A	40	e	225
4-39	A	40	None	350
4-40	A	40	f	100
4-41	A	40	g	225
4-42	A	40	None	350
4-43	A	40	None	100
4-44	A	40	f	225
4-45	A	40	None	350
4-46	A	40	g	100
4-47	A	40	None	225
4-48	A	40	e	350
4-49	A	40	None	100
4-50	A	40	None	225
4-51	A	40	None	350
4-52	A	40	a	100
4-53	A	40	None	225
4-54	A	40	f	350
4-55	A	40	None	100
4-56	A	40	None	225
4-57	A	40	None	350
4-58	BL	65	None	100
4-59	BL	65	None	225
4-60	BL	65	None	350
4-61	A	40	None	100
4-62	A	40	a	225
4-63	A	40	None	350
4-64	A	40	c	100
4-65	A	40	None	225
4-66	A	40	a	350
4-67	A	40	None	100
4-68	A	40	None	225
4-69	A	40	None	350
4-70	A	40	f	100
4-71	A	40	None	225
4-72	A	40	c	350
4-73	A	40	None	100
4-74	A	40	None	225
4-75	A	40	None	350
4-76	A	40	None	100
4-77	A	40	None	225

Table XLI. Abbreviated Life Test Duty Cycle (Concluded)

Sequence No.	Duty Cycle	Propellant and Shroud Temperature °F	40°F Catalyst Bed Start on Subsequence No.	Feed Pressure psia
4-78	A	40	g	350
4-79	A	40	None	100
4-80	A	40	c	225
4-81	A	40	None	350
4-82	A	40	b	100
4-83	A	40	None	225
4-84	A	40	b	350
4-85	A	40	None	100
4-86	BL	65	None	100
4-87	BL	65	None	225
4-88	BL	65	None	350
4-89	A	40	f	225
4-90	A	40	None	350
4-91	A	40	e	100
4-92	A	40	None	225
4-93	A	40	g	225
4-94	A	40	None	100
4-95	A	40	e	225
4-96	A	40	None	350
4-97	A	40	a	100
4-98	A	40	None	225
4-99	A	40	e	350
4-100	A	40	None	100
4-101	A	40	None	225
4-102	A	40	f	350
4-103	C	40	a	100
4-104	C	40	a	225
4-105	C	40	a	350
4-106	A	40	b	100
4-107	A	40	b	225
4-108	BL	65	None	100
4-109	BL	65	None	225
4-110	BL	65	None	350

NOTE: All 40°F catalyst bed temperature starts are preceded by a 12 hour (minimum) cool down.

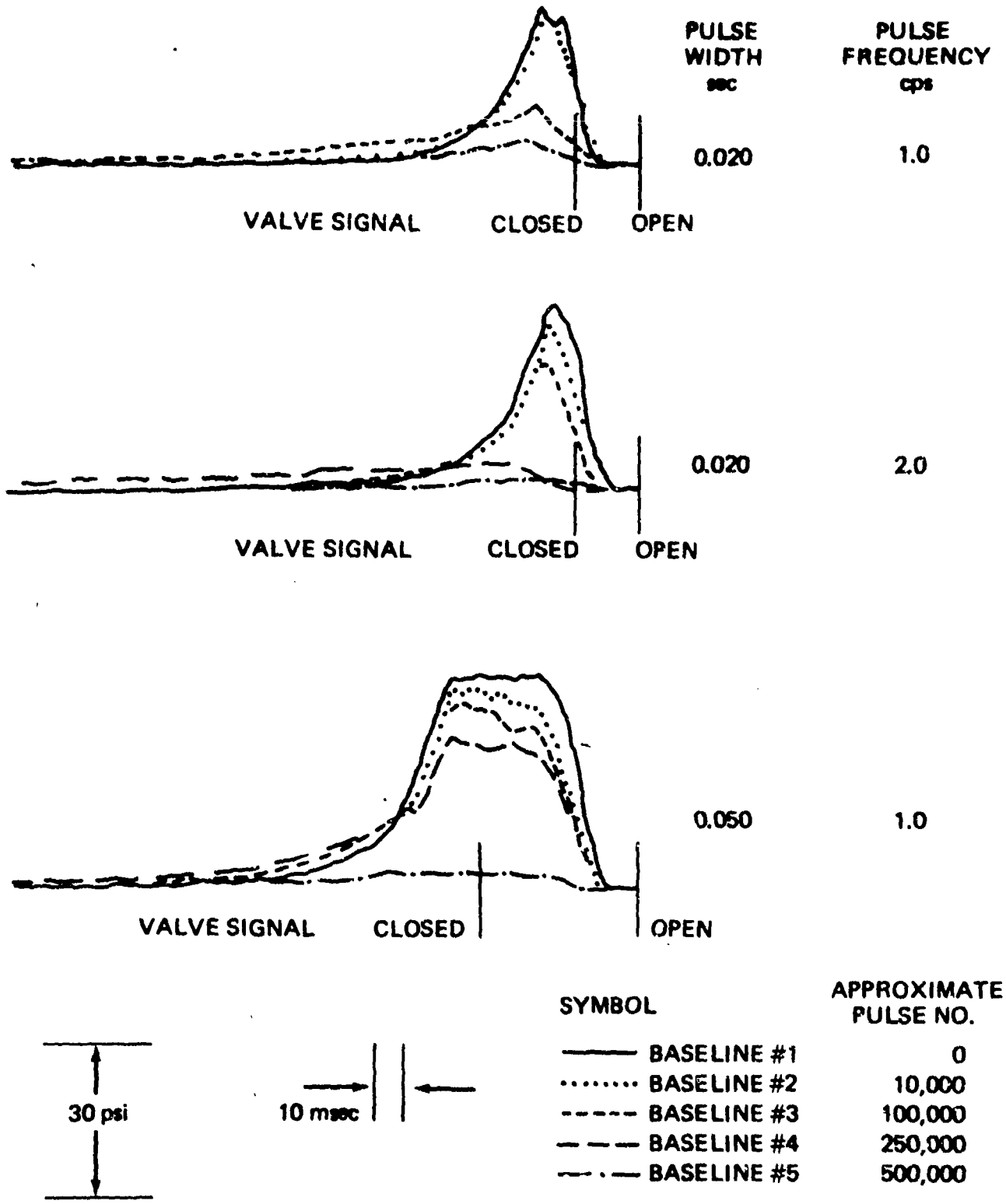

Figure 54. Phase 1A Long-Life Test Results

Oscillograph Chamber Pressure Tracings -- Feed Pressure 100 psia

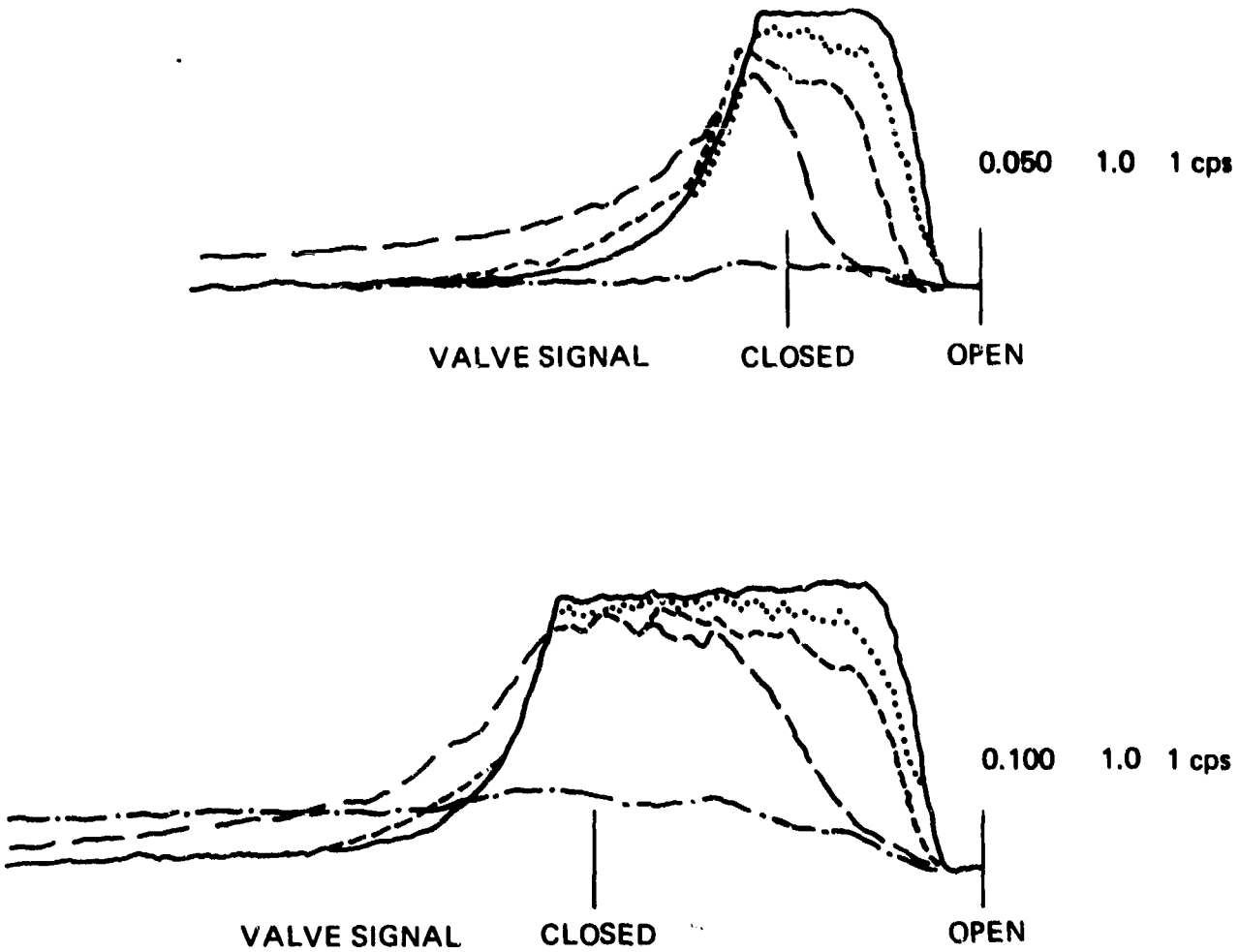

Figure 54. Phase 1A Long-Life Test Results
Oscillograph Chamber Pressure Tracings — Feed Pressure 100 psia (Continued)

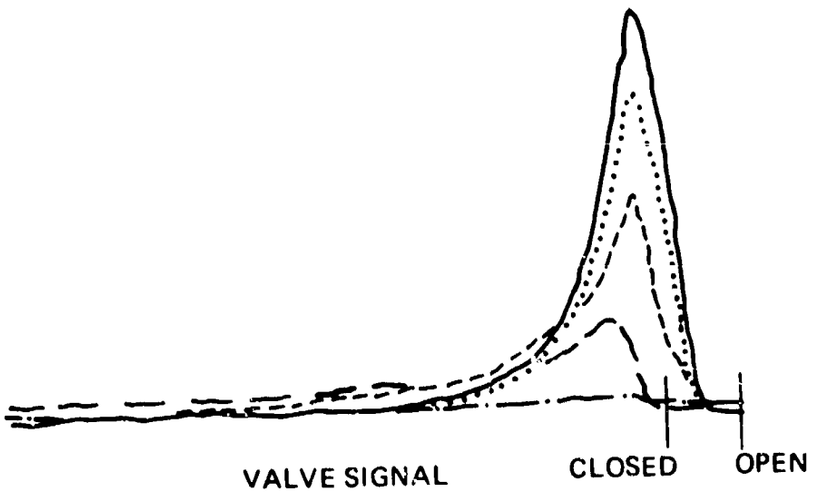

0.020 1.0

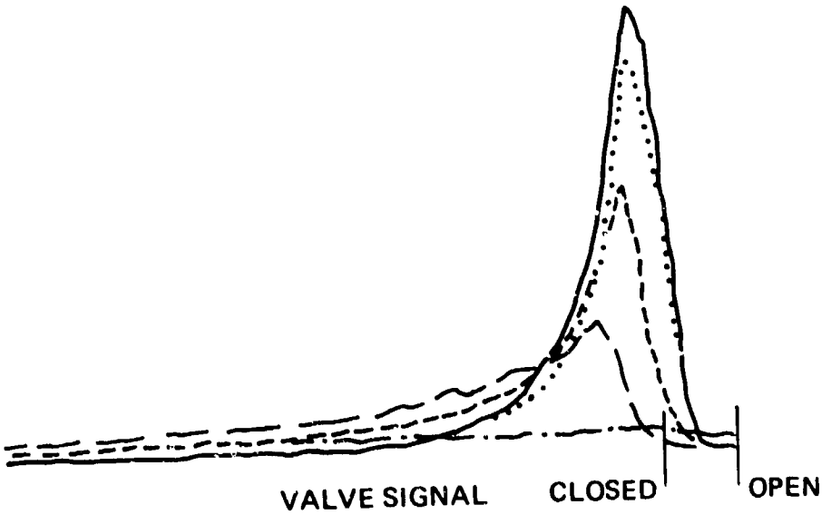

0.020 2.0

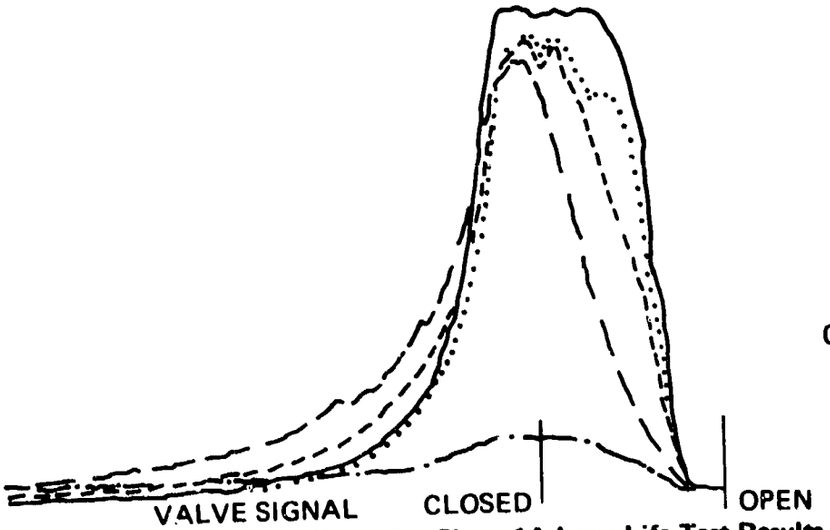

0.050 1.0

Figure 54. Phase 1A Long-Life Test Results
Oscillograph Chamber Pressure Tracings — Feed Pressure 225 psia (Continued)

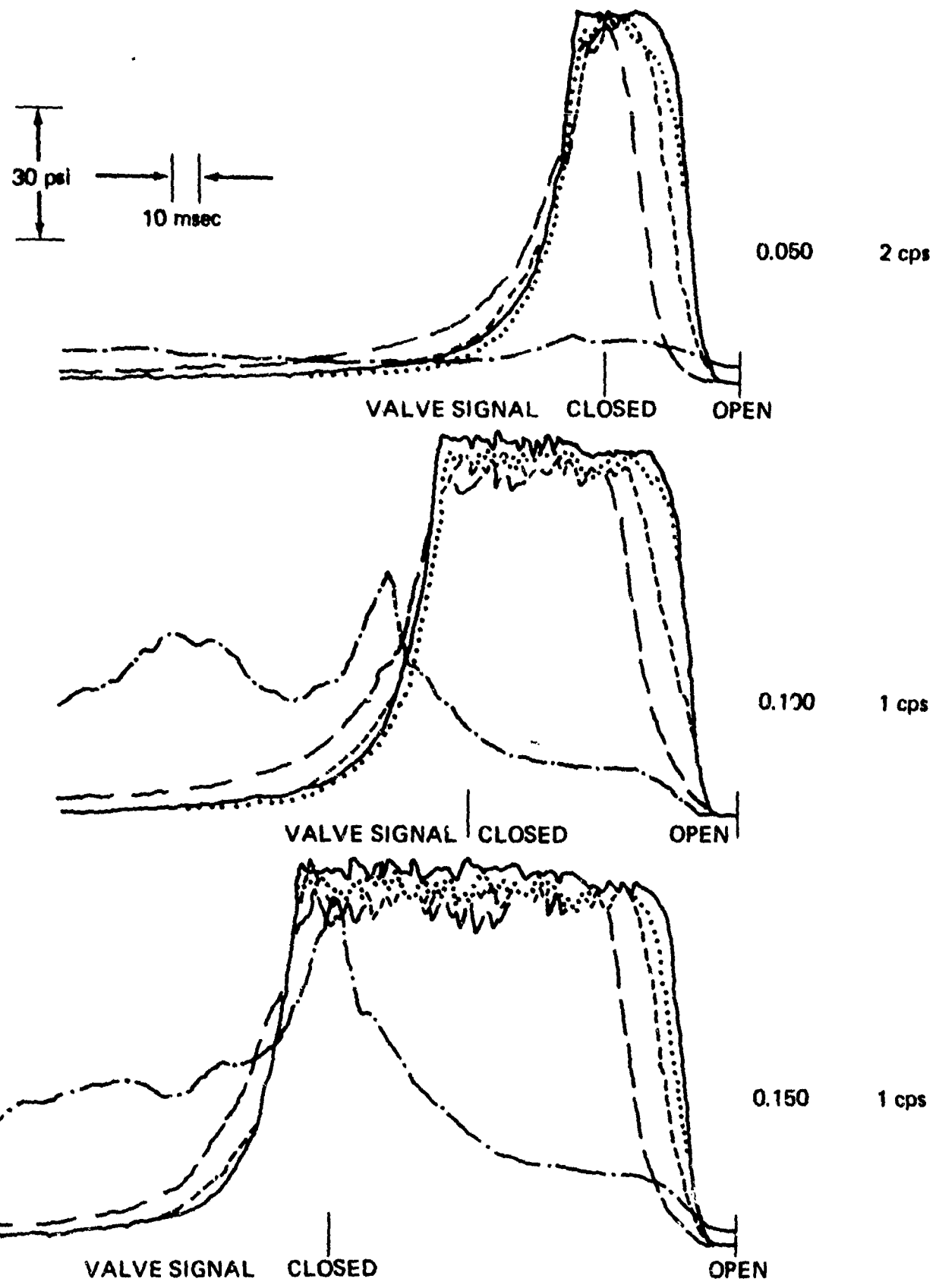

Figure 54. Phase 1A Long-Life Test Results
Oscillograph Chamber Pressure Tracings — Feed Pressure 225 psia (Continued)

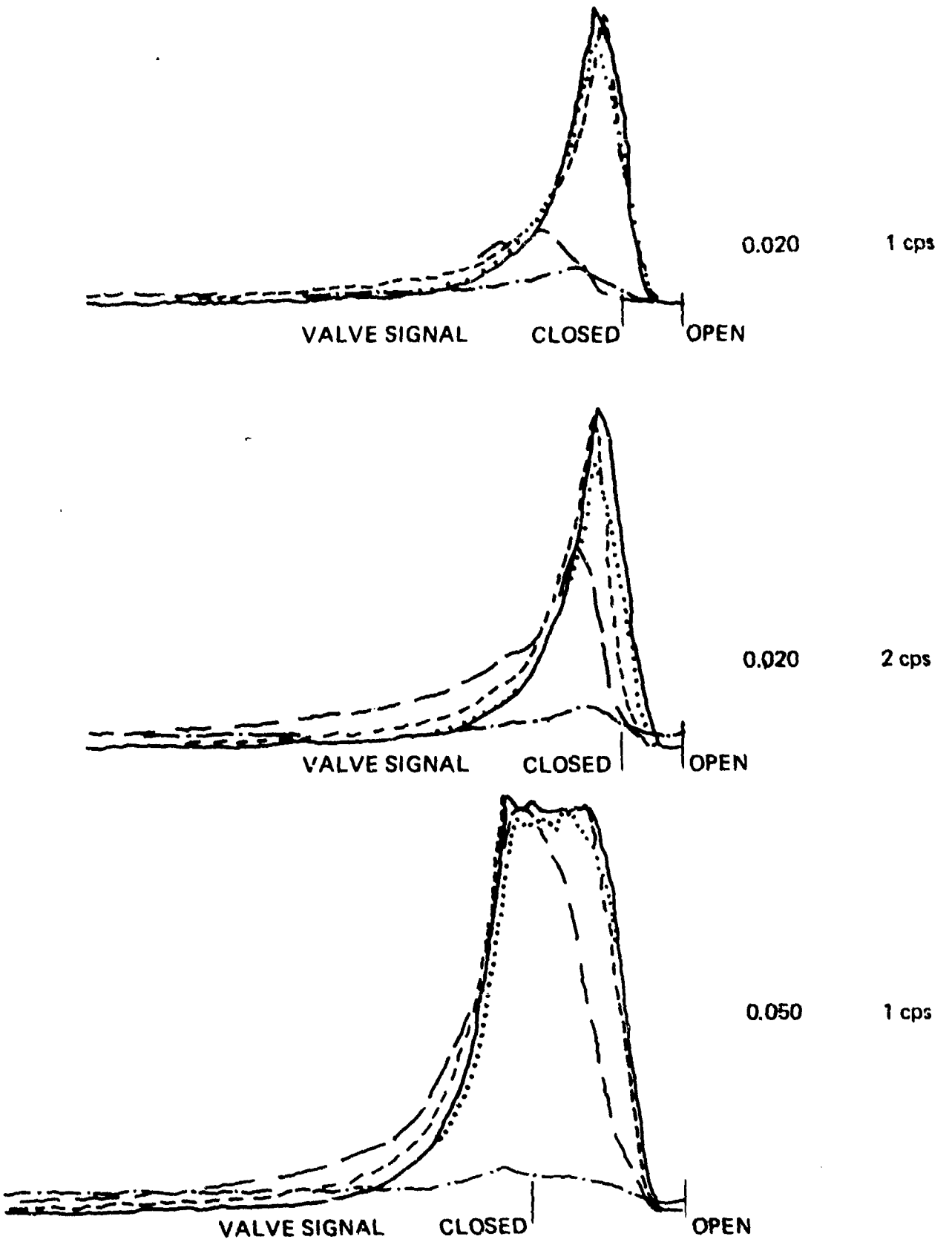

Figure 54. Phase 1A Long-Life Test Results
Oscillograph Chamber Pressure Tracings – Feed Pressure 350 psia (Continued)

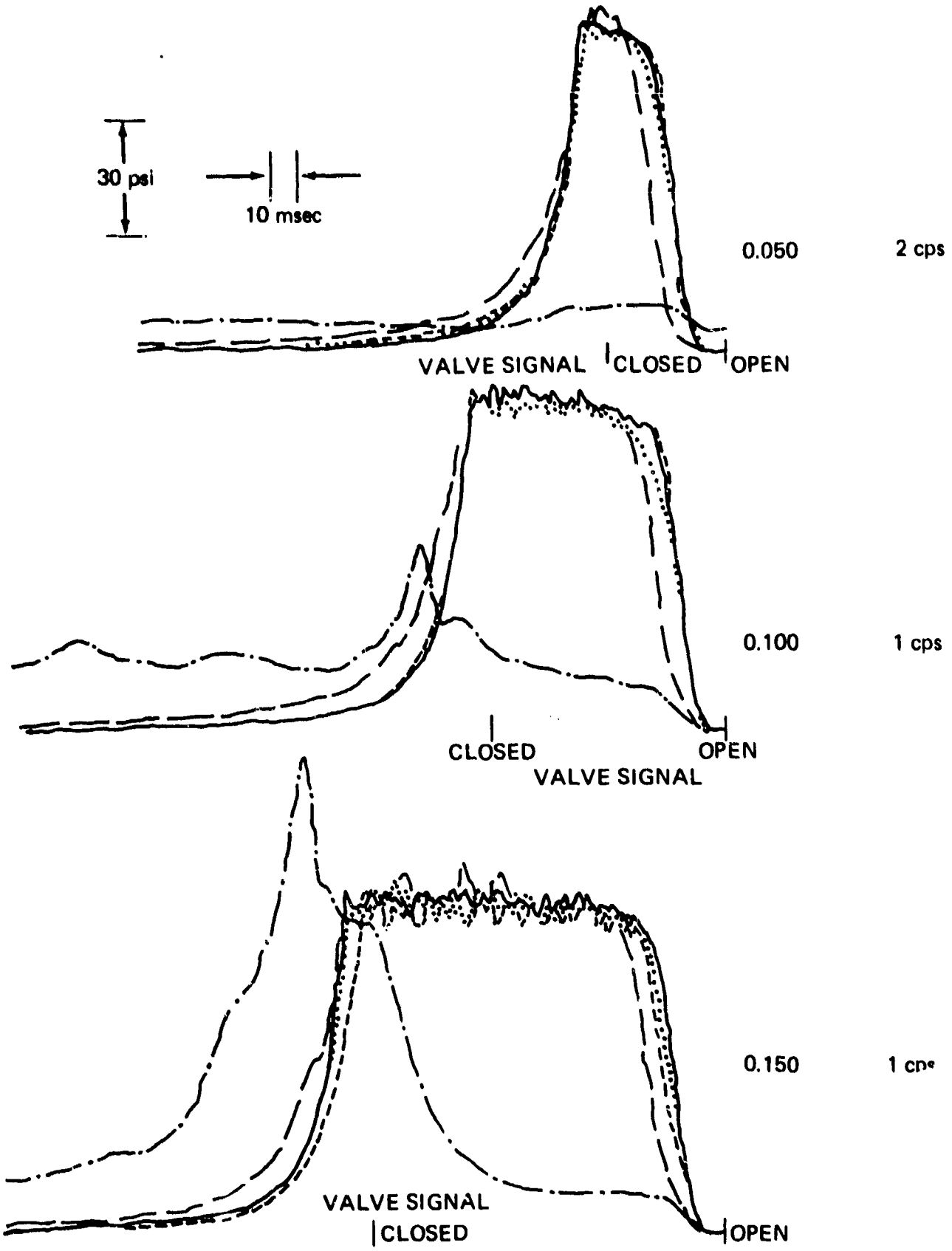

Figure 54. Phase 1A Long-Life Test Results
Oscillograph Chamber Pressure Tracings – Feed Pressure 350 psia (Concluded)

Table XLII. Impulse Bit and Spread

P_f psia	On/Off Time sec	Baseline No. 1		Baseline No. 2		Baseline No. 3		Baseline No. 4		Baseline No. 5	
100	0.020/.980	N/A	NA	0.03803	2.6%	0.04179	3.7%	0.03240	7.9%	0.02365	8.3%
100	0.020/.480	0.05062	1.4%	0.04479	2.3%	0.04093	1.9%	0.03468	2.3%	0.00539	43.7%
100	0.050/.950	0.12313	0.6%	0.11276	1.1%	0.10667	1.5%	0.09322	1.4%	0.02861	39.5%
100	0.050/.450	0.12637	0.4%	0.11440	0.6%	0.10867	1.1%	0.10577	2.0%	0.01630	74.9%
100	0.100/.900	0.22652	0.6%	0.21025	0.9%	0.20008	1.0%	0.19784	0.9%	0.11558	20.0%
100	0.150/.850	0.33413	0.5%	0.31132	0.3%	0.29929	0.5%	0.28563	0.7%	0.15676	30.2%
225	0.020/.930	0.08436	0.9%	NA	NA	0.07631	3.7%	0.07234	2.9%	0.00197	55.4%
225	0.020/.480	0.09673	0.4%	NA	NA	0.08157	1.0%	0.07388	2.5%	0.00111	41.3%
225	0.050/.950	0.23166	0.1%	NA	NA	0.21525	0.7%	0.19742	1.4%	0.12066	23.5%
225	0.050/.450	0.23144	1.4%	NA	NA	0.21378	0.7%	0.18221	1.4%	0.03820	82.9%
225	0.100/.900	0.44895	0.4%	NA	NA	0.41399	0.3%	0.36321	0.4%	0.24268	21.3%
225	0.150/.850	0.67156	0.2%	NA	NA	0.62770	0.3%	0.53599	0.5%	0.37878	5.8%
350	0.020/.980	0.07589	3.9%	NA	NA	0.08101	5.9%	0.06334	3.5%	0.03671	11.4%
350	0.020/.480	0.09448	2.1%	NA	NA	0.08818	6.6%	0.09399	3.3%	0.01893	26.7%
350	0.050/.950	0.23613	1.2%	NA	NA	0.28374	0.5%	0.24718	0.9%	0.13052	25.5%
350	0.050/.450	0.23052	0.9%	NA	NA	0.27870	0.4%	0.20208	4.0%	0.06327	70.7%
350	0.100/.900	0.45565	0.4%	NA	NA	0.44879	2.0%	0.40744	5.4%	0.29189	2.9%
350	0.150/.850	0.68541	0.4%	NA	NA	0.68859	3.2%	0.60396	2.3%	0.46485	3.6%
Approximate Pulse Number		Initial		10,000		100,000		250,000		500,000	

Table XLV summarizes the start transients for each of the twenty-two 40°F catalyst bed start conditions. The minimum hold time preceding each cold start was 12 hours and as shown on Table XLV, no excessive chamber pressure spikes resulted. Both ignition delay and peak chamber pressure are in excellent agreement with the Phase I results on REA S/N 6 reported in paragraph 2.3.5 *(REA S/N 6)*.

2.5.2 Teardown and Inspection

Following removal from the altitude chamber, REA S/N 007 was oven purged for 1 hour with heated (190°F) GN_2 at 5 psig and vacuum dried for 1 hour. An internal leak check of the REA was conducted with no GN_2 leakage recorded over a 5-minute test period at inlet pressures of 10,85 and 285 psig. Two X-rays of the REA 90 degrees apart revealed a catalyst void in the upper bed of approximately 40%. These X-rays further showed that the rigimesh injection element was detached from the injector face. The REA was disassembled and the catalyst weighed. Weight loss in the upper catalyst bed was 32.7% (2.19 grams) and a weight gain of 4.3% was recorded for the lower bed. This weight gain (0.72 gram) was undoubtedly catalyst which had migrated from the upper catalyst bed, through broken screens on the intermediate bed plate. The resultant overall net weight loss for the entire engine was 6.3% (1.47 grams).

Table XLIII. Centroid and I_{sp}

P_f psia	On/Off Time sec	Baseline No. 1		Baseline No. 2		Baseline No. 3		Baseline No. 4		Baseline No. 5	
100	0.020/0.980			0.034	137.8	0.077	119.8	0.224	104.5	0.154	80.7
100	0.020/0.480	0.031	173.3	0.033	177.0	0.037	169.1	0.124	116.4	0.055	19.2
100	0.050/0.950	0.046	209.8	0.048	206.1	0.052	202.4	0.056	184.2	0.249	50.1
100	0.050/0.450	0.046	222.9	0.048	224.3	0.051	217.8	0.086	173.1	0.095	33.1
100	0.100/0.900	0.070	206.1	0.073	209.6	0.079	203.1	0.105	186.8	0.281	121.7
100	0.150/0.850	0.096	209.9	0.099	212.7	0.106	211.1	0.130	189.2	0.307	121.5
225	0.020/0.980	0.030	167.7			0.049	169.6	0.133	151.3	0.049	3.1
225	0.020/0.480	0.030	196.6			0.044	186.2	0.085	145.7	0.034	2.7
225	0.050/0.950	0.045	217.9			0.051	221.9	0.063	193.0	0.306	121.0
225	0.050/0.450	0.047	220.4			0.052	223.2	0.061	180.6	0.162	41.9
225	0.100/0.900	0.072	216.3			0.077	219.7	0.088	196.1	0.272	129.8
225	0.150/0.850	0.098	254.1			0.103	230.0	0.112	199.3	0.191	156.0
350	0.020/0.980	0.031	198.1			0.047	169.1	0.148	140.4	0.164	78.6
350	0.020/0.480	0.030	246.7			0.043	178.3	0.064	168.7	0.093	43.1
350	0.050/0.950	0.045	223.6			0.049	225.0	0.057	192.4	0.297	124.2
350	0.050/0.450	0.047	225.8			0.049	223.1	0.059	185.9	0.193	61.9
350	0.100/0.900	0.073	226.6			0.077	218.2	0.086	193.1	0.228	142.2
350	0.150/0.850	0.099	227.5			0.100	220.2	0.110	199.5	0.183	158.8

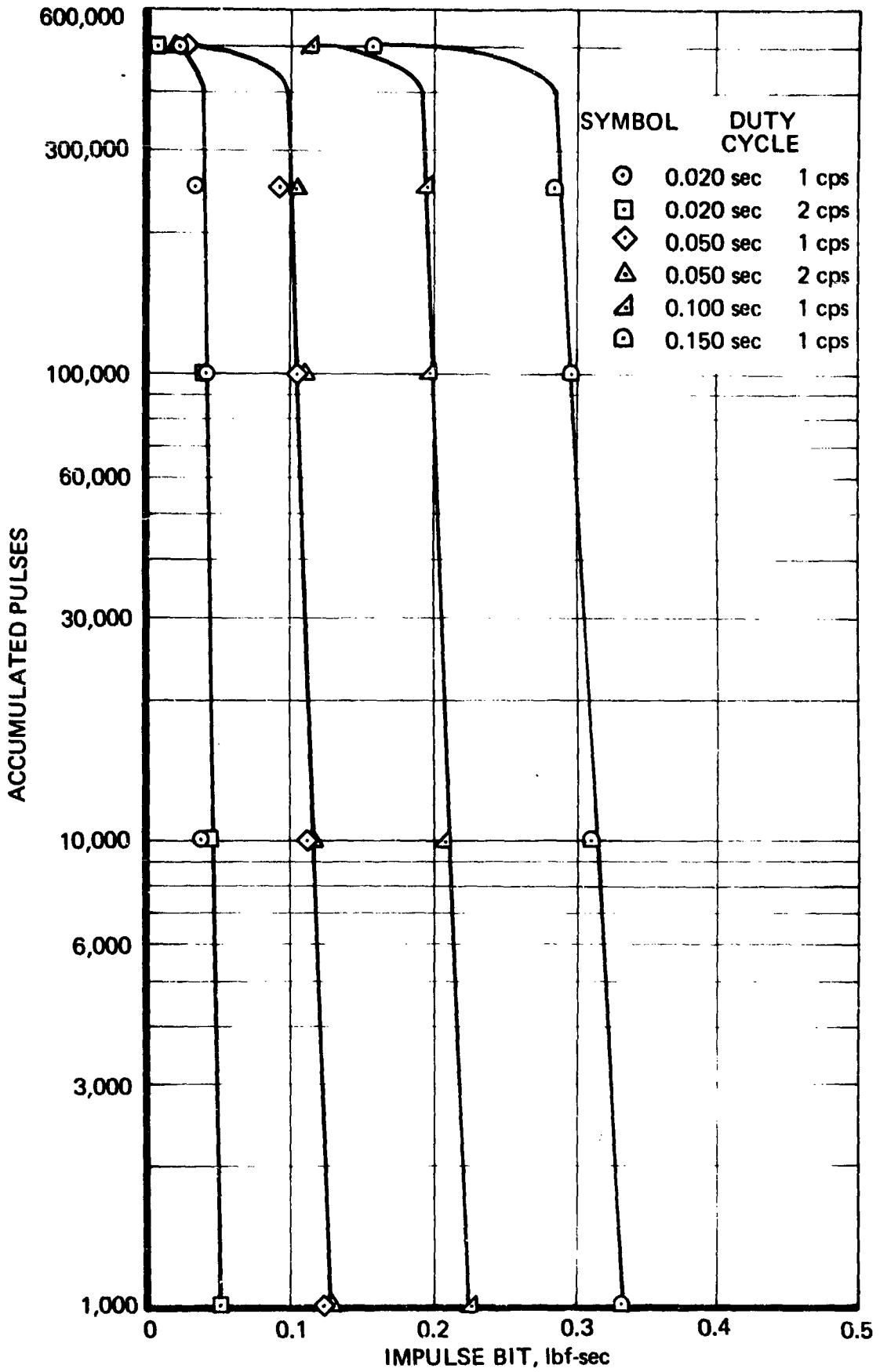

Figure 55. Life Test REA S/N 7 Pulse-Mode Performance at P_{feed} = 100 psia

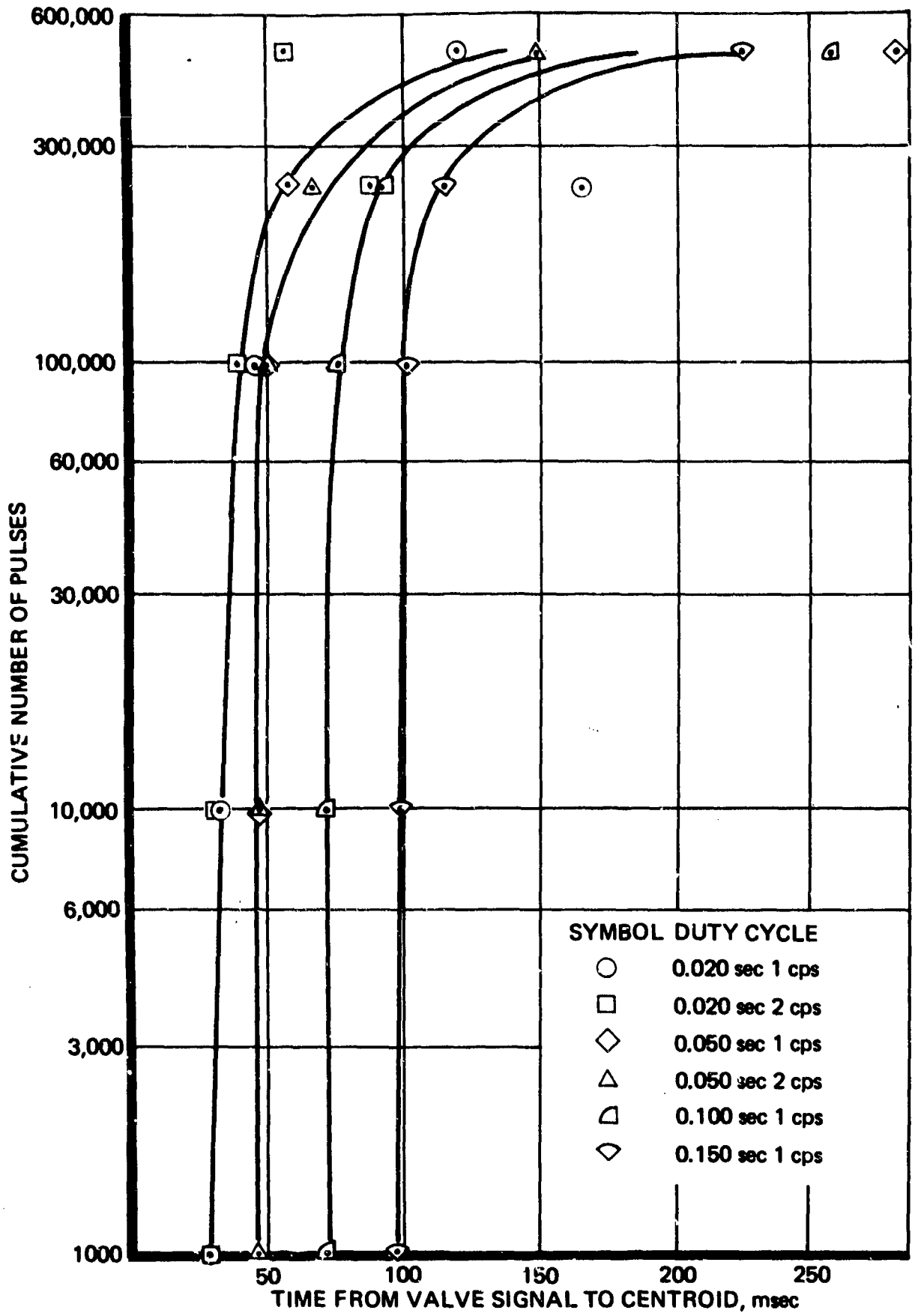

Figure 56. Baseline Centroid as a Function of Cummulative Pulse.

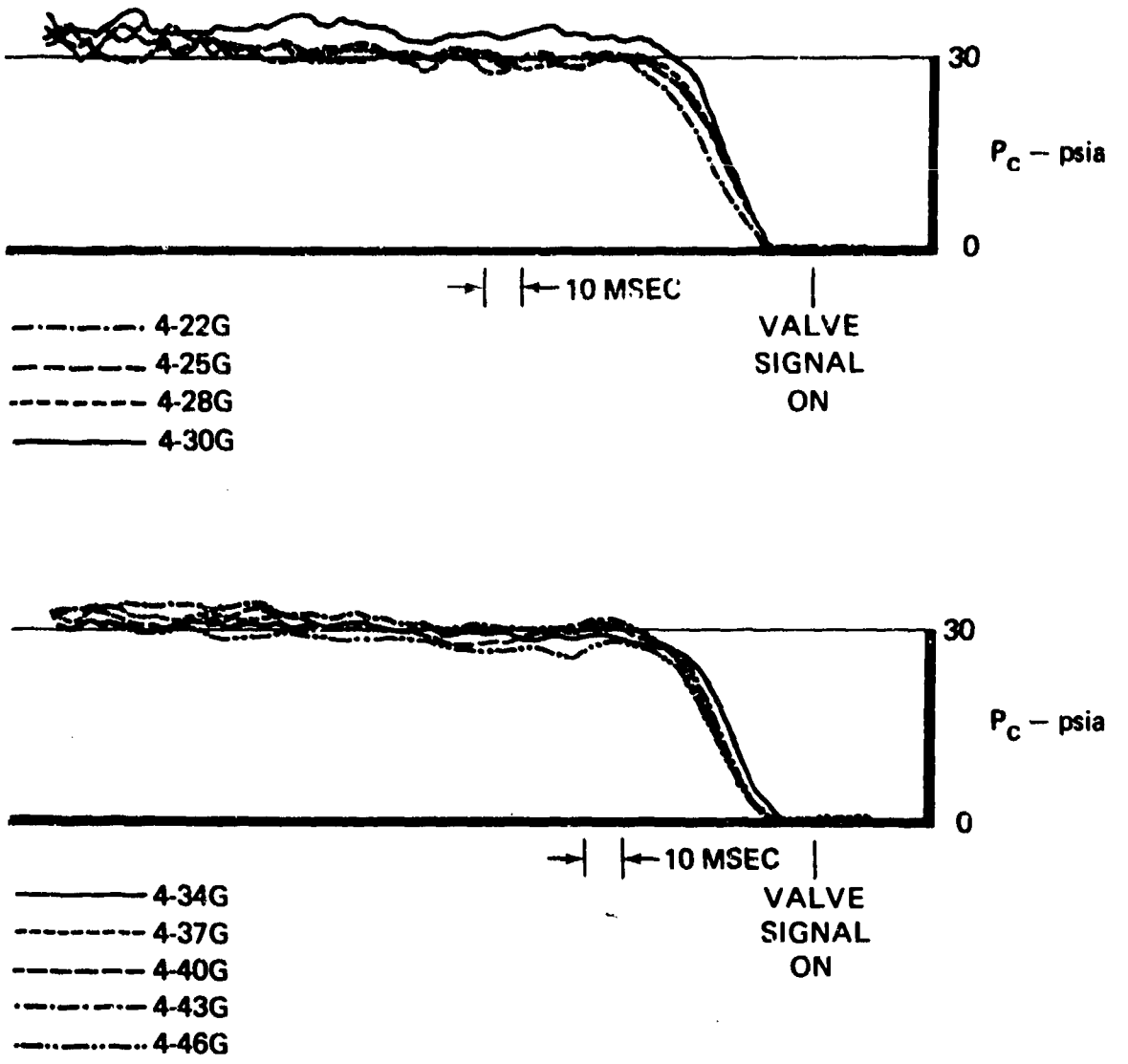

Figure 57. Phase 1A Long-Life Test Results Steady-State Chamber Pressure Start Transient Feed Pressure 100 psia

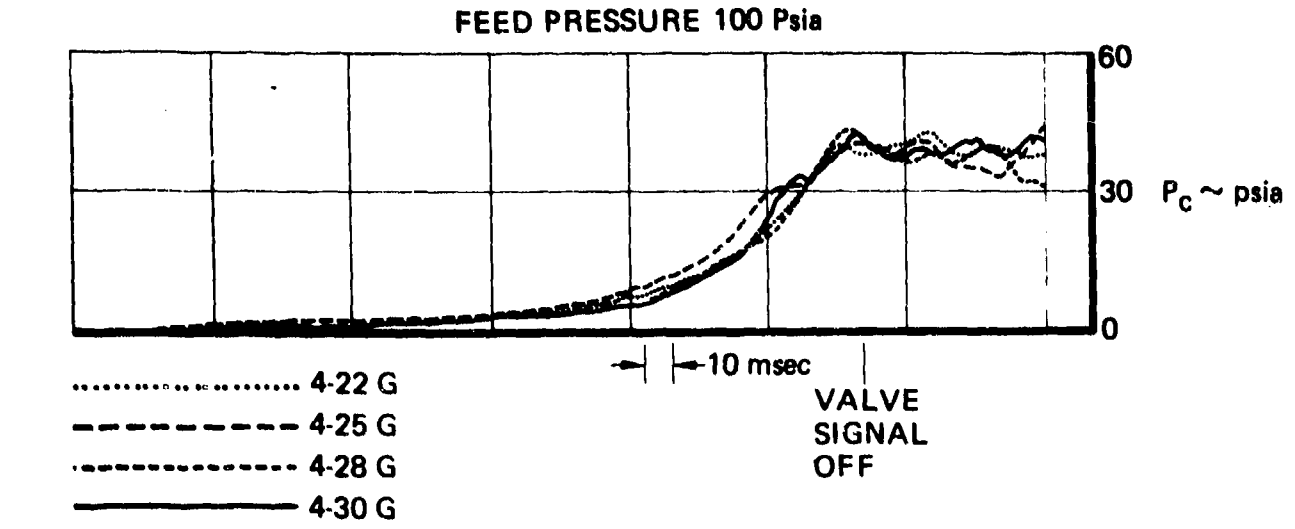

Figure 58. Phase 1A Long-Life Test Results Steady-State Chamber Pressure Shutdown Transient

Table XLIV. Phase IA Long Life Test Results Baseline Steady State Data (Burn Time 10.0 Sec)

Baseline Number	Feed Pressure psia	Thrust lbf	Roughness %	Isp lbf-sec/lbm	Ignition Delay msec	Response to 90% Pc msec	Decay to 10% Pc msec
1	100	2.13	2.5	208.3	9	23	46
2	100	2.29	7.3	215.0	8	40	47
3	100	2.10	11.3	212.0	10	40	70
4	100	2.07	10.3	222.6	10	43	97
5	100	1.18	32.6	112.6	12	446	NA
		2.05 ± 27.1%					
		*2.15 ± 5.1%					
1	225	3.49	3.2	218.5	7	28	46
2	225	3.73	7.7	227.1	10	29	44
3	225	3.60	8.9	215.4	8	28	48
4	225	4.25	13.7	231.0	10	135	61
5	225	1.75	42.9	137.7	10	140	200
		3.36 ± 37.2%					
		*3.77 ± 10.1%					
1	350	4.70	4.7	224.2	8	94	44
2	350	4.66	7.1	228.8	9	63	45
3	350	4.67	9.1	NA	9	30	43
4	350	4.82	10.9	222.3	10	138	60
5	350	3.82	42.0	209.9	11	180	161
		4.53 ± 11.0%					
		*4.71 ± 1.7%					

*Excluding baseline No. 5

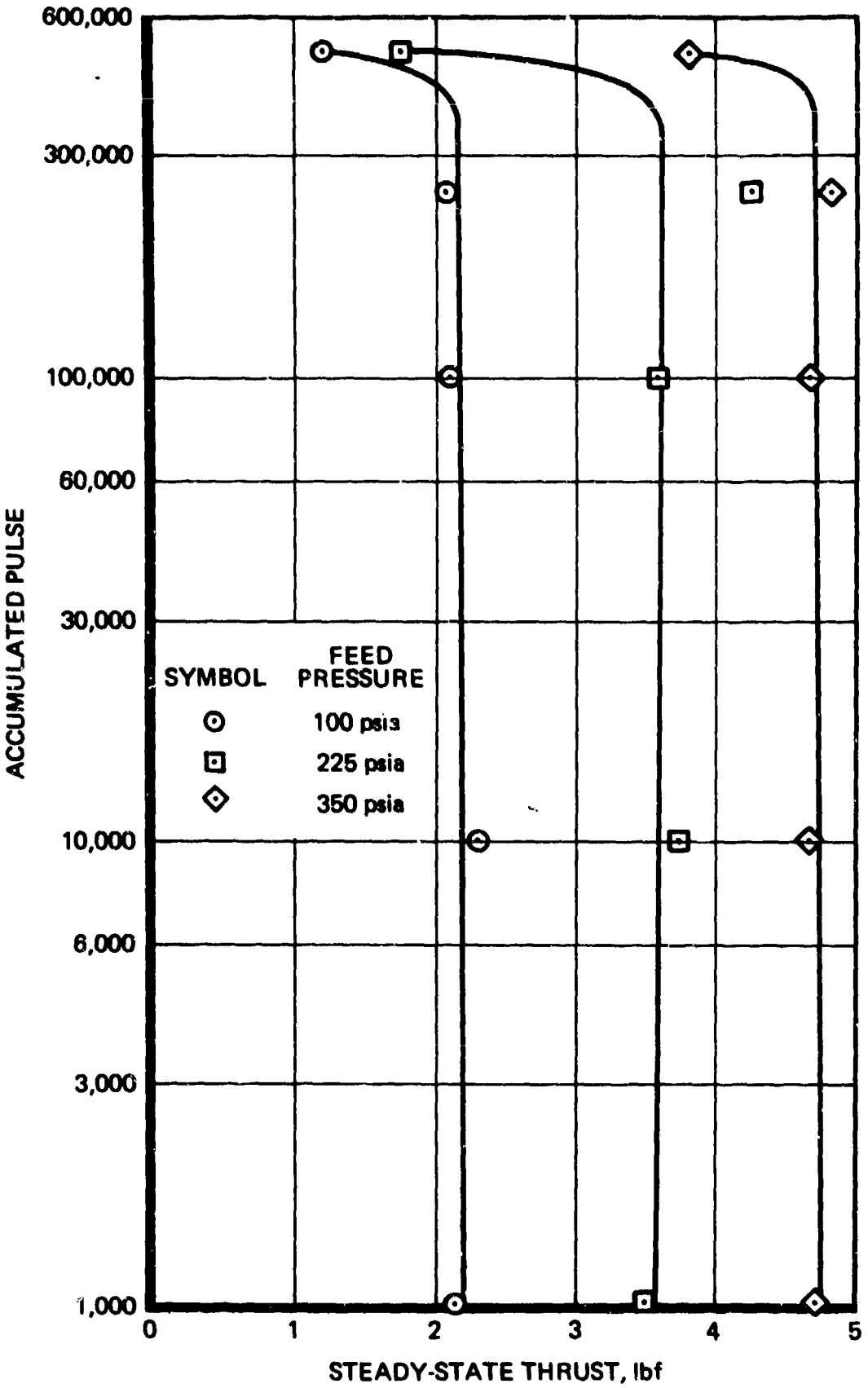

Figure 59. Life Cycle Test REA S/N 7 Steady-State Thrust as a Function of Cumulative Pulses

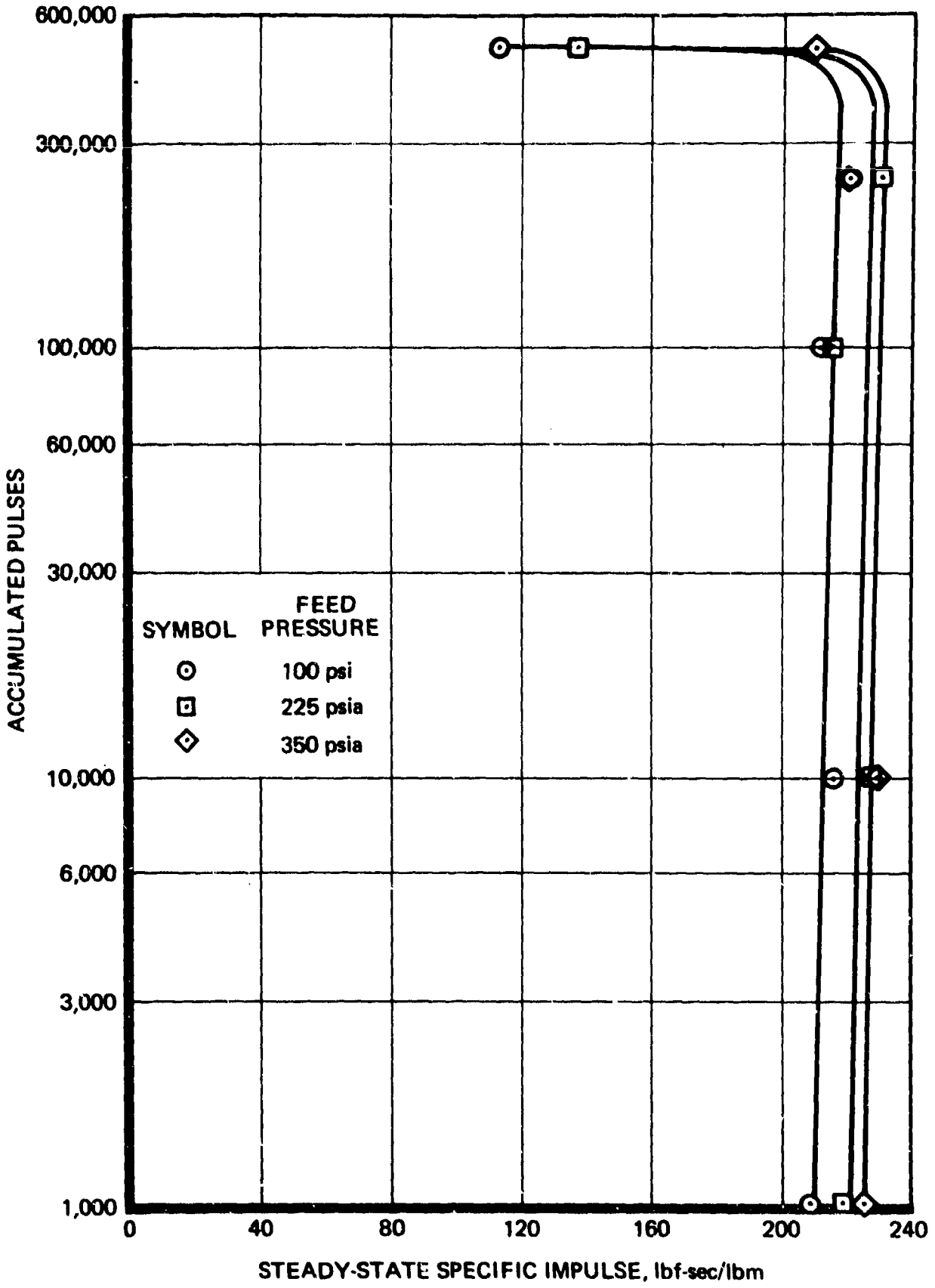

Figure 60. Life Test REA S/N 7 Steady-State Specific Impulse as a Function of Cumulative Pulses

Table XLV. Phase IA Long Life Test Results Cold Start Ignition Data
(Catalyst Bed = 40°F, Propellant = 40°F)

Sequence Number	Date	Time	Feed Pressure psia	Duty Cycle On/Off Time sec/sec	Ignition Delay msec	Peak Chamber Pressure psia
4-4a	2/17	0210	100	0.020/.980	70	9.0
4-8a	2/18	1555	100	0.050/.450	62	29.4
4-9a	2/19	0830	225	0.050/.450	57	62.7
4-10a	2/22	1131	350	0.050/.450	25	46.5
4-11a	2/23	0429	225	0.020/.980	75	6.0
4-16c	2/25	1409	100	0.050/.950	66	16.5
4-18c	2/26	0909	350	0.050/.950	63	38.4
4-20c	3/1	0210	225	0.050/.950	35	25.5
4-22b	3/1	2021	100	0.020/.480	75	3.0
4-24a	3/2	1729	350	0.020/.980	57	16.2
4-27g	3/3	2107	350	s.s	70	106.2
4-29b	3/4	1339	225	0.020/.480	68	11.0
4-34e	3/8	0250	100	0.100/.900	43	21.0
4-36b	3/8	2012	350	0.020/.480	55	21.6
4-38e	3/9	1900	225	0.100/.900	NA	NA
4-40f	3/10	1819	100	0.150/.850	78	35.4
4-41g	3/11	1435	225	s.s	58	77.7
4-44f	3/12	1339	225	0.150/.850	60	57.8
4-46g	3/15	0334	100	s.s	48	29.6
4-48e	3/15	2324	350	0.100/.900	NA	NA
4-52a	3/16	2112	100	0.020/.980	71	2.5
4-54f	3/17	1947	350	0.150/.850	176	148.0

Metallographic examination of all screens in the catalyst bed are summarized on Table XLVI. It is postulated that the intermediate bed plate upstream screen was exposed to extremely severe nitriding environment following the injector failure, resulting in the complete nitridation noted. The relatively negligible nitriding depth measured at the edges of the intermediate bed plate is consistent with that found throughout after normal REA operation.

Figure 61 shows the downstream face of the injector following disassembly at seven X magnification. Detailed examination reveals extensive cracking over the complete propellant flow surface. Figure 62 is a photograph of the injector body following sectioning, the cracks shown in Figure 61 are sectioned in this view and considerable additional cracking is shown throughout the body. Figure 63 is a photomicrograph of one of these cracks in the vicinity of the rigimesh weld

Table XLVI. REA S/N 007 Metallographic Screen Analysis

Position	Material	Depth of Nitrided Layer	
		At Edge	At Center
Intermediate bed plate–upstream	50-mesh Haynes 25 0.009-inch diameter wire	0.0013 inch	Complete
Intermediate bed plate–downstream	60-mesh Haynes 25 0.007-inch diameter wire	0.0014 inch	Complete
Lower bed plate	60-mesh Haynes 26 0.007-inch diameter wire	0.0006 inch	0.0010 inch

preparation at 50 X magnification. A gray, classical nitride layer is shown over the complete crack. If the crack were due to nitriding, the layer would be significantly thicker at the base of the crack rather than the more uniform (surface area dependent) layer shown. The conclusion, therefore, is that the nitriding progressed down the crack following its failure, and the crack itself is the result of thermal fatigue. Further examples of this classical type thermal fatigue crack are presented in Reference 4.

The separation plane between the rigimesh injection element and the injector face is composed of both weld material and parent injector body material. The nitride layer on these planes is very similar to that shown in Figure 62 and the failure mechanism is considered to be thermal fatigue. During testing of this REA the injector was at elevated temperature in excess of 105 hours. In comparison during REM-Mono qualification (an eight-REA program), the maximum time at temperature on any single REA was 20 hours with the majority of the REA's seeing 6.5 hours.

2.5.3 REA S/N 7 Catalyst Characterization

Following the teardown and inspection, the catalyst from the Phase 1A test REA (S/N 7) was characterized. Table XLVII compares the size distribution and crush strength test results with the equivalent data from REA S/N 4 and sample REA which were subjected to the Phase I cold-start test series. This crush strength data reverses the trend indicated by the Phase I cold-start tests. The conclusion to which that data led was a definite weakening of the catalyst as a result of the cold-start spikes. Conversely REA S/N 7 catalyst meets all the requirements of the RRC Acceptance Test Procedure (MS-0110 ATP) and thus has not been weakened by its 22 cold starts or 500,000 pulses. This further confirms the changes in test procedure used on REA S/N 7 to eliminate ground effects, i.e., gas poisoning, etc.

Table XLVIII presents the hydrogen chemisorption test results compared to all applicable previous data. This table shows that the second batch of 90% attrited catalyst post RRC shrinkage data is not appreciably different from the first batch, or the average for 50% attrited. The effect of 500,000 cycles of operation is shown, however, to decrease still further the hydrogen chemisorption, i.e. metal surface area. As pointed out in paragraph 2.3.4 (*Catalyst Evaluation Test Results*), the RRC shrinkage procedure does stabilize the catalyst by minimizing the amount of surface area change

Figure 61. REA S/N 007 Injector Face Following 500,000 Cycle Test (7X Magnification)

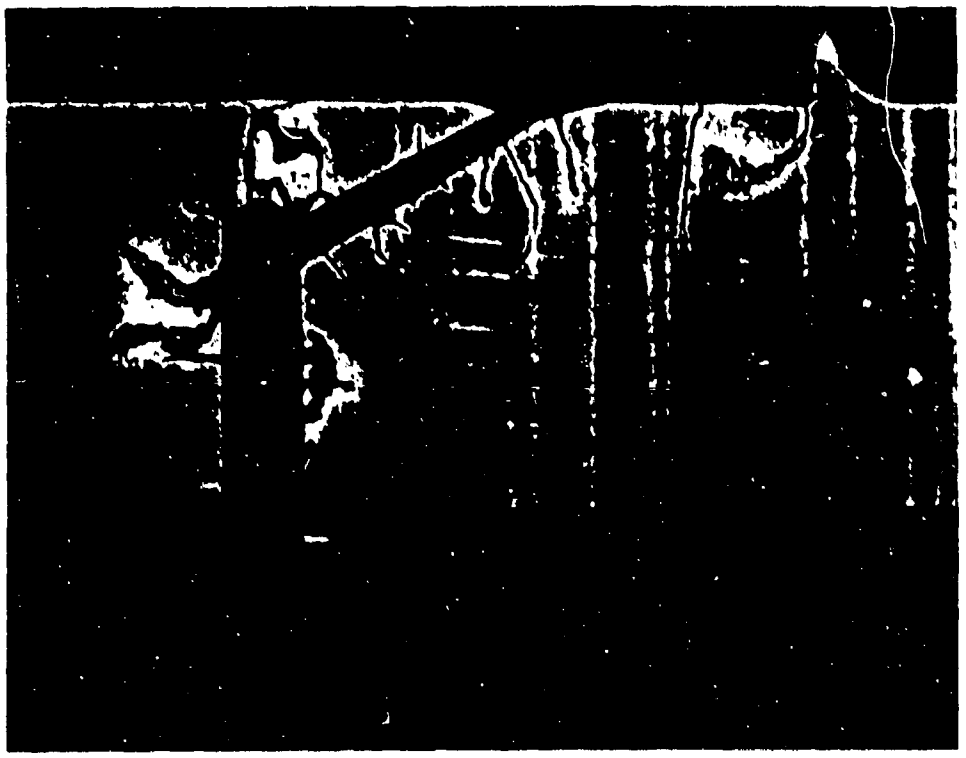

Figure 62. REA S/N 007 Post Fire Injector Body Cutaway Showing Thermal Cracks

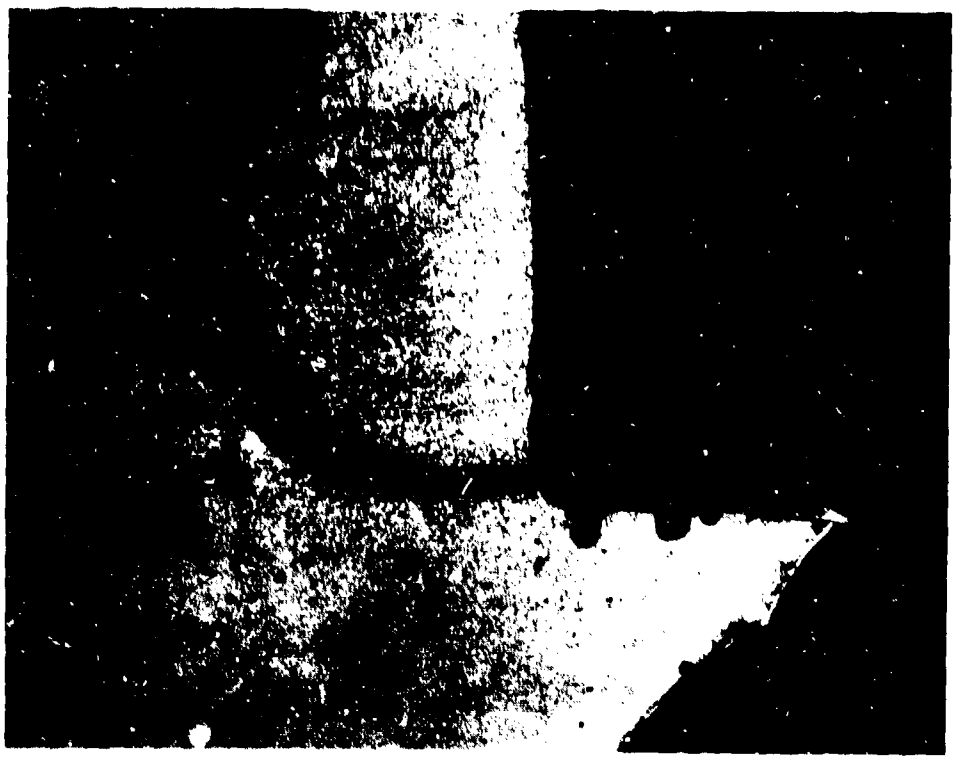

Figure 63. REA S/N 007 Post Fire Injector Body Cutaway Showing Detail of a Thermal Crack (50X Magnification)

Table XLVII. Catalyst Characterization Test Results

Size Distribution[1] 25 - 30 Mesh
% by Weight

		30 Mesh	40 Mesh	50 Mesh	Fines
Phase I Cold Start Test	Fired sample (REA S/N 4)	79.48	10.01	3.04	7.47
	Unfired sample	97.80	1.84	0.15	0.21
Phase IA life test (REA S/N 7)		70.00	16.70	5.50	7.80

Crush Strength Test Results
25 - 30 Mesh

		Dimensionless Deflection at 1000 psi	Dimensionless Recovery at 20 psi	Weight % <30 Mesh After Test
Phase I Cold Start Test	Fired sample (REA S/N 4)	0.105	0.0209	70.0
	Unfired sample	0.0725	0.0155	82.5
	MS-0110 ATP	<0.100	>0.015	>75
Phase IA life test (REA S/N 7)		0.050	0.0190	83.6

14 - 18 Mesh

		Dimensionless Deflection at 1000 psi	Dimensionless Recovery at 20 psi	Weight % <18 Mesh After Test
Phase I Cold Start Test	Fired sample (REA S/N 4)	0.120	0.171	54.7
	Unfired sample	0.113	0.0205	59.5
	MS-0110 ATP	<0.180	>0.015	>55
Phase IA life test (REA S/N 7)		0.129	0.0210	59.5

(1) Percent retained on indicated mesh size screen

Table XLVIII. Hydrogen Chemisorption Test Results

25–30 Mesh		
	50% attrited as received (average)	390 μ moles/gram
	50% attrited after shrinkage	145 μ moles/gram
	90% attrited as received	356 μ moles/gram
	90% attrited after shrinkage	154 μ moles/gram
	90% attrited from cold-start REA	136 μ moles/gram
	90% attrited from sample REA	155 μ moles/gram
	50% attrited from REM-Mono qual S/N 1001 SY REA	122.6 μ moles/gram
	90% attrited after shrinkage (Phase IA catalyst)	162 μ moles/gram
	Phase IA life test – REA S/N 7	108.9 μ moles/gram
14–18 Mesh		
	As received (average)	400 μ moles/gram
	After shrinkage	135 μ moles/gram
Phase I Cold Start Test	Fired REA (S/N 4)	139 μ moles/gram
	Sample REA	144 μ moles/gram
Phase IA Life Test REA S/N 797.6		97.6 μ moles/gram

during firing. The data on Table XLVIII shows that without shrinkage the life test catalyst hydrogen chemisorption would have changed by 247. 1 μ moles/gram during the test. As a result of shrinking however, the change in hydrogen chemisorption during the test was only 53.1 μ moles/gram.

Table XLIX shows the BET surface area and median pore radius determined by nitrogen adsorption analysis. As shown, the BET surface area and median pore sizes for all samples are approximately equal. A comparison of pore size distribution is presented on Table L.

Table XLIX. Nitrogen Absorption Test Results

25–30 Mesh

		BET Area m^2/g	Median Pore Radius A^o
	As received after shrinking	47.9	56.4
Phase I Cold Start Test	Unfired sample	49.2	57.6
	Fired sample (REA S/N 4)	48.8	58.9
Phase IA life test (REA S/N 7)		48.6	59.9

Table L. Pore Size Distribution 25 - 30 Mesh Catalyst

Pore Radius A°	Volume – Percent				Area – Percent			
	As Received and Shrunk	Phase I Cold Start Test		REA S/N 7	As Received and Shrunk	Phase I Cold Start Test		REA S/N 7
		Unfired Sample	REA S/N 7			Unfired Sample	REA S/N 4	
300 - 250	2.8	2.8	2.8	5.1	0.5	0.5	0.5	0.9
250 - 200	4.5	4.9	5.1	5.9	1.0	1.1	1.1	1.4
200 - 150	6.0	6.5	6.6	7.0	1.7	1.9	1.9	2.1
150 - 100	9.2	9.9	10.0	10.8	3.8	4.0	4.1	4.6
100 - 90	3.2	3.4	3.6	4.2	1.7	1.8	1.9	2.3
90 - 80	4.8	4.9	5.4	5.3	2.8	2.8	3.2	3.2
80 - 70	7.0	6.7	6.4	7.9	4.5	4.3	4.3	5.4
70 - 60	9.2	8.6	9.1	8.0	7.0	6.6	7.0	6.4
60 - 50	10.2	10.2	9.9	3.7	9.1	9.1	9.0	3.5
50 - 45	6.5	5.8	6.0	6.0	6.7	5.9	6.3	6.5
45 - 40	6.9	6.4	6.4	6.0	8.0	7.4	7.5	7.2
40 - 35	6.8	6.5	6.4	6.4	8.9	8.5	8.5	8.7
35 - 30	6.3	6.2	6.2	6.2	9.4	9.3	9.4	9.8
30 - 25	6.8	6.9	6.3	7.5	12.1	12.2	11.4	14.0
25 - 20	5.9	5.7	5.8	7.2	12.8	12.4	12.8	16.6
20 - 15	3.8	4.5	4.0	2.7	10.0	12.2	11.1	7.3
15 - 10	0.0	0.0	0.0	0.0	0.0	0.0	0.0	0.0
10 - 7	0.0	0.0	0.0	0.0	0.0	0.0	0.0	0.0

The catalyst characterization tests establish changes that do occur as the result of extended firing (500,000 pulses, 107,635 lbf-sec delivered impulse, 8.7 hours total burn time with over 500 lbm of propellant through the engine). Not yet firmly established, however is whether the material is completely stabilized or will undergo further losses in surface area with accrued burn time, and what the magnitude of these losses will be.

2.5.4 Cold Start Catalyst Evaluation

The objective of the cold start catalyst evaluation test series was to characterize the effects on catalyst attrition of the following:

a. Propellant inlet temperature
b. Initial catalyst bed temperature
c. Catalyst bed loading

A workhouse reaction engine design was adapted from the flightweight design to facilitate assembly and disassembly of the engine in order to allow a large number of tests to be conducted on the same hardware with a minimum of assembly and disassembly time.

This design, schematically presented in Figure 64, incorporates a catalyst bed configuration and injector design identical to those employed in the flightweight REA. The major changes made are those which allow the REA to be bolted together, the incorporation of a reusable O-ring joint between the injector inlet and the thrust chamber valve, and additional instrumentation (upstream chamber pressure, bed and gas temperatures). Also, in the interest of fabrication economy and ease of handling, the 40:1 expansion ratio nozzle was deleted as well as the heat shield. As a result of difficulties with attaining a reliable seal between the injector assembly and the thrust chamber, the stainless steel O-ring was replaced with copper-asbestos seals (MS35769-30) early in the test series. Similarly, the O-ring seal between the propellant valve and injector assembly was extruded into the flow passage, necessitating its replacement with aluminum gaskets fabricated by RRC. With these two modifications the workhorse engines proved capable of accurately simulating flight-type REA operation.

The workhorse REA test installation was identical to the flightweight REA installation (Figure 52) with the exception of cell modification to allow two REA's to be tested simultaneously in the same vacuum tank when operating conditions permitted (i.e. identical feed pressures and temperatures). Vacuum chamber No. 4 schematically shown in Figure 51 was used for these tests. Table LI presents the instrumentation list and recording method used for these tests. The test series as run is included in Table LII, each test representing a new workhorse engine buildup. Following each test, the engines were allowed to cool to ambient, removed from the vacuum tank, and sealed in a glove box with a dessicated nitrogen environment where they were disassembled. This procedure minimized catalyst weight gain which would result from oxygen or water adsorption. Following disassembly, the catalyst weights were measured and the upper bed (25- to 30-mesh) catalyst sieved to determine size distribution. This work also was accomplished in the glove box. Table LIII presents the results of these measurements for each of the tests conducted. The object of the first four tests was to determine the number of cold starts required to see significant catalyst loss. These tests were conducted at 65°F conditions to ensure sufficient data on the effect of temperatures.

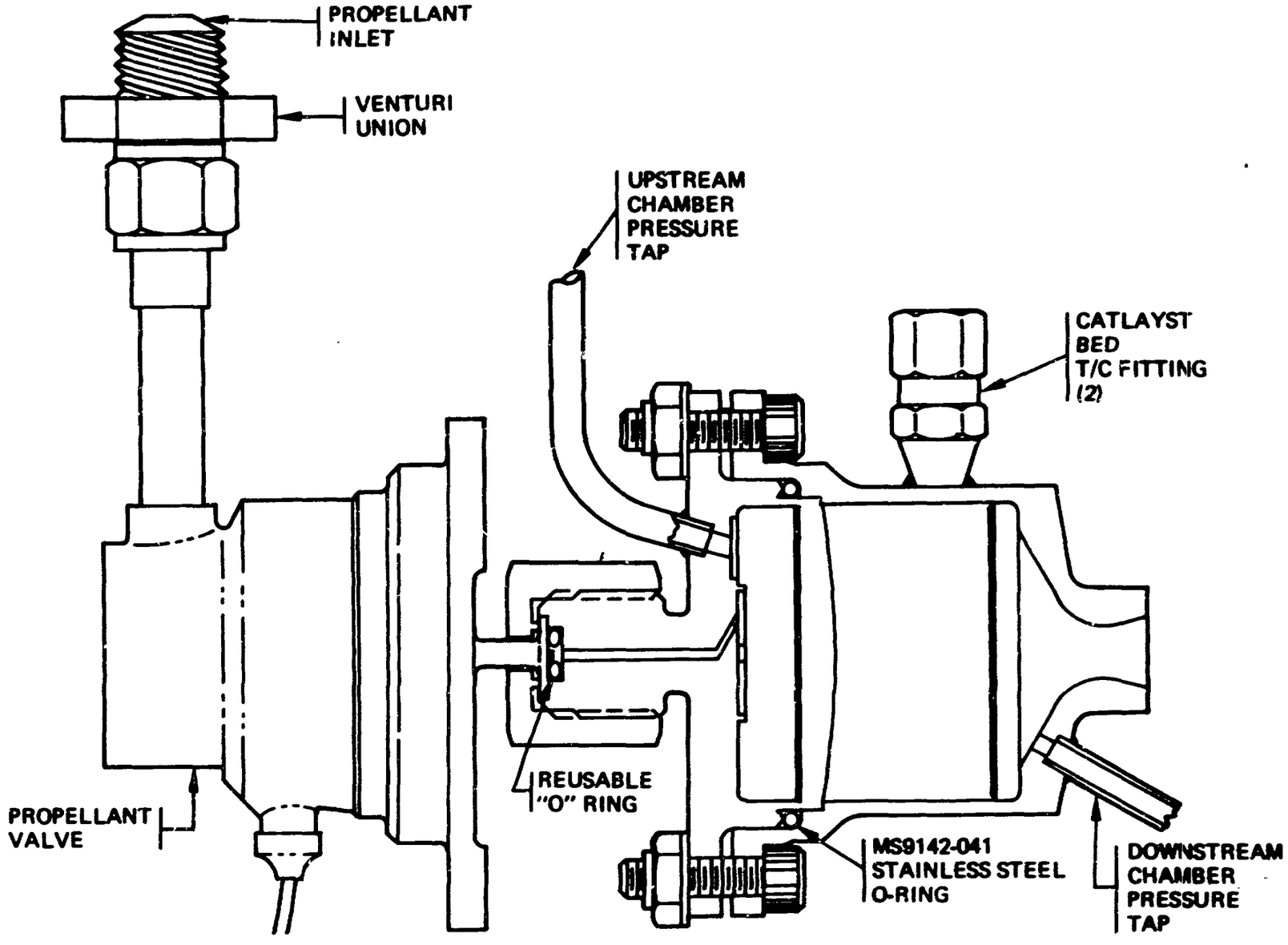

Figure 64. Cold Start Workhorse REA Schematic.

Table LI. Cold-Start Catalyst Evaluation Instrumentation List

Parameter	Symbol	Range	Recording Method				
			Dymec	Cimron	Monsanto*	Osc	Strip Chart
Downstream chamber	P_{cd}	0–150 psia				X	X
Pressure (dual range)		0–500 psia				X	
Upstream chamber	P_{cu}	0–150 psia				X	X
Pressure (dual range)		0–500 psia				X	
Feed pressure	P_f	0–500 psia				X	X
Test cell pressure	P_a	0–0.5 psia				X	
TCV temperature	T_v	0–10 mv		X			
Injector head temperature	T_v	0–100 mv		X			
Upper catalyst temperature	T_{cu}	0–100 mv		X			
Lower catalyst temperature	T_{cl}	0–100 mv		X			
Gas temperature	T_g	0–100 mv		X		X	
Chamber wall temperature	T_w	0–100 mv		X			X
Propellant inlet temperature	T_{fi}	0–10 mv		X			
Flowmeter temperature	T_{fm}	0–10 mv		X			
Fuel flow	W	0–1 KHz				X	
TCV voltage	V_e	0–30 vdc				X	
TCV current	V_i	0–1 adc				X	
Time reference	Hz	500 ± Hz				X	

Table LII. Catalyst Attrition Tests

Test No.*	Feed Pressure psia	Bed Temp. at Start, °F**	Propellant Temp., °F	Number of Starts	Remarks
5-1	350	40	40	5	4 sec on time each
5-2	350	40	40	10	2 sec on time each
5-3	350	40	40	15	1.3 sec on time each
5-4	350	40	40	20	1 sec on time each
5-5	350	40	40	10	2 sec on time each
5-6	350	65	40	10	2 sec on time each
5-7	350	120	40	10	2 sec on time each
5-8	350	300	40	10	2 sec on time each
5-9	350	40	65	10	2 sec on time each
5-10	350	65	65	10	2 sec on time each
5-13	350	40	120	10	2 sec on time each
5-14	350	65	120	10	2 sec on time each
5-15	350	120	120	10	2 sec on time each
5-16	350	300	120	10	2 sec on time each
5-21	225	40	40	10	2 sec on time each
5-22	225	120	120	10	2 sec on time each
5-23	100	40	40	10	2 sec on time each
5-24	100	120	120	10	2 sec on time each

NOTE: *The following tests above were conducted simultaneously: 5-1 and 5-2, 5-3 and 5-4, 5-5 and 5-6, 5-7 and 5-8, 5-9 and 5-10, 5-13 and 5-14 and 5-15 and 5-16.

**During cool down, the warmer of the two catalyst bed temperatures was maintained at temperatures indicated with an injector head heater.

The upper bed catalyst loss plus fines as a percent of the original load is plotted versus the number of starts for these first four tests on Figure 62. Based upon these tests, ten starts were selected for the remaining tests. This represented the maximum potential for data within reasonable test time. The constraint to maintain a 12-hour minimum cool-down time between starts constrained the number of tests to be run within schedule. As shown on Figure 65, data beyond this point appeared to be in the area of diminishing returns.

Figure 66 summarizes in matrix format the remaining tests which were conducted. Test data is included in Table LIII, and upper bed catalyst loss is plotted as a function of initial bed temperature on Figure 67. As noted from the data shown in Figure 67, the catalyst loss rates for repetitive starts are mainly a function of the catalyst bed temperature. At a given catalyst bed temperature the loss rates are not markedly affected by either propellant temperature or bed loading for the range of

Table LIII. Cold Start Catalyst Evaluation Test Series Results

Test No.	REA S/N	No. of Starts	Feed Press. psia	Initial REA Temp. °F	Propellant Temp., °F	14-18 Mesh Loss % Loaded	25-30 Mesh Loss % Loaded	25-30 Mesh Distribution % Remaining				25-30 Mesh Loss & Fines % Loaded
								>30 mesh	>40 mesh	>50 mesh	Fines	
5-0	Inj 102B	0	—	—	—	—	0.0	97.9	1.6	0.2	0.3	0.3
5-1R	103	5	350	65	65	2.8	1.3	98.4	0.6	0.6	0.3	1.6
5-2R	105	10	350	65	65	2.6	3.3	96.8	2.4	0.3	0.5	3.8
5-3R	113	15	350	65	65	2.3	2.9	95.4	3.3	0.5	0.8	3.7
5-4R	104	20	350	65	65	1.9	2.7	95.0	2.5	0.8	1.7	4.4
5-5	115	10	350	40	40	2.1	3.4	95.9	2.1	0.3	1.7	5.0
5-6	121	10	350	65	40	2.3	1.6	96.0	2.1	0.3	1.6	3.2
5-7	114	10	350	120	40	1.6	1.8	97.5	2.1	0.2	0.2	1.9
5-8	123	10	350	300	40	1.5	0.6	96.1	2.9	0.8	0.2	0.8
5-9	131	10	350	40	65	0.9	2.8	94.4	2.4	0.8	2.4	5.2
5-10	125	10	350	65	65	2.4	1.5	95.7	1.8	0.8	1.7	3.1
5-13	133	10	350	40	120	2.0	1.8	90.4	5.0	0.3	3.3	5.0
5-14	124	10	350	65	120	1.2	1.9	93.5	4.1	0.8	1.6	3.5
5-15	135	10	350	120	120	1.7	2.6	97.5	1.3	0.3	0.8	3.4
5-16	141	10	350	300	120	2.3	1.9	97.6	1.9	0.2	0.3	2.2
5-21	143	10	225	40	40	1.6	5.5	88.9	6.8	0.9	3.4	8.7
5-22	134	10	225	120	120	0.4	0.8	94.4	4.0	0.8	0.8	0.8
5-23	151	10	100	40	40	1.7	5.5	95.0	4.2	0.3	0.5	6.0
5-24	145	10	100	120	120	1.2	0.6	96.9	1.5	0.8	0.8	1.4

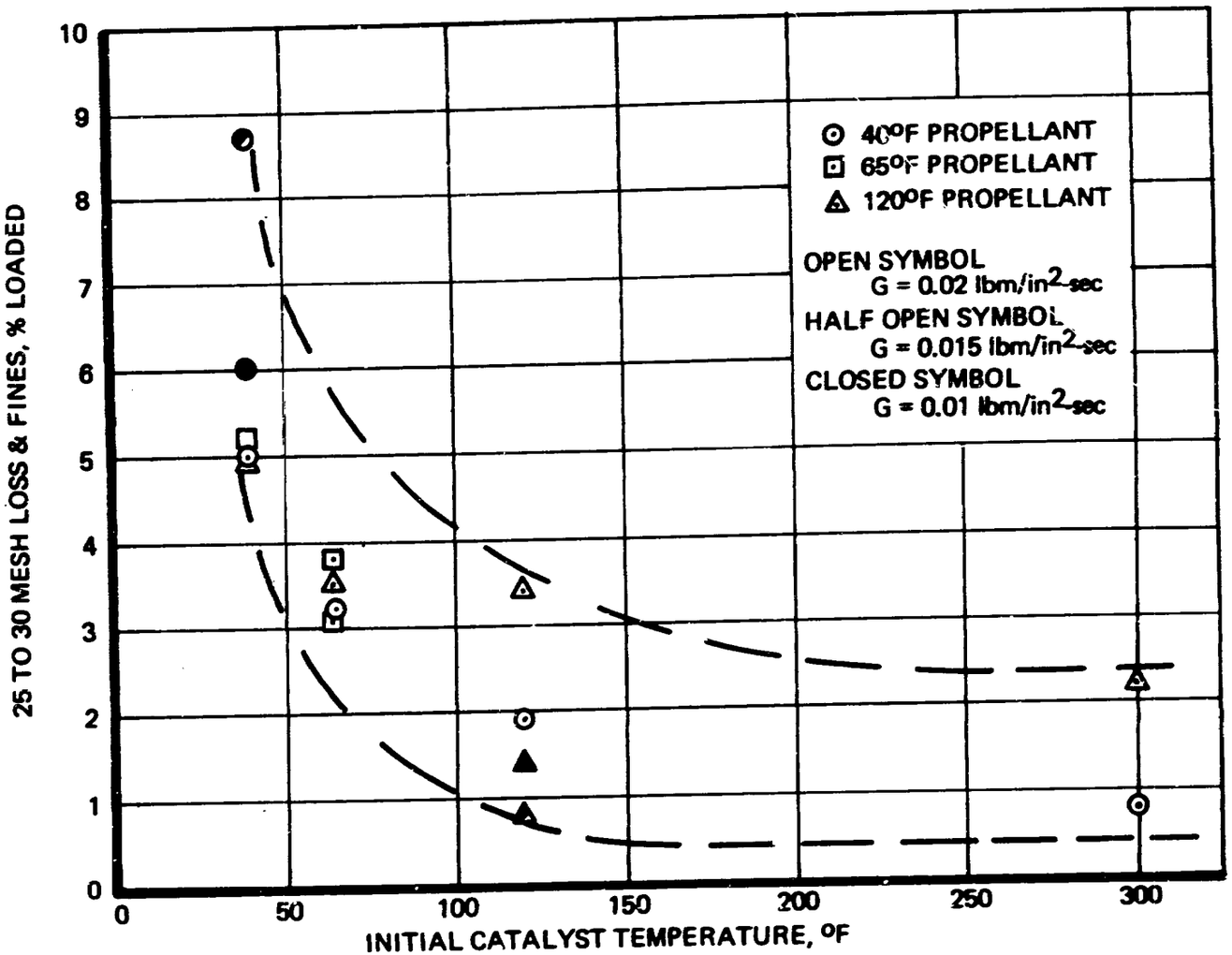

Figure 67. Upper Bed Catalyst Loss as a Function of Propellant/Catalyst Temperature
(All Data for 10 Starts)

variables tested. It is strongly believed that the data average of approximately 1.5% loss at 300°F bed temperature probably represents a reduction in catalyst weight from adsorbed water rather than a true loss rate. If so, then the catalyst loss rates are reduced by a factor of five by increasing the catalyst bed temperature from 40 to 90°F.

BLANK PAGE

SECTION III

RELIABILITY AND MAINTAINABILITY ASSESSMENT

3.1 INTRODUCTION

This section presents the reliability analysis for the long-life monopropellant hydrazine engine as developed by RRC for AFRPL under Contract FO4611-C-0036. The prediction is based upon operational requirements and duty cycles specified by AFRPL and the final design configuration developed by RRC.

3.2 PREDICTION SUMMARY

The predicted value for the subject engine, based on the Long-Life Monopropellant Hydrazine Development Program failure rate data shown in paragraph 3.3 and the following duty cycles is 0.177. The operational duty cycles incorporated in the prediction are:

Number of cycles (pulses)	1×10^6
Number of cold starts	42
Cumulative operational (burn) time	17.5 hours
Length of mission (10 years)	87,600 hours

On the basis of overall hydrazine engine experience at RRC, the predicted value is 0.793 by incorporation of the design modifications identified in this program.

3.3 FAILURE RATES

3.3.1 Discussion

The failure rates used in this numerical prediction are based on the test data generated by the Long-Life Hydrazine Engine Development Program. This applies specifically to the failure rate for hot pulsing.

The continuous hot-pulsing data characteristic of this program indicated a dominant failure mode specifically resulting from this type of operation. This mode (metal fatigue, cracking, and nitriding in the injector area) is fully discussed in the technical analysis. It is apparent that design and material changes will eliminate or minimize this failure, and the failure rate will be greatly reduced. However, the rate used herein is applicable to the present state of development, which is the level requested by paragraph 3.3 of the AFRPL Exhibit "A".

The subject program testing indicated that 400,000 cycles of hot-pulsing were achieved before tolerances or required operational limits of impulse parameters were exceeded. These data are used in the formula below to derive the related failure rate.

3.3.2 Failure Rate Derivation

The chi-square model is used to derive failure rates from developed data, as follows:

$$\lambda_{ct} = X^2/2T$$

Where:

$\lambda_{c/t}$ = Reactor and injector (TCA) failure rate (failure/hour or failures/cycle)

X^2 = Chi-square percentile based on 2r + 2 degrees of freedom and a one-sided 50% confidence level, and "r" = zero accountable failures

T = Cumulative test units in hours or cycles

Hence:

$$\lambda_{c/H} \text{ (hot-pulse – program level)} = \frac{1,386}{2\,(400,000)} = 1.73 \times 10^{-6}$$

3.3.3 Application

Table LIV presents the operating times and cycles (listed in paragraph 3.2), in combination with the derived failure rates and the resultant exponent summations. The application of these values to the prediction is discussed under paragraph 3.4. The predicted reliability based on these values is 0.177.

3.3.4 Applicable Data

Since this program identified specific design modifications which should eliminate the observed failure mechanism, a predicted reliability was evaluated for this configuration.

The failure mode associated with cold starts is a disturbance of the catalyst bed, leading to out-of-specification impulse characteristics. Although RRC has developed a great number of purely cold-start data, including that from the subject program, these are not sufficient to yield a valid failure rate. They are sufficient, however, to yield a ratio for comparing the severity effects of intermittent cold-start cycles to intermittent (noncontinuous) pulse-mode operation. This comparative ratio, established by engineering judgement and data evaluation, is that cold starts are 100 times more deteriorating to impulse characteristics than hot starts (pulsing) in the resultant catalyst bed failure mode aforementioned. Hence, as a base, RRC's more than 3,000,000 cumulative hot-start cycles are applied to the foregoing formula.

Similarly, steady-state thrust ("burn") is considered to have a 50 times greater failure rate (made up of combined failure modes) than pulsing. Steady-state "burn" is any pulse long enough to raise the catalyst bed and injector to equilibrium temperature, generally variable from 0.5 to 10 seconds, depending on the size and design of the unit. In this prediction, the cumulative "burn" time is handled by a steady-state failure rate, this parameter being in addition to those of pulsing and cold starts.

Once again, applying the chi-square model of paragraph 3.3.2 yields:

$$\lambda_c \text{ (intermittent pulsing – cumulative RRC data)} = \frac{1,386}{2\,(3,000,000)} = 0.231 \times 10^{-6}$$

Table LIV. Failure Rate Data

SYSTEM/SUBSYSTEM AFRPL Long-Life Reactor Engine

PART OR COMPONENT	QUANTITY (n)	OPERATING PHASES		NONOPERATING PHASES (HOURS)		FAILURE RATES x 10^{-6}			$\lambda_t T_n \times 10^{-6}$			$\lambda_c N_n \times 10^{-6}$	$\Sigma\lambda_{T/N} \times 10^{-6}$
		TIME, HRS (T)	CYCLES No. (N)	MISSION K_M =	BOOST K_B =	OPERATING λ_t	NON OPERATING λ_t	CYCLIC λ_c	OPERATING	NON OPERATING	BOOST	CYCLIC	
Reactor	1		1×10^6 (pulse)	87,600	—		0.001	1.73		87.6	—	1.730.000	1.730.091
						$R = e^{-1.7307} = 0.177$							

NOTES

RRC R 040

$$\lambda_{c/C}\ \text{(cold-start)} = 100\ (0.23 \times 10^{-6}) = 23.1 \times 10^{-6}$$
$$\lambda_t\ \text{(steady-state)} = 50\ (0.23 \times 10^{-6}) = 11.6 \times 10^{-6}$$

These failure rates are applied to the mission requirements of paragraph 3.2 in Table LV. As shown on this table, the prediction for the final engine design is 0.793.

3.4 MATHEMATICAL MODELS AND CALCULATIONS

The reaction engine assembly operates in both the time and cyclic domain; therefore the analysis combines appropriate time-related or cyclic-related failure rates.

The basic exponential distribution and failure relationship is assumed.

Therefore:

$$R = e^{-K\lambda_t}\ Tn$$

in which:

- R = Reliability (probability of no failure)
- λ_t = Failure rate (failures/hour)
- T = Time (hours)
- n = Number of identical elements
- K = Failure rate modifier

Expressed in cycles, this becomes:

$$R = e^{-K\lambda_c}\ Nn$$

in which.

- λ_c = Failure rate (failures/cycle)
- N = Number of cycles

Hence, for components that experience both types of failures (e.g., the thruster engine), the following is used to express combined effects:

$$R = e^{-(\lambda_t T + \lambda_c N)}$$

For this analysis, the exponent is made a summation of the failure rates, times, and cycles for all mission phases, when multiplied by "K" and "n", according to standard procedures, and listed in the last column of Table LIV.

These are the basic building blocks used to derive the engine reliability consistent with the mission profile. The data from Table LIV, discussed in paragraph 3.3, have been substituted as required in the foregoing models to perform the reliability calculations. The summation values (last column of Table LIV) provide the exponent for deriving the reliability.

Table LV. Failure Rate Data

SYSTEM/SUBSYSTEM AFRPL Long-Life Reactor Engine

PART OR COMPONENT	QUANTITY (n)	OPERATING PHASES		NONOPERATING PHASES (HOURS)		FAILURE RATES x 10^{-6}			$\lambda_t T_n \times 10^{-6}$			$\lambda_c N_n \times 10^{-6}$	$\Sigma\lambda_{T/N} \times 10^{-6}$
		TIME, HRS (T)	CYCLES No. (N)	MISSION K_M =	BOOST K_B =	OPERATING λ_t	NON OPERATING λ_t	CYCLIC λ_c	OPERATING	NON OPERATING	BOOST	CYCLIC	
Reactor	1	17.5	1×10^6 (pulse)	87,600	—	11.6	0.01	0.231	203	87.6	—	231.000	231.291
			42 (cold starts)					23.1				970.2	970
													232.261
							$R = e^{-.232261} = 0.793$						

NOTES

RRC R 040

3.5 MAINTAINABILITY

The final design reaction engine assembly requires no periodic maintenance during or following long periods of storage. The reactor is an all-welded assembly, and is welded to the valve. Therefore, even though refurbishment can be accomplished, the operation is a major disassembly and reassembly, and not a normal maintenance action.

SECTION IV

CONCLUSIONS AND RECOMMENDATIONS

The major results and conclusions of the Long-Life Monopropellant Engine Development Program are summarized as follows:

a. The 90% water attrited catalyst has superior strength characteristics as compared to standard Shell 405 catalyst (50% water attrited). It is believed that this is primarily the result of better packing density because of a more spherically produced granule.

b. Materials of low iron content have superior nitriding resistance in the typical environment of a monopropellant hydrazine rocket engine assembly. A laboratory test was successfully developed to evaluate nitride resistance. Of those material evaluated, Hastelloy B appears to offer superior nitriding resistance.

c. The catalyst bed may be temporarily poisoned by decomposition gas products and this poisoning will result in significantly higher ignition delay time and increased catalyst attrition.

d. With improvements in catalyst and injector design, a 5-lbf engine was developed capable of delivering 400,000 pulses and 80,000 lbf-sec total impulse before significant change in performance. This represents a fourfold increase in total impulse capability and a greater than twofold increase in numbers of pulses over which it was previously qualified.

e. Material thermal fatigue has been identified as a major development problem in meeting the requirement of the long-life 1,000,000-pulse duty cycle which includes delivering in excess of 200,000 lbf-sec total impulse.

f. Parametric tests on a simulated flight-type rocket engine assembly showed a significant effect of initial catalyst bed temperature upon upper bed catalyst loss rates under repeated ambient temperature starts. The effect of initial propellant temperature on these loss rates was negligible on the range tested.

g. Catalyst characterization tests conducted on samples with various firing durations show no effect of life on catalyst strength. These tests show a gradual loss in activity (hydrogen chemisorption) with a corresponding growth in median pore size as a function of life. These changes are minimized by thermal treatment of the catalyst upon its receipt from Shell Development Company.

h. The analytical thermal program developed for this contract was verified by worst-case thermal duty cycle operation. The resultant final design has been proven capable of all duty cycles.

As a result of the work accomplished under the Long-Life Engine Development Program, it is recommended that additional work be conducted in the following areas to complete the development of this long-life monopropellant hydrazine engine:

a. The materials program to evaluate nitride resistance should be continued to evaluate all candidate engine materials. This test should be expanded to evaluate material resistance

to thermal fatigue. This evaluation should consider material types as well as processing techniques. Materials identified as superior in this program should be substituted into the long-life engine final design and subjected to the same life test duty cycle, with results directly comparable to the baseline established in this Phase I effort.

b. A more fundamental program to define and determine fully the mechanisms of catalyst loss and sensitivities thereof is needed. Catalyst loss rates can be influenced by many means, including cold starts, catalyst poisoning, continued hot pulsing, thermal shock, etc. Until these mechanisms are fully understood, engine design solutions for long-life may not be made on a rational engineering basis which may cover the combined effects of large total impulse, high numbers of pulses, and a substantial number of cold starts.

c. It is recommended that the operational limits of the long-life engine final design be determined relative to cold-start capabilities. The cold-start test series conducted in Phase I were directed at establishing the trends of influencing variables on flight-type engine catalyst attrition. Insufficient tests were conducted on the cold-start test series to correlate performance degradation with catalyst loss and/or number of starts. The definition of operational limits corresponding to nominal performance limits will allow mission planners to conduct tradeoff analyses (e.g., heater power and attendant weight versus reliability with redundancy).

REFERENCES

1. Tong, L. S., *Boiling Heat Transfer and Two Phase Flow*, L. S. Wiley & Sons, p 61

2. Noel, M. B., *JPL T.R. #32-109*, June 1961, p 7

3. Knudsen, J. G. and Katz, D. L., *Fluid Dynamics and Heat Transfer*, 1958, p 403

4. "Metals Engineering Quarterly," Volume 10, No. 3, August 1970 (Figure 9, p 28)

5. Wilson, W. W., *Reaction Engine Module, Monopropellant Repeatability Analysis Report*, RRC-68-R-149R2, April 10, 1970

BLANK PAGE

APPENDIX I – FACILITIES

All test work on contract FO4-611-0036 was conducted at the York Center engineering test laborabory, building 63. This laboratory was designed specifically to accommodate testing of rocket engines and associated hardware. The test cell configuration is standard, about one-third being used for sea-level test activities with the remaining two-thirds equipped for altitude testing. Seven vacuum test chambers of the following sizes can be used for high altitude propulsion system tests:

Chamber No.	Diameter (ft)	Length (ft)	Max. Altitude (ft)
1	7	22	400,000
2	5	6	300,000
3	5	5	300,000
4	4-1/2	5	300,000
5	4-1/2	5	300,000
6	9	11	400,000
7	5	5	300,000

Cells 1, 2, and 3 are shown in Figure I-1, and Cells 4 and 5 which were utilized on Contract FO4-611-0036 are shown in Figure I-2.

Thermal conditioning was provided by circulating ethylene glycol, methyl alcohol, or liquid nitrogen through the walls of a shroud surrounding the engine being tested. The type of fluid used was a function of the temperatures required. When ethylene glycol or methyl alcohol was used as a circulating fluid, it was heated with electric heaters or cooled with liquid nitrogen in a heat exchanger system.

All firings at RRC are controlled remotely from the test control room (Figure I-3). This room provides maximum protection for operating personnel by being constructed of reinforced concrete and pressurized slightly by the building's ventilation system. Injection of toxic vapors into the building through the inlet of the ventilation system is unlikely because of the remote location of the fresh air inlet in relation to the test cells. Fire protection systems, isolated power for instrumentation, high-pressure nitrogen distribution, and remotely controlled propellant systems are included in this facility.

Data acquisition equipment was located in the control room area (Figure I-3). This equipment includes analog, digital, and FM recording devices to meet varied frequency response and real-time data requirements of each test. A Monsanto Digital Data Acquisition System, shown in Figure I-4, consists of a digital magnetic tape recorder with an integrated computer to perform "engineering units" computations. The system collected data from various rocket engine transducers (such as

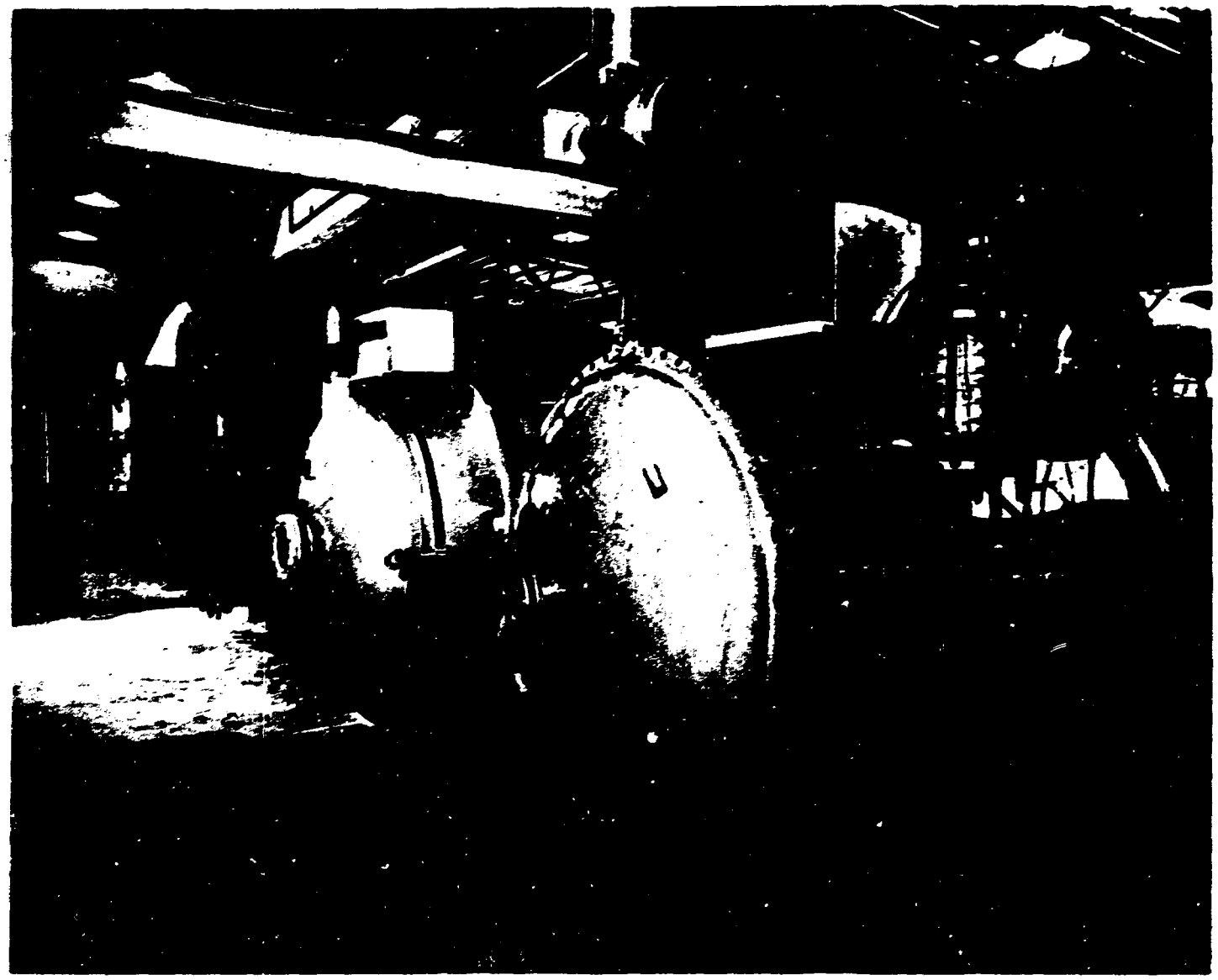

11038-63

Figure I-1. RRC Vacuum Test Cells Numbers 1, 2, & 3

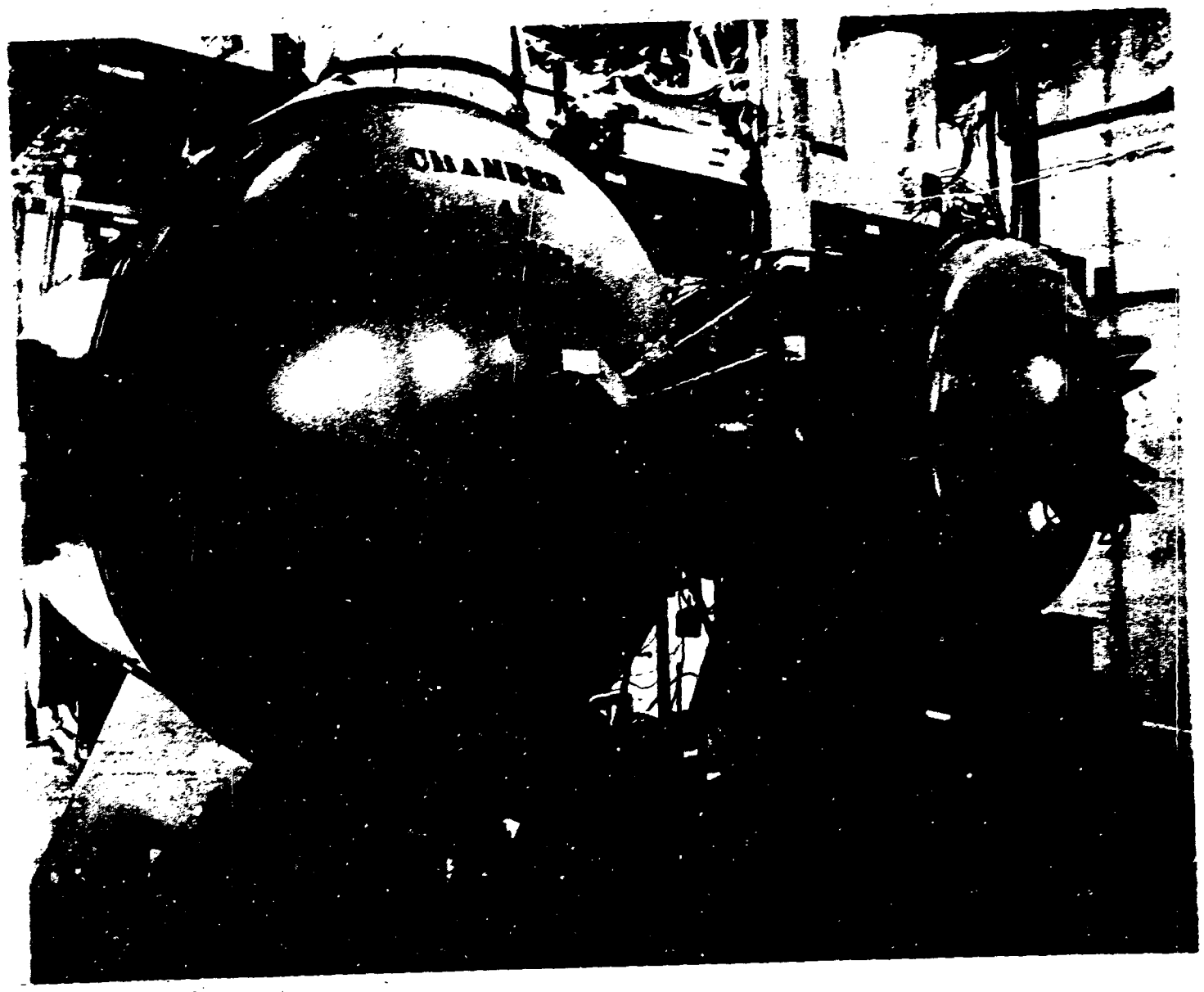

Figure I-2. Attitude Firing Chambers – Cells 4 and 5

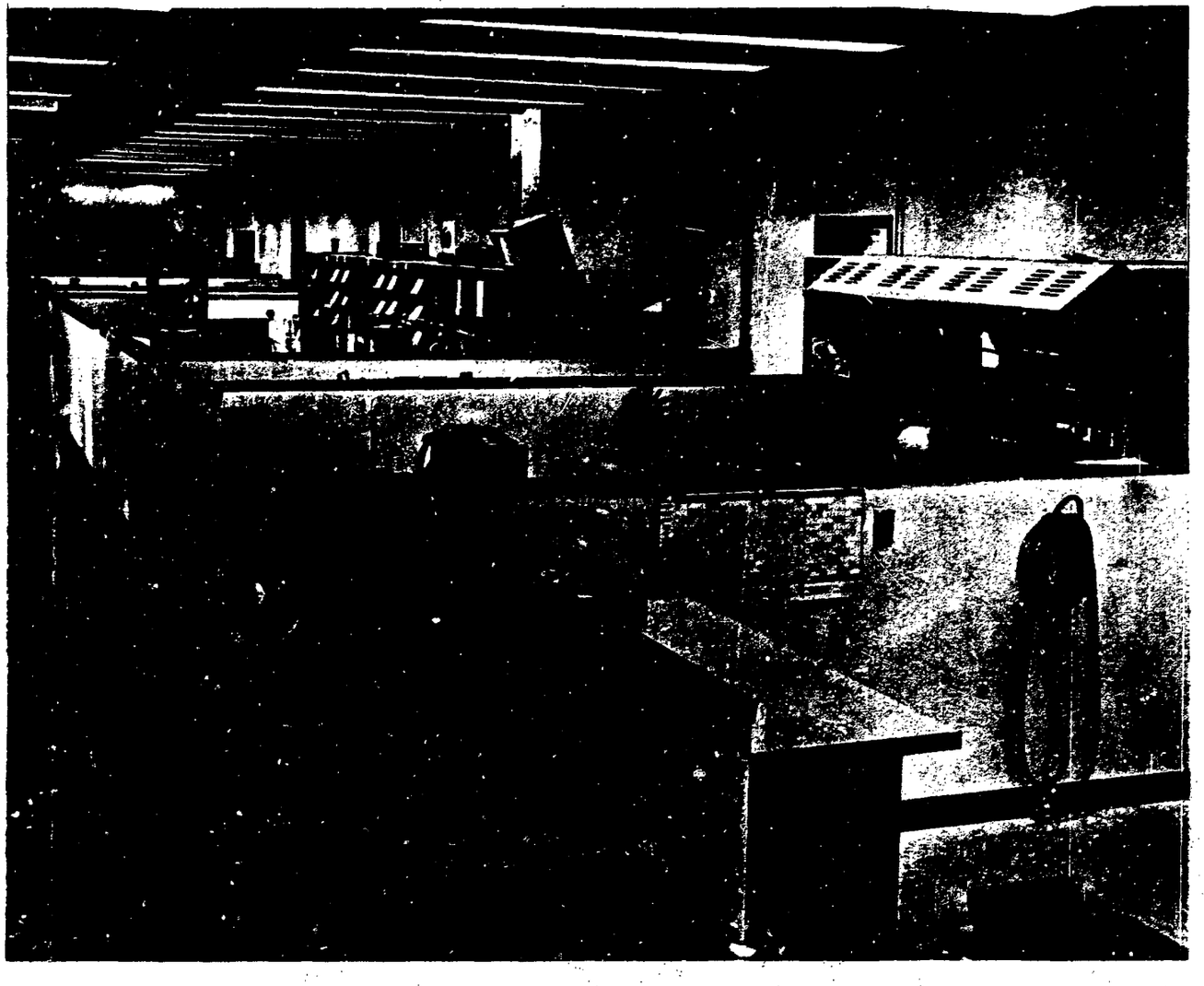

Figure I-3. Rocket Test Laboratory – Test Firing Control Bays

02147A

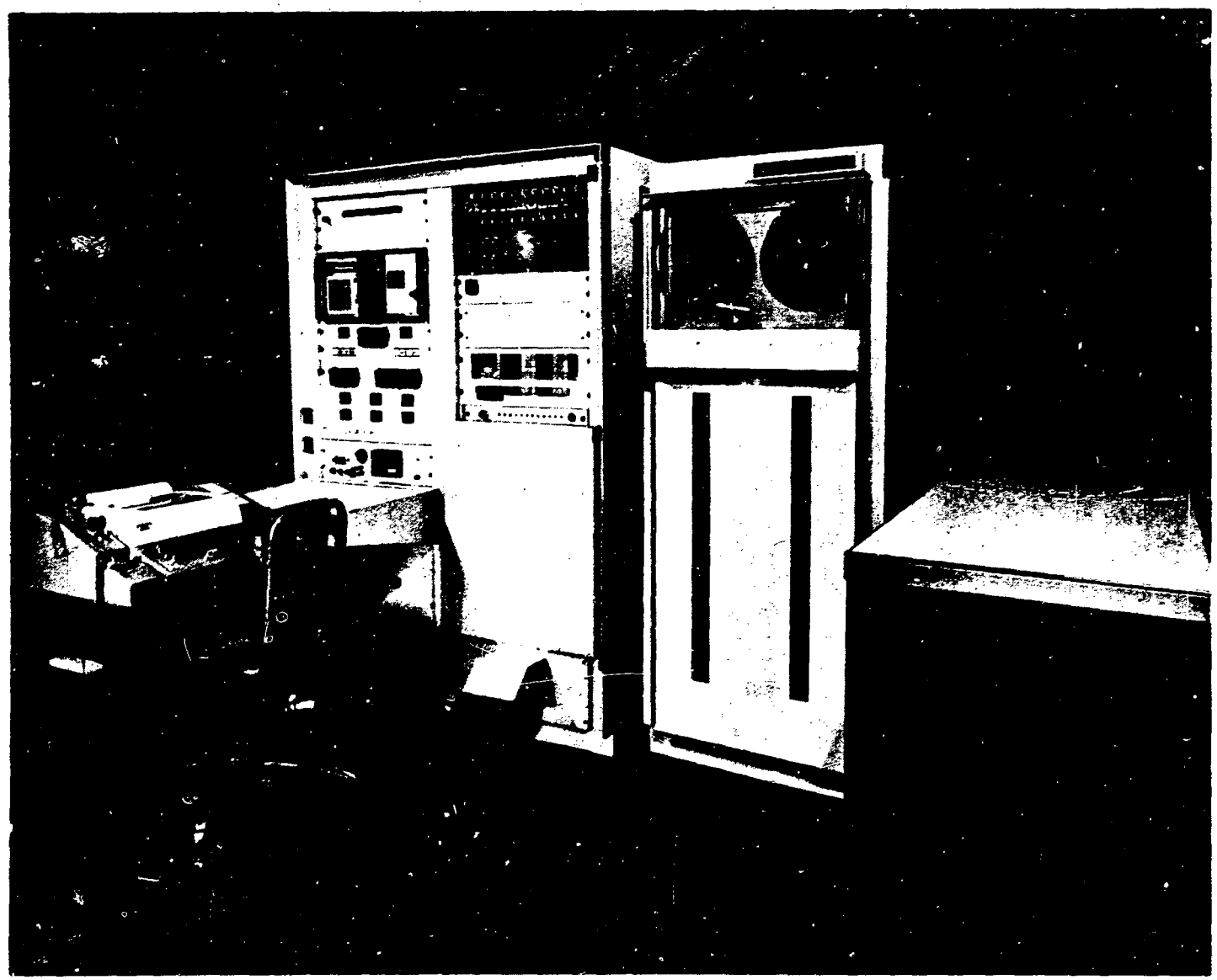

Figure I-4. Rocket Test Laboratory – Monsanto Digital Data System

pressure, fuel flow, temperature) and records it on magnetic tape in IBM 360 compatible format. The data was then processed by IBM 360 computer to produce a printed output of required engineering performance parameters.

Test sequences were programmed by tape systems which control the firing operations electronically. Pulse width and frequency are independently variable over extreme ranges with minute accuracy, and were programmed for each duty cycle.

To support the rocket test facility, a calibration unit periodically calibrates and maintains all instrumentation. Records of each item of equipment are maintained to ensure accuracy during test operations. Calibration standards used by the calibration laboratory are in turn checked for accuracy and certified by a local metrology laboratory at regular time intervals.

APPENDIX II – DATA REDUCTION

All data from the Phase IA life test was reduced from the digital data types on a Model 50 IBM 360 computer. The data acquisition/reduction flow chart is presented in Figure II-1, and a typical computer printout is shown in Figure II-2. For all duty cycles tested, digital data acquisition was continuous over at least a 10-pulse train. To compensate for line noise and/or zero shift, the five samples of chamber pressure preceeding the valve open signal were defined as zero reference for that pulse. At sample size and scan rates utilized, this is equivalent to 3 milliseconds prior to valve signal. Valve signal was determined from the valve voltage measurement. Parameters determined from chamber pressure measurement were:

a. *Ignition Delay* – Time from valve signal open to 1% of equilibrium chamber pressure (steady state for pulse width >0.050 second; peak for pulse width ≤0.050 second).

b. *Time to 90%* – Time from valve signal open to 90% equilibrium chamber pressure.

c. *Time to 10%* – Time from valve signal closed to 10% equilibrium chamber pressure.

d. *Roughness* – Average maximum pressure minus average minimum pressure divided by the mean chamber pressure. Measured over the last 10% of the electrical pulse width if greater than 0.050 second. Not calculated for pulse widths less than 0.050 second.

e. *Steady-State Chamber Pressure* – Calculated only for pulse widths in excess of 0.150 second, defined as average chamber pressure over the last 10% of electrical pulse width.

f. *Pulse Chamber Pressure Integral* – Calculated for all pulses ≤0.150 second. Defined as the overall time integral of chamber pressure from valve signal on to less than twice ambient pressure (unchoked nozzle).

g. *Centroid* – Time from valve signal to deliver 50% of pulse chamber pressure integral.

The foregoing parameters were combined with appropriate constants to calculate steady-state thrust and pulse-mode impulse bit from:

$$F = P_c A_{t_H} C_{f_s} \tag{1}$$

and:

$$I_{BIT} = C_{f_p} A_{t_H} \int P_c \, d\tau \tag{2}$$

Where:

F	=	Steady-state thrust
P_c	=	Chamber pressure
A_{t_H}	=	Hot throat area
C_{f_s}	=	Steady-state thrust coefficient

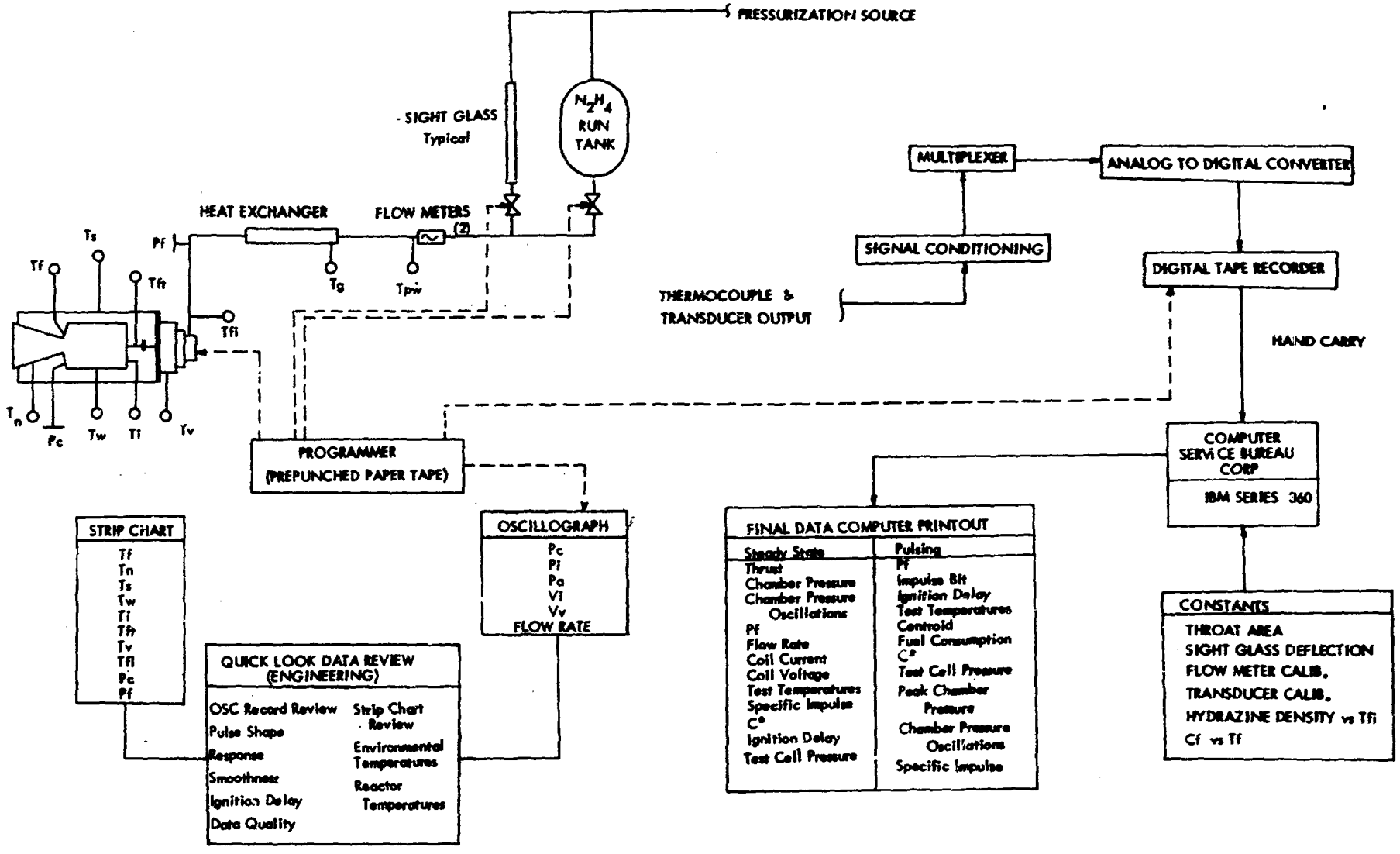

11046-87

Figure II-1. Long-Life Data Acquisition Flow Chart

TEST NO. 430 SEQUENCE NO. 4-0016 PULSE WIDTH 0.020 SEC PULSE FREQUENCY 2.0 CPS

PULSE NO.	PF AVG. PSIA	PA AVG. PSIA	FROM VALVE SIGNAL 10% SEC	90 RES SEC	10 DEC SEC	CENTROID SEC	60 RPM SEC	PC AVG. PSIA	PC MAX. PSIA	ROUGH NESS	I-SIT LBF-SEC	W P LBM	ISP SEC	C-STAR FT/SEC	TEMPERATURES DEG F PROP THROAT	CHAMBER NO1.	NO2.	ROTATIONAL IMPULSE EFF
1	95.8	0.000	0.009	0.024	0.046	0.032	0.044	20.7	20.7	0.0	0.03371	0.000337	91.1	1000.0	72.3	431.0	417.	459.	94.94
2	95.7	0.000	0.010	0.025	0.049	0.034	0.048	24.3	24.3	0.0	0.03383	0.000337	115.2	2099.2	72.3	431.0	416.	459.	95.44
3	95.6	0.001	0.010	0.025	0.050	0.034	0.047	24.3	24.3	0.0	0.03383	0.000337	114.7	2089.7	72.6	431.0	423.	454.	95.78
4	95.7	0.001	0.009	0.025	0.049	0.033	0.046	24.5	24.5	0.0	0.03389	0.000337	113.9	2075.1	72.6	431.0	422.	449.	96.07
5	95.7	0.002	0.010	0.024	0.049	0.033	0.045	24.9	24.9	0.0	0.03374	0.000337	115.0	2094.3	72.4	431.0	424.	424.	97.19
AVG.	95.7	0.001	0.009	0.024	0.048	0.033	0.046	23.7	23.7	0.0	0.03387	0.000337	110.0	2003.6	72.4	431.0	420.	447.	96.21
SPREAD	0.1		3.2	1.2	4.3	2.7	4.5	8.7	8.7		11.0		11.0	11.0	0.2	-0.0	1.0	4.0	1.2
91	96.8	0.005	0.008	0.022	0.044	0.030	0.038	33.5	33.5	0.0	0.05084	0.000292	173.4	3096.2	65.6	584.5	798.	528.	98.43
92	96.7	0.009	0.010	0.023	0.044	0.031	0.037	33.6	33.6	0.0	0.04978	0.000292	170.5	3043.6	65.5	584.5	798.	539.	98.97
93	96.8	0.005	0.009	0.022	0.044	0.031	0.038	33.4	33.4	0.0	0.05045	0.000292	172.8	3084.7	65.4	584.5	804.	539.	98.60
94	96.7	0.005	0.009	0.022	0.044	0.031	0.038	33.5	33.5	0.0	0.05036	0.000292	172.5	3079.2	65.3	584.5	803.	539.	98.62
95	96.7	0.005	0.009	0.022	0.044	0.031	0.039	33.7	33.7	0.0	0.05083	0.000292	174.1	3107.9	65.6	584.5	804.	542.	98.40
96	96.8	0.005	0.010	0.023	0.044	0.031	0.038	33.5	33.5	0.0	0.05042	0.000292	172.7	3083.2	65.5	584.5	810.	553.	98.56
97	96.7	0.005	0.009	0.022	0.045	0.031	0.039	33.5	33.5	0.0	0.05122	0.000292	175.4	3131.8	65.4	584.5	813.	551.	98.36
98	96.8	0.005	0.010	0.023	0.044	0.031	0.039	33.5	33.5	0.0	0.05080	0.000292	174.0	3106.0	65.5	584.5	813.	548.	98.51
99	96.8	0.005	0.010	0.022	0.044	0.031	0.039	33.7	33.7	0.0	0.05106	0.000292	174.9	3122.1	65.4	584.5	815.	553.	98.49
100	96.7	0.005	0.009	0.022	0.044	0.031	0.038	33.7	33.7	0.0	0.05064	0.000292	173.4	3096.1	65.4	584.5	817.	560.	98.70
AVG.	96.7	0.005	0.009	0.022	0.044	0.031	0.038	33.6	33.6	0.0	0.05082	0.000292	173.3	3095.1	65.5	584.5	806.	545.	98.58
SPREAD	0.1		0.5	2.7	1.4	2.0	2.3	0.4	0.4		1.4		1.4	1.4	0.2	-0.0	2.1	2.9	0.3

Figure II-2. Typical Computer Printout

C_{f_p} = Pulse-mode thrust coefficient

τ = Time

Hot throat area is calculated from the measured throat diameter corrected for thermal expansion of the nozzle. This is accomplished by the following:

$$A_{t_H} = \frac{\pi}{4} (D_t)^2 \, 0.9925 \, [1 + 2a \, (T_t - 70)] \tag{3}$$

Where:

D_t = Throat diameter measured at 70°F

a = Linear coefficient of expansion of nozzle material (Figure II-3)

T_t = Throat temperature

Thrust coefficient for this 40:1 RAO nozzle was thoroughly mapped during the REM-Mono development program. As a result of statistical correlation studies completed on this data, the steady-state and pulse-mode thrust coefficients are described by:

$$C_{f_s} = 1.791 - 3.957/P_c \tag{4}$$

Where:

P_c = Chamber pressure, psia

$$C_{f_p} = 7.12656 \times 10^{-4} \, T_t - 1.49930 \times 10^{-7} \, T_t^2 - 6.73398 \times 10^{-11} \, T_t^3 + 1.297716 \tag{5}$$

Where:

T_t = Flight thermocouple, °R

The pulse-mode data used to develop Equation (5) covered pulse widths of 0.011 to 0.066 second duration. Equation (4) was therefore used for pulse widths greater than 0.050 second.

Steady-state propellant flow rate was determined from turbine flowmeters, the cyclic output of which was converted to analog voltage prior to recording on the digital data system. Pulse-mode flow rate was recorded via closed-circuit television to the propellant cart sight glasses. This raw data was converted to mass consumed per pulse by the data reduction group and input via data cards to the data reduction program. These flow rates were then combined with the foregoing parameters to determine characteristic exhaust velocity and specific impulse.

$$C^*_s = \frac{P_c \, A_{t_H} \, g}{\dot{w}} \tag{6}$$

Where:

C^*_s = Steady-state characteristic exhaust velocity

g = Gravitational constant = 32.174 lbm-ft/lbf sec^2

$\dot{w}$ = Equilibrium flow rate

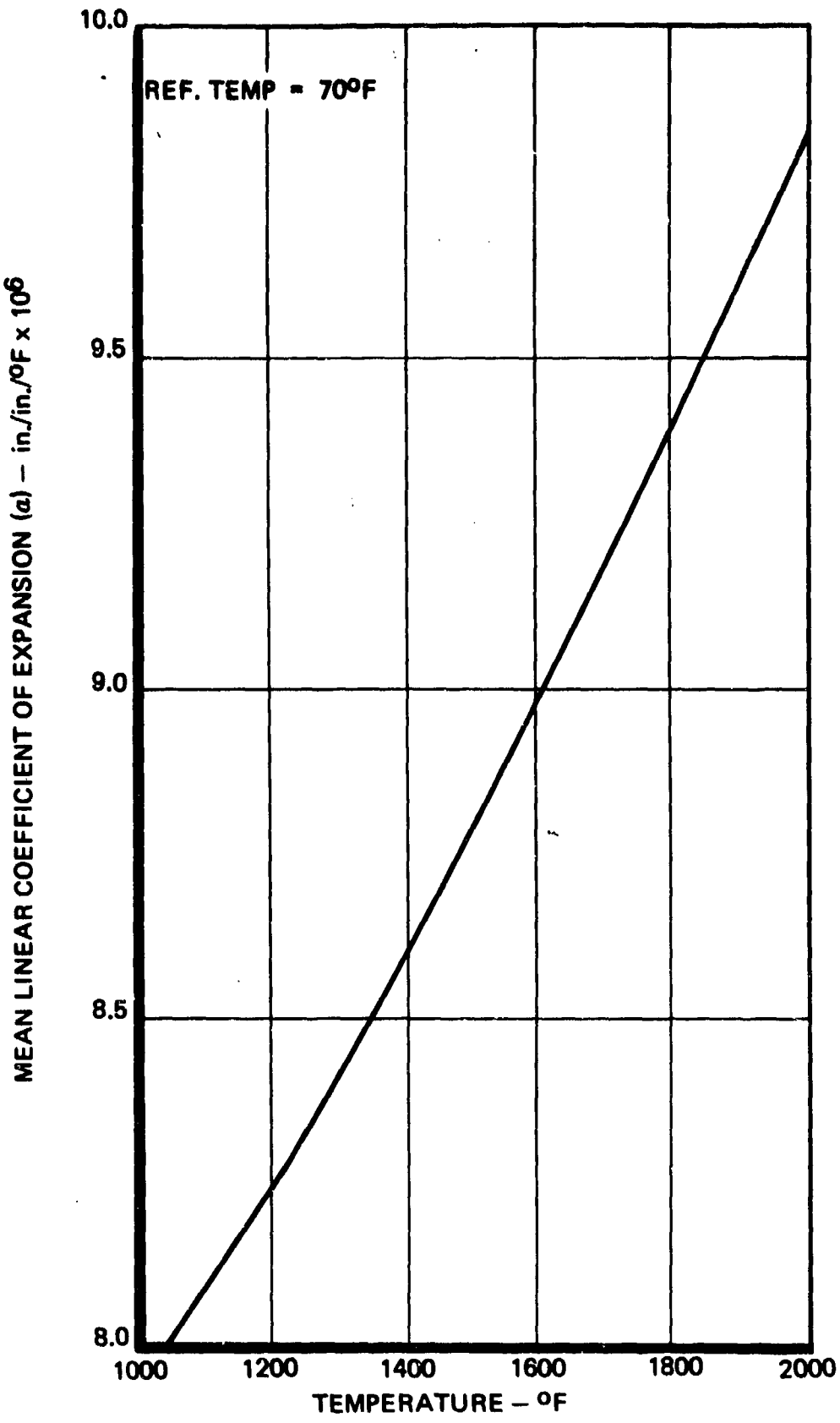

Figure II-3. MEAN LINEAR COEFFICIENT OF THERMAL EXPANSION VS TEMPERATURE FOR HAYNES #25

$$C^*_p = \frac{A_{t_H} g \int P_c \, dt}{w_p} \tag{7}$$

Where:

C^*_p = Pulse-mode characteristic exhaust velocity

w_p = Average propellant consumption per pulse

Steady-state specific impulse is calculated by:

$$I_{sp_s} = \frac{F}{\dot{w}} \tag{8}$$

Pulse-mode specific impulse is calculated by:

$$I_{sp_p} = \frac{I_{BIT}}{w_p} \tag{9}$$

APPENDIX III – ERROR ANALYSIS

An analysis was conducted to estimate the instrumentation errors which are included in the reduced performance data. These analyses are broken down into the three main categories of reduced data.

Timing Errors – All measured times were calculated on the IBM 360 computer using the Monsanto digital data tape. The Monsanto sampling rate is 20,000 samples per second, with 11 continuous record channels and one multiplex channel. Since all times are measured from valve voltage, this parameter was on continuous record as well as chamber pressure. This combination means that each individual continuous channel is sampled every 0.0006 second, resulting in a maximum uncertainty on any time measurement of ±0.0006 second.

Instrumentation Errors – Table III-1 lists the basic accuracy of the instrumentation system utilizing the Monsanto digital data acquisition system. As shown on the table, the overall accuracies assume that each component in series could simultaneously bias the measurement in the same direction (stacked tolerances). All of the pressure measurements shown on Table III-1 were calibrated "end-to-end" with the use of a primary standard dead weight tester certified to 0.015% and traceable to the National Bureau of Standards.

Table III-1. Long-Life Monopropellant Hydrazine Engine Development Program

Instrumentation Error

Parameter	Accuracy, ±% Full Scale		
	Transducer	Recording	Combined
Chamber pressure	0.2	0.1	0.3
Feed pressure	0.2	0.1	0.3
Ambient pressure	0.2	0.1	0.3
Temperature	1.0	0.1	1.1
Voltage	0.2	0.1	0.3
Propellant flow			
Turbine meter, redundant measurements	0.5	0.2	0.5
Sight glass	±1.0 millimeter height accuracy (manual)		

Performance Parameters – The overall accuracy of each reduced performance parameter is determined by applying the appropriate influence coefficient to the uncertainty of the independent constituent measurements and root sum squaring the results. Table III-2 combines these accuracies

with the influence coefficients established for the REM-Mono REA (Reference 5). Pulse mode uncertainties are evaluated at worst-case condition of 0.020 second pulse width, 1.0 cps pulse frequency.

Table III-2. Long-Life Monopropellant Hydrazine Engine Development Program

Accuracy of Reduced Performance Parameters

Parameter	Measurement Accuracy	Influence Coefficient	Overall Parameter Uncertainty
Steady-state thrust			0.6%
Measurements			
Chamber pressure	0.3%	0.0534 lbf/psi	
Throat area	0.5%	39.09 lbf/in^2	
Pulse-mode impulse bit			0.9%
Measurements			
Integrated chamber pressure	0.7%	0.01080 lbf-sec/psi	
Throat area	0.5%	0.695 lbf-sec/in^2	
Steady-state specific impulse			0.8%
Measurements			
Steady-state thrust	0.6%	46.0 sec/lbm	
Steady-state flow rate	0.5%	9,635 lbf	
Pulse-mode specific impulse			1.3%
Measurements			
Pulse-mode impulse bit	0.9%	2,000 lbm^{-1}	
Pulse-mode flow rate	1.0%	50,000 lbf-sec	